

Berichtsblatt

1. ISBN oder ISSN	2. Berichtsart Abschlussbericht
3a. Titel des Berichts SO178-KOMEX: "Kurilen Ochotskisches Meer EXperiment"	
3b. Titel der Publikation	
4a. Autoren des Berichts (Name, Vorname(n)) Dullo, Wolf-Christian; Werner, Reinhard; Haeckel, Matthias; Lembke-Jene, Lester; Abelmann, Andrea; Nürnberg, Dirk; Tiedemann, Ralf; Wallmann, Klaus; Biebow, Nicole; Georgeleit, Katharina	5. Abschlußdatum des Vorhabens 30. November 2006
4b. Autoren der Publikation (Name, Vorname(n))	6. Veröffentlichungsdatum
8. Durchführende Institution(en) (Name, Adresse) Leibniz-Institut für Meereswissenschaften IFM-GEOMAR Gebäude Ostufer Wischhofstr. 1-3 24148 Kiel	7. Form der Publikation Bericht
13. Fördernde Institution (Name, Adresse) Bundesministerium für Bildung und Forschung (BMBF) 53170 Bonn	9. Ber.Nr. Durchführende Insitution -
	10. Förderkennzeichen *) 03G0178A
	11a. Seitenzahl Bericht 13 + Anlagen
	11b. Seitenzahl Publikation --
	12. Literaturangaben 41 (ohne Anlagen)
	14. Tabellen 0 (ohne Anlagen)
	15. Abbildungen 3 (ohne Anlagen)
16. Zusätzliche Angaben	
17. Vorgelegt bei (Titel, Ort, Datum)	
18. Kurzfassung Im Rahmen von SO178-KOMEX wurden strukturgeologische, geochemische, paläo-ozeanographische und petrologische Untersuchungen im Ochotskischen Meer (Russland) durchgeführt. Diese multidisziplinären Arbeiten waren eine Ergänzung zum BMBF-geförderten russisch-deutschen Verbundvorhaben KOMEX. Die Expedition mit FS Sonne war die letzte Ausfahrt in diesem Projekt und diente dazu, abschließende Arbeiten im Ochotskischen Meer durchzuführen, die aus technischen und logistischen Gründen nicht von Bord russischer Forschungsschiffe realisiert werden konnten (u.a. der präzise Einsatz von TV-gesteuerten Geräten, langen Kolbenloten bis 25 m oder von dynamischer Positionierung). Einige der wichtigsten Ergebnisse von SO178-KOMEX sind: (1) die Entwicklung einer verbesserten Theorie zum POC-Abbau und Gashydratbildung, die erstmals verlässliche Vorhersagen global auch für andere Regionen erlaubt; (2) die Erkenntnis, dass in den Organik-reichen Sedimenten des Ochotskischen Meeres intensive Verwitterung von Silikatmineralen stattfindet mit Raten, die vergleichbar mit Verwitterungsraten an Land sind, und dass marine Silikatverwitterung potentiell eine sehr signifikante CO ₂ -Senke mit Relevanz im globalen Kohlenstoffkreislauf ist; (3) die Rekonstruktion der holozänen Dynamik von Methan-Venting Ereignissen vor Sachalin und deren möglichen Ursachen; (4) die Differenzierung der Inkorporationsmechanismen von Methan-induziertem Kohlenstoff in benthische Foraminiferen aus Cold-Seep-Gebieten, die Einblicke in Überlebensstrategien und Kalzifizierungsprozesse unter extremen Umweltbedingungen verschafft; (5) die verbesserte Rekonstruktion von Paläo-Methanentgasungs-Ereignissen anhand der Klassifizierung taphonomischer und frühdigenetischer Veränderungen in Foraminiferen-Faunen aus Cold-Seep-Gebieten; (6) die Entschlüsselung der Wachstumsmodi in Tiefwasserkorallen der Gattung <i>Keratoisis</i> spp. und die Entwicklung einer regional unabhängigen Sklerochronologie, die eine zukünftige Anwendung dieser Gattung als höchstauflösendes (subannuales) und langlebiges Klima-Archiv im tiefen Ozean ermöglicht; (7) die Entdeckung, vulkanologische und geochemische Charakterisierung und Datierung von Vulkanbauten auf dem Nordwesthang des Kurilenbeckens als entscheidender Baustein zur Entschlüsselung der geodynamischen Entwicklung des Kurilen-Systems.	
19. Schlagwörter Ochotskisches Meer, Kurilenbecken, Biogeochemie, Paläo-Ozeanographie, Cold Seeps, Gashydrate, Venting, Submarine Verwitterung, Vulkanologie, Magmatische Geochemie, Plattentektonik, Tiefwasserkorallen, Foraminiferen	
20. Verlag	21. Preis --

*) Auf das Förderkennzeichen des BMBF soll auch in der Veröffentlichung hingewiesen werden.

Document Control Sheet

1. ISBN or ISSN	2. Type of Report Final Report
3a. Report Title SO178-KOMEX: "Kurilen Ochotskisches Meer EXperiment"	
3b. Title of Publication	
4a. Author(s) of the Report (Family Name, First Name(s)) Dullo, Wolf-Christian; Werner, Reinhard; Haeckel, Matthias; Lembke-Jene, Lester; Abelmann, Andrea; Nürnberg, Dirk; Tiedemann, Ralf; Wallmann, Klaus; Biebow, Nicole; Georgeleit, Katharina	5. End of Project November 30, 2006
4b. Author(s) of the Publication (Family Name, First Name(s))	6. Publication Date
8. Performing Organization(s) (Name, Address) Leibniz-Institut für Meereswissenschaften IFM-GEOMAR Gebäude Ostufer Wischhofstr. 1-3 24148 Kiel	7. Form of Publication Report
13. Sponsoring Agency (Name, Address) Bundesministerium für Bildung und Forschung (BMBF) 53170 Bonn	9. Originator's Report No.
	10. Reference No. 03G0178A
	11a. No. of Pages Report 13 + Appendices
	11b. No. of Pages Publication --
	12. No. of References 41 (without appendices)
	14. No. of Tables none (without appendices)
	15. No. of Figures 3 (without appendices)
16. Supplementary Notes	
17. Presented at (Title, Place, Date)	
<p>18. Abstract</p> <p>In the framework of SO178-KOMEX structural-geological, geochemical, paleoceanological, and petrological investigations were carried out in the Okhotsk Sea (Russia). These multidisciplinary investigations were a completion to the Russian-German project KOMEX funded by the BMBF. The cruise of RV Sonne was the last one in this project with the aim to conduct final investigations in the Okhotsk Sea which – for technical or logistical reasons - could not be carried out during former cruises on Russian research vessels (e.g., exact deployment of TV-guided instruments, deployment of up to 25 m long corers, dynamic vessel positioning).</p> <p>Some of the most important results of SO178-KOMEX are the following:</p> <p>(1) improvement of the theory about the degradation of particulate organic matter and the formation of gas hydrates. This theory for the first time allows reliable forecasts for other regions on a global basis.</p> <p>(2) knowledge that intensive weathering of silicate minerals takes place in the organic-rich sediments of the Okhotsk Sea at such rates which are similar to the weathering rates ashore as well as the knowledge that marine silicate weathering is a significant potential CO₂ sink being relevant in the global carbon turnover;</p> <p>(3) reconstruction of the Holocene dynamics of methane venting events off Sakhalin and their possible causes;</p> <p>(4) differentiation of the inclusion of methane-induced carbon in benthic foraminifera in cold-seep regions giving insights into survival strategies and calcification processes in extreme environmental conditions;</p> <p>(5) improved reconstruction of paleo-methane degassing events by means of classification of taphonomic and early diagenetic changes in foraminifera in cold-seep regions;</p> <p>(6) decoding of growth modes of the deep-water coral species <i>Keratoisis</i> spp. and the development of a regionally independent sclerochronology allowing a future use of this species as high-resolution (subannual) and long-living climate archive in the deep ocean;</p> <p>(7) discovery, volcanological and geochemical characterization and dating of volcanic edifices on the NW slope of the Kurile Basin as important step towards the decoding of the geodynamic development of the Kurile system.</p>	
19. Keywords Ochotsk Sea, Kurile Basin, Biogeochemistry, Paleo-Oceanography, Cold Seeps, Gas Hydrates, Venting, Submarine Weathering, Volcanology, Magmatic Geochemistry, Plate Tectonics, Marine Biology, Deep-Sea Corals, Foraminifera	
20. Publisher	21. Price --

S O 1 7 8 - K O M E X

**Kurilen Ochotskisches Meer EXperiment:
Stoffaustauschprozesse und -bilanzen im Ochotskischen
Meer: Wirkungsweise von klimatologischen,
ozeanographischen, sedimentären und krusten-
geologischen Steuerungsfaktoren**

Abschlussbericht

- 03G0178A -

Berichtszeitraum: 01. Juni 2004 bis 31. Mai 2006

W.-Chr. Dullo

unter Mitarbeit von

***R. Werner, M. Haeckel, L. Lembke-Jene, A. Abelmann, D. Nürnberg,
R. Tiedemann, K. Wallmann, N. Biebow, K. Georgeleit***

I.1. Aufgabenstellung

Im Rahmen von SO178-KOMEX sollten umfangreiche strukturgeologische, geochemische, paläo-ozeanographische und petrologische Untersuchungen im Ochotskischen Meer durchgeführt werden. Diese multidisziplinären Arbeiten waren als Ergänzung zum BMBF-geförderten russisch-deutschen Verbundvorhaben KOMEX (Kurilen Ochotskisches Meer EXperiment) geplant. Die Expedition mit FS Sonne war als letzte Ausfahrt in diesem Projekt geplant und sollte dazu dienen, abschließende Arbeiten im Ochotskischen Meer durchzuführen, die aus technischen und logistischen Gründen nicht von Bord russischer Forschungsschiffe realisiert werden konnten (u.a. der präzise Einsatz von TV-gesteuerten Geräten, langen Kolbenloten bis 25 m oder von dynamischer Positionierung).

Das Ziel des KOMEX-Projektes war es, die Funktionsweise des Systems „Ochotskisches Meer“ zu untersuchen und seine Wirkung auf Stoffverteilung, Stoffkreislauf, Wassermassenbildung, Zirkulation und Klima sowie dessen plattentektonische Stellung zu bewerten. Das Ochotskische Meer eignet sich besonders für derartige Untersuchungen, da in diesem räumlich eng begrenzten Meeresgebiet die Wechselwirkungen zwischen Geosphäre, Biosphäre, Kryosphäre, Hydrosphäre und Atmosphäre exemplarisch untersucht werden können. Das Ochotskische Meer und seine Umgrenzungen stellen ein klimasteuerndes Meeresgebiet dar, dem eine globale Schlüsselfunktion zukommt. So weist das Ochotskische Meer beispielsweise die höchste potentielle Methanproduktionsrate der nördlichen Hemisphäre auf, die durch die für diese Breiten ungewöhnliche saisonale Eisbedeckung (ca. 7 Monate im Jahr) in besonderer Weise reguliert wird, und ist damit eine bedeutende Quellenregion für den Eintrag klimarelevanter Gase in die Atmosphäre. Das Ochotskische Meer hat auch entscheidenden Einfluss auf die Wassermassenbildung im Pazifik und damit auf das Klima und Paläoklima im gesamten pazifischen Raum. Die geplanten Untersuchungen im Ochotskischen Meer bieten deshalb die Möglichkeit, die steuernden ozeanographischen und klimatischen Parameter für die Entwicklung des größten Ozeans der Welt exemplarisch zu studieren und in globale Klimamodelle einfließen zu lassen.

Die Forschungsschwerpunkte von SO178 sollten zu den übergeordneten Zielen von KOMEX beitragen und konzentrierten sich auf Fragen nach:

- der Rekonstruktion des tektonischen Aufbaus und der Entwicklung des Ochotskischen Meeres mit strukturgeologischen und vulkanologisch-petrologischen Methoden,
- der geochemischen, hydrochemischen, marin-geologischen und biologischen Charakterisierung der zwei verschiedenen Vent-Systeme am Schelf und Kontinentalhang vor NE-Sachalin und im Deruginbecken,
- der Rekonstruktion der paläo-ozeanographischen und paläoklimatischen Entwicklung des Ochotskischen Meeres auf Zeitskalen von Dekaden bis Jahrhunderten,
- der Etablierung einer neuen Methode zur Charakterisierung von Wassermassenstrukturen in der geologischen Vergangenheit anhand von Isotopenanalysen an biogenem Silikat und
- der Erfassung und Beprobung von Tiefwasserbiohermen am Kontinentalhang vor Sachalin.

I.2. Voraussetzungen

Ein großer Teil des Kenntnisstandes über die im Rahmen von SO178-KOMEX im Ochotskischen Meer zu bearbeitenden Fragestellungen beruhte zum Zeitpunkt der Ausfahrt auf Daten, die in den Jahren 1998 bis 2004 während des BMBF-geförderten Verbundvorhabens KOMEX gewonnen wurden (> 70 Publikationen). Alle KOMEX-Aktivitäten wurden gemeinsam vom P.P. Shirshov Institute of Oceanology in Moskau, dem Pacific Oceanological Institute in Wladiwostok und dem IFM-GEOMAR in Kooperation mit zahlreichen weiteren russischen und deutschen Instituten organisiert. Die Kontakte, die durch diese gemeinsamen Untersuchungen zu russischen Wissenschaftlern hergestellt wurden, waren grundlegend für SO178-KOMEX und konnten im Rahmen dieses Projektes weiter intensiviert werden. Die Voraussetzung für die Realisierung des Forschungsvorhabens SO178-KOMEX war somit der erfolgreiche Abschluss der Verbundvorhaben KOMEX I und II.

SO178-KOMEX stellte die Fortsetzung der Forschungsaktivitäten im Rahmen des KOMEX-Verbundvorhabens dar. Im Vordergrund der Untersuchungen stand daher, die noch offenen Fragen zu klären und die verschiedenen Forschungsansätze des Verbundprojektes durch einige abschließende Untersuchungen zu verdichten.

I.3. Planung und Ablauf des Vorhabens

Der Ablauf des Vorhabens entsprach im Wesentlichen der von uns im Antrag vorgeschlagenen Arbeits-, Zeit- und Ausgabenplanung

Die Vermessungs- und Beprobungsarbeiten auf der Ausfahrt SO178 (22.07. – 15.09.2004) verliefen außerordentlich erfolgreich. Insgesamt wurden 86 Stationen angefahren. Dabei wurden Kolbenlot (bis 25m), Schwerelot, Kastenlot, Hydrocorer, TV-Multicorer, TV-Greifer, OFOS, CTD, Kettensackdredgen und Multinetz eingesetzt sowie umfangreiche hydroakustische Vermessungen (SIMRAD, PARASOUND) durchgeführt. Der Verlauf von SO178 sowie die Ergebnisse der Beprobungs- und Vermessungsarbeiten sowie der bereits an Bord durchgeführten Analytik sind ausführlich im Fahrtbericht (Dullo et al. 2003, <http://www.ifm-geomar.de/div/projects/komex/sonne/index.html>) beschrieben.

Die sich an die Ausfahrt anschließenden präparativen und analytischen Laborarbeiten sowie die Datenauswertung und Interpretation wurde zwischen Herbst 2004 und Sommer 2006 an den an SO178 beteiligten Instituten weitestgehend planmäßig durchgeführt (s.a. Abschnitt I.5.). Insgesamt bildete das auf der Expedition gewonnene Daten- und Probenmaterial eine hervorragende Grundlage für die verschiedenen weiterführenden, im Antrag umfassend dargestellten Laborarbeiten und Analysemethoden, aus denen die unten vorgestellten Ergebnisse resultieren.

I.4. Wissenschaftlich-technischer Stand (an den angeknüpft wurde)

Der wissenschaftlich-technische Stand war im Antrag zu dem Forschungsvorhaben ausführlich beschrieben.

I.5. Zusammenarbeit mit anderen Stellen

Während der Laufzeit des Vorhabens wurde mit verschiedenen Stellen im In- und Ausland, vor allem in Russland, intensiv und erfolgreich zusammengearbeitet. Diese Kooperationen, die zukünftig im Rahmen anderer Projekte (z.B. des kürzlich bewilligten BMBF-Verbundvorhabens KALMAR) fortgeführt werden, erbrachten zahlreiche Ergebnisse, die in Abschnitt II.1. dargestellt und bereits in gemeinsame Publikationen eingeflossen sind. Unsere wichtigsten Kooperationspartner sind (in alphabetischer Reihenfolge der Institute/ Firmen):

Alfred-Wegener-Institut Bremerhaven

Dr. H. Jacot des Combes (Mikropaläontologie, biogene Silikate)
Dr. H. Meyer (Mikropaläontologie, biogene Silikate)

Alfred-Wegener-Institut Potsdam

Dr. H. Meyer (Mikropaläontologie, biogene Silikate)

Dalhousie University, Oceanography, Halifax (Kanada)

Dr. B.P. Boudreau (Transport-Reaktions-Modellierung)

Far Eastern Geological Institute FEB RAS, Wladiwostok (Russland)

Dr. I. Tararin (Petrologie)

Geosphere-Biosphere Science Centre, Universität Lund (Schweden)

U. Kokfelt (terrestrische Pollenanalysen)

IFM-GEOMAR Leibniz-Institut für Meereswissenschaften, Kiel

Prof. Dr. A. Eisenhauer (U/Th-Datierungen)

IODP-Bremen Core Repository, DFG-Forschungszentrum Ozeanränder, Bremen

Dr. U. Röhl (Universität Bremen; Sedimentlogging)

Institut für Geowissenschaften der CAU, Kiel

Prof. Dr. M. Sarnheim (Paläoozeanographie des Nordpazifik)
 Dr. B. Bader (REM/EDX-Labor)
 Dr. G. Bartoli (Mg/Ca Analytik von Benthosforaminiferen)

Institut für Paläontologie der Universität, Erlangen

Dr. S. Noé (Biomineralisation von Gorgonien, Sclerochronologie)
 Prof. Dr. A. Freiwald (Ökologie von Tiefwasserkorallen-Habitaten)

Institute of Geological and Nuclear Sciences, Wellington (New Zealand)

Dr. J. Greinert (Bathymetrie, Karbonate, Baryte)

Institute of Ocean Sciences, Sidney (Kanada)

Dr. C.S. Wong (Thermodynamik)

Leibniz-Institut für Altersbestimmung und Isotopenforschung, Kiel

Prof. Dr. P.M. Grootes (AMS ¹⁴C-Datierungen)
 Dr. H. Erlenkeuser (konvent. ¹⁴C-Datierungen, Wasserchemie)
 Dr. N. Andersen (stabile Isotopen an Wasserproben)

Pacific Oceanological Institute FEB RAS, Wladiwostok (Russland)

Dr. A. Astakhov (Haupt- und Nebenelementverteilungen in Oberflächensedimenten)
 A. Bosin (Primärproduktivitäts-Proxies)
 Dr. A. Derkachev (authigene Karbonate der Vent-Gebiete)
 Dr. S. Gorbarenko (regionale Paläo-Ozeanographie)
 Dr. N. Nikolaeva (Bestimmung lithogener Komponenten, Tephren)
 Dr. A. Obzhirov (Methan-Analytik)
 Dr. A. Salyuk (regionale physikalische Ozeanographie)
 Dr. P. Tishchenko (Geochemie, Thermodynamik, Bathymetrie, ak. Detektion von Gasflares)
 Dr. G. Pavlova (Geochemie, Thermodynamik, Bathymetrie, ak. Detektion von Gasflares)
 Dr. V. Sosnin (Geochemie, Thermodynamik, Bathymetrie, ak. Detektion von Gasflares)
 Dr. V. Shevstov (Geochemie, Thermodynamik, Bathymetrie, ak. Detektion von Gasflares)

P.P. Shirshov Institute of Oceanology RAS, Moskau (Russland)

Dr. B. Baranov (Bathymetrie, Tektonik, Vulkanologie)
 Prof. Dr. M. Barash (Mikropaläontologie, Foraminiferen)
 Dr. N. Bubenchshikova (Benthosforaminiferen-Vergesellschaftungen)
 Dr. A. Matul (Mikropaläontologie, biogene Silikate)

Université Lyon, Laboratoire de Paléoenvironnements et Paléobiosphère (Frankreich)

Dr. G. Aloisi (Geochemie, Isotopensysteme)

University of California Santa Cruz, Bodega Marine Laboratory (USA)

Prof. Dr. T.M. Hill (Methanventing, Tiefwasserkorallen im NE-Pazifik)

Tethys Geoconsulting GmbH, Kiel

Dr. N. Biebow (Vorbereitung und Durchführung der Ausfahrt, Paläo-Ozeanographie)
 Dr. R. Werner (Bathymetrie, Vulkanologie, magmatische Geochemie)
 L. Lembke-Jene (Paläo-Ozeanographie)
 Dr. S. Noé (Biomineralisation von Gorgonien, Sklerochronologie)

Weizmann Institute of Science, Rehovot (Israel)

Prof. Dr. A. Shemesh (Mikropaläontologie, biogene Silikate)

II.1. Darstellung der erzielten Ergebnisse**II.1.1. Publierte oder in Manuskripten vorliegende Ergebnisse**

Ein Großteil der wissenschaftlich-technischen Ergebnisse von SO178-KOMEX ist in eine Reihe von Artikeln eingeflossen, die bereits zur Publikation eingereicht wurden oder in Kürze eingereicht werden. Daher werden diese Ergebnisse hier nicht detaillierter erläutert.

Stattdessen sind die im Folgenden aufgelisteten Manuskripte dem Abschlussbericht im Anhang beigelegt:

- (a) Wallmann K, Aloisi G, Haeckel M, Obzhairov A, Pavlova G, Tishchenko P (2006) Kinetics of organic matter degradation, microbial methane generation, and gas hydrate formation in anoxic marine sediments. *Geochimica et Cosmochimica Acta* 70: 3905-3927

Geochemische Daten aus anoxischen Sedimenten, die in einem S-N verlaufenden Schnitt entlang des Sachalin-Schelfs (Ochotskisches Meer) gewonnen wurden, wurden mit einem numerischen Transport-Reaktions-Modell ausgewertet. Dabei konnte festgestellt werden, dass die Abbaurate von partikulärem organischem Kohlenstoff (POC) von dessen Konzentration, einer altersabhängigen kinetischen Konstante und der Konzentration gelöster Metaboliten abhängt. Eine neue mathematische Formulierung wurde entwickelt und erfolgreich auf gut untersuchte Lokationen, wie z.B. Blake Ridge, angewandt. Unsere neue kinetische Formulierung verbessert die Abschätzungen von Methanhydrat-Mengen für einen sehr viel weiteren Bereich von Sedimentationsraten und Wassertiefen als dies mit den bisherigen Modellansätzen möglich war. Ein Sonderdruck dieser Arbeit liegt diesem Bericht in Anlage 3 bei.

- (b) Noé SU, Dullo W-Chr (2006) Skeletal morphogenesis and growth mode of modern and fossil deep-water isidid gorgonians (Octocorallia) in the West Pacific (New Zealand and Sea of Okhotsk). *Coral Reefs*, 25: 303-320.

Diese Studie untersucht vergleichend Skelett-Morphogenese und Wachstumsmodus rezenter und fossiler Kaltwasserkorallen der Gattung *Keratoisis* sp. aus dem Ochotskischen Meer (SO178-KOMEX) und dem Südwestpazifik (SO168-ZEALANDIA). Hierbei wurden Ultrastruktur, Wachstumsstrukturen und lineare Extensionsraten der Mg-calcitischen Internodien bestimmt. Letztere deuten auf eine subannuale Auflösung innerhalb einzelner Wachstums-Inkrementen hin, die eine zukünftige Verwendung von *Keratoisis* spp. als hochauflösendes paläozeanographische Archiv aus intermediären Wassertiefen ermöglichen wird. Ein Sonderdruck dieser Arbeit liegt diesem Bericht in Anlage 4 bei.

- (c) Lembke-Jene L, Tiedemann R, Nürnberg D, Wallmann K, Obzhairov A, Dullo W-Chr (eingereicht) Variable Holocene Methane Emissions from Cold Seeps on the Sakhalin Margin, Okhotsk Sea Linked to seismo-tectonic Activity. *Geochemistry Geophysics Geosystems*

Diese Studie ermittelt anhand stabiler Isotope aus Foraminiferen die Chronologie möglicher Paläo-Methanentgasungsereignisse am Kontinentalhang von Sachalin während der letzten ca. 7.000 Jahre vor heute. Diese Entgasungsereignisse lassen sich stromabwärts des unmittelbaren „Obzhairov-Flare“ Cold-Seep-Gebietes in $\delta^{13}\text{C}$ -Profilen planktischer Foraminiferen aus zwei Sedimentkernen früherer KOMEX II-Expeditionen wiederfinden. Dies, sowie die Korrelation der Anomalien mit regionalen Indikatoren seismisch-tektonischer Aktivität, legt nahe, dass Methanentgasungsereignisse evt. größer als heute bekannt waren, von regionaler Bedeutung sein können und möglicherweise an tektonische Aktivität entlang der Plattengrenzen im Japan- bzw. Kurilen-Kamtschatka-Bogen gekoppelt sind. Ein Vorabdruck dieser Arbeit liegt diesem Bericht in Anlage 5 bei.

- (d) Aloisi G, Wallmann K, Tishchenko P, Haeckel M, Pavlova G, Greinert J, Eisenhauer A (eingereicht) A possible long-term CO_2 sink through submarine weathering of detrital silicates. *Geochimica et Cosmochimica Acta*.

In dieser Studie wird gezeigt, dass in den Organik-reichen Sedimenten im Ochotskischen Meer intensive Verwitterung von Silikaten stattfindet. Dieser Prozess wird begünstigt durch den Eintrag von frischen Silikatmineralen aus dem Amur-Becken mit kaltem Wasser und mikrobielle Aktivität, die den pH-Wert des Porenwassers senkt und gelöste Huminstoffe freisetzt. Numerische Simulationen der frühdiagenetischen Prozesse zeigen, dass die Verwitterungsraten im Untersuchungsgebiet denen an Land ähnlich sind. Silikatverwitterung an Land stellt die größte Senke für atmosphärisches CO_2 auf langen

Zeitskalen (Mio. Jahre) dar. Somit könnte die marine Silikatverwitterung in Organikreichen Sedimenten auch eine signifikante CO₂-Senke darstellen, die bislang nicht berücksichtigt wurde. Ein Vorabdruck dieser Arbeit liegt diesem Bericht in Anlage 7 bei.

- (e) Lembke-Jene L, Tiedemann R, Wallmann K, Dullo C, Obzhairov A, Andersen N, Nürnberg D (in Vorbereitung) Incorporation of Methane-Derived Carbon in $\delta^{13}\text{C}$ of selected rose Bengal-Stained benthic foraminifera from Cold Seep Sites in the Okhotsk Sea. Manuscript 72 pp and fig, Deep-Sea Research I

In dieser Studie werden anhand einer Reihe von Multicorer-Sedimentprofilen charakteristische Signaturen von $\delta^{13}\text{C}$ und $\delta^{18}\text{O}$ an lebenden Benthosforaminiferen ermittelt, wobei die gewonnenen Proben ein breites Spektrum von verschiedenen Methan-Cold Seeps mit unterschiedlich starker Aktivität und differierenden Porenwassergradienten abdecken. Es wurden Spezies-spezifischer Inkorporationsmechanismen von $\delta^{13}\text{C}$ in Foraminiferen vergleichend erfasst, um damit biologische Adaption und Kalzifizierungsmechanismen unter extremen Umweltbedingungen besser zu verstehen. Gleichzeitig konnte ermittelt werden, unter welchen Umständen $\delta^{13}\text{C}$ -Daten von benthischen Foraminiferen geeignete Proxies zur Rekonstruktion von Paläo-Methanentgasungsereignissen darstellen. Die Ergebnisse stellen darüber hinaus den ersten rezenten $\delta^{13}\text{C}$ - $\delta^{18}\text{O}$ -Kalibrierungsdatensatz für paläo-ozeanographische Rekonstruktionen mit benthischen Foraminiferen aus dieser Region bereit. Ein Vorabdruck dieser Arbeit liegt diesem Bericht in Anlage 8 bei.

Weiterhin wurde bisher auf zahlreichen nationalen oder internationalen Tagungen über Ergebnisse von SO178-KOMEX berichtet (s. Abschnitt II.4. „Erfolge und geplante Veröffentlichungen“).

II.1.2. Weitere Ergebnisse

Darüber hinaus wird noch an einigen Teilaspekten der Daten gearbeitet, weitere Publikationen sind in Vorbereitung. Die wichtigsten Ergebnisse von SO178-KOMEX, die nicht in den beiliegenden Manuskripten publiziert werden, werden daher im Folgenden kurz zusammengefasst:

A. Vulkanologie, magmatische Geochemie und Tektonik (R. Werner, B. Baranov et al.)

Die im Folgenden zusammengefassten Ergebnisse werden zur Zeit zur Veröffentlichung vorbereitet. Es ist vorgesehen, während eines Besuches von Dr. Baranov in Kiel im Dezember 2006 die Arbeiten an diesem Manuskript abzuschließen und es zur Publikation einzureichen. Dieses Manuskript wird dann umgehend nachgereicht.

Ein Ziel der Ausfahrt SO178 war es, mit strukturgeologischen und vulkanologisch-petrologischen Methoden zur Rekonstruktion der Öffnungsgeschichte und Entwicklung des Kurilenbeckens im Ochotskischen Meer beizutragen und damit neue Erkenntnisse über die Öffnung von „Back Arc“-Becken zu gewinnen. Hierzu wurden Kartierungen mit dem Fächerecholot (SIMRAD) und dem Sedimentecholot (PARASOUND) unter anderem am nordwestlichen Hang des Kurilenbeckens durchgeführt. Dabei wurde dort eine NNE-SSW verlaufende Kette von Vulkanen in ca. 1.500 bis 2.600 m Wassertiefe entdeckt, kartiert und beprobt, die von den Fahrtteilnehmern „Sonne Chain“ genannt wurde. Die Vulkankette liegt in der Verlängerung eines Basement-Rückens („Sakura Ridge“) im zentralen Kurilenbecken, der als Spreizungszentrum interpretiert wird (Abb. 1; Baranov et al. 2002a, b).

OFOS-Beobachtungen am südlichsten (und am tiefsten gelegenen) Vulkan des „Sonne Chain“ haben gezeigt, dass zumindest sein oberer Bereich im Wesentlichen aus geschichteten Vulkaniklastika besteht. Diese Ablagerungen (und auch die dort gewonnenen Proben) zeigen deutliche Merkmale phreatomagmatischer Ablagerungen, was auf eine ehemalige Aktivität dieses Vulkanes im Flachwasser (oder auch an Land) hindeutet. Diese Beobachtung ist konsistent mit dem aus KOMEX I und II resultierenden Modell, dass das Kurilenbecken (infolge von Kompression) stark abgesunken ist (Baranov et al. 2002c).

⁴⁰Ar/³⁹Ar-Laserdatierungen ergaben ein einheitliches Alter von knapp 26 Mio. Jahren für die am „Sonne Chain“ gedredgeten Laven. Haupt- und Spurenelementanalysen an diesen Laven zeigen, dass diese eine sehr einheitliche, trachytische Zusammensetzung haben und

somit wahrscheinlich aus einer Quelle stammen. Sie besitzen verstellte Seltene Erden Element Muster, d.h. sie sind an leichten Seltene Erden angereichert und zeigen in Multielementdiagrammen typische „Inselbogenmuster“, die weitestgehend denen der Gesteine des Kurilenbogens entsprechen. Auch ihre Sr- und Nd-Isotopenverhältnisse fallen in das Feld der Gesteine des Kurilenbogens. Dagegen sind die Pb-Isotopenzusammensetzungen der Gesteine der „Sonne Chain“-Vulkane etwas weniger radiogen als die des Kurilenbogens und weisen auf eine Assimilation von unterer kontinentaler Kruste und/oder angereichertem sub-lithosphärischen Mantel („EM I“-Typ) hin. Letzteres kann jedoch auf die Lage der Vulkane auf kontinentaler Kruste am Nordrand des Kurilenbeckens zurückgeführt werden. Auch könnte der Aufstieg der Magmen durch bzw. deren Stagnation in der kontinentalen Kruste des Nordhangs die trachytische Zusammensetzung der Laven erklären.

Abgesehen von diesen „kontinentalen Effekten“ unterscheiden sich die geochemischen Signaturen der „Sonne Chain“-Vulkane von denen des Kurilenbogens kaum. Dies weist darauf hin, dass diese Vulkane vor 26 Mio. Jahren aus der gleichen (oder zumindest einer sehr ähnlichen) Magmenquelle gespeist wurden wie die deutlich jüngeren Inselbogenvulkane der heutigen Kurilen. Dabei konnte sich der Magmatismus in der kontinentalen Kruste aber offenbar nicht richtig entwickeln und verursachte dort nur relativ geringvolumigen Vulkanismus.

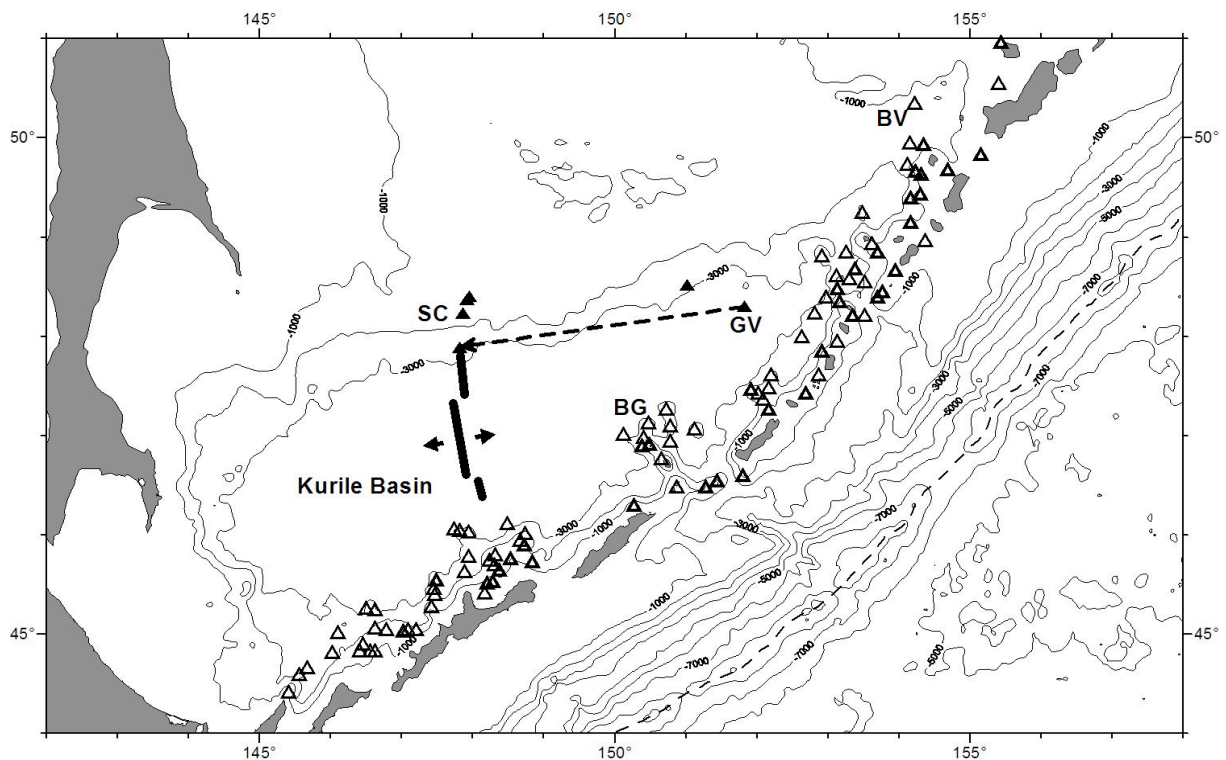


Abb. 1: Karte des Kurilenbeckens und des Kurilen-Inselbogens. Die offenen Dreiecke markieren die Vulkane in diesem Gebiet nach Avdeiko et al. (1992), die schwarzen Dreiecke submarine Vulkane im Kurilenbecken und auf dessen Nordwesthang, die im Rahmen von SO178 und weiteren Ausfahrten im Rahmen des Projektes KOMEX untersucht wurden (SC=Sonne Chain, BG=Browton Group, GV=Geophysicist, BV=Belyankina). Die dicke schwarze Linie kennzeichnet den Sakura-Rücken, der als Spreizungszentrum interpretiert wird (Baranov et al. 2002a, b) und die dicke gestrichelte Linie die mögliche Bewegung des „Sonne Chain“ (dünne gestrichelte Linie: Achse des Kurilen-Tiefseegrabens; Kontourintervall: 1.000 m).

Die Entdeckung dieser „Paläo-Kurilenvulkane“ erlaubt Rückschlüsse auf die Öffnungsgeschichte des Kurilenbeckens. Die Vulkane des „Sonne Chain“ sind Relikte aus der Bildungsphase des Kurilen-Inselbogens (Oligozän-Miozän) und markieren

wahrscheinlich den Beginn der Öffnung des Kurilenbeckens, da sie offenbar vor ca. 26 Mio. Jahren durch tektonische Prozesse von ihren Magmenquellen und damit vom Inselbogen wegbewegt wurden. Junge bzw. ±rezent aktive "Back Arc"-Vulkane des Kurilen-Inselbogens wie z.B. der im Rahmen von KOMEX untersuchte Geophysicist Vulkan (ca. 1 Mio. Jahre alt, Baranov et al. 2002c) befinden sich heute in maximal 280 km Entfernung vom Kurilen-Tiefseeegraben, während die Entfernung vom Graben bis zum nördlichsten Vulkan des „Sonne Chain“ etwa 500 km beträgt. Bei einer Öffnung des Kurilenbeckens in Ost-West-Richtung deutet dies darauf hin, dass der „Sonne Chain“ sich heute mindestens 300 km von seiner ursprünglichen Quelle entfernt befindet und dass sich das Kurilenbecken mit durchschnittlich 12 mm pro Jahr geöffnet hat (Abb. 1). Zusammen mit den Ergebnissen einer kürzlich abgeschlossenen russischen Ausfahrt (2006) könnten die Erkenntnisse von den „Sonne Chain“-Vulkanen ein entscheidender Baustein zur Entschlüsselung der geodynamischen Entwicklung des Kurilen-Systems sein.

Zitierte Literatur:

- Avdeiko GP, Volynets ON, Antonov AYu, Bondarenko VI, Rashidov VA, Gladkov NG (1992) Catalogue of submarine volcanoes of the Kurile Arc, North Iturup group. In: Yu.M. Puscharovsky (Editor). Submarine Volcanism and Zonality of the Kurile Island Arc. Science, Moscow: 172-198 (in Russian).
- Baranov BV, Wong HK, Dozorova KA, Karp BYa, Lüdmann T, Karnaukh VN (2002a) Opening geometry of the Kurile Basin (Sea of Okhotsk) as inferred from structural data. *The Island Arc* 11, 3: 206-219.
- Baranov BV, Dozorova KA, Karp BYa., Karnaukh, VN, Wong HK, Lüdmann T (2002b) Origin of basement height in the central Kurile Basin: shear zone or spreading ridge?. *Papers of Russian Academy of Sciences* 382, 4: 513-516. (in Russian)
- Baranov, BV, Werner R, Hoernle K, Tsoy I, Bogaard Pvd, Tararin IA (2002c) Volcanological, geochemical, paleo-oceanological and geophysical evidence for compressionally-induced high subsidence rates in the Kurile basin (Okhotsk Sea). *Tectonophysics* 350: 63-97

B. Isotopensignale in biogenem Silikat, ein neuer Ansatz zur Charakterisierung der Wassermassenstruktur in der geologischen Vergangenheit (A. Abelmann)

Das Ochotskische Meer ist eines der hochproduktivsten Ozeangebiete des Weltozeans und durch hohe Akkumulation von biogenem Opal gekennzeichnet. Die zweite Besonderheit dieses Randmeeres ist, dass hohe Umsatzraten des Mesozooplanktons auf eine effektive Abspeicherung von organischem Kohlenstoff hinweisen (Hays & Morley 2002). Radiolarien sind ein wesentlicher Bestandteil des mesopelagischen Zooplanktons im Ochotskischen Meer (Abelmann & Nimmergut 2005, Nimmergut & Abelmann 2002). Aufgrund ihrer fossilen Überlieferbarkeit sind Radiolarien wichtige Informationsträger, die dazu beitragen, den Einfluss des Mesopelagials auf die Abspeicherung von organischem Kohlenstoff im Ozean in der Vergangenheit zu entschlüsseln. Diatomeen gehören dem Phytoplankton an und geben wichtige Informationen über die Produktivität an der Ozeanoberfläche. Isotopenuntersuchungen an biogenem Opal ($\delta^{18}\text{O}$, $\delta^{13}\text{C}$, $\delta^{15}\text{N}$, $\delta^{30}\text{Si}$) stellen damit eine relativ neu entwickelte Methode zur Rekonstruktion von Änderungen der Oberflächensalzgehalte sowie Abschätzung der biologischen Produktion und Nährstoffnutzung dar (Shemesh et al. 1994, 2002; De La Rocha et al. 1998, Sigmann et al. 1999, Brzezinski et al. 2002, Crosta & Shemesh 2002, Robinson et al. 2004, 2005; Schneider-Mor et al. 2005). Mit der Messung stabiler Isotope an den silikatischen Hartteilen beider Organismengruppen kann dazu beigetragen werden, Prozesse zur Produktionsbiologie und Kohlenstoffabspeicherung sowie zur Bildung von Wassermassenstrukturen in der geologischen Vergangenheit besser zu verstehen. Damit können wesentliche Informationslücken bei der Rekonstruktion vergangener Umwelt- und Klimabedingungen und der Einfluss der dort ablaufenden Prozesse für die Klimaentwicklung besser abgeschätzt werden.

Um diesen Fragestellungen nachzugehen, wurde auf der SO178-Expedition auf einem N-S-Profil, entlang des hochproduktiven Kontinentalhanges vor Sachalin, Planktonproben aus verschiedenen Wasserstockwerken (bis 1.000 m) entnommen. Die Beprobung erfolgte mit dem Multinetz, einem Vertikalnetz, das eine Beprobung von 5 Tiefenintervallen ermöglicht.

Parallel dazu wurden Wasserproben für isotopechemische Untersuchungen aus denselben Tiefenbereichen wie die der Planktonproben entnommen. Diese Messungen sollen als Vergleichsdaten für die Planktonmessungen genutzt werden. Um die Radiolarien aus dem mesopelagischen Bereich anzureichern, wurde das Multinetz an jeder Station auf dem NS-Profil dreimal eingesetzt. Dabei wurden insgesamt 9 Netze aus einer Wassertiefe von 600-200 m und jeweils 3 Netze aus dem Bereich 200-50 m und 50-0 m entnommen. Parallel zu der Probenentnahme wurden hydrographische Daten mit einer CTD-Sonde gemessen. Die Proben wurden in drei Größenklassen fraktioniert ($>500\mu\text{m}$, $40-500\mu\text{m}$, $<40\mu\text{m}$). Zur Konservierung für die isotopegeochemischen Messungen wurden die Proben tiefgefroren.

Die Methode zur Aufbereitung, Trennung und Anreicherung der kieseligen Komponenten (Diatomeen und Radiolarien) wurde in der Zwischenzeit am AWI in einem dazu neu eingerichteten Labor entwickelt. Dabei geht es um die quantitative Trennung der kieseligen Skelette vom Restsediment und die Trennung von unterschiedlichen kieseligen Mikrofossilgruppen (Radiolarien/Diatomeen) sowie die Abtrennung von Artengruppen mit unterschiedlichen Umweltansprüchen. Wesentlicher Teil dieser Aufbereitung ist der Einsatz hydraulischer Trennverfahren mit Hilfe von Splitkanälen (Abb. 1). Dazu werden in einem laminierten Strom Partikel unterschiedlicher Größe und Form von einander getrennt. In umfangreichen Testläufen wurden am AWI bereits Parameter entwickelt, um Diatomeen und Radiolarien von einander zu trennen (Abb. 2). Darüber hinaus ist es möglich, verschiedene Artengruppen abzutrennen. Die Methode wird derzeit weiter entwickelt.

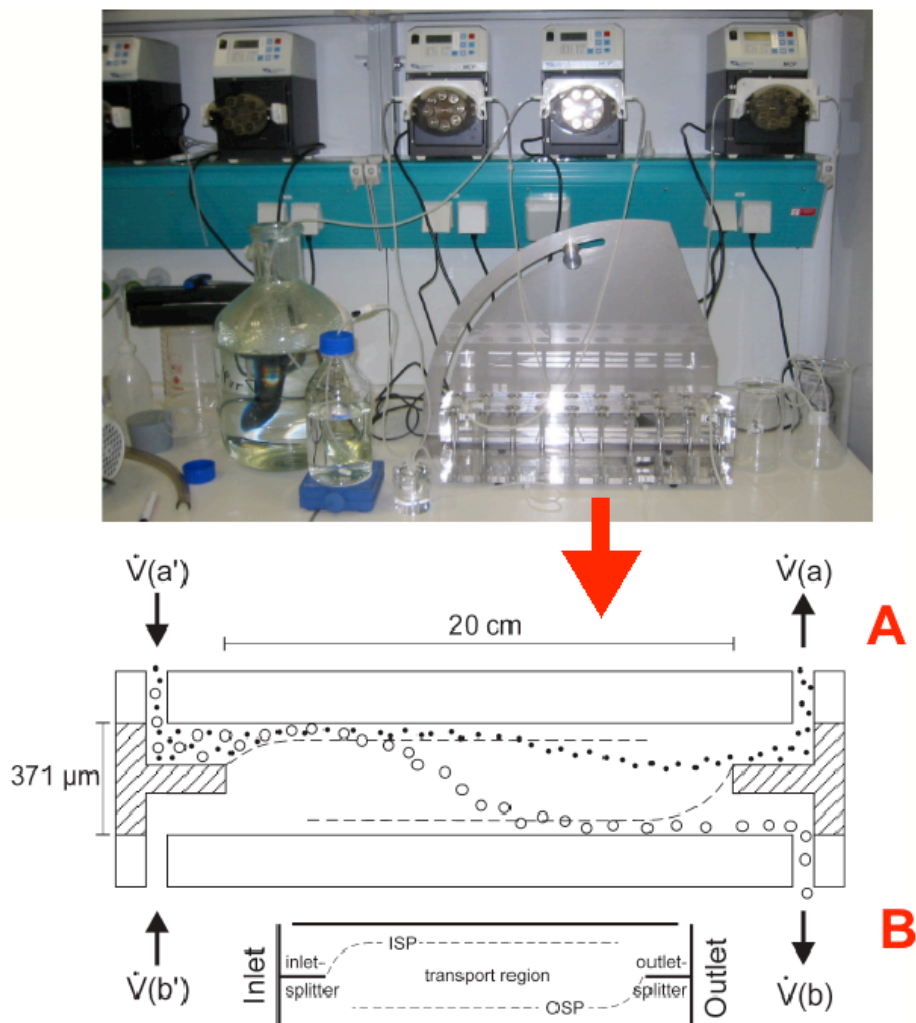


Abb. 1: Splitkanal am AWI und schematische Darstellung nach Rings et al. (2004).

Die Messungen werden an einem MAT 253 ($\delta^{30}\text{Si}$, $\delta^{15}\text{N}$, $\delta^{13}\text{C}$) in Bremerhaven und einem mit Laser ausgestatteten PDZ Europa Massenspektrometer ($\delta^{18}\text{O}$) in Potsdam durchgeführt. Erste Messungen an Diatomeen an einem Kern aus dem Südozean aus dem Stadium 5.5 haben gezeigt, dass die $\delta^{18}\text{O}$ -Werte mit denen von Shemesh et al. (1994, 2002) übereinstimmen. Am MAT 253 (AWI Bremerhaven) werden derzeit erste Kalibrierungsmessungen von $\delta^{15}\text{N}$ und $\delta^{13}\text{C}$ durchgeführt. Für $\delta^{30}\text{Si}$ -Messungen wird eine Automatisierung mit Hilfe eines für $\delta^{30}\text{Si}$ -Messungen modifizierten „Kiel III Carbonate Device“ eingerichtet (Brzezinski et al. 2006), das in ca. 6 Monaten in Betrieb genommen werden soll.

Auf der Expedition SO178 konnte erstmals kieseliges Plankton aus verschiedenen Wasserstockwerken angereichert werden. Dieses weltweit einzigartige Probenmaterial ermöglicht es, Isotopenmessungen an verschiedenen kieseligen Organismengruppen aus verschiedenen Wasserstockwerken im Vergleich zu der Isotopenzusammensetzung des Wassers aus diesen Tiefenintervallen und unter der Einbeziehung biologischer Informationen durchzuführen. Die Aufbereitung und Messung dieses Probenmaterials soll allerdings erst dann erfolgen, wenn die Massenspektrometer in den Routinebetrieb übergegangen sind, um zu gewährleisten, dass die relativ geringen Mengen ohne Verluste gemessen werden können.

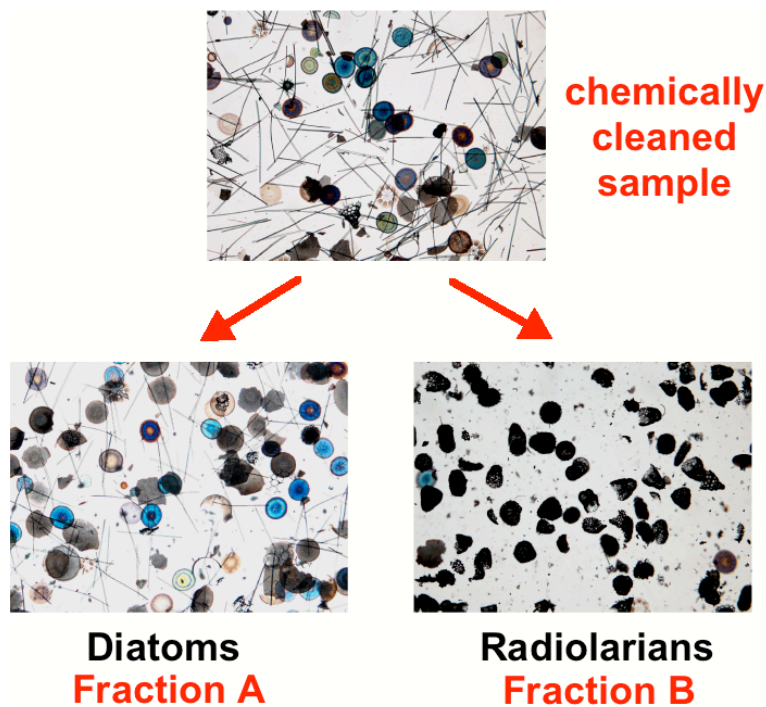


Abb. 2: Beispiel zur Trennung von Diatomeen und Radiolarien (Kern PS1768-8, 102 cm) mit Hilfe des Splitkanal-Trennverfahrens.

Zitierte Literatur

- Abelmann A, Nimmergut A (2005) Radiolarians in the Sea of Okhotsk and their ecological implication for paleoenvironmental reconstructions. *Deep Sea Research II* 52: 2302-2331
- Brzezinski MA, Pride CJ, Franck VM, Sigman DM, Sarmiento JL, Matsumoto K, Gruber N, Rau GH, Coale KH (2002) A switch from $\text{Si}(\text{OH})_4$ to NO_3 depletion in the glacial Southern Ocean. *Geophysical Research Letters* 29(12): 1564, doi: 10.1029/2001GL014349
- Brzezinski MA, Jones JL, Beucher CP, Demarest MS and Berg HL (1998) Automated determination of silicon isotope natural abundance by the acid decomposition of cesium hexafluorosilicate. *Anal Chem* 78:6109-6114.
- Crosta X, Shemesh A (2002) Reconciling downcore anti-correlation of diatom carbon and nitrogen isotopic ratios from the Southern Ocean. *Paleoceanography* 17(1): 1010, doi: 10.1029/2000PA000565
- DeLa Rocha CL, Brzezinski MA, DeNiro MJ and Shemesh A (1998) Silicon-isotope composition of diatoms as an indicator of past oceanic change. *Nature* 395 (15): 680-683

- Hays JD, Morley JJ (2003) The Sea of Okhotsk: A window on the Ice Age Ocean. *Deep Sea Res I* 50:1481-1506
- Nimmergut A and Abelmann A (2002) Spatial and seasonal changes of radiolarian standing stocks in the Sea of Okhotsk. *Deep Sea Res. I* 49:463-493
- Rings A, Lücke A, Schleser GH (2004) A new method for the quantitative separation of diatom frustules from lake sediments. *Limnology and Oceanography: Methods* 2:25-34
- Robinson, RS, Brunelle G, and Sigman D M (2004) Revisiting nutrient utilization in the glacial Antarctic: Evidence from a new method for diatom-bound N isotope analysis. *Paleoceanography* 19, PA3001, doi:10.1029/2003PA000996
- Robinson, R S, Sigman DM, DiFiore PJ, Rohde MM, Mashiotta TA, and Lea DW (2005) Diatom-bound 15N/14N: New support for enhanced nutrient consumption in the ice age subantarctic. *Paleoceanography* 20, PA3003, doi:10.1029/2004PA001114
- Schneider-Mor A, Yam R, Bianchi C, Kunz-Pirring M, Gersonde R and Shemesh A (2005) Diatom stable isotopes, sea ice presence and seasurface temperature records of the past 640 ka in the Atlantic sector of the Southern Ocean, *Geophys. Res Lett* 32, L10704, doi:10.1029/2005GL022543
- Shemesh A, Burckle LH and Hays JD (1994) Meltwater input to the Southern Ocean during the Last Glacial Maximum. *Science* 266:1542-1544
- Shemesh, A. et al. (2002). Sequence of events during the last deglaciation in Southern Ocean sediments and Antarctic ice cores. *Paleoceanography* 17 1056 doi:1029/200PA000599
- Sigman, D.M., Altabet, M.A., Francois, R., McCorkle, D.C. and Gaillard, J-F (1999) The isotopic composition of diatom-bound nitrogen in Southern ocean sediments. *Paleoceanography* 14:118-134

II.2. Voraussichtlicher Nutzen, Verwertbarkeit

Ein wichtiger Bestandteil von SO178-KOMEX, der von allen Partnern gefördert wurde, war und ist die zügige Veröffentlichung der gemeinsam erzielten Ergebnisse in nationalen und vor allem internationalen Fachzeitschriften. Dadurch wird sicher gestellt, dass diese Ergebnisse allgemein zugänglich gemacht werden. Die Veröffentlichung in der Fachliteratur hat zudem auch einen Werbeeffect für die deutsche Meeresforschung, aus dem Nachfrage nach Expertise, Verfahren und Instrumenten erwachsen mag. Weiterhin wurden Daten und Ergebnisse, soweit sinnvoll (z.B. Bathymetrie), an die nationalen und internationalen Datenbanken transferiert. Zusätzlich wurden Probensätze und Kartenmaterial russischen Stellen zur Verfügung gestellt, um dazu beizutragen, die Voraussetzungen für die Nutzung der Meeresressourcen und die Bekämpfung der marinen Umweltprobleme in diesem Bereich zu verbessern. Die Ergebnisse aus SO178-KOMEX können somit für Fragen des Umweltschutzes und der nachhaltigen Entwicklung beim marinen Management sowie für Risikoanalysen (Vulkanismus, Erdbeben, Tsunamigefahren, Klimaänderung) genutzt werden. Proxydaten fossiler Klimasituationen sowie Daten zum Volatiltransfer zwischen Lithosphäre und Hydrosphäre (und Atmosphäre) können z.B. als Eingangsparameter für numerische Klimamodelle dienen, die für Energieversorgung, Rückversicherung, Ernährung, Tourismus, Küsten- und Landschaftsschutz sowie Verkehr und Transport von großer Bedeutung sind. Eine potentielle wirtschaftliche Bedeutung für unsere russischen Kollegen und gegebenenfalls für interessierte Unternehmen der Wirtschaft haben aber auch die Untersuchungen an den Gashydraten, die eine potentielle fossile Energiequelle der Zukunft darstellen, und die Untersuchungen über Sedimentationsprozesse, die möglicherweise Hinweise auf Erdöllagerstätten geben können. Die im Rahmen von SO178-KOMEX gewonnene Erkenntnis, dass mikrobielle Konsortien Baritsulfat letztendlich auflösen, könnte wichtige Konsequenzen für die Abdichtung von Bohrlöchern und die Gewinnung von Erdgas haben.

SO178-KOMEX hat aber vor allem die bilaterale wissenschaftlich-technische Zusammenarbeit mit Russland weiter vorantreiben können und speziell durch die Kooperation mit Instituten aus dem Fernen Osten Russlands, deren wissenschaftliche und technische Perspektiven zur Zeit sehr schlecht sind, die wissenschaftlich-technische Anbindung Russlands an die europäische Meeresforschung gestärkt.

II.3. Fortschritt bei anderen Stellen

Die Fortschritte bei anderen Stellen sind unter Abschnitt II.1. „Darstellung der Ergebnisse“ zusammengefasst.

II.4. Erfolgte und geplante Veröffentlichungen

Artikel (peer-reviewed)

- Aloisi G, Wallmann K, Tishchenko P, Haeckel M, Pavlova G, Greinert J, Eisenhauer A (eingereicht) A possible long-term CO₂ sink through submarine weathering of detrital silicates. *Geochimica et Cosmochimica Acta*. Tishchenko P, Hensen C, Wallmann K, Wong CS (2005) Calculation of the stability and solubility of methane hydrate in seawater. *Chemical Geology* 219: 37-52
- Lembke-Jene L, Tiedemann R, Nürnberg D, Wallmann K, Obzhairov A, Dullo W-Chr (eingereicht) Variable Holocene Methane Emissions from Cold Seeps on the Sakhalin Margin, Okhotsk Sea Linked to seismo-tectonic Activity. *Geochemistry Geophysics Geosystems*
- Lembke-Jene L, Tiedemann R, Wallmann K, Dullo C, Obzhairov A, Andersen N, Nürnberg D (in Vorbereitung) Incorporation of Methane-Derived Carbon in $\delta^{13}\text{C}$ of Selected rose Bengal-Stained benthic foraminifera from Cold Seep Sites in the Okhotsk Sea. *Deep-Sea Research I*
- Lembke-Jene L, Tiedemann R, Nürnberg D, Dullo W-Chr (in Vorbereitung) Rapid Changes in North Pacific Intermediate Water Ventilation during the last Deglaciation. *Geophysical Research Letters*
- Noé SU, Dullo W-Chr (2006) Skeletal morphogenesis and growth mode of modern and fossil deep-water isidid gorgonians (Octocorallia) in the West Pacific (New Zealand and Sea of Okhotsk). *Coral Reefs*, 25: 303-320.
- Wallmann K, Aloisi G, Haeckel M, Obzhairov A, Pavlova G, Tishchenko P (2006) Kinetics of organic matter degradation, microbial methane generation, and gas hydrate formation in anoxic marine sediments. *Geochimica et Cosmochimica Acta* 70: 3905-3927
- Werner R, Baranov B, Hoernle K, Hauff F, Bogaard Pvd, Taratin I (in Vorbereitung) Geodynamic evolution of the Kurile Basin (Okhotsk Sea): Constraints from morphology, geophysics, volcanology, and geochemistry.

Weitere Artikel, erschienen in nationalen russischen Fachzeitschriften (Auswahl):

- Derkachev AN, Nikolaeva NA, Markov YuD, Mozherovsky AV (in press) Specific features of authigenic mineralogenesis within near-continental sedimentary basins of Eastern Asia. *Investigations of the Far Eastern Seas* (in Russian)
- Derkachev AN, Nikolaeva NA, Mozherovsky AV, Grigoryeva TN, Ivanova ED, Pletnev SP, Barinov NN, Chubarov VM (in press) Indications of periodic existence of anoxic sedimentary environments in local basins in the Okhotsk Sea during the Late Pleistocene-Holocene. *Pacific Geology* (in Russian)
- Obzhairov AI, Ageev AA, Shakirov RB, Pestrikova NL, Venicova AL, Yanovskaya OS, Korovitskaya EV, Sorochinskaya AV, Veselov OV (2005) Gas hydrates in the Okhotsk Sea: economical and ecological significance. *Underwater Technology & Ocean World* no 1: 52-60
- Obzhairov AI, Derkachev AN, Baranov BV, Aloisi G, Greinert J, Wallmann K, Bohrmann G, Biebow N (2006) Methane anomalies and related barite occurrence in the Derugin Basin of the Sea of Okhotsk. *Submarine Technology and Ocean World* no 2: 4-16 (in Russian)

Berichte, Dissertationen etc.

- Dullo W-Chr, Biebow N, Georgeleit K (eds) (2004) *Fahrtbericht/Cruise Report SO178-KOMEX: 125pp+app* (<http://www.ifm-geomar.de/div/projects/komex/sonne/index.html>)
- Lembke-Jene L.: "Characteristics of methane venting and rapid paleoceanographic changes in the Okhotsk Sea during the last 25,000 years." *Dissertation*. Abgabe: Dezember 2006

Vorträge und Poster auf Tagungen

- Aloisi G, Wallmann K, Tishchenko P, Haeckel M, Pavlova G, Greinert J, Eisenhauer A (2006) A possible long-term CO₂ sink through submarine weathering of detrital silicates. 16th Annual Goldschmidt Conference Abstracts 2006, Melbourne, Australia
- Aloisi G (2006) Un possible piège de CO₂ par alteration sousmarine de silicates détritiques. *Journées Biominéralisation, Société Française de Minéralogie et Cristallographie*, Nancy, France

- Aloisi G, Wallmann K, Drews M, Bohrmann G, Greinert J, Eisenhauer A (2005) A possible CO₂ sink through submarine weathering of detrital silicate minerals. 15th Annual Goldschmidt Conference Abstracts 2005, Moscow, USA
- Dullo W-Chr, Biebow N, Baranov B, Werner R, Lembke L (2005) SO178 - KOMEX: Stoffaustauschprozesse und -bilanzen im Ochotskischen Meer, Hintergrund und erste Ergebnisse, Statusseminar 2005 Meeresforschung mit FS SONNE, FZ Jülich, Projektträger BMBF und BMWi, Warnemünde. März 9-11
- Haeckel M, Wallmann K, Aloisi G, Obzhairov A, Tishchenko P (2006) Kinetics of organic matter degradation, microbial methane generation and gas hydrate formation in anoxic marine sediments, 5th International Workshop on Methane
- Haeckel M, Boudreau BP (2006) Bubble-induced porewater irrigation: A 3-D model for porewater mixing, Geotechnologien-Statusseminar "Methane in the Geo-Bio-System", Kiel, Germany
- Haeckel M, Boudreau BP (2005) Bubble-induced porewater irrigation: A 3-D model for porewater mixing, International Workshop on Methane in sediments and water column of the Black Sea: Formation, transport pathways and the role within carbon cycle, Sevastopol, Ukraine
- Haeckel M, Wallmann K (2004) Rising gas bubbles – A model for mixing porewater, 5th Workshop on Russian-German Cooperation in the Sea of Okhotsk – Kurile Island Arc System, Vladivostok, Russia
- Haeckel M, Boudreau BP (2004) Rising gas bubbles – A model for mixing porewater, ASLO/TOS 2004 Ocean Research Conference, Honolulu, Hawaii
- Kokfelt U, Lembke-Jene L, Tiedemann R, Nürnberg D (eingereicht) Vegetation Changes and Continent–Ocean Linkages During Deglaciation and the Holocene in the Okhotsk Sea and the Siberian Hinterland. AGU Fall Meeting, San Francisco, Dezember 11-15.
- Lembke-Jene L, Tiedemann R, Nürnberg D, Röhl U, Dullo C (2006) Holocene Climatic and Oceanographic Changes in the Okhotsk Sea and their Significance for teleconnections. ESF-HOLIVAR Final Open Science Conference, London, UK, Juli 12-15
- Lembke-Jene L, Tiedemann R, Nürnberg D, Gorbarenko S, Dullo C (eingereicht) Holocene Variability in Intermediate Water Ventilation and Upper Mixed Layer Hydrography in the Okhotsk Sea and North Pacific. AGU Fall Meeting, San Francisco, Dezember 11-15
- Lembke-Jene L, Tiedemann R, Dullo W-Chr, Nürnberg D, Biebow N, Derkachev A, Nikolaeva N, Bosin A (2005) Variabilität von Klima und Ozeanographie im NW-Pazifik anhand hochauflösender Sedimentkerne aus dem Ochotskischen Meer - Vorläufige Ergebnisse, Statusseminar 2005 Meeresforschung mit FS SONNE, FZ Jülich, Projektträger BMBF und BMWi, Warnemünde. März 9-11
- Lembke-Jene L, Tiedemann R, Nürnberg D, Wallmann K, Dullo W-Chr, Obzhairov A, Biebow N (2005) Is Methane-derived Carbon recorded in Benthic Foraminiferal Tests' $\delta^{13}\text{C}$ at Cold Seep Sites? A Case Study from the Okhotsk Sea. Geophysical Research Abstracts vol.7, EGU 2nd General Assembly, Wien, April 24-29
- Lembke-Jene L, Tiedemann R, Nürnberg D, Kokfelt U, Kozdon R, Biebow N, Röhl U, Gorbarenko S, Dullo C (2005) Millennial- to Centennial-Scale Climatic and Oceanographic Changes in the Okhotsk Sea during the past 15,000 Years. Geophysical Research Abstracts vol.7, EGU 2nd General Assembly, Wien, April 24-29
- Lembke-Jene L, Tiedemann R, Nürnberg D, Bubenchshikova N, Dullo W-Chr (2005) Rapid Paleooceanographic Changes in the Okhotsk Sea – Implications for North Pacific Intermediate Water. Eos Transactions AGU, Fall Meeting Suppl., San Francisco, December 5-9
- Lembke-Jene L, Tiedemann R, Nürnberg D, Dullo W-Chr, Biebow N, Röhl U, Gorbarenko S (2004) Holocene Millennial- to Interdecadal-scale Paleooceanographic Changes in the Okhotsk Sea – Implications for subarctic N-Pacific Teleconnection Patterns. VIII. International Conference on Paleoceanography, Biarritz, September 5-10
- Noé S, Pfeiffer M, Dullo W-Chr (2006) Skeletal Mg/Ca in deep-water isidid gorgonians (Octocorallia): relationship to paleotemperature? ISCR 2006, Bremen

- Noé S, Lembke-Jene L, Dullo W-Chr, Freiwald A (eingereicht) Sclerochronology of a mid-Holocene bamboo coral skeleton: Incremental growth and radiocarbon dating. AGU Fall Meeting, San Francisco, Dezember 11-15
- Noé S, Lembke-Jene L, Dullo W-Chr, Biebow N, Tiedemann R (2005) Tiefwasserkorallen aus dem Ochotskischen Meer (KOMEX-SO178) - Vorläufige Erkenntnisse zu Taxonomie, Biomineralisation und Chemismus. Statusseminar 2005 Meeresforschung mit FS SONNE, FZ Jülich, Projektträger BMBF und BMWi, Warnemünde. März 9-11
- Noé S, Lembke-Jene L, Dullo W-Chr, Eisenhauer A (2005) Deep-Water Isidid Gorgonians As High-Resolution Archives of Paleoceanographic Dynamics In The Western Pacific (Chatham Rise, New Zealand And Sea Of Okhotsk). Eos Transactions AGU, Fall Meeting Suppl., San Francisco, December 5-9
- Noé S, Dullo W-Chr (2005) Growth mode and skeletal morphology of deep-water isidid gorgonians (New Zealand and Sea of Okhotsk). 2. Internationales Alfred-Wegener-Symposium, Bremerhaven, Tagungsband
- Noé S, Dullo W-Chr (2005) Skeletal morphogenesis and growth mode of living and fossil isidid gorgonians in the West Pacific. International Conference and Annual Meeting on System Earth Biosphere Coupling, Erlangen
- Noé S, Lembke-Jene L, Dullo W-Chr (2005) Growth and age validation of living, sub-Recent and fossil isidid gorgonians in the West Pacific (New Zealand, Sea of Okhotsk). International Conference and Annual Meeting on System Earth Biosphere Coupling, Erlangen
- Noé S, Dullo, W-Chr (2004) Micro- and ultrastructural heterogeneity of a fossil deep-water isidid gorgonian skeleton: primary versus diagenetic fabrics. 174. Jahrestagung Paläontologische Gesellschaft, Göttingen
- Tiedemann R, Lembke-Jene L, Kozdon R, Nürnberg D, Dullo W-Chr, Biebow N, Kokfelt, Röhl U, Gorbarenko S (2005) Millennial- to Centennial-Scale Climatic and Oceanographic Changes in the Okhotsk Sea During the Past 15,000 Years. 2. Alfred-Wegener-Konferenz, Bremerhaven, Tagungsband

Danksagung

Wir danken dem BMBF für die gewährte Unterstützung und dem Projektträger PTJ-Warnemünde für die unbürokratische administrative Abwicklung. Unser besonderer Dank gilt Kapitän Papenhagen und der Besatzung des F.S. „Sonne“ für ihre hervorragende Kooperation während der Ausfahrt. Sehr dankbar sind Dr. A. Chichaev (Agentur für Wissenschaft und Innovationen des Ministeriums für Bildung und Wissenschaft der Russischen Föderation) und dem Auswärtigen Amt der Bundesrepublik Deutschland, die uns bei der Beantragung der erforderlichen Genehmigung der Ausfahrt unterstützt haben. Den russischen Behörden danken wir für die Erteilung aller für SO178 erforderlichen Genehmigungen.

Verzeichnis der Anlagen

- Anlage 1: Erfolgsprotokollbericht
- Anlage 2: Sonderdruck der Arbeit Wallmann et al. (2006)
- Anlage 3: Sonderdruck der Arbeit Noé und Dullo (2006)
- Anlage 4: Vorabdruck der Arbeit Lembke-Jene et al. (eingereicht)
- Anlage 5: Vorabdruck der Arbeit Aloisi et al. (eingereicht)
- Anlage 6: Vorabdruck der Arbeit Lembke-Jene et al. (in Vorb.)

Erfolgsprotokollbericht

1. Beitrag der Ergebnisse zu den förderpolitischen Zielen des Förderprogramms

Das Vorhaben SO178-KOMEX war als Fortsetzung des Verbundvorhabens KOMEX ein Beispiel für ein bilaterales Projekt im Rahmen der wissenschaftlich-technischen Zusammenarbeit zwischen Russland und Deutschland. Dementsprechend nahmen deutsche und russische Wissenschaftler nicht nur etwa zu gleichen Teilen an der Ausfahrt teil, sondern kooperierten auch eng bei der Analytik, Datenauswertung und Interpretation.

Außerdem lieferte das Vorhaben SO178-KOMEX wichtige Beiträge zu verschiedenen internationalen und nationalen Programmen der Meeres- und Polarforschung:

Die heutige Stellung Kamtschatkas und des Ochotskischen Meeres im globalen plattentektonischen Muster wird allgemein kontrovers beurteilt. So weisen kinematische Modelle im Bereich der Ränder zwischen der Nordamerikanischen und der Eurasischen Platte keine eindeutige Grenze auf. Auch ist die Entstehung des Ochotskischen Meeres nicht mit den „klassischen“ Entwicklungsphasen eines „Back Arc“-Beckens zu erklären. Durch großräumige bathymetrische Vermessungen sowie durch die Beprobung vulkanischer Strukturen am Hang des Kurilenbeckens konnten neue Erkenntnisse über Öffnung des Kurilenbeckens gewonnen und somit ein wichtiger Beitrag zum Verständnis der geodynamischen Prozesse im Nordwestpazifik geleistet werden. Mit den Untersuchungen an submarinen Fluidaustritten und der Rekonstruktion des Einflusses submariner Fluid- und Gasaustritte auf Ökologie, Sedimentologie, Wasserchemie und die atmosphärische Spurengaszusammensetzung heute und in der geologischen Vergangenheit hat SO178-KOMEX einen wesentlichen Beitrag zu nationalen und internationalen Schwerpunkten in der Meeresforschung geliefert. Zudem kann die im Rahmen von SO178-KOMEX gewonnene Erkenntnis, dass mikrobielle Konsortien Baritsulfat letztendlich auflösen, wichtige Konsequenzen für die Abdichtung von Bohrlöchern und die Gewinnung von Erdgas haben. Die Zwischenwassermassen des Pazifik werden in den Randmeeren hoher Breiten neu gebildet und dabei ventiliert. Detaillierte Erkenntnisse über die Wechselwirkungen dieser Wassermassen mit dem Weltklima waren bislang nur ansatzweise bekannt. Es wird aber heute bereits davon ausgegangen, dass diese Zwischenwassermassen rasch und hochempfindlich auf globale Klimawandel reagieren, mit weitreichenden Folgen z.B. für die CO₂-Speicherkapazität des Pazifik. Die Kenntnis der natürlichen Variabilität dieser Wassermassen auf längeren Zeitskalen durch paläo-ozeanographische Rekonstruktionen ist daher von hohem Interesse zur Abschätzung anthropogen verursachter Änderungen jüngster Zeit. Das Ochotskische Meer bot die Möglichkeit, innerhalb einer begrenzten Schlüsselregion die paläo-ozeanographische Entwicklung des größten Ozeans der Welt zu erfassen. Die „Fingerabdrücke“, die das Ochotskische Meer im gesamten Nordpazifik hinterlässt, wurden direkt an der Bildungsquelle mithilfe hochauflösender Sedimentkerne aufgenommen; diese Ergebnisse können nun in Paläozirkulations- und -klimamodelle für den Pazifik einfließen. Damit helfen die Untersuchungen im Ochotskischen Meer, diese Modelle in Zukunft zu verifizieren und weiter abzustimmen. Das Vorhaben trug so dazu bei, wichtige Erkenntnisse zur Rolle des Ozeans im Klimageschehen zu gewinnen, einem Schwerpunkt der Meeresforschung in kommenden Jahren (Senatskommission für Ozeanographie der Deutschen Forschungsgemeinschaft).

2. Wissenschaftlich-technische Ergebnisse des Vorhabens

Die wissenschaftlichen Erfolge von SO178-KOMEX sind in Abschnitt II.1. des Abschlussberichts und in den dem Abschlussbericht beigelegten 5 Publikationen sowie im Fahrtbericht ausführlich beschrieben. Auf zahlreichen Tagungen wurde über das Projekt berichtet, und weitere Arbeiten, die auf den vorgelegten Ergebnissen aufbauen, wurden bereits initiiert.

3. Fortschreibung des Verwertungsplans

Die Ergebnisse wurden bzw. werden zur Zeit in der internationalen Fachliteratur publiziert und damit allgemein zugänglich gemacht. Sie bilden auch nicht nur wichtige Grundlagen für laufende Projekte, sondern stellen auch die Basis für weiterführende Programme dar, mit deren Realisierung teilweise bereits begonnen wurde. Dabei handelt es sich vornehmlich um rein wissenschaftliche Zielsetzungen, die jedoch auch eine umweltpolitische und wirtschaftliche Relevanz haben. Weiterhin wurden Daten und Ergebnisse, soweit sinnvoll, an die internationalen Datenbanken transferiert. Sie können somit zu Fragen der Seerechtskonvention („Kontinentalrandschelf“), für die zukünftige Abschätzung mineralischer und biologischer Rohstoffe, für Fragen des Umweltschutzes und für Risikoanalysen (Vulkanismus, Erdbeben, Klimaänderung) von den dafür zuständigen nationalen und internationalen Stellen genutzt werden.

4. Arbeiten, die zu keiner Lösung geführt haben

Die im Antrag formulierten Zielsetzungen des Vorhabens konnten weitestgehend erreicht werden. Aus den gewonnenen Daten und Ergebnissen haben sich aber einige neue Fragestellungen ergeben, deren Bearbeitung Gegenstand zukünftiger Forschungsvorhaben sein soll.

5. Präsentationsmöglichkeiten für mögliche Nutzer

Die Art des Vorhabens lässt hierzu keine Angaben zu.

6. Einhaltung der Zeit- und Ausgabenplanung

Der im Antrag vorgestellte Finanzierungs- und Zeitplan wurde weitestgehend eingehalten. Die einzige Abweichung war:

(1) Im Haushaltsjahr 2005 konnten 5.800,- € aus der Position 0835 „Vergabe von Aufträgen“, die ursprünglich für Analytik beantragt und bewilligt waren, aufgrund des Einsatzes neuer, leistungsfähigerer Analysegeräte, die bei Antragstellung noch nicht zur Verfügung standen, eingespart werden. Diese Mittel wurden innerhalb der Position 0835 „Vergabe von Aufträgen“ umgewidmet, um eine Firma, die über einen Mitarbeiter (Herrn Dipl.-Geol. Lembke-Jene) mit entsprechender Erfahrung verfügte, mit der Auswertung von mittels eines XRF-Scanners generierten Daten beauftragen zu können. Diese Umwidmung erfolgte mit Zustimmung des PtJ und war kostenneutral.

Kinetics of organic matter degradation, microbial methane generation, and gas hydrate formation in anoxic marine sediments

K. Wallmann ^{a,*}, G. Aloisi ^b, M. Haeckel ^a, A. Obzhairov ^c, G. Pavlova ^c, P. Tishchenko ^c

^a IFM-GEOMAR Research Center, Wischhofstrasse 1-3, 24148 Kiel, Germany

^b Laboratoire de Paléoenvironnements et Paléobiosphère, Université Claude Bernard, Lyon I, 2, rue Dubois, F-69622 Villeurbanne cedex, France

^c Pacific Oceanological Institute (POI), 43, Baltiyskaya Street, 690041 Vladivostok, Russia

Received 28 February 2006; accepted in revised form 5 June 2006

Abstract

Seven sediment cores were taken in the Sea of Okhotsk in a south-north transect along the slope of Sakhalin Island. The retrieved anoxic sediments and pore fluids were analyzed for particulate organic carbon (POC), total nitrogen, total sulfur, dissolved sulfate, sulfide, methane, ammonium, iodide, bromide, calcium, and total alkalinity. A novel method was developed to derive sedimentation rates from a steady-state nitrogen mass balance. Rates of organic matter degradation, sulfate reduction, methane turnover, and carbonate precipitation were derived from the data applying a steady-state transport-reaction model. A good fit to the data set was obtained using the following new rate law for organic matter degradation in anoxic sediments:

$$R_{\text{POC}} = \frac{K_C}{C(\text{DIC}) + C(\text{CH}_4) + K_C} \cdot k_x \cdot \text{POC}$$

The rate of particulate organic carbon degradation (R_{POC}) was found to depend on the POC concentration, an age-dependent kinetic constant (k_x) and the concentration of dissolved metabolites. Rates are inhibited at high dissolved inorganic carbon (DIC) and dissolved methane (CH_4) concentrations. The best fit to the data was obtained applying an inhibition constant K_C of 35 ± 5 mM. The modeling further showed that bromide and iodide are preferentially released during organic matter degradation in anoxic sediments. Carbonate precipitation is driven by the anaerobic oxidation of methane (AOM) and removes one third of the carbonate alkalinity generated via AOM. The new model of organic matter degradation was further tested and extended to simulate the accumulation of gas hydrates at Blake Ridge. A good fit to the available POC, total nitrogen, dissolved ammonium, bromide, iodide and sulfate data was obtained confirming that the new model can be used to simulate organic matter degradation and methane production over the entire hydrate stability zone (HSZ). The modeling revealed that most of the gas hydrates accumulating in Blake Ridge sediments are neither formed by organic matter degradation within the HSZ nor by dissolved methane transported to the surface by upward fluid flow but rather through the ascent of gas bubbles from deeper sediment layers. The model was further applied to predict rates of hydrate accumulation in Sakhalin slope sediments. It showed that only up to 0.3% of the pore space is occupied by gas hydrates formed via organic matter degradation within the HSZ. Gas bubble ascent may, however, significantly increase the total amount of hydrate in these deposits.

© 2006 Elsevier Inc. All rights reserved.

1. Introduction

Degradation rates of particulate organic matter (POM) in marine surface sediments have been studied in detail

over the past decades (Berner, 1980; Boudreau, 1997 and references therein). They decrease with age of the degrading POM and with sediment depth because labile fractions are preferentially consumed reducing the overall reactivity of the remaining POM fractions (Westrich and Berner, 1984). Various kinetic models have been introduced to consider the age effects on degradation rates. These include multi-G models where POM is divided into two or three

* Corresponding author.

E-mail address: kwallmann@ifm-geomar.de (K. Wallmann).

fractions of different reactivity each being degraded with its own kinetic constant (Westrich and Berner, 1984; Boudreau, 1996b; Luff et al., 2000) and reactive continuum models, which consider sedimentary POM to be composed of an unlimited number of different fractions each having its own reactivity (Middelburg, 1989; Boudreau and Ruddick, 1991). The concentration of terminal electron acceptors used in microbial POM degradation (e.g., sulfate in anoxic marine sediments) are often considered in the kinetic equations applying Monod terms (Rabouille and Gailard, 1991). It has also been shown that sedimentary organic matter degrades more efficiently under oxic than anoxic conditions (Hedges et al., 1999; Kristensen and Holmer, 2001). However, the concentrations of degradation products, such as methane or CO₂, accumulating in the pore waters of anoxic sediments were not taken into account even though simple thermodynamic reasoning (Le Chatelier's principle) would suggest that the gain in Gibb's free energy and, hence, the degradation rates should be diminished by the accumulation of metabolites.

The kinetics of POM degradation in anoxic sediments have recently gained renewed interest because methane gas hydrates are formed in these sedimentary environments often by microbial rather than thermogenic degradation processes (Kvenvolden and Lorenson, 2001). Gas hydrates might have had a significant effect on the global carbon cycle and climate of the geological past if they are indeed as abundant as commonly assumed (Dickens et al., 1995). However, an updated estimate of global hydrate abundance gave very low numbers suggesting that the effects of hydrates on climate might have been grossly over-stated (Milkov, 2004). State-of-the-art models of biogenic methane and hydrate formation use rather simple kinetic formulations (Rempel and Buffett, 1998; Davie and Buffett, 2001, 2003a). They have been applied to estimate the global abundance of biogenic gas hydrates in marine sediments (Buffett and Archer, 2004; Archer and Buffett, 2005). The outcome of these models may, however, be significantly enhanced applying improved rate laws for POM degradation.

Anoxic marine sediments occur along productive continental margins. Methane formation rates are especially high where sedimentation rates are enhanced by the delivery of fine-grained riverine particles. The north-eastern slopes of Sakhalin Island are an important example for this kind of setting. The productivity of the area located in the northern Sea of Okhotsk is very high and the adjacent Amur River delivers abundant clay minerals so that slope sediments composed of fine-grained terrigenous matter, biogenic opal and POM accumulate at high rates. Sedimentation rates are as high as 1 m kyr⁻¹ and seismic data indicate the occurrence of gas hydrates (Lüdmann and Wong, 2003).

In this paper, we present and evaluate sediment and pore water data from the slope of Sakhalin Island. We demonstrate that rates of sulfate reduction and methane generation depend not only on the reactivity of buried POM but also on the concentrations of methane and

dissolved inorganic carbon prevailing in the pore waters of these organic matter-rich deposits. Based on these observations, we develop a new kinetic rate law for the degradation of organic matter in anoxic sediments. Subsequently, this rate law is further tested and applied to simulate gas hydrate formation in Blake Ridge and Sakhalin slope sediments.

2. Study area

Sedimentary processes in the Sea of Okhotsk were intensively studied within the joint Russian-German project KOMEX (Kurile-Okhotsk Sea Marine Experiment). Sakhalin Island is situated at the north-western boundary of the Sea of Okhotsk, a large marginal sea located in the north-western Pacific (Fig. 1). During the cold season, the Sea of Okhotsk is largely covered with sea-ice. Primary production is low during winter and summer but very intense during spring and autumn (Broerse et al., 2000). The spring bloom is dominated by diatoms whereas the autumn peak is mainly caused by calcareous plankton. During spring and early autumn, primary production calculated from remote sensing data is high with an average of 120–160 g C m⁻² y⁻¹ (Antoine et al., 1996). The annual export production derived by inverse modeling of nutrient and oxygen profiles in the water column amounts to more than 72 g C m⁻² y⁻¹ (Schlitzer, 2000). The East Sakhalin Current flows southwards along the Sakhalin coast transporting cold surface waters and Amur River water from north to south. The northern slope and shelf of Sakhalin Island are strongly influenced by fresh water and sediment input from the adjacent Amur. Here, primary production is at its maximum and may reach values of up to 250 g C m⁻² y⁻¹ during the warm season (Antoine et al.,

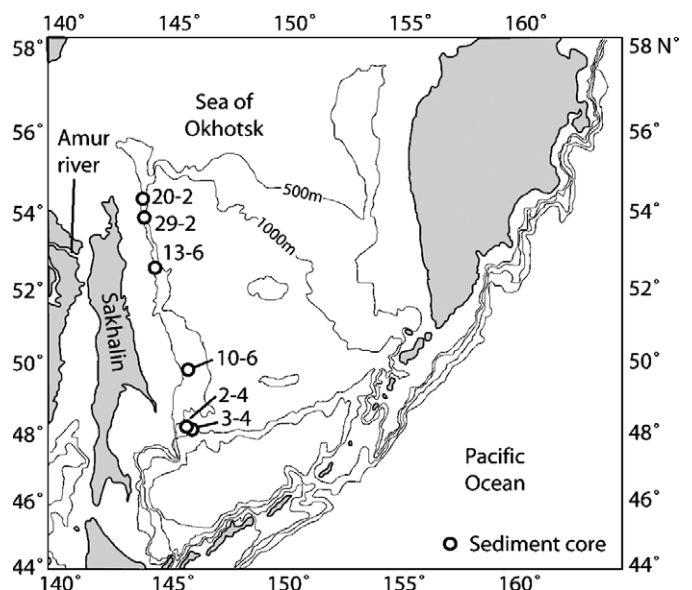


Fig. 1. Map of the study area and sampling sites (3-4, SO178 3-4 KAL; 2-4, LV28 2-4 SL; 10-6, SO178 10-6 SL; 13-6, SO178 13-6 KL; 29-2, SO178 29-2 KL; 20-2, LV28 20-2 KL).

1996). Sedimentation is dominated by biogenic opal and terrigenous inputs from the Amur River. The Holocene sedimentation rates are as high as 100 cm ky^{-1} in the northern slope area and decrease towards the south by one order of magnitude (Wong et al., 2003).

Gas hydrates, free gas and mud diapirism have been imaged by seismic reflection data (Lüdmann and Wong, 2003). The total amount of methane preserved in the hydrate stability zone and trapped as free gas beneath the bottom simulating reflector (BSR) was estimated to $17 \pm 14 \times 10^{12} \text{ m}^3$ for the north-western Sea of Okhotsk (Lüdmann and Wong, 2003). A BSR—marking the boundary between the hydrate stability zone and underlying gas-bearing sediments—was found throughout the entire northern slope area off Sakhalin Island (Lüdmann and Wong, 2003). Hydro-acoustic anomalies (“flares”) caused by rising methane gas bubbles and enhanced methane concentrations in bottom waters demonstrate active gas venting processes at numerous sites along the northern slope (Obzhirov et al., 2004). Methane gas hydrates were sampled repeatedly in surface sediments of active vent sites at the northern slope area and stable isotopic data indicate their dominantly biogenic origin (Ginsburg et al., 1993; Matveeva et al., 2003).

3. Sampling and analytical techniques

Samples were taken during joint Russian-German expeditions with *RV Akademik M. A. Lavrentyev* in August–September 1998 (LV28) and *RV SONNE* in July–September 2004 (SO178). Sediments were taken using different coring techniques and instruments including a gravity corer (SL), a piston corer (KL), and a Kasten corer (KAL). Core recovery was 5–24 m, depending on location and coring gear (see Table 1 and Fig. 1).

Sediment cores were cut into meter pieces and stored in the cold room at 4°C . Subsequently, they were opened with a saw and immediately sub-sampled every 0.1–1 m. At each depth position, 50 cm^3 of wet sediment were taken for pore water sampling, and 5 cm^3 for the determination of physical properties (water content, porosity). Wet sediments were also transferred to gas-tight vials to determine the methane concentration using the head-space technique (Niewöhner et al., 1998). Pore waters were separated from the sediment matrix via squeezing in a cold room at 4°C

temperature and 2–4 bar using a polypropylene apparatus pressurized by argon and equipped with $0.45 \mu\text{m}$ cellulose acetate membrane filters. All vials used for pore water storage were previously washed with acid and Milli-Q water to prevent sample contamination. As pore water samples rapidly lose alkalinity and Ca during storage, these parameters were determined within a few hours after sampling while sub-samples for sulfide determination were taken within two hours after squeezing and conserved with zinc-acetate solution.

Samples for dissolved calcium (Ca) in pore water were analyzed by complexometric titration of 1 ml of pore water dispensed in 10 ml de-ionized water (Grasshoff et al., 1983). The Brinkman/Dosimat 665 motor-driven piston burette reproducible to $\pm 0.001 \text{ ml}$ in the delivered volume was applied for analysis. Based on analysis in pore water replicates analytical precision of $\pm 7 \mu\text{mol/kg}$ ($n = 8$) for calcium in pore water was achieved in this study. Ca was also measured using ICP-AES. The results of the two-independent methods usually agreed within 1% when the titration was performed within a few hours after sampling and when sub-samples for on-shore ICP-AES analysis were taken and acidified within the same short period of time. Prolonged storage without acid addition reduced the dissolved Ca concentrations significantly due to CaCO_3 precipitation.

Samples for total alkalinity (TA) in pore water were analyzed by direct titration in an open cell of 1 ml of pore water dispensed in 10 ml deionized water with 0.02 N HCl using Bruevich’s method (Ivanenkov and Lyakhin, 1978). The acid was standardized daily with Na_2CO_3 solution prepared from crystals dried at 280°C and dissolved in CO_2 -free deionized water. To remove CO_2 and H_2S during titration, the samples and standards were flushed with a continuous stream of pure nitrogen. A mixture of methylene blue and methyl red was used as indicator and titration was completed when the green color of the solution turned to light-pink (pH of the end point is equal to 5.4–5.5). The method is convenient to work with small sample volumes and avoids the errors caused by H_2S oxidation during titration. Replicate measurements ($n = 8$) indicated an analytical precision of $\pm 10 \mu\text{mol/kg}$ for total alkalinity in pore waters. Replicate measurements of pore water samples over a time span of several hours revealed that the total alkalinity of anoxic pore water samples is not stable but decreases with time. The two most important reactions that cause alkalinity reduction are carbonate precipitation and sulfide oxidation. Carbonate precipitation is induced by the loss of CO_2 and H_2S from the pore waters to the atmosphere and the resulting shift in the dissolution/precipitation equilibrium. Sulfide oxidation consumes alkalinity via acid production. The sulfide oxidation rate and its impact on total alkalinity were tested under shipboard conditions using a 30 mM solution of Na_2S in 0.5 M NaCl. The initial pH was adjusted to 7.1 with concentrated HCl and the solution was titrated repeatedly at room temperature ($24\text{--}25^\circ\text{C}$). The data showed that total alkalinity is reduced by about

Table 1
List of coring stations in geographic order going from south to north along the Sakhalin slope

Station	Location	Water depth (m)	Recovery (m)
SO178 3-4 KAL	48°11.83'N 146°08.74'E	1602	10.0
LV28 2-4 SL	48°22.73'N 146°02.22'E	1265	6.0
SO178 10-6 SL	49°44.88'N 146°00.48'E	613	11.5
SO178 13-6 KL	52°43.88'N 144°42.65'E	713	23.7
SO178 29-2 KL	53°50.00'N 144°14.23'E	771	24.3
LV28 20-2 SL	54°26.52'N 144°04.09'E	685	5.9

5% within a few hours. Thus, total alkalinity of anoxic samples was determined as fast as possible (within 2 h) after pore water retrieval.

Sulfide samples were conserved with zinc acetate gelatin solution (23.8 mM in Zn acetate) adding 4 ml solution to 1 ml pore water. The gelatin inhibits the precipitation of sulfide by fixing sulfide in a colloidal ZnS solution. The resulting colloidal solution was mixed with 40 μ l phenylene-diamine and 40 μ l FeCl₃·6H₂O and the absorbance was measured after 10 min to 1 h at 670 nm using a Hitachi UV/VIS Spectrometer. A linear calibration curve was obtained in the concentration range of 0–57 μ M Σ H₂S. The sulfide standard solution was titrated with sodium thiosulfate to determine the true concentration of the standard. Samples were diluted into the calibration range before reagent addition.

Dissolved ammonium was measured applying a standard photometric procedure on a Hitachi UV/VIS Spectrometer. The analysis of nutrient concentrations was disturbed in anoxic samples with high Σ H₂S concentrations. Thus, sulfide-bearing samples were acidified with HCl (20 μ l conc. HCl per 3 ml sample) and bubbled with nitrogen gas prior to analysis. By this procedure sulfide was converted into hydrogen sulfide and stripped from the solution. For the ammonium determination, 1 ml water sample or standard were diluted with 4 ml Milli-Q water and 0.2 ml phenol solution were added. After 2 min 0.1 ml citrate buffer and 0.2 ml DTT reagent were added and the samples were kept at room temperature protected from sunlight for about 24 h before the absorbance was measured at 630 nm.

Dissolved chloride, bromide, iodide, and sulfate were determined using ion-chromatography. We used a Methrom ion-chromatograph equipped with a conventional anion-exchange column and carbonate-bicarbonate solution as solvent. UV-detection was used for the determination of iodide while a conductivity sensor was applied for the measurement of the other anions. Standard deviations were found to be 1% for chloride, 2% for sulfate, and 5% for bromide and iodide.

Squeezed sediment samples were freeze-dried and ground in an agate mortar for further analysis. Desalting with distilled water was avoided because this procedure reduces the C and S contents of the solids due to the leaching of dissolved organic carbon and oxidized sulfur compounds. The chloride contents in dried and ground aliquots were determined by extraction with distilled water and titration with AgNO₃ solution to calculate the contribution of dissolved and exchangeable salts to the total mass and to the total sulfur content. The fine-grained sediments contained 2–3 wt% Cl mainly as exchangeable ion (Sayles and Mangelsdorf, 1977) whereas the sand sediments usually contained less than 0.5 wt% Cl from desiccated pore water. In this paper, the exchangeable salts are regarded as integral part of the solid sediment and the small salt contribution from pore water preserved after squeezing was ignored in the calculation of dry weights and solid phase

concentrations. Only the sulfur data were corrected because pore water and exchangeable sulfate contributed significantly to the total sulfur in dried samples. The sulfate content was calculated using the sulfur/chlorine ratio previously determined in the corresponding pore water sample and the chloride concentration in the dried sample. It was subtracted from the sulfur concentration in dried sediments to calculate the sulfur concentrations in the solid phase.

Total C, N, and S were determined by combustion of squeezed sediment samples and gas-chromatographic detection of CO₂, N₂, and SO₂ produced in the combustion process using a Carlo-Erba element analyzer (NA 1500). Additional samples were repeatedly acidified with HCl and desiccated till complete dryness to release CO₂ from carbonate minerals. The residues were analyzed for C to determine the contents of particulate organic carbon. The carbonate content was determined from the difference between total and organic carbon. Sediment and soil standards with certified concentrations of C, N, and S were analyzed during each run (marine sediment MAG-1, United States geological Survey; soil standard 1, HEKAtech GmbH). The recovered values were always within the certified range. Replicate measurements of sediment samples ($n = 5$) revealed the following relative standard deviations: POC: 1%; CaCO₃: 2%; N: 3%; and S: 5%.

4. Numerical modeling procedure

A numerical transport-reaction model was developed and applied to simulate the degradation of particulate organic matter (POM) in anoxic marine sediments. The model calculates the concentration–depth profiles of 3 solid species (particulate organic carbon, particulate organic nitrogen, and adsorbed ammonium) and 7 dissolved species (sulfate, methane, ammonium, bromide, iodide, dissolved inorganic carbon, and calcium). Major processes considered in the model are POM degradation via sulfate reduction, methanogenesis, anaerobic oxidation of methane (AOM), carbonate precipitation, and ammonium adsorption. A detailed description of the model is given in Appendix A.

Partial differential equations for solids and solutes were set-up following the classical approach used in early diagenesis modeling:

Solutes:

$$\Phi \cdot \frac{\partial C}{\partial t} = \frac{\partial(\Phi \cdot D_s \cdot \frac{\partial C}{\partial x})}{\partial x} - \frac{\partial(\Phi \cdot v \cdot C)}{\partial x} + \Phi \cdot R, \quad (1)$$

Solids:

$$(1 - \Phi) \cdot \frac{\partial G}{\partial t} = - \frac{\partial((1 - \Phi) \cdot w \cdot G)}{\partial x} + (1 - \Phi) \cdot R, \quad (2)$$

where x is depth, t is time, Φ is porosity, C is the concentration of dissolved species in pore water, v is the burial velocity of solutes, G is the concentration of solids in dry

sediments, w gives the burial velocity of solids, and R defines the reactions occurring in the simulated sediment column. The model considers the decrease in porosity with sediment depth, advective transport of solutes and solids via burial and steady-state compaction, molecular diffusion of dissolved species and various microbial and chemical reactions.

The sampling gear and the sub-sampling procedure adopted in our study are not well suited to resolve concentration gradients within the top few decimeters of the sediment column where the transport of solids and solutes is accelerated by bioturbation and bioirrigation. Hence, these biogenic transport processes were neglected in the modeling. Our data showed steep concentration gradients between the uppermost sampling points and no indication of deep reaching mixing thus confirming our modeling approach (Figs. 2–7).

A novel rate law was introduced to describe the effect of metabolite concentrations on the anaerobic degradation of particulate organic carbon (POC) in anoxic marine sediments:

$$R_{\text{POC}} = \frac{K_C}{C(\text{DIC}) + C(\text{CH}_4) + K_C} \cdot k_x \cdot \text{POC}, \quad (3)$$

where R_{POC} is the POC degradation rate, $C(\text{DIC})$ is the concentration of dissolved inorganic carbon ($\text{CO}_3 + \text{HCO}_3 + \text{CO}_2$) in the considered depth interval, $C(\text{CH}_4)$ is the ambient methane concentration in pore waters, k_x is an age-dependent kinetic constant, POC is the POC concentration and K_C is a Monod constant describing the inhibition of POC degradation by DIC and CH_4 . The age effects on POC degradation are considered using the approach introduced by Middelburg (1989). Ages were calculated from sediment depth and burial rate. The rate law predicts that the microbial degradation of organic matter is inhibited by metabolites accumulating in adjacent pore fluids since the Gibb's free energy available for the microbial metabolism is reduced in the presence of high concentrations of reaction products.

A new approach was developed to derive sedimentation rates from a nitrogen mass balance at steady-state. The fluxes of total particulate nitrogen and dissolved ammonium at sediment depths below the bioturbated and bio-irrigated zones are given by:

Flux of N:

$$J_{\text{PN}} = \Phi \cdot w \cdot r(\text{N}) \cdot N, \quad (4)$$

Flux of NH_4 :

$$J_{\text{NH}_4} = \Phi \cdot \left(v \cdot C(\text{NH}_4) - D_S \cdot \frac{dC(\text{NH}_4)}{dx} \right), \quad (5)$$

where J is the flux (in $\text{mmol N cm}^{-2} \text{ yr}^{-1}$), N is the concentration of total particulate nitrogen including both adsorbed ammonium and organic nitrogen in wt%, $r(\text{N})$ is a unit conversion factor for solids defined in the appendix (see Table A1), and $C(\text{NH}_4)$ is the ammonium concentra-

tion in pore waters (in mmol cm^{-3}). Considering two different sediment layers situated at shallow depth ($x = S$) and close to the base of the core ($x = L$), the mass balance for nitrogen at steady-state reads as:

$$J_N(S) - J_N(L) + J_{\text{NH}_4}(S) - J_{\text{NH}_4}(L) = 0. \quad (6)$$

Inserting the flux definition into the mass balance and considering also the definitions given in Table A1, an equation for the sedimentation rate w_f can be derived as:

$$w_f = \frac{D_M \cdot \left(\frac{dC(\text{NH}_4)}{dx}(L) \cdot \Phi(L)^3 - \frac{dC(\text{NH}_4)}{dx}(S) \cdot \Phi(S)^3 \right)}{\frac{d_s \cdot (1 - \Phi_f) \cdot (N(L) - N(S))}{1.4} + \Phi_f \cdot (C(\text{NH}_4)(L) - C(\text{NH}_4)(S))}, \quad (7)$$

where D_M is the coefficient for molecular diffusion of ammonium ($\text{cm}^2 \text{ yr}^{-1}$), d_s is the density of dry solids (2.5 g cm^{-3}) and Φ_f is porosity at large depth (see Appendix A for further definitions). Appropriate functions are fitted through the data so that porosity, N and ammonium concentrations and the first derivative of $C(\text{NH}_4)$ with respect to depth can be derived from the data at two different depth positions (S and L) and inserted into the equation to yield sedimentation rates for each of the investigated cores (in cm yr^{-1}).

A simple exponential function was used for data fitting:

$$y = y_f + (y_0 - y_f) \cdot e^{-ax}, \quad (8)$$

where y is the depth-dependent variable (porosity, ammonium, N), y_f and y_0 are the values of the variables at large depth and at the surface, respectively, and a is an attenuation coefficient. Sedimentation rates derived by this novel approach are very suitable for steady-state modeling because they are internally consistent with the model assumptions.

Constant concentrations of dissolved species were prescribed at the upper and lower boundary of the model column (Dirichlet boundary conditions) while the vertical distribution of solids was simulated applying Dirichlet conditions at the upper boundary. The upper boundary of the model domain is situated not directly at the sediment/water interface but at the transition between oxic and suboxic surface layers affected by bioturbation and bioirrigation and the underlying anoxic sediment column. Undisturbed surface sediments were collected with a multi-corer along the Sakhalin slope and pore water analysis revealed nitrate penetration depths of only 2–8 cm (Biebow and Hütten, 2000). Hence, anoxic conditions prevailed already at shallow sediment depths. In most sediment cores we found significant gradients of dissolved species at the lower boundary indicating that dissolved species released in deeper sediment horizons were transported to the surface via diffusion. We applied Dirichlet rather than imposed flux (Neumann) conditions at the lower boundary to consider the effect of these solutes on the simulated pore water profiles. Concentrations of dissolved species used as boundary values were taken from our data set using samples taken at the uppermost and deepest points of the studied sediment

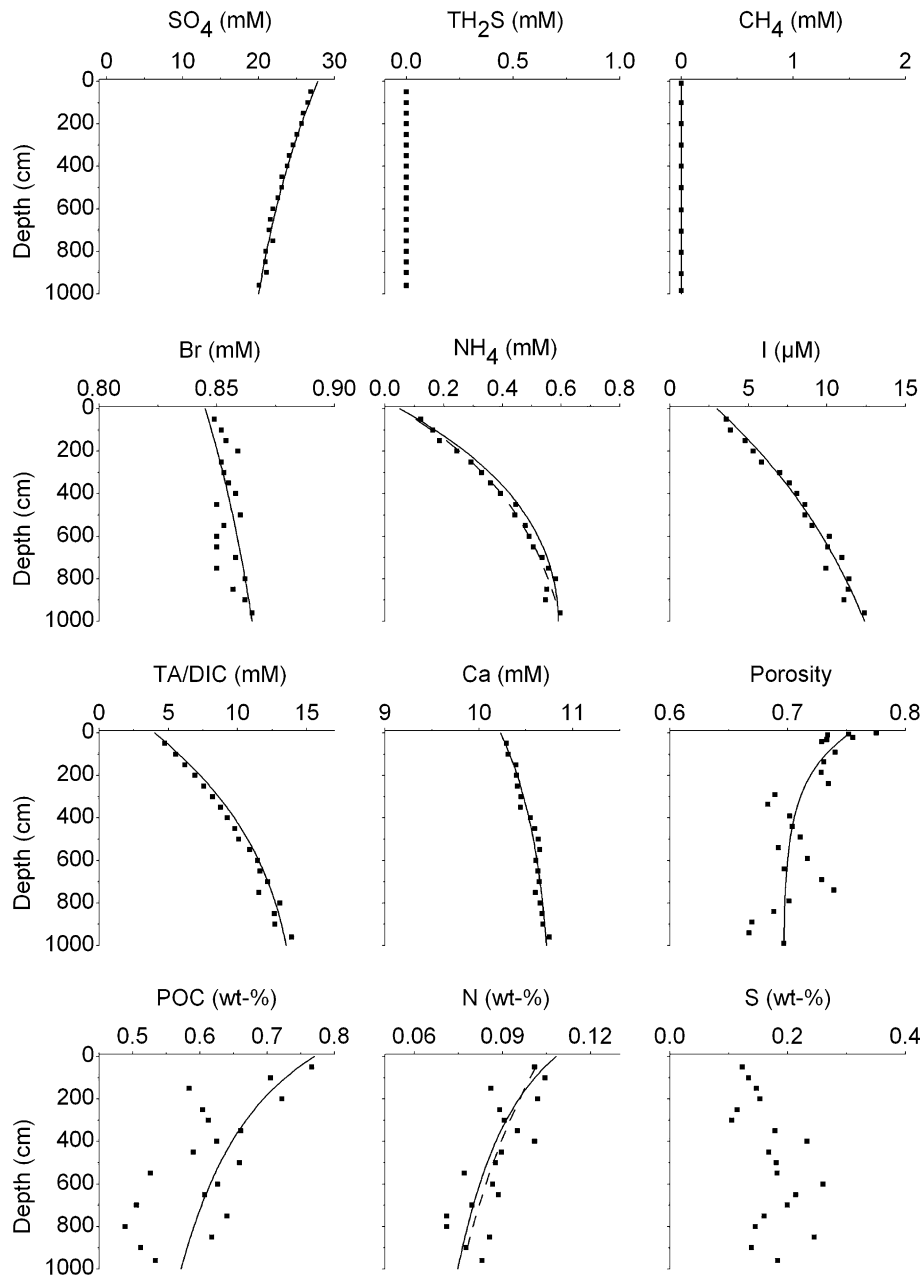


Fig. 2. Data (solid squares) and model results (solid lines) for core SO178 3-4 KL. Top row: Concentrations of sulfate (SO_4), total dissolved sulfide ($\text{TH}_2\text{S} = \text{H}_2\text{S} + \text{HS}^-$) and methane (CH_4) in pore water. Second row: Concentrations of bromide (Br), ammonium (NH_4) and iodide (I) in pore water. Third row: Concentrations of dissolved inorganic carbon ($\text{DIC} = \text{CO}_3^{2-} + \text{HCO}_3^- + \text{CO}_2$) calculated in the model, total alkalinity ($\text{TA} \approx \text{HCO}_3^- + 2\text{CO}_3^{2-} + \text{HS}^-$) measured in pore fluids, dissolved calcium (Ca) in pore water, and porosity of bulk sediments. Bottom row: Concentrations of particulate organic carbon (POC), total nitrogen ($N = \text{organic N} + \text{adsorbed NH}_4$) and total sulfur (S) in sediments. Pore water concentrations are given in mmol dm^{-3} (mM) or $\mu\text{mol dm}^{-3}$ (μM) and are related to the pore water volume while solid phase concentrations are given in weight-percent (wt%) with respect to the weight of dry solids. The broken lines represent functions fitted through the ammonium and total nitrogen data to derive sedimentation rates.

cores. Upper boundary values for solids were also taken from the data.

Finite difference techniques (the method-of-lines code) which have been successfully applied in previous models of early diagenesis (Boudreau, 1996b; Luff et al., 2000; Luff and Wallmann, 2003) were used to solve the model. The set of 10 partial differential equations defining the model (one for each species) is converted into a large

number of ordinary differential equations (ODE) giving the temporal change of species concentrations at each depth interval. A centered finite difference scheme was used for dissolved species while an upward scheme was applied for the transport of solids. The ODE system was set-up on an uneven grid with high resolution at the surface. It was solved and run into steady-state using the NDSolve object of MATHEMATICA Version 5. A

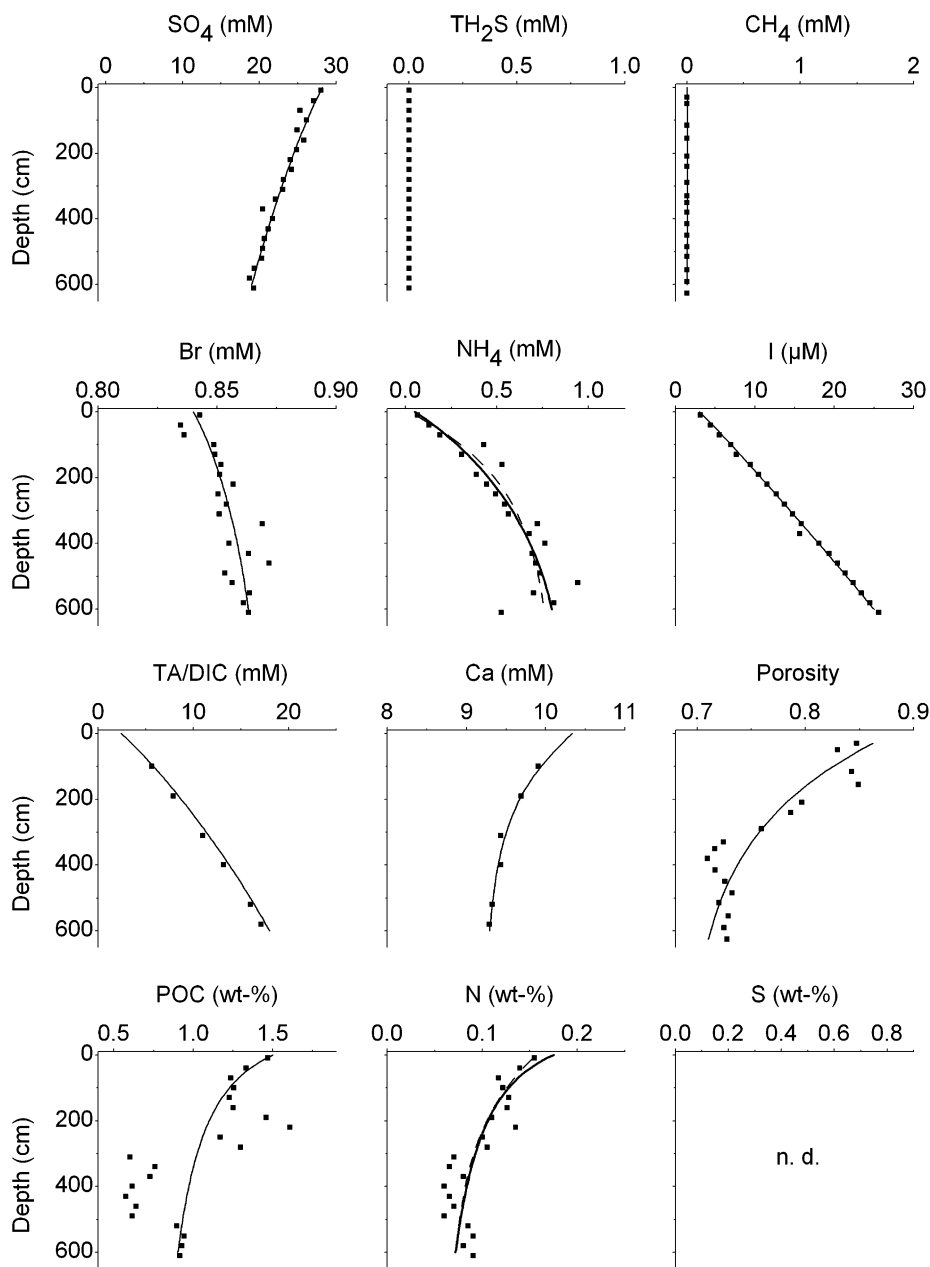


Fig. 3. Data (solid squares) and model results (solid lines) for core LV28 2-4 SL. For further information see legend of Fig. 2.

typical model run took about one minute on a Pentium 4 PC. MATHEMATICA notebooks containing the complete model code can be obtained from the first author upon request.

5. Results and discussion

5.1. Sedimentation rates

Patterns and rates of sedimentation in the Sea of Okhotsk rates have been studied by sediment coring (Gorbarenko et al., 2002) and seismic stratigraphy (Lüdmann and Wong, 2003; Wong et al., 2003). These studies show that Holocene sedimentation rates are as high

as 50–140 cm kyr⁻¹ at the northern Sakhalin slope and decrease by about one order of magnitude towards the southern slope area. On-board observations during cruise SO178 confirmed these general trends (Dullo et al., 2004). In the southernmost core SO178 3-4 KL, a tephra layer (K2, age 26 kyr) was found at a sediment depth of 153 cm indicating a sedimentation rate of about 6 cm kyr⁻¹. Considering, however, that the upper decimeters of this particular core were lost during coring, the sedimentation rate is probably higher than indicated by the uncorrected depth of the tephra layer. In core SO178 10-6 SL located further to the northern, the upper 200–220 cm of the sediment column were probably deposited during the Holocene indicating a sedimentation rate of

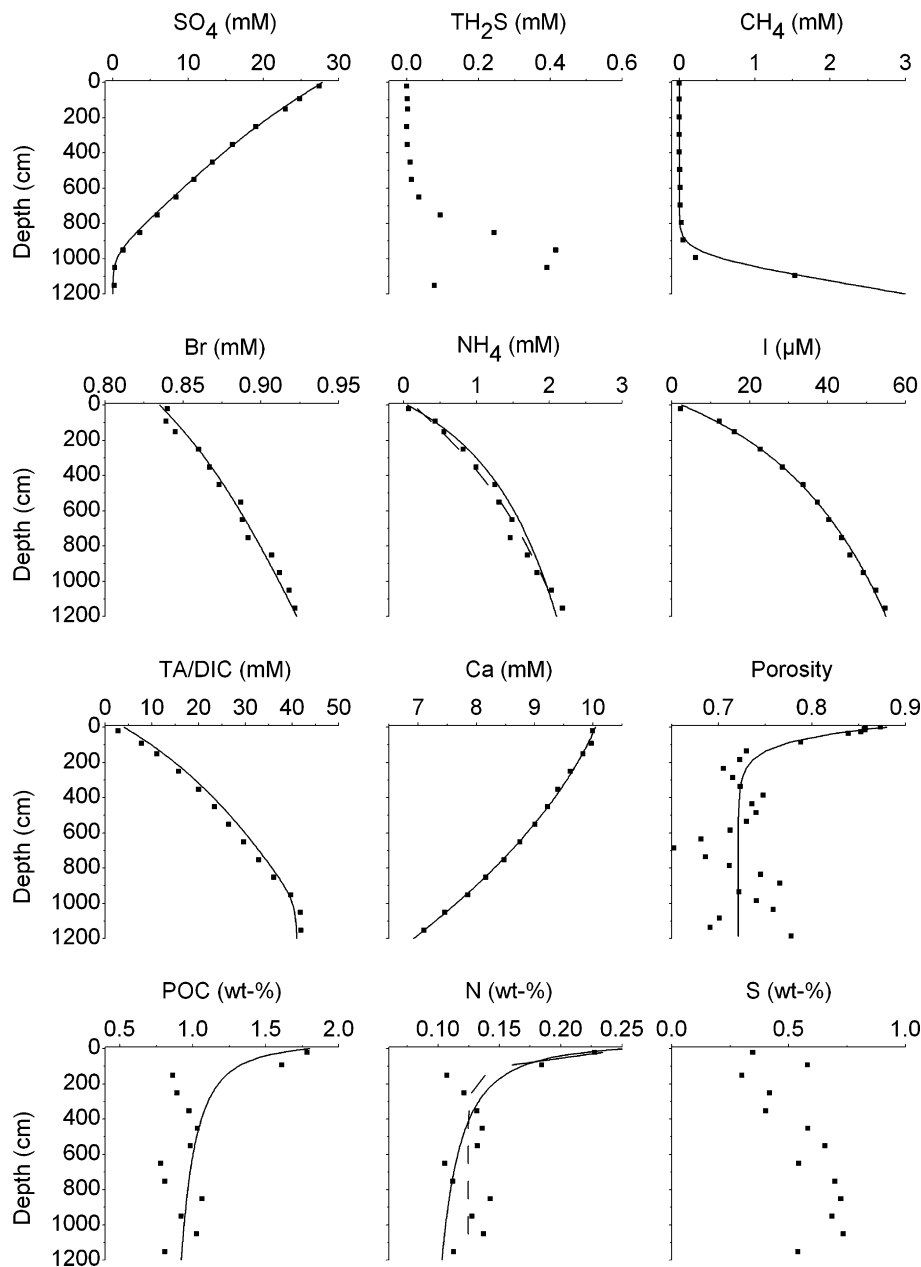


Fig. 4. Data (solid squares) and model results (solid lines) for core SO178 10-6 SL. For further information see legend of Fig. 2.

about 20 cm kyr^{-1} . In the northern core SO178 13-6 KL, the top 10–20 m of the sampled sediments are apparently of Holocene origin indicating sedimentation rates as high as $100\text{--}200 \text{ cm kyr}^{-1}$ (Dullo et al., 2004). It was, however, difficult to develop a good stratigraphy for the slope sediments because of their low carbonate contents and the varying input of terrestrial materials by ice-rafting, erosion of adjacent shelf deposits, and the Amur River.

Hence, we developed a new approach to derive sedimentation rates from a nitrogen mass balance at steady-state. Sedimentation rates (Table 2) were derived from ammonium, particulate nitrogen, and porosity data as outlined in Section 4. The calculations were done repeatedly using different concentrations measured within the uppermost and

lowermost meter of the sediment column. At stations SO178 13-6 KL and SO178 29-2 KL, we considered only the upper 10 and 15 m of the sediment column, respectively, because POC and solid N concentrations increased below these depths indicating enhanced POM depositional rates in the underlying sediments. The resulting values depend on the chosen depth level but were found to fall within the error range given in Table 2.

The calculated sedimentation rates confirm both the order of magnitudes and the regional trend previously observed. Sedimentation rates are low in the southern slope area and strongly increase towards the north due to enhanced marine productivity and supply of suspended matter by the Amur River. The good correspondence between

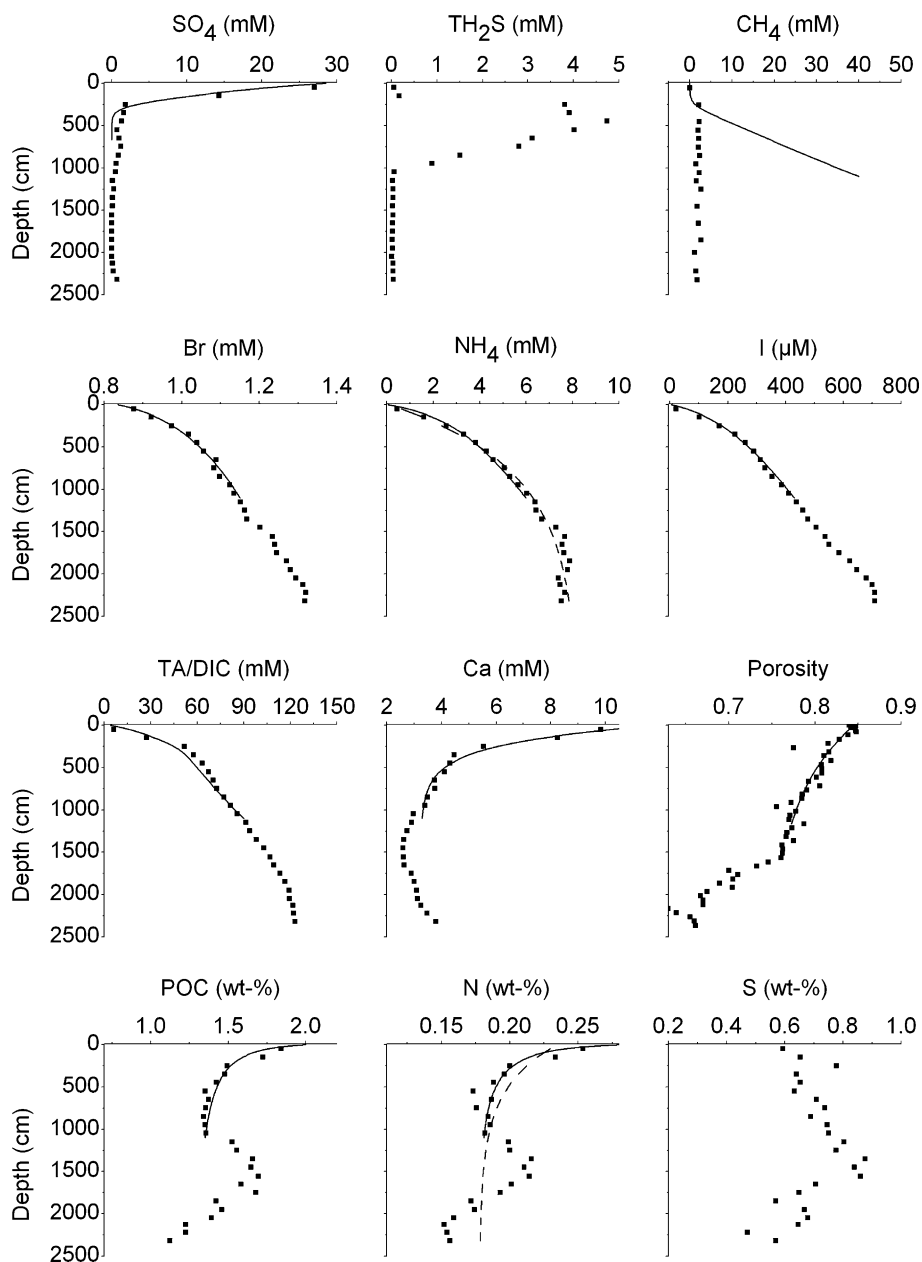


Fig. 5. Data (solid squares) and model results (solid lines) for core SO178 13-6 KL. For further information see legend of Fig. 2.

our results and the previous estimates confirms the validity of the new approach. Sedimentation rates derived from the nitrogen mass balance are particularly well suited for studies on early diagenesis because they provide rates appropriate for steady-state modeling.

5.2. Kinetics of organic matter degradation

Solid phase and pore water data give evidence for high rates of organic matter deposition and degradation in the investigated slope sediments (Figs. 2–7). Concentrations of particulate organic carbon (POC) and total nitrogen (N) increased towards the north due to the enhanced productivity and high sedimentation rates in the northern

slope area. A strong south–north gradient in organic matter supply and degradation is also seen in the shoaling of the sulfate penetration depth caused by enhanced rates of microbial sulfate reduction. At the southern stations (SO178 3-4 KL and LV28 2-4 SL) sulfate penetrates to the base of the cores and dissolved methane was not detected. Other electron acceptors such as oxygen, nitrate, manganese and iron oxides were probably consumed within the top few decimeters so that the decrease in dissolved sulfate with depth and the curvature of the sulfate profile reflect the rates of organic matter degradation in the southern cores. In core SO178 10-6 SL, sulfate was depleted at 1050 cm sediment depth (Fig. 4). Below that depth, methane concentrations rapidly increased towards the base of

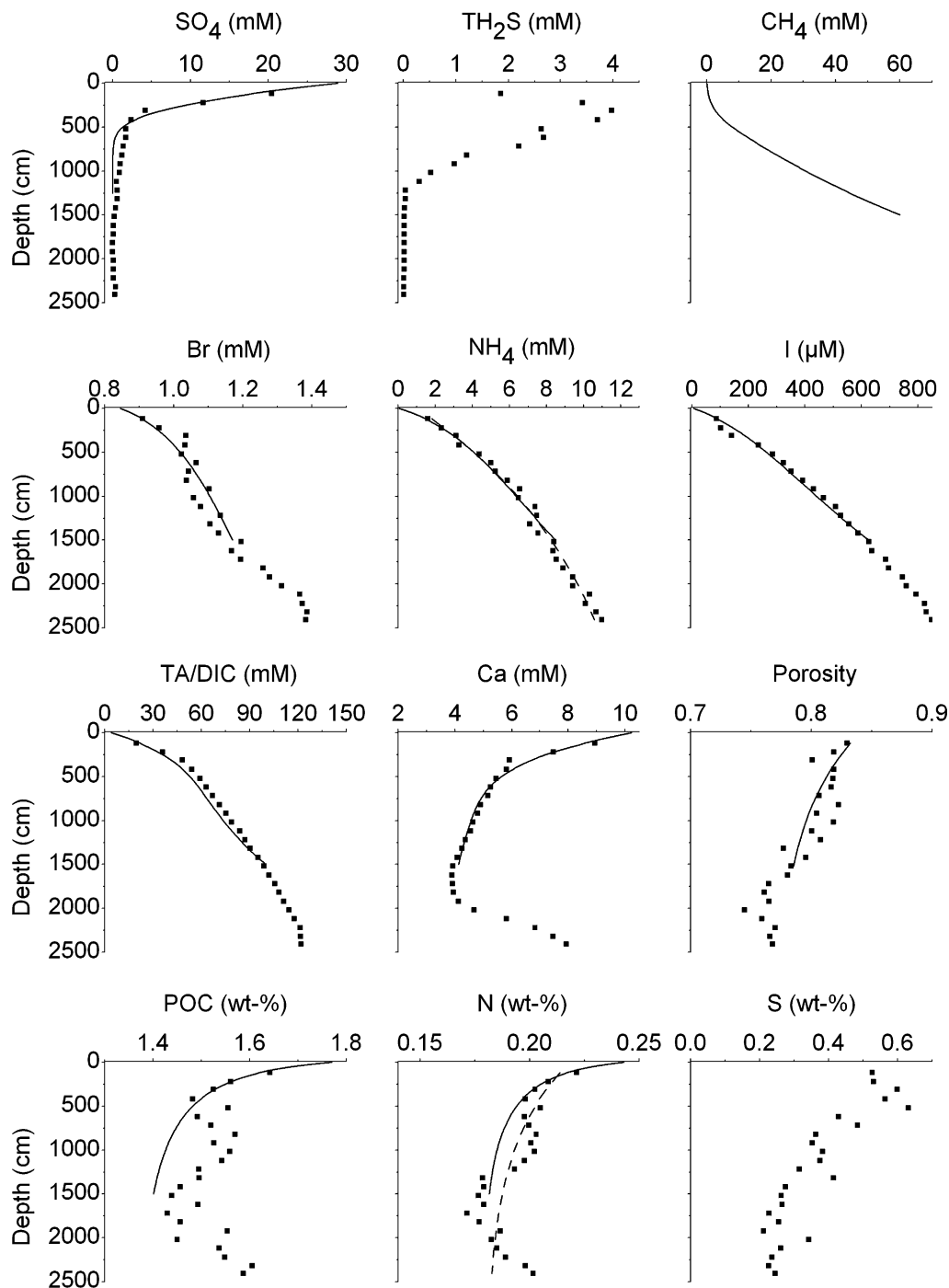


Fig. 6. Data (solid squares) and model results (solid lines) for core SO178 29-2 KL. For further information see legend of Fig. 2.

the core. The AOM layer at around 1000 cm sediment depth is also marked by a strong increase in dissolved sulfide concentration. In the northern cores (SO178 13-6 KL, SO178 29-2 KL, and LV28 20-2 SL) sulfate is already consumed at shallow depths (2–5 m) and methane concentrations start to increase below the sulfate penetration depth.

The initial age of organic matter (a_0) and the constant for the inhibition of organic matter degradation by dissolved

inorganic carbon and methane (K_C) were constrained using the decrease in POC and N with sediment depth and the curvature of the dissolved ammonium and sulfate profiles (see Section 4). The initial age needed to calculate the depth and age-dependent kinetic constant k_x (Middelburg, 1989) controls the interfacial gradients in POC and N . Hence, a_0 was varied until the model reproduced the gradients measured in the top meter of the sediment cores. The resulting values (300–3000 yr, Table 2) reflect the age of organic

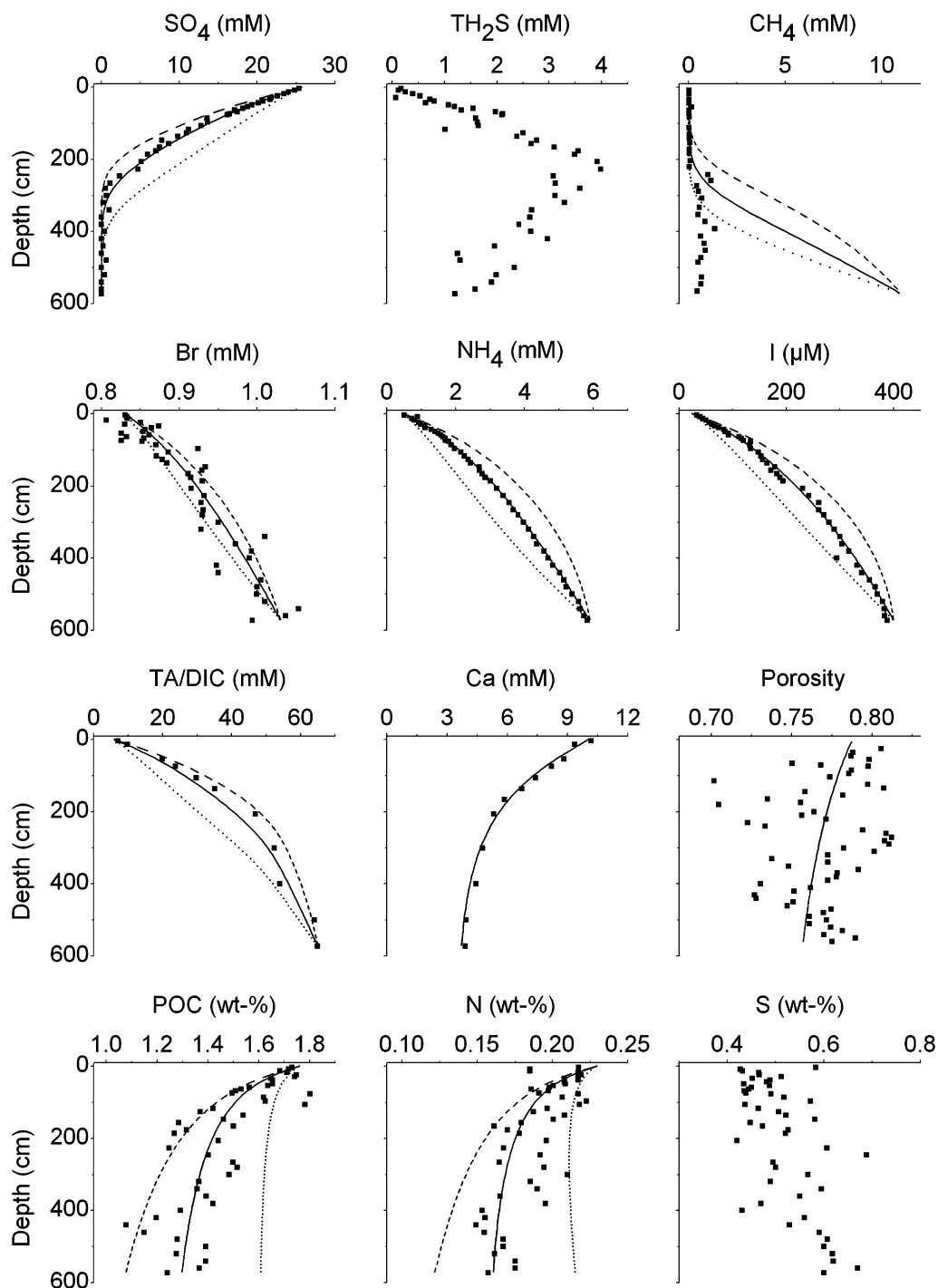


Fig. 7. Data (solid squares) and model results for core LV28 20-2 SL. Solid lines show the best fit to the data attained with an inhibition constant of $K_C = 40$ mM. Dotted lines indicate the results of a model run with $K_C = 4$ mM and broken lines show the model results using $K_C = 400$ mM. For further information see legend of Fig. 2.

matter buried below the bioturbated surface layer which was not resolved by the data and the model. A very large value ($a_0 = 30\,000$ yr) was used for core SO178 3-4 KL, because the upper decimeters of that particular core were lost during sampling by over-penetration of the coring device. The value of the inhibition constant (K_C) was determined using the curvature of the sulfate and ammonium profiles and the

gradients in POC and N in the deeper sediment layers. Sulfate is consumed not only via organic matter degradation but also during AOM. Hence, sulfate data were only applied to constrain organic matter degradation rates in methane-free cores (SO178 3-4 KL and LV28 2-4 SL). Modeled rather than measured concentrations of dissolved inorganic carbon (DIC) and methane were considered in the modeling of

Table 2
Parameter values derived by fitting the model to the data

Parameter (symbol)	SO178 3-4 KAL	LV28 2-4 SL	SO178 10-6 SL	SO178 13-6 KL	SO178 29-2 KL	LV28 20-2 SL	ODP 997
Sedimentation rate (cm kyr ⁻¹)	10 ± 1	10 ± 5	13 ± 5	93 ± 2	115 ± 5	90 ± 3	22 ^a
Initial age of POM (<i>a</i> ₀ in yr)	30,000	3000	1000	300	1000	580	2E + 5
Monod constant for the inhibition of POM degradation by DIC and CH ₄ (<i>K</i> _C in mM)	30	40	30	40	30	40	35
Monod constant for the inhibition of CH ₄ formation by SO ₄ (<i>K</i> _{SO₄} in mM)	1.0	1.0	1.0	1.0	1.0	1.0	1.0
Kinetic constant for AOM (<i>k</i> _{AOM} in cm ³ yr ⁻¹ mmol ⁻¹)	1.0	1.0	30	10	1.0	20	1.0
Constant for ammonium adsorption (<i>k</i> _{ADS} in cm ³ g ⁻¹)	1.7	1.7	1.7	1.7	0.3	1.7	0.6
Atomic N/C ratio for POM degradation (<i>r</i> _N)	16/106	16/106	16/106	16/106	16/106	16/106	16/106
Atomic I/C ratio for POM degradation (<i>r</i> _I)	1.2E-3	1.5E-3	3.5E-3	8.0E-3	8.0E-3	1.0E-2	2.8E-3
Atomic Br/C ratio for POM degradation (<i>r</i> _{Br})	2.0E-3	4.0E-3	3.0E-3	7.0E-3	7.0E-3	4.0E-3	4.0E-3

^a Sedimentation rate at Site 997 taken from (Davie and Buffett, 2001).

organic matter degradation since most of the dissolved methane and some of the dissolved CO₂ were lost during sampling due to the decrease in pressure upon core retrieval. Methane concentrations at the core base were varied until the resulting AOM rates produced sulfate penetration depths consistent with the data. DIC concentrations at the core base were set according to the measured values of total alkalinity. The resulting *K*_C values fall into a narrow range of 30–40 mM indicating that the kinetic rate law defined in Eq. 3 is well suited to describe the inhibiting effect of DIC and methane on organic matter degradation over a large range of sedimentary environments (Table 2).

The sensitivity of the model results with respect to the value of the inhibition constant (*K*_C) is shown in Fig. 7. The best fit to the data was obtained using *K*_C = 40 mM. Two additional model runs were performed applying *K*_C values of 4 mM (dotted lines) and 400 mM (broken lines). The other model parameters were not changed in these model runs but maintained at the values listed in Table 2. Organic matter degradation rates were diminished applying the reduced *K*_C value because the degradation rates were now suppressed already at low concentrations of DIC and methane. Consequently, the concentrations of POC and *N* increased at the core base while the concentrations of dissolved metabolites were substantially reduced. A large *K*_C value decreased the solid phase concentrations at the core base and substantially increased the curvature of the metabolite profiles. Not only the ammonium pore water data but also the profiles of DIC, bromide and iodide were strongly affected by the variation of the inhibition constant. The well constrained iodide data thus give further evidence for the inhibition of organic matter degradation. The strong sensitivity of the model results with respect to the value of the inhibition constant and the good fit obtained in the standard run (*K*_C = 40 mM) demonstrate that the data set used in this study can be explored to both trace the inhibition of organic matter degradation by metabolites and constrain the inhibition constant.

In the following, the new kinetic model is compared with previous models of organic matter degradation. Multi-G models have been commonly used to simulate the

degradation of organic matter in marine sediments (Westrich and Berner, 1984; Boudreau, 1996b; Luff et al., 2000). In these models, the organic matter is separated into several fractions with different reactivity. Here, a 2-G model is tested where the organic matter is assumed to be composed of a labile (G1) and a more refractory fraction (G2). The rate of organic carbon degradation is calculated as:

$$R_{\text{POC}} = k_1 \cdot G_1 + k_2 \cdot G_2, \quad (9)$$

and the particulate organic carbon concentration is defined as:

$$\text{POC} = f_{\text{POC}} \cdot G_1 + (1 - f_{\text{POC}}) \cdot G_2. \quad (10)$$

The parameters of the kinetic model were constrained by fitting the model to the pore water and solid phase data of core LV28 2-4 SL. The best fit was obtained applying $k_1 = 3 \times 10^{-4} \text{ yr}^{-1}$ as kinetic constant for the labile fraction and $k_2 = 5 \times 10^{-6} \text{ yr}^{-1}$ for the refractory fraction assuming that 20% of the total organic carbon occur in the labile form ($f_{\text{POC}} = 0.2$).

The other commonly used type of kinetic rate law considers organic matter to be composed of a very large number of different molecules each having its own reactivity. The first and most popular version is Middelburg's age-dependent model:

$$R_{\text{POC}} = k_x \cdot \text{POC} = 0.16 \cdot \left(a_0 + \frac{x}{w} \right)^{-0.95} \cdot \text{POC}. \quad (11)$$

It predicts that the reactivity of organic matter decreases continuously with age and sediment depth and serves as base for the new kinetic model presented in this paper. Both traditional models assume that degradation rates are not affected by the pore water composition whereas the new kinetic rate law presented in this paper predicts that rates are suppressed by the accumulation of dissolved metabolites.

Fig. 8 compares the results obtained with 2-G kinetics, the age-dependent approach and the new rate law. The fully anoxic core LV28 20-2 SL was used for these simulations because this core was sampled with the highest depth resolution. The parameter values applied in the previous

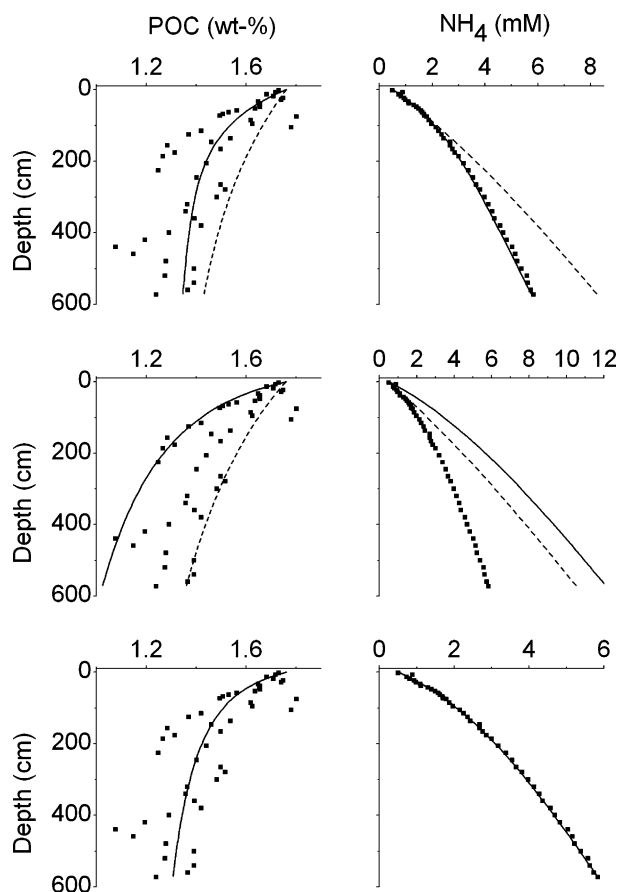


Fig. 8. Data (solid squares) and model results for core LV28 20-2 SL. The upper two panels show the results obtained with the 2-G model. Solid lines indicate the best fit produced with $k_1 = 1 \times 10^{-3} \text{ yr}^{-1}$ and $k_2 = 8 \times 10^{-6} \text{ yr}^{-1}$ whereas broken lines were calculated applying the rate constants derived from core LV28 2-4 SL ($k_1 = 3 \times 10^{-4} \text{ yr}^{-1}$ and $k_2 = 5 \times 10^{-6} \text{ yr}^{-1}$). The middle panels show results produced with the age-dependent model (solid line: $a_0 = 580 \text{ yr}$; broken line $a_0 = 2000 \text{ yr}$) while the bottom panels depict the results obtained with the new rate law.

standard model run (Table 2) were also used in these addition model simulations. Constant gradients rather than prescribed concentrations were, however, applied at the lower boundary to better evaluate the prognostic capacity of the different kinetic models. In other words, the concentration gradients of dissolved species in the last interval of the model column (n) were now set to the value calculated for the overlying depth interval ($n - 1$).

$$\frac{\delta C}{\delta x}(n) = \frac{\delta C}{\delta x}(n - 1). \quad (12)$$

Applying the kinetic parameters derived from core LV28 2-4 SL to core LV28 20-2 SL, the 2-G model was not able to reproduce the data (Fig. 8). A good fit was, however, obtained when the kinetic constants were adjusted to $k_1 = 1 \times 10^{-3} \text{ yr}^{-1}$ and $k_2 = 8 \times 10^{-6} \text{ yr}^{-1}$. The organic matter at the northern site LV28 20-2 SL was, thus, more reactive than the sedimentary organic matter retrieved at the southern station LV28 2-4 SL. This significant difference in reactivity probably reflects the large contrast in sedimentation rate between the two sites. At the southern

location sedimentation was low (10 cm kyr^{-1}) whereas the northern station receives more terrigenous sediments from the adjacent Amur River inducing a much higher sedimentation rate (90 cm kyr^{-1}). The age of sedimentary organic matter at a given depth level, therefore, increases towards the south. Since, the reactivity of organic matter decreases with sediment age, the kinetic constants are lower at the southern station. Several authors recognized that the reactivity of organic matter during anaerobic degradation depends on sedimentation rate (Boudreau, 1997). Thus, Tromp et al. (1995) provided an empirical equation relating the kinetic constant for POC degradation via sulfate reduction to sedimentation rate. This equation correctly predicts that the reactivity of organic matter increases with sedimentation rate but does not consider the decrease in reactivity with sediment depth observed in our data. The 2-G model applied here mimics the decrease in reactivity with sediment depth. It proved to be a useful tool to fit pore water and solid phase data. The best-fit values for the kinetic parameters differed, however, considerably among individual cores. To this date, no a priori method is available for predicting the rate constants of organic matter degradation in anoxic sediments over a wide range of sedimentary environments and sediment depths. The available multi-G models are, hence, not suitable for prognostic modeling.

Degradation rates predicted by the age-dependent model without inhibition term were too high over the deeper part of the sediment column (Fig. 8). An increase in the initial age a_0 from the standard value (580 yr) to 2000 yr reduced the overall degradation rates but could not mimic the strong decrease in degradation with sediment depth observed in the data. The original model was mainly calibrated using short sediment cores with low dissolved metabolite concentrations (Middelburg, 1989). The data and modeling presented in this paper indicate that organic matter is more slowly degraded in anoxic sediments with high metabolite concentrations than predicted by Middelburg's model for a given sediment age.

The new rate law introduced in this paper produced an excellent fit to the data also with the constant gradient condition applied at the lower boundary (Fig. 8). The good fit obtained in the previous standard simulation with a constant ammonium concentration prescribed at the base of the core is, thus, not a result of the lower boundary condition but rather reflects the inherent reactivity of organic matter in core LV28 20-2 SL. In contrast to the previous kinetic models, the new model correctly predicts organic matter degradation rates in anoxic slope deposits over a wide range of sedimentation rates and sediment depths.

5.3. Bromine and iodine cycling

Dissolved bromide and iodide concentrations in the pore water increased with sediment depth and towards the north (Figs. 2–7). Both halogens are released into the

pore water by the microbial degradation of POM. The pore fluids were significantly enriched in dissolved bromide. Bromide release rates were calculated from the POC degradation rates applying Br/POC ratios (r_{Br}) that produced a good fit the pore water profiles. The resulting values ($r_{Br} = 2\text{--}7 \times 10^{-3}$; Table 2) were on average higher than the plankton ratio (2.2×10^{-3}). Previous work showed that atomic Br/POC ratios in surface sediments ($0.3\text{--}2 \times 10^{-3}$) are lower than the plankton ratio and decrease with depth implying a preferential degradation of Br-bearing organic matter (Martin et al., 1993). This preferential release of bromide is confirmed by our data.

Extremely high iodide concentrations of more than 0.8 mM were found at the base of core SO178 29-2 KL (Fig. 6). Comparable concentrations were previously found in sediment cores retrieved by deep-sea drilling albeit at much larger sediment depth (Martin et al., 1993; Egeberg and Dickens, 1999). The high iodide concentrations reflect the enormous burial flux of organic matter in the northern slope region produced by a combination of very high marine productivity and intense terrigenous sedimentation. Atomic ratios between the release of iodide and inorganic carbon (r_I) were determined by fitting the model to the data. They were found to increase towards the north by one order of magnitude (Table 2). All ratios were significantly higher than the atomic I/POC ratio of plankton (1.4×10^{-4} ; Elderfield and Truesdale, 1980) indicating additional iodine sources or the preferential degradation of iodine-bearing organic compounds. Previous studies showed that iodide released at depth diffuses to the sediment surface to be taken-up at the oxic interface by microbially mediated redox processes (Kennedy and Elderfield, 1987). Oxic surface sediments attain very high I/POC ratios in the solid phase (up to 3×10^{-3}) due to the uptake of iodide from the pore water (Kennedy and Elderfield, 1987). Moreover, previous pore water data suggest that I is preferentially released into solution during microbial degradation processes. Hence, I/POC regeneration ratios of $0.1\text{--}34 \times 10^{-3}$ were found in oxic to suboxic marine surface sediments (Kennedy and Elderfield, 1987). The values derived

for our anoxic slope cores ($1\text{--}10 \times 10^{-3}$) fall into this range (Table 2). They indicate that the preferential release of iodide is not limited to the more oxidizing surface sediments but occurs also in deeper anoxic layers. The regular increase in these ratios towards the more productive northern slope indicates that high regeneration ratios are maintained in strongly anoxic sediments receiving a large flux of marine organic matter.

5.4. Sulfur cycling

Dissolved sulfate and sulfide profiles and concentrations of total sulfur in the solid phase were used to characterize the turnover of sulfur in the studied anoxic sediments (Figs. 2–7). Among these parameters, dissolved sulfate is most suitable for the modeling since sulfide is partly lost during core retrieval and pore water separation while pyrite formation may start already within the bioturbated surface layer not resolved by the model (Fossing et al., 2000). Solid phase sulfur concentrations were indeed high in the uppermost sediment samples (Figs. 2–7) reflecting the formation of pyrite in reactive surface sediments. Dissolved sulfide profiles showed distinct maxima in the sulfate-methane transition zone where sulfide was rapidly produced by AOM. In contrast, the dissolved sulfide concentrations were low and close to the detection limit in methane-free sediments indicating that sulfide produced during sulfate reduction via organic matter degradation was almost completely removed from the pore water by the formation of pyrite and other authigenic sulfur phases.

The benthic sulfate fluxes at the sediment surface (Table 3) ranging in between 10 and 200 $\text{mmol m}^{-2} \text{yr}^{-1}$ are a measure for the total sulfate consumption in sediments underlying the bioturbated surface layer. These fluxes increase towards the north due to enhanced rates of organic matter sedimentation. They are similar to those reported for other reactive continental margins such as the western Argentine Basin (Hensen et al., 2003), and the Black Sea (Jørgensen et al., 2001). The benthic fluxes are driven by sulfate reduction via organic matter

Table 3
Depth-integrated turnover rates and fluxes (in $\text{mmol m}^{-2} \text{yr}^{-1}$) calculated in the model and length of the sediment column considered in the modeling (in m)

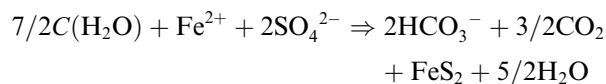
Rate/flux	SO178 3-4 KAL	LV28 2-4 SL	SO178 10-6 SL	SO178 13-6 KL	SO178 29-2 KL	LV28 20-2 SL	ODP 997
Length of model column	10	6	12	11	15	5.7	451
POC degradation	12.7	39.5	68.3	325	207	233	27.2
PON degradation	1.91	5.96	10.3	49.1	31.3	35.2	4.11
POI degradation	0.015	0.059	0.239	2.60	1.66	2.33	0.076
POBr degradation	0.025	0.158	0.205	2.28	1.45	0.934	0.108
SO ₄ reduction via POC degr.	6.08	19.0	31.6	122	76.9	104	2.76
Methane formation	0.25	0.76	2.50	40.4	26.7	13.0	10.8
AOM	0.205	0.467	16.1	78.5	59.0	45.4	10.5
Ammonium adsorption	0.071	0.101	0.319	6.00	1.68	5.48	3.00
CaCO ₃ precipitation	-0.48	3.38	-0.54	29.6	15.5	21.6	n.d.
Benthic SO ₄ flux	10.4	27.9	47.9	201	136	149	13.4
POC burial	36.2	58.8	69.5	662	772	641	303
N burial	4.06	4.00	6.67	76.0	85.7	68.1	37.7

degradation and AOM. Depth-integrated rates of these processes increased towards the north (Table 3). In the three northern cores, sulfate was consumed via organic matter degradation at a mean rate of $101 \pm 23 \text{ mmol m}^{-2} \text{ yr}^{-1}$ while the average AOM rate was $61 \pm 17 \text{ mmol m}^{-2} \text{ yr}^{-1}$. Hence, about 40% of sulfate was consumed by AOM in the northern slope area. The fraction of sulfate being consumed by AOM rather than organic matter degradation seems to be highly variable at different continental margin sites. Thus, Fossing et al. (2000) and Jørgensen et al. (2001) performed sulfate reduction rate measurements in continental margin sediments off Namibia and in the Black Sea showing that only a minor portion of the depth-integrated sulfate consumption is due to AOM. In contrast, Niewöhner et al. (1998) observed linear sulfate gradients in surface sediments at the U.S. North Atlantic and Namibia continental margins overlying major gas hydrate deposits and concluded that sulfate reduction is almost completely driven by AOM at these sites. The significant curvature in the sulfate, ammonium, bromide and iodide profiles observed in the sediments off Sakhalin (Figs. 2–7) demonstrates, however, that organic matter degradation contributes significantly to the overall sulfate reduction in these slope deposits.

5.5. CaCO_3 turnover

Solid phase concentrations of CaCO_3 were low over the entire slope area ranging in between 0 and 2 wt% with a mean value of 0.5 wt% in the sampled slope sediments (data not shown). Pore water profiles of dissolved Ca indicate, however, that both carbonate dissolution and precipitation may occur in anoxic slope deposits off Sakhalin (Figs. 2–7). In the southernmost core (SO178 3-4 KAL) Ca concentrations increased with depth suggesting a depth integrated CaCO_3 dissolution rate of $0.48 \text{ mmol m}^{-2} \text{ yr}^{-1}$ (Table 3). Core LV28 2-4 SL experienced CaCO_3 precipitation over the entire core length (Fig. 3) while the dissolved Ca profile in core SO178 10-6 SL suggests CaCO_3 dissolution in the upper layers and CaCO_3 precipitation at the base of the core (Fig. 4). The northern cores (Figs. 5–7) showed signs of CaCO_3 precipitation in the upper ~15 m followed by CaCO_3 dissolution in the deeper layers.

Carbonate dissolution/precipitation are mainly driven by the release of CO_2 and HCO_3^- during the anaerobic degradation of organic matter and the oxidation of methane. During degradation of organic matter (here represented as simple carbohydrate $\text{C}(\text{H}_2\text{O})$) via sulfate reduction both CO_2 and HCO_3^- are released while sulfide is fixed in pyrite:



Fe^{2+} may either originate from the microbial reduction of iron oxides or iron-bearing clay minerals and carbonates.

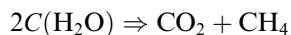
Models show that CaCO_3 is dissolved at low rates and during the initial phase of sulfate reduction while CaCO_3 precipitation prevails at high rates of sulfate reduction via organic matter degradation (Boudreau and Canfield, 1993). These model predictions are confirmed by some of our data showing CaCO_3 dissolution at low sulfate reduction rates (core SO178 3-4 KL) and in the upper section of the sulfate reduction zone (core SO178 10-6 SL).

During AOM, carbonate alkalinity is generated and bisulfide accumulates in the pore water:



Hence, AOM induces CaCO_3 precipitation in marine sediments (Wallmann et al., 1997; Luff and Wallmann, 2003). The pore water data clearly show that Ca concentrations always decrease towards the base of the sulfate-bearing zone confirming that CaCO_3 is precipitated during the anaerobic oxidation of methane. The average depth-integrated rate of carbonate precipitation in the three northern cores is $22 \pm 7 \text{ mmol m}^{-2} \text{ yr}^{-1}$ while the AOM rate amounts to $61 \pm 17 \text{ mmol m}^{-2} \text{ yr}^{-1}$ in these cores (Table 3). The data hence suggest that one third of the carbonate alkalinity generated via AOM is removed from the pore water via authigenic CaCO_3 precipitation. A similar proportion was previously found at active cold vent sites where methane-charged fluids ascend to the sediment surface (Luff et al., 2004).

In the underlying zone, methane and CO_2 are generated during the degradation of organic matter:



Carbonates should hence be dissolved in the methanogenic zone as indeed suggested by the increase in dissolved Ca towards the base of cores SO178 13-6 KL and SO178 29-2 KL (Figs. 5,6). We observed however a remarkable increase in total alkalinity within the methanogenic zone which is probably not driven by the degradation of organic matter or the dissolution of CaCO_3 but rather by the chemical weathering of silicate phases as previously observed in other anoxic marine sediments (Aloisi et al., 2004; Maher et al., 2004).

5.6. Organic matter degradation and gas hydrate formation at Blake Ridge

Gas hydrate formation at Blake Ridge, a large drift deposit located at the passive continental margin of the south-eastern United States, has been studied in detail during ODP Leg 164 (Dickens et al., 1997). According to the ODP data, hydrates occupy in between 4% and 7% of pore space in these sediments between 186 and 451 mbsf. The excellent set of pore water data retrieved from Site 997 has been used repeatedly to constrain the velocity of upward fluid flow, rates of methane oxidation and gas hydrate formation and the hydrate distribution in these deposits. Egeberg and Dickens (1999) used the curvature of the bromide and iodide pore water profiles and the

dissolved Br/I ratio to constrain the velocity of upward fluid flow as 0.2 mm yr^{-1} . This values should, however, be considered as a maximum estimate since pore water burial and the in situ production of halogens from organic matter degradation processes were neglected by the authors. They further used the dissolved chloride profiles to derive rates of gas hydrate formation. These rates were not related to the organic carbon data and the concentrations of dissolved metabolites in pore fluids but were prescribed as a rather arbitrary source function satisfying the chloride observations. Davie and Buffett published a series of papers on the rates and mechanisms of hydrate formation at Black Ridge (Davie and Buffett, 2001, 2003a,b). They finally concluded that the Blake Ridge observations (dissolved sulfate and chloride profiles, gas hydrate concentrations) can be explained by microbial methane production within the lower part of the HSZ combined with an inflow of fluids (0.23 mm/yr) transporting methane and acetate from the deep underground into the HSZ (Davie and Buffett, 2003b). Since an unreasonable large fraction of sedimentary organic matter has to be degraded to produce the observed hydrate accumulation, inflowing acetate rather than POC might be the main substrate for methane production at this site (B. Buffett, pers. communication).

We used Site 997 to test our new kinetic model on a well studied reference location and to calculate rates of methane production and hydrate precipitation within the HSZ. In contrast to previous modeling studies at Blake Ridge, we evaluate the entire biogeochemical data set including concentration profiles of dissolved metabolites (ammonium, bromide, and iodide), dissolved sulfate, particulate organic carbon, and total nitrogen (Fig. 9). Based on this comprehensive approach, the gas hydrate formation through organic matter degradation was quantified much more reliably than in previous model studies. The model was modified to consider the specific conditions at Blake Ridge (Appendix B). Thus, organic matter concentrations measured in surface sediments are significantly lower than those observed at large sediment depths (see POC and N in Fig. 9). This important observation strongly suggests a decrease in organic matter deposition over time. To mimic this non-steady-state situation, we applied a time-dependent POC concentration at the top of the model column. Interfacial POC concentrations were kept constant at a value of 1.6 wt% over a period of 5 Myr and were forced to decrease linearly over the last 0.7 Myr of the model period to a modern value of 0.65 wt%. Sedimentation rates and temperature gradients were taken from Davie and Buffett (2001) while pressures were calculated from water and sediment depths assuming hydrostatic conditions. Moreover, hydrate precipitation, upward fluid flow, and the temperature effect on molecular diffusion were included in the extended model version applied to Blake Ridge (Appendix B).

The best fit to the data was obtained with the set of parameter values listed in Table 2 and an interstitial fluid flow velocity of 0.12 mm yr^{-1} at the sediment surface.

The initial age of the decaying organic matter was set to a high value since the almost linear sulfate profiles at Blake Ridge suggest low rates of organic matter degradation in surface sediments. Black Ridge is a sediment drift that consists of hemipelagic silt and clay-rich contourite deposits originating from northern continental slope areas (Paull et al., 2000). Late Quaternary sedimentation rates are about one order of magnitude lower than the average sedimentation rate applied in the modeling (Paull et al., 2000). The high initial age may thus reflect the slow deposition of reworked old organic matter at the sediment surface. The good fit to the pore water and sediment data (Fig. 9) shows that the kinetic model can be used to constrain rates of organic matter degradation and microbial methane formation not only in surface sediments of the Sakhalin slope area but also over the entire HSZ of Blake Ridge and presumably other continental margin sites.

Rates of biogenic methane production decreased over time due to the diminished deposition of organic carbon at the top of the model column (Fig. 10). The rate profile at 0.7 Myr represents the steady-state attained after the interfacial POC concentration was maintained at a constant value of 1.6 wt% over a period of 5 Myr. The subsequent decrease in the interfacial POC values induced a significant drop in methane production over the top 200 m of the sediment column. The rate maximum was shifted from 22 m at 0.7 Myr to 28 m sediment depth for the modern situation since the reduced methane production allowed for a deeper penetration of dissolved sulfate. Methane production was suppressed in the sulfate-bearing surface layer and decreased below the rate maximum due to the low reactivity of old organic matter and the increasing concentrations of DIC and methane. The shallow rate maximum is a result of the new kinetic law applied in the model. It induces a significant methane production at shallow depth which does not directly contribute to the formation of hydrates since methane is lost by rapid diffusion into the adjacent sulfate-bearing layer where methane is consumed by anaerobic oxidation.

Hydrate concentrations calculated in the model are at least one order of magnitude lower than the values obtained during ODP drilling. This significant difference suggests that most of the hydrate-bound methane is neither formed by in situ organic matter degradation nor transported to the HSZ by the ascent of methane-charged fluids. Gas bubbles ascending from deep sediments were recently found to deliver abundant methane to the HSZ at Hydrate Ridge (Torres et al., 2004). A similar process may also take place at Blake Ridge. Thus Gorman et al. (2002) presented seismic data suggesting that gas bubbles from below the HSZ migrate upwards into the HSZ at Blake Ridge. Flemings et al. (2003) showed that lithostatic gas pressures prevail in the interconnected gas column formed below the HSZ at Site 997. They propose that this over-pressured gas reservoir may exceed the strength of the sediment above driving fractures that vent methane gas into the HSZ. Our model analysis supports this view and implies

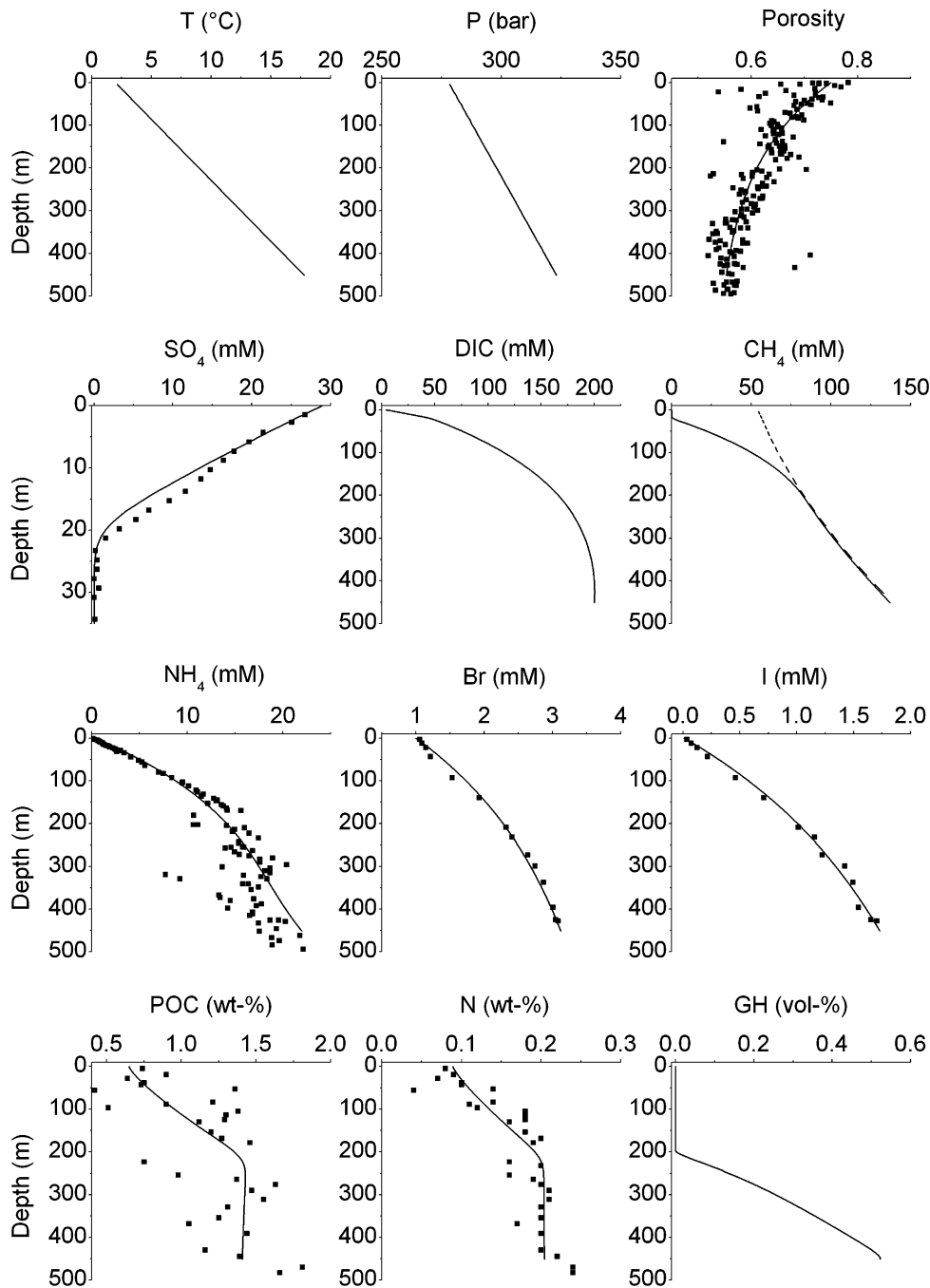


Fig. 9. Data (solid squares) and model results (solid lines) for ODP Site 997. Top row: Temperature (T), pressure (P), and porosity. Second row: Concentrations of dissolved sulfate (SO_4 , note that only the upper 35 m of the sediment column are plotted since sulfate is depleted in deeper sediment layers), concentrations of dissolved inorganic carbon (DIC), dissolved methane (CH_4 , solid line: calculated concentrations, broken line: solubility of gas hydrates). Third row: Dissolved ammonium (NH_4), bromide (Br), and iodide (I). Bottom row: Concentrations of particulate organic carbon (POC), total nitrogen (N = organic N + adsorbed NH_4) and gas hydrates (GH, given in % of pore volume filled by hydrate).

that most of the Blake Ridge hydrates are formed by bubble ascent.

5.7. Gas hydrate formation in Sakhalin slope sediments

The new kinetic model was applied to quantify rates of gas hydrate formation via organic matter degradation along the Sakhalin slope. Modeling was performed for

slope sediments located at a constant water depth of 700 m. Lüdmann and Wong (2003) estimated an average geothermal gradient of $33 \pm 9 \text{ }^\circ\text{C km}^{-1}$ from seismic BSR observations in the northern slope area. Considering the ambient bottom water temperature ($2 \text{ }^\circ\text{C}$) and hydrostatic loading, this estimate implies that the thermodynamically controlled transition from pure hydrate to free gas should occur at a sediment depth of 300 m (Tishchenko et al.,

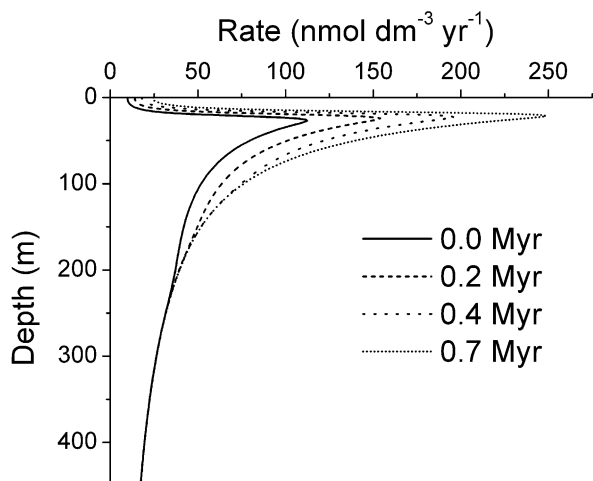


Fig. 10. Rates of biogenic methane production in Blake Ridge sediments as calculated in the non-steady-state model. Rate profiles are plotted for four different times. The highest values were attained at 0.7 Myr before present after a constant POC concentration of 1.6 wt% was applied over a period of 5 Myr at the top of the model column. Subsequently the interfacial POC value was linearly reduced to a modern value of 0.65 wt%. In response to this model forcing rates of methane production significantly decreased over time.

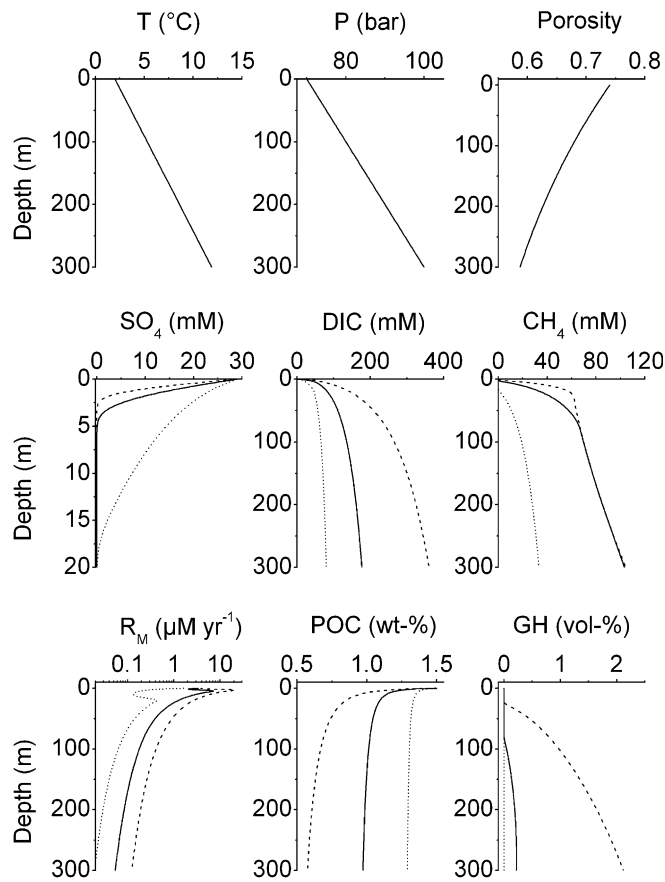


Fig. 11. Inhibition of gas hydrate formation in Sakhalin slope sediments. Top row: Temperature (T), pressure (P), and porosity. Second row: Concentrations of dissolved sulfate (SO_4 , note that only the upper 20 m of the sediment column are plotted since sulfate is depleted in deeper sediment layers), concentrations of dissolved inorganic carbon (DIC), dissolved methane (CH_4). Third row: Rate of methane formation (R_M , note the logarithmic scale), concentrations of particulate organic carbon (POC) and gas hydrates (GH, given in % of pore volume filled by hydrate). Dotted line: $K_C = 3.5$ mM; solid line $K_C = 35$ mM (standard value); broken line: $K_C = 350$ mM.

2005). The model was hence run for a column extending from the sediment surface to a depth of 300 m covering the entire HSZ. The porosity profile was adjusted to fit ODP observations in diatomaceous clayey silt sediments as summarized in Einsele (2000). The inhibition constant was varied over two orders of magnitude to investigate the effect of metabolite inhibition on gas hydrate formation while the sedimentation rate was varied in between 10 and 100 cm kyr^{-1} in order to mimic the south-north gradient in sediment accumulation. Equations and parameter values applied in the modeling are presented in Appendix B.

A first set of steady-state models was run applying a sedimentation rate of 50 cm kyr^{-1} , an interfacial POC concentration of 1.5 wt% and an initial age of 1000 yr. No external pore water flow was prescribed so that solutes were transported via diffusion, burial and compaction, only. A constant gradient condition was applied at the lower boundary and the inhibition constant (K_C) was varied in between 3.5 and 350 mM (Fig. 11). Applying a high K_C value of 350 mM, concentrations of dissolved methane and DIC have only a small effect on organic matter degradation. Consequently, POC concentrations decrease rapidly with depth and considerable amounts of gas hydrate accumulate in the model column. Hydrate concentrations increase with depth and reach a maximum value of 2.1 vol% at the base of the core. Applying a small K_C value of 3.5 mM, organic matter degradation is already suppressed at low metabolite concentrations. Methane production and hydrate formation are, thus, inhibited and dissolved methane is under-saturated with respect to gas hydrate over the entire model column. Using the previously derived K_C value of 35 mM, hydrates start to accumulate below a sediment depth of 78 m and reach a maximum

concentration of only 0.23 vol% at 300 m depth. The strong sensitivity of hydrate accumulation towards the K_C value clearly demonstrates that the amount of gas hydrate formed within the hydrate stability zone is regulated by the extent of metabolite inhibition.

The effect of sedimentation rate on hydrate accumulation was tested in a second set of model runs. The inhibition constant was set to the value previously derived by the systematic evaluation of pore water and sediment data from the Sakhalin slope ($K_C = 35$ mM) and the sedimentation rate was varied in between 10 and 100 cm kyr^{-1} applying the same set of parameter values as in the previous sensitivity test. Both, the thickness of the hydrate-bearing zone and the average hydrate concentration in that zone strongly increase with sedimentation rate (Fig. 12). Below a sedimentation rate of 30 cm kyr^{-1} , methane production rates are too low to induce hydrate formation. The steady increase in hydrate accumulation with sedimentation rate is caused by the age-dependent

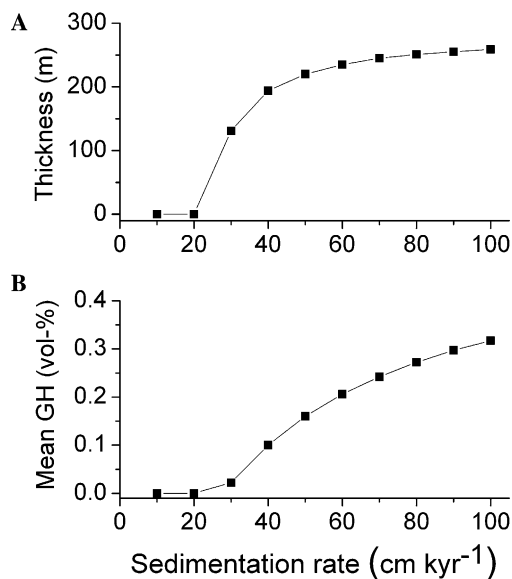


Fig. 12. Gas hydrate formation in Sakhalin slope sediments as a function of sedimentation rate. (A) Thickness of the hydrate-bearing layer (hydrate concentration >0.001 vol%). (B) Mean gas hydrate concentration in the hydrate-bearing layer (given in % of pore volume filled by hydrate).

reactivity of organic matter. In rapidly accumulating sediments, young organic matter is buried to large sediment depths so that abundant methane is formed also in deep layers where the diffusive loss of methane is minimized by low methane gradients.

The model predicts that hydrates do not form along the southern slope of Sakhalin where sedimentation is low whereas hydrates should accumulate in the northern slope area. Lüdmann and Wong (2003) detected a strong BSR in the entire northern slope region and an overlying broad zone of ~ 180 m thickness in which the amplitudes of the reflectors were significantly reduced. They proposed that finely dispersed gas hydrate reduced the reflection coefficients and estimated an average hydrate filled pore volume of 3–10% in this hydrate-bearing zone. Hydrate concentrations calculated in our model are one order of magnitude lower than this rough estimate. If the estimate based on seismic data would hold, the model would imply that less than 10% of the hydrate accumulating in the slope deposits is formed by the degradation of organic matter within the hydrate stability zone. More than 90% would be delivered to the near-surface sediments by methane ascending from deeper layers. In the northern Sakhalin slope area numerous gas escape structures were imaged using seismic techniques (Lüdmann and Wong, 2003). Seafloor observations, hydro-acoustic surveys, and methane measurements in the water column showed that gas bubbles are released in the northern slope area at more than 100 different locations (Obzhirov et al., 2004; Shoji et al., 2005). At these sites gas hydrates are found in shallow surface sediments (Ginsburg et al., 1993; Matveeva et al., 2003). It thus seems to be likely that most of

the hydrates accumulating within the HSZ of the northern Sakhalin slope are formed by gas bubbles ascending from deep sedimentary layers situated below the BSR.

6. Conclusions

The new kinetic rate law of organic matter degradation presented and successfully tested in this paper has profound implications for microbial degradation processes in deep anoxic marine sediments. The rate law predicts that organic matter degradation is severely hindered in anoxic sediments where high dissolved metabolite concentrations accumulate while organic matter of the same age may be degraded at a considerably higher rate if the dissolved metabolites (DIC and methane) are removed from the system. Degradation should thus proceed more rapidly in sediments with high porosity since dissolved species are rapidly lost to the overlying water by molecular diffusion in these “open” systems. Ancient organic matter conserved over extended periods of time in deep sediment layers may also be degraded when the diffusive loss is promoted by low modern depositional rates or the erosion of surface sediments. The removal of dissolved metabolites by seawater inflow and sediment reworking (erosion and re-deposition) should also enhance microbial degradation rates.

In contrast to other more detailed models of microbial respiration (Jin and Bethke, 2003) and organic matter degradation (Wirtz, 2003), the new empirical rate law does not resolve the complex microbial mechanisms involved in the anaerobic degradation of organic matter. It has rather been designed as a simple tool for the prognostic modeling of organic matter degradation, sulfate reduction and methane formation in anoxic sediments on large spatial and temporal scales. The model is based on the age-dependent kinetics introduced by Middelburg (1989) and converges to this model at low metabolite concentrations. Thus, the degradation rates in fully anoxic sediments with DIC and CH₄ concentrations of 100 mM, each, are reduced by 85% through metabolite inhibition whereas degradation in oxic sediments with DIC concentration of 2 mM are diminished by only 5% through the new inhibition term at a given POC concentration and sediment age. As the original age-dependent model has been tested and calibrated over a wide range of sedimentary environments, the new model should also correctly predict organic matter degradation in other settings such as oxic deposits at the deep-sea floor. It is, however, not well suited to predict organic matter degradation rates within the top 10 cm of the sediment column, since the age of organic matter is not well defined in these bioturbated surface layers.

The new rate law predicts that most of the hydrates found in marine sediments are not formed by organic matter degradation within the hydrate stability zone but rather by the ascent of fluids and gases. Significant concentrations of gas hydrates (>1 vol%) may thus only accumulate where fluids or methane gas bubbles originating from deeper

sediment layers are transported into the hydrate stability zone. Recent model estimates of the global hydrate abundance rely heavily on the kinetic rate law of organic matter degradation applied in the modeling procedure (Buffett and Archer, 2004; Archer and Buffett, 2005). Our model results show that the rates of methane formation in the hydrate stability zone have been over-estimated by these previous models. Hence, the new rate law presented in this paper would yield much lower estimates of the global hydrate abundance if applied in this model concept. It should however be noted that gas ascent from below the BSR was not considered in these previous models (Buffett and Archer, 2004) while our analysis of the Blake Ridge and Sakhalin slope data implies that gas ascent could be a common process at many continental margin sites.

Sediment temperature may also affect the rate of microbial methane generation. Wellsbury et al. (1997) showed that the microbial production of acetate is dramatically increased when sediments are heated. The highest acetate production was observed at temperatures of 20–60 °C and field data from Blake Ridge showed that most of the methane generated below the BSR is formed by microorganisms using acetate as substrate. Temperatures within the HSZ are usually lower than 20 °C. Considering an average thermal gradient of 30 ° km⁻¹, the experiments imply that methane production may be much higher in deeper sediment layers (~0.5–2 km depth) underlying the HSZ. Field data demonstrate that free gas produced in these deep layers may ascend to the surface to form gas hydrates. The conditions allowing for the rise of gas bubbles through sediments are, however, poorly understood. It is usually assumed that an interconnected network of gas bubbles occupying at least 10% of the pore space has to be formed to fracture the sediment and drive gas towards the seafloor (Buffett and Archer, 2004). New experimental studies show, however, that fine grained sediments act as elastic solids which are easily fractured by individual gas bubbles (Boudreau et al., 2005). It may thus be possible that gas bubbles rise to the surface without forming an interconnected network in the subsurface source area. Current estimates of the regional and global abundance of gas hydrates are not reliable because the methane production rates in deep and warm sediment layers underlying the HSZ are unknown and the upward transport of methane into the HSZ has only been studied at very few locations. More reliable model-based estimates will only emerge after the temperature effect on microbial methane formation and the mechanisms of gas bubble ascent through sediments have been studied in more detail.

Acknowledgments

The captains and crew members of the research vessels *Akademik Lavrentyev* and *Sonne* provided helpful assistance at sea, their work is greatly appreciated. We would like to thank N. Biebow for organizing the cruises and E. Suess for initiating our work in the Sea of Okhotsk.

Special thanks go to Bettina Domeyer, Anke Bleyer, and Regina Surberg for having carried out the chemical analyses. The helpful comments of two anonymous reviewers and B. Buffett are greatly appreciated. This work was funded by the BMBF within the framework of the German-Russian KOMEX project (Grant 03G0534A).

Associate editor: Jack J. Middelburg

Appendix A. Modeling procedure used in the evaluation of the Sea of Okhotsk data

In the following, details of the modeling procedure are presented and discussed while model equations are summarized in Tables A1–A3. All depth-dependent variables are listed in Table A1. Porosity is assumed to decay exponentially with depth (x) due to steady-state compaction

Table A1
Depth-dependent constitutive equations used in the modeling

Parameter	Constitutive equation
Porosity	$\Phi = \Phi_f + (\Phi_0 - \Phi_f) \cdot e^{-P \cdot x}$
Molecular diffusion in sediments	$D_S = \Phi^2 \cdot D_M$
Burial of solids	$w = \frac{w_f \cdot (1 - \Phi_f)}{1 - \Phi}$
Burial of pore water	$v = \frac{\Phi_f \cdot w_f}{\Phi}$
Age-dependent kinetic constant for POM degradation	$k_x = 0.16 \cdot (a_0 + \frac{x}{w})^{-0.95}$
Factor converting G (wt%) in C (mmol cm ⁻³)	$r = \frac{10 \cdot d_s \cdot (1 - \Phi)}{MW \cdot \Phi}$

Table A2
Rate laws used in the modeling

Rate	Kinetic rate law
Sulfate reduction	$R_{SR} = 0.5 \cdot \frac{C(SO_4)}{C(SO_4) + K_{SO_4}} \cdot r(POC) \cdot R_{POC}$
Methanogenesis	$R_M = 0.5 \cdot \frac{K_{SO_4}}{C(SO_4) + K_{SO_4}} \cdot r(POC) \cdot R_{POC}$
Anaerobic oxidation of methane	$R_{AOM} = k_{AOM} \cdot C(SO_4) \cdot C(CH_4)$
PON degradation	$R_{PON} = \frac{14}{12} \cdot \frac{16}{106} \cdot R_{POC}$
Ammonium adsorption	$R_{ADS} = k_{ADS} \cdot (1 - \frac{ADS}{C(NH_4) \cdot K_{ADS}})$
CaCO ₃ precipitation	$R_{CaCO_3} = k_{CaCO_3} \cdot (C(Ca) - C(Ca)_{OBS})$

Table A3
Rate expressions applied in the differential equations

Species	Rates
Particulate organic carbon (POC)	$R(POC) = -R_{POC}$
Particulate organic nitrogen (PON)	$R(PON) = -R_{PON}$
Adsorbed ammonium (ADS)	$R(ADS) = +R_{ADS} \cdot \frac{d_s \cdot (1 - \Phi)}{\Phi}$
Sulfate (SO ₄)	$R(SO_4) = -R_{SR} - R_{AOM}$
Methane (CH ₄)	$R(CH_4) = +R_M - R_{AOM}$
Bromide (Br)	$R(Br) = +r_{Br} \cdot r(POC) \cdot R_{POC}$
Ammonium (NH ₄)	$R(NH_4) = +r(PON) \cdot R_{PON} - R_{ADS}$
Iodide (I)	$R(I) = +r_I \cdot r(POC) \cdot R_{POC}$
Dissolved inorganic carbon (DIC = CO ₃ ²⁻ + HCO ₃ ⁻ + CO ₂)	$R(DIC) = +r(POC) \cdot R_{POC} + R_{AOM} - R_M - r(CaCO_3) \cdot R_{CaCO_3}$
Calcium (Ca)	$R(Ca) = -r(CaCO_3) \cdot R_{CaCO_3}$

(Berner, 1980) where the initial porosity at zero depth (Φ_0), the porosity at infinite depth (Φ_f), and the attenuation coefficient (p) are derived from the data applying non-linear fitting techniques. Molecular diffusion coefficients (D_M) are calculated for the prevailing temperature (2 °C) and salinity (35) using equations given in Boudreau (1997). Dissolved inorganic carbon (DIC) is transported using the diffusion coefficient of HCO_3^- because bicarbonate is the major DIC species at the near-neutral pH conditions prevailing in anoxic sediments. Archie's law is applied to consider the effects of tortuosity on diffusion and to calculate the coefficients for diffusion in sediments (D_S). The applied coefficient (Φ^2 corresponding to $m = 3$ in Archie's law) is a good approximation for the fine-grained and water-rich sediments of the study area (Ullman and Aller, 1982). Burial of solids and pore water is calculated considering steady-state compaction (Berner, 1980). Sedimentation rates (w_f) are calculated using nitrogen mass balances as outlined in Section 4. The age-dependent kinetic constant for POC degradation is taken from Middelburg (1989) while the initial age (a_0) is determined by fitting the model to the data. Concentrations of dissolved species (C in mmol cm^{-3} of pore water) are related to the corresponding concentrations of solid species (G given in wt%) using conversion factors (r) which include the depth-dependent porosity, the average density of dry solids ($d_s = 2.5 \text{ g cm}^{-3}$) and the appropriate molecular weights (MW) of C and N . These factors are applied to calculate the release and consumption of solutes resulting from the turnover of solids (Tables A2 and A3).

Kinetic rate laws are defined using Monod kinetics and applying appropriate stoichiometric coefficients (Table A2). The rate of sulfate reduction is related to the POC degradation rate (R_{POC}) considering that reduction rates decrease at very low sulfate concentrations ($K_{\text{SO}_4} = 1 \text{ mM}$). Methane formation is inhibited in the presence of sulfate and is driven by POC degradation. The anaerobic oxidation of methane (AOM) is assumed to follow second order kinetics depending on both sulfate and methane concentrations (Luff and Wallmann, 2003). The value of the kinetic constant (k_{AOM}) is defined by fitting the model to the sulfate and methane data. Degradation of particulate organic nitrogen (PON) is linked to POC degradation considering Redfield stoichiometry and the appropriate $N:C$ weight ratio (14/12).

Ammonium adsorption can be modeled as a linear equilibrium reaction where the depth-independent equilibrium constant K_{ADS} is defined as the ratio between adsorbed ammonium (ADS in mmol NH_4 ($\text{g dry solids})^{-1}$) and dissolved ammonium ($C(\text{NH}_4)$ in mmol NH_4 (cm^3 pore water) $^{-1}$) at equilibrium (Berner, 1980). In fine-grained marine sediments K_{ADS} attains a value of $1.7 \text{ cm}^3 \text{ g}^{-1}$ (Mackin and Aller, 1984). We prefer to model ammonium adsorption using a kinetic approach because the equilibrium approach would demand the use of rather complicated differential-algebraic equations. The kinetic constant is,

however, set to a large value ($k_{\text{ADS}} = 1 \text{ mM yr}^{-1}$) so that equilibrium between dissolved and adsorbed ammonium is always maintained ($\text{ADS}/C(\text{NH}_4) = K_{\text{ADS}}$).

Carbonate precipitation in anoxic sediments has been modeled successfully by different authors using numerically rather demanding procedures (Luff and Wallmann, 2003; Luff et al., 2004). It is controlled by pH and saturation states of pore waters which are calculated only with a considerable numerical effort (Boudreau, 1987; Van Cappellen and Wang, 1996). Here, we prefer to use a rather simple approach to avoid extensive integration times. Carbonate precipitation is driven by the measured calcium concentrations in pore water. For this purpose appropriate functions are fitted through the Ca data to obtain representative concentrations for each depth interval ($C(\text{Ca})_{\text{OBS}}$). The rate is set proportional to the difference between modeled ($C(\text{Ca})$) and measured concentrations ($C(\text{Ca})_{\text{OBS}}$) and a large value is assigned to the corresponding kinetic constant ($k_{\text{CaCO}_3} = 0.05 \text{ wt\% CaCO}_3 \text{ yr}^{-1}$) so that concentrations calculated in the model are always very close to measured values.

Reaction rates are combined appropriately to define reaction terms which are applied in the differential equations for each solid and dissolved species (Table A3). Conversion factors (r) are introduced to maintain the correct dimensions for solid and dissolved species concentrations. Stoichiometric coefficients are used to derive the release rates of metabolites (ammonium, bromide, and iodide) from POC degradation rates. Finally, the reaction terms are combined with other terms describing the transport of solids and solutes (see Section 4) and the resulting system of differential equations is solved to calculate the concentration–depth profiles of 10 species at steady-state.

Appendix B. Modeling of gas hydrate formation

The model described in Appendix A was extended and modified in order to simulate gas hydrate formation at Black Ridge (ODP Site 997) and in Sakhalin slope deposits (Table A4). Since the model columns extend over several 100 m, the effect of sediment temperature on diffusion was considered. Molecular diffusion coefficients were calcu-

Table A4
Equations used in the modeling of gas hydrate formation

Parameter	Constitutive equation
Molecular diffusion in sediments	$D_S = \frac{D_M}{1-2 \cdot \ln(\Phi)}$
Upward fluid flow and pore water burial	$v = \frac{\Phi_f \cdot w_f - v_0 \cdot \Phi_0}{\Phi}$
Rate of hydrate formation	$R_{\text{GH}} = k_{\text{GH}} \cdot \left(\frac{C(\text{CH}_4)}{C_{\text{SAT}}} - 1 \right)$ If $\left[\frac{C(\text{CH}_4)}{C_{\text{SAT}}} > 1 \right]$
Rate of hydrate dissolution	$R_{\text{GHD}} = k_{\text{GHD}} \cdot \left(1 - \frac{C(\text{CH}_4)}{C_{\text{SAT}}} \right) \cdot G(\text{GH})$ If $\left[\frac{C(\text{CH}_4)}{C_{\text{SAT}}} \leq 1 \right]$
Factor converting wt% in vol%	$r_{\text{GH}} = \frac{d_s \cdot (1-\Phi)}{d_{\text{GH}} \cdot \Phi}$

lated as a function of sediment temperature (Boudreau, 1997) and hence increased with sediment depth. Moreover, the effect of porosity on diffusion was considered using the logarithmic equation given by (Boudreau, 1996a) rather than applying Archie's Law since the former equation is valid over a wider range of sediment compositions and porosities (Boudreau, 1997). Dissolved inorganic carbon (DIC) was transported applying the mean diffusion coefficient of HCO_3^- and CO_2 since CO_2 is a major species under the acidic conditions prevailing in deep methanogenic sediments. Upward fluid flow was considered in the Blake Ridge simulation, only, using the approach described in Luff and Wallmann (2003). The interstitial velocity at zero depth (v_0) was varied to fit the pore water data.

Gas hydrate was precipitated from the pore solution when the concentration of dissolved methane calculated in the model surpassed the solubility of gas hydrates (C_{SAT}). We used a kinetic approach to simulate hydrate precipitation and dissolution (Torres et al., 2004) and a modified Pitzer-approach for the calculation of hydrate solubility (Tishchenko et al., 2005). The kinetic constant for hydrate precipitation was set to a large value ($k_{\text{GH}} = 2 \times 10^{-2} \text{ wt\% yr}^{-1}$) to prevent over-saturation with respect to gas hydrate. Hydrates were allowed to dissolve in under-saturated pore solutions applying a corresponding kinetic constant of $k_{\text{GHD}} = 2 \times 10^{-2} \text{ wt\% yr}^{-1}$. Hydrate concentrations ($G(\text{GH})$) were initially calculated in wt% and were subsequently converted into percent of pore volume filled by hydrate considering the density of dry sediments ($d_s = 2.5 \text{ g cm}^{-3}$) and gas hydrates ($d_{\text{GH}} = 0.916 \text{ g cm}^{-3}$).

Boundary conditions for dissolved species applied at the base of the model column have a strong effect on the amount of hydrate formed in the model sediments. At Blake Ridge, we prescribed constant concentrations at the base of the hydrate stability zone corresponding to the values measured at that depth (451 m). Only for dissolved methane, the lower boundary value was calculated assuming equilibrium with pure methane gas hydrate (type I, Tishchenko et al., 2005). In the prognostic modeling of hydrate formation in Sakhalin slope deposits, we applied constant gradient conditions for SO_4 , DIC, and CH_4 Eq. (12). With this approach methane and DIC continuously produced in deeper sediment sections situated below the base of the model column (300 m), is allowed to enter the model domain via molecular diffusion.

References

- Aloisi, G., Wallmann, K., Drews, M., Bohrmann, G., 2004. Evidence for the submarine weathering of silicate minerals in Black Sea sediments: possible implications for the marine Li and B cycles. *Geochem. Geophys. Geosyst.* **5** (4), Q04007, 10.1029/2003GC000639.
- Antoine, D., André, J.-M., Morel, A., 1996. Oceanic primary production 2. Estimation of global scale from satellite (coastal zone color scanner) chlorophyll. *Global Biogeochem. Cycles* **10** (1), 57–69.
- Archer, D., Buffett, B., 2005. Time-dependent response of the global ocean clathrate reservoir to climatic and anthropogenic forcing. *Geochem. Geophys. Geosyst.* **6** (3), 10.1029/2004GC000854.
- Berner, R.A., 1980. *Early Diagenesis—A Theoretical Approach*. Princeton University Press.
- Biebow N. and Hütten E. 2000. KOMEX Cruise Reports. GEOMAR Research Center.
- Boudreau, B.B., Canfield, D.E., 1993. A comparison of closed- and open-system models for porewater pH and calcite-saturation state. *Geochim. Cosmochim. Acta* **57**, 317–334.
- Boudreau, B.B., Ruddick, B.R., 1991. On a reactive continuum representation of organic matter diagenesis. *Am. J. Sci.* **291**, 507–538.
- Boudreau, B.P., 1987. A steady-state diagenetic model for dissolved carbonate species and pH in the pore waters of oxic and suboxic sediments. *Geochim. Cosmochim. Acta* **51**, 1985–1996.
- Boudreau, B.P., 1996a. The diffusive tortuosity of fine-grained un lithified sediments. *Geochim. Cosmochim. Acta* **60** (16), 3139–3142.
- Boudreau, B.P., 1996b. A method-of-lines code for carbon and nutrient diagenesis in aquatic sediments. *Comput. Geosci.* **22** (5), 479–496.
- Boudreau, B.P., 1997. *Diagenetic Models and Their Implementation*. Springer-Verlag.
- Boudreau, B.P., Algar, C., Johnson, B.D., Croudace, I., Reed, A., Furukawa, Y., Dorgan, K.M., Jumars, P.A., Grader, A.S., Gardiner, B.S., 2005. Bubble growth and rise in soft sediments. *Geology* **33** (6), 517–520.
- Broerse, A.T.C., Ziveri, P., Honjo, S., 2000. Coccolithophore ($-\text{CaCO}_3$) flux in the Sea of Okhotsk: seasonality, settling and alteration processes. *Mar. Micropaleontol.* **39**, 179–200.
- Buffett, B., Archer, D., 2004. Global inventory of methane clathrate: sensitivity to changes in the deep ocean. *Earth Planet. Sci. Lett.* **227**, 185–199.
- Davie, M.K., Buffett, B.A., 2001. A numerical model for the formation of gas hydrate below the seafloor. *J. Geophys. Res.* **106** (B1), 497–514.
- Davie, M.K., Buffett, B.A., 2003a. Sources of methane for marine gas hydrate: inferences from a comparison of observations and numerical models. *Earth Planet. Sci. Lett.* **206**, 51–63.
- Davie, M.K., Buffett, B.A., 2003b. A steady state model for marine hydrate formation: constraints on methane supply from pore water sulfate profiles. *J. Geophys. Res.* **108** (B10), 2495. doi:10.1029/2002JB002300.
- Dickens, G.R., O'Neil, J.R., Rea, D.K., Owen, R.M., 1995. Dissociation of oceanic methane hydrate as a cause of the carbon isotope excursion at the end of the Paleocene. *Paleoceanography* **10** (6), 965–971.
- Dickens, G.R., Pauli, C.K., Wallace, P., Party, t.O.L.S., 1997. Direct measurement of in situ methane quantities in a large gas-hydrate reservoir. *Nature* **385**, 426–428.
- Dullo, W.-C., Biebow, N., and Georgeleit, K. 2004. SO178 KOMEX Cruise Report, IFM-GEOMAR, pp. 125.
- Egeberg, P.K., Dickens, G.R., 1999. Thermodynamics and pore water halogen constraints on gas hydrate distribution at ODP Site 997 (Blake Ridge). *Chem. Geol.* **153**, 53–79.
- Einsele, G., 2000. *Sedimentary Basins: Evolution, Facies, and Sediment Budget*. Springer.
- Elderfield, H., Truesdale, V.W., 1980. On the biophilic nature of iodine in seawater. *Earth Planet. Sci. Lett.* **50**, 105–114.
- Flemings, P.B., Liu, X., Winters, W.J., 2003. Critical pressure and multiphase flow in Blake Ridge gas hydrates. *Geology* **31** (12), 1057–1060.
- Fossing, H., Ferdelman, T.G., Berg, P., 2000. Sulfate reduction and methane oxidation in continental margin sediments influenced by irrigation (South-East Atlantic off Namibia). *Geochim. Cosmochim. Acta* **64** (5), 897–910.
- Ginsburg, G.D., Soloviev, Cranston, R.E., Lorenson, T.D., Kvenvolden, K.A., 1993. Gas hydrates from the continental slope, offshore Sakhalin Island, Okhotsk Sea. *Geo-Mar. Lett.* **13**, 41–48.
- Gorbarenko, S.A., Nürnberg, D., Derkachev, A.N., Astakhov, A.A., Southon, J.R., Kaiser, A., 2002. Magnetostratigraphy and tephrochronology of the Upper Quaternary sediments in the Okhotsk Sea: implication of terrigenous, volcanogenic and biogenic matter supply. *Mar. Geol.* **183**, 107–129.

- Gorman, A.R., Holbrook, W.S., Hornbach, M.J., Hackwith, K.L., Lizarralde, D., Pecher, I., 2002. Migration of methane gas through the hydrate stability zone in a low-flux hydrate province. *Geology* **30** (4), 327–330.
- Grasshoff, K., Ehrhardt, M., Kremling, K., 1983. *Methods of Seawater Analysis*. Verlag Chemie.
- Hedges, J.H., Hu, F.S., Devol, A.H., Hartnett, H.E., Tsamakis, E., Keil, R.G., 1999. Sedimentary organic matter preservation: a test for selective degradation under oxic conditions. *Am. J. Sci.* **299**, 529–555.
- Hensen, C., Zabel, M., Pfeifer, K., Schwenk, T., Kasten, S., Riedinger, N., Schulz, H.D., Boetius, A., 2003. Control of sulfate pore-water profiles by sedimentary events and the significance of anaerobic oxidation of methane for the burial of sulfur in marine sediments. *Geochim. Cosmochim. Acta* **67** (14), 2631–2647.
- Ivanenkov, V.N., Lyakhin, Y.I., 1978. Determination of total alkalinity in seawater. In: Bordovsky, O.K., Ivanenkov, V.N. (Eds.), *Methods of Hydrochemical Investigations in the Ocean*. Nauka Publ. House, pp. 110–114, in Russian.
- Jin, Q., Bethke, C.M., 2003. A new rate law describing microbial respiration. *Appl. Environ. Microbiol.* **69** (4), 2340–2348.
- Jørgensen, B.B., Weber, A., Zopfi, J., 2001. Sulfate reduction and anaerobic methane oxidation in Black Sea sediments. *Deep-Sea Res. I* **48**, 2097–2120.
- Kennedy, H.A., Elderfield, H., 1987. Iodine diagenesis in pelagic deep-sea sediments. *Geochim. Cosmochim. Acta* **51**, 2489–2504.
- Kristensen, E., Holmer, M., 2001. Decomposition of plant materials in marine sediment exposed to different electron acceptors (O_2 , NO_3^- , and SO_4^{2-}), with emphasis on substrate origin, degradation kinetics, and the role of bioturbation. *Geochim. Cosmochim. Acta* **65** (3), 419–433.
- Kvenvolden, K.A., Lorenson, T.D., 2001. The global occurrence of natural gas hydrate. *Geophys. Monogr.* **124**, 87–98.
- Lüdmann, T., Wong, K.K., 2003. Characteristics of gas hydrate occurrences associated with mud diapirism and gas escape structures in the northwestern Sea of Okhotsk. *Mar. Geol.* **201**, 269–286.
- Luff, R., Wallmann, K., 2003. Fluid flow, methane fluxes, carbonate precipitation and biogeochemical turnover in gas hydrate-bearing sediments at Hydrate Ridge, Cascadia Margin: numerical modeling and mass balances. *Geochim. Cosmochim. Acta* **67** (18), 3403–3421.
- Luff, R., Wallmann, K., Aloisi, G., 2004. Numerical modeling of carbonate crust formation at cold vent sites: significance for fluid flow and methane budgets and chemosynthetic biological communities. *Earth Planet. Sci. Lett.* **221**, 337–353.
- Luff, R., Wallmann, K., Grandel, S., Schlüter, M., 2000. Numerical modelling of benthic processes in the deep Arabian Sea. *Deep-Sea Res. II* **47** (14), 3039–3072.
- Mackin, J.E., Aller, R.C., 1984. Ammonium adsorption in marine sediments. *Limnol. Oceanogr.* **29** (2), 250–257.
- Maher, K., DePaolo, D.J., Lin, J.C.-F., 2004. Rates of silicate dissolution in deep-sea sediment: in situ measurement using $^{234}U/^{238}U$ of pore fluids. *Geochim. Cosmochim. Acta* **68** (22), 4629–4648.
- Martin, J.B., Gieskes, J.M., Torres, M., Kastner, M., 1993. Bromine and iodine in Peru margin sediments and pore fluids: implications for fluid origins. *Geochim. Cosmochim. Acta* **57**, 4377–4389.
- Matveeva, T., Soloviev, V., Wallmann, K., Obzhairov, A., Biebow, N., Poort, J., Salomatin, A., Shoji, H., 2003. Geochemistry of gas hydrate accumulation offshore NE Sakhalin Island (the Sea of Okhotsk): results from the KOMEX-2002 cruise. *Geo-Mar. Lett.* **23**, 278–288.
- Middelburg, J.J., 1989. A simple model for organic matter decomposition in marine sediments. *Geochim. Cosmochim. Acta* **53**, 1577–1581.
- Milkov, A.V., 2004. Global estimates of hydrate-bound gas in marine sediments: how much is really out there? *Earth Sci. Rev.* **66** (3–4), 183–197.
- Niewöhner, b., Hensen, C., Kasten, S., Zabel, M., Schulz, H.D., 1998. Deep sulfate reduction completely mediated by anaerobic methane oxidation in sediments of the upwelling area off Namibia. *Geochim. Cosmochim. Acta* **62** (3), 455–464.
- Obzhairov, A., Shakirov, R., Salyuk, A., Suess, E., Biebow, M., Salomatin, A., 2004. Relations between methane venting, geological structure and seismo-tectonics in the Okhotsk Sea. *Geo-Mar. Lett.* **24**, 135–139.
- Paull C. K., Matsumoto R., Wallace P. J., Dillon W. P., 2000. Proceedings of the Ocean Drilling Program, Scientific Results, Vol. 164.
- Rabouille, C., Gaillard, J.-F., 1991. Towards the EDGE: early diagenetic global explanation. A model depicting the early diagenesis of organic matter, O_2 , NO_3^- , Mn, and PO_4 . *Geochim. Cosmochim. Acta* **55**, 2511–2525.
- Rempel, A.W., Buffett, B.A., 1998. Mathematical models of gas hydrate accumulation. In: Henriot, J.-P., Mienert, J. (Eds.), *Gas Hydrates: Relevance to World Margin Stability and Climate Change*, vol. 137. Geological Society, pp. 63–74.
- Sayles, F.L., Mangelsdorf Jr., P.C., 1977. The equilibration of clay minerals with seawater. *Geochim. Cosmochim. Acta* **41**, 951–960.
- Schlitzer, R., 2000. Applying the adjoint method for biogeochemical modeling: export of particulate organic matter in the world ocean. In: Kasibhatla, P., Heimann, M., Rayner, P., Mahowald, N., Prinn, R.G., Hartley, D.E. (Eds.), *Inverse Methods in Global Biogeochemical Cycles*, Vol. 114. American Geophysical Union, pp. 107–124.
- Shoji, H., Soloviev, V., Matveeva, T., Mazurenko, L., Minami, H., Hachikubo, A., Sakagami, H., Hyakutake, K., Kaulio, V., Gladysch, V., Logvina, E., Obzhairov, A., Baranov, B., Khlystov, O., Biebow, N., Poort, J., Jin, Y.K., Kim, Y., 2005. Hydrate-bearing structures in the sea of Okhotsk. *EOS* **86** (2), 13/18.
- Tishchenko, P., Hensen, C., Wallmann, K., Wong, C.S., 2005. Calculation of the stability and solubility of methane hydrate in seawater. *Chem. Geol.* **219**, 37–52.
- Torres, M.E., Wallmann, K., Trehu, A.M., Bohrmann, G., Borowski, W.S., Tomaru, H., 2004. Gas hydrate growth, methane transport, and chloride enrichment at the southern summit of Hydrate Ridge, Cascadia margin off Oregon. *Earth Planet. Sci. Lett.* **226**, 225–241.
- Tromp, T.K., Cappellen, P.V., Key, R.M., 1995. A global model for the early diagenesis of organic carbon and organic phosphorus in marine sediments. *Geochim. Cosmochim. Acta* **59** (17), 1259–1284.
- Ullman, W.J., Aller, R.C., 1982. Diffusion coefficients in near-shore marine sediments. *Limnol. Oceanogr.* **27**, 552–556.
- Van Cappellen, P., Wang, Y., 1996. Cycling of iron and manganese in surface sediments: a general theory for the coupled transport and reaction of carbon, oxygen, nitrogen, sulfur, iron, and manganese. *Am. J. Sci.* **296**, 197–243.
- Wallmann, K., Linke, P., Suess, E., Bohrmann, G., Sahling, H., Schlüter, M., Dählmann, A., Lammers, S., Greinert, J., von Mirbach, N., 1997. Quantifying fluid flow, solute mixing, and biogeochemical turnover at cold vents of the eastern Aleutian subduction zone. *Geochim. Cosmochim. Acta* **61** (24), 5209–5219.
- Wellsbury, P., Goodman, K., Barth, T., Cragg, B.A., Barnes, S.P., Parkes, J., 1997. Deep marine biosphere fuelled by increasing organic matter availability during burial and heating. *Nature* **388**, 573–576.
- Westrich, J.T., Berner, R.A., 1984. The role of sedimentary organic matter in bacterial sulfate reduction: the G model tested. *Limnol. Oceanogr.* **29** (2), 236–249.
- Wirtz, K.W., 2003. Control of biogeochemical cycling by mobility and metabolic strategies of microbes in the sediments: an integrated model study. *FEMS Microbiol. Ecol.* **46**, 295–306.
- Wong, H.K., Lüdmann, T., Baranov, B.V., Karp, B.Y., Konerding, P., Ion, G., 2003. Bottom current-controlled sedimentation and mass wasting in the northwestern Sea of Okhotsk. *Mar. Geol.* **201**, 287–305.

S. U. Noé · W.-Chr. Dullo

Skeletal morphogenesis and growth mode of modern and fossil deep-water isidid gorgonians (Octocorallia) in the West Pacific (New Zealand and Sea of Okhotsk)

Received: 15 July 2005 / Accepted: 16 January 2006
© Springer-Verlag 2006

Abstract Fabric and growth mode of deep-water isidid gorgonian skeletons showing bright Mg-calcitic internodes and dark proteinaceous nodes were investigated on modern, subrecent and fossil skeletons. The internodal microstructure is characterised by three-dimensionally interfingering calcitic fascicles accreting around a central axis. Macroscopic colour banding results from varying orientations of organic-rich fascicle bundles and intercalated bands of organic-poor granular crystals. This skeletal structure of isidid gorgonians strikingly differs from the density banding of scleractinians. Radiocarbon dating of a fossil skeleton gave an age of $3,985 \pm 35$ to $3,680 \pm 35$ years before present (BP) with a record of 305 ± 35 years (\pm range). Linear extension rates of 0.4 mm year^{-1} average allow for an annual to sub-annual resolution on micrometer scale of colour bands or fascicles, respectively. The growth mode of branched skeletons is characterised by simultaneous secretion of vertically alternating nodes/internodes and lateral accretion of concentric increments enveloping the entire skeleton. Bifurcations at various growth stages imply that adjacent branches have different ages and show varying numbers of growth bands at any skeletal cross section. The scleroprotein gorgonin plays a crucial role in the formation of organic nodes and the secretion of calcitic internodes by providing a structural framework in the biomineralisation process.

Keywords Isidid gorgonians · Micro- and ultrastructure · Radiocarbon ageing · Growth mode · Biomineralisation · West Pacific

Communicated by Geology Editor P.K. Swart

S. U. Noé (✉) · W.-Chr. Dullo
Leibniz Institute of Marine Sciences, IFM-GEOMAR,
Wischofstr. 1-3, D-24148 Kiel, Germany
E-mail: snoe@ifm-geomar.de
Tel.: +49-431-6002837
Fax: +49-431-6002941

Introduction

Deep-water isidid gorgonians or “bamboo corals”, named after their similarity with bamboo plants, are horny octocorals which first appeared in the Cretaceous (Helm and Schülke 2003), showing some local occurrences in Paleocene to Pleistocene sediments (Grant 1976; Grasshoff 1980; Langer 1989; Kocurko 1989; Bernecker and Weidlich 2005). Modern specimens are widespread along the present-day Indo-Pacific and Atlantic margins, ranging from less than 100 m to more than 4,000 m depth (Roark et al. 2005). The azooxanthellate corals usually grow in areas of high hydrodynamic energy and sufficient flux of zooplankton and particulate organic matter, both factors being responsible for food supply to the gorgonian habitats (Heikoop et al. 2002). Living bamboo coral colonies are characterised by a gelatinous coenenchyme stiffened by Mg-calcitic spicules, bearing polyps with eight pinnate tentacles (Kocurko 1989). The coenenchyme surrounds a supporting central axis which consists of Mg-calcite and gorgonin, a flexible scleroprotein of collagen fibres in a proteinaceous matrix (Grasshoff and Zibrowius 1983; Lewis et al. 1992; Macintyre et al. 2000).

Due to the concentric growth of the mineral and organic parts of their skeletal axes, isidids and related gorgonian families have recently aroused the interest of paleoceanographers and paleoclimatologists. In contrast to deep-water scleractinians such as *Lophelia pertusa* (Adkins et al. 1998; Smith et al. 2000; Risk et al. 2005; Lutringer et al. 2005) and *Desmophyllum cristagalli* (Risk et al. 2002; Adkins et al. 2004), the slow-growing skeletons of gorgonian octocorals with a longevity potential on the order of 100s of years (Heikoop et al. 2002; Andrews et al. 2005) form on sub-annual to centennial time scales and hence represent potential archives of past oceanic and climatic dynamics in intermediate and deep-water masses. Grigg (1974) was the first who noted an annual pattern of growth ring formation in the

gorgonian genus *Muricea*. Annual periodicity was also proved for the light and dark growth bands of the precious red coral *Corallium rubrum* (Marschal et al. 2004), which were interpreted to correspond to fast and slow growth (Weinbauer et al. 2000). A sub-annual (seasonal) growth pattern is documented in the fan-shaped calcitic loculi of the shallow-water gorgonian species *Plexaurella dichotoma* (Bond et al. 2005). According to previous paleoceanographic investigations, the deep-water gorgonian species *Primnoa resedaeformis* provides a valuable proxy of deep ocean temperature variations (Heikoop et al. 2002; Thresher et al. 2004; Sherwood et al. 2005; Sinclair et al. 2005) and surface productivity fluctuations (Heikoop et al. 2002). In contrast to the Primnoidae, only few investigations focused on the gorgonian family Isididae so far, though “bamboo coral” skeletons show conspicuous growth rings. Roark et al. (2005) presented radiocarbon-based ages and growth rates of sub-fossil isidid skeletons from the Gulf of Alaska, whereas independent verification of growth rates by means of counting growth rings and measuring Sr/Ca ratios in skeletal cross sections allowed for reconstruction of lunar cycle growth bands. Nevertheless, isidid gorgonian skeletons are relatively unexplored archives, and their potential for the reconstruction of environmental parameters is still at experimental stage.

Previous studies of coral biomineralisation strongly focused on scleractinians (see Cohen and McConnaughey 2003 for review), whereas the organic matrix-mediated calcification mode of the gorgonian skeletal axis and spicules embedded in the coenenchyme is largely unknown for most gorgonian families and has not been touched for the Isididae so far. Investigations focused on the precious red coral *C. rubrum* with respect to biochemical analysis of the organic matrices (Allemand et al. 1994) and histology/cytology of the cellular structure of the calcite-precipitating epithelium (Grillo et al. 1993).

In spite of these investigations our present knowledge of the fine-scale morphological features and growth mode of isidid gorgonian skeletons is very poor. Hence, studies of the skeletal micro- and ultrastructure in combination with absolute age determinations on a set of isidid gorgonians from the southwestern and northwestern Pacific which we present in this paper are a prerequisite for reconstruction of their growth mode and thus for evaluation of their usefulness as archives of paleoceanographic dynamics. In addition, implications for a biomineralisation model of the isidid skeletal axis will be addressed.

Materials and methods

Sampling areas

During the cruises SO168 ZEALANDIA, SO178 KOMEX II and LV29, living, subrecent and fossil isidid gorgonians (Octocorallia) were recovered by dredge

hauls on Chatham Rise east of New Zealand from 600 to 800 m water depth and in Okhotsk Sea from 1,500 to 3,000 m depth (Fig. 1). Coral occurrences on the southern slope of Chatham Rise are tied to the boundary of the Subantarctic Mode Water and the underlying Antarctic Intermediate Water (Fenner et al. 1992; Nelson et al. 1993; Cooke et al. 2002), where topographically focused currents concentrate organic particles, thus maintaining nutrient flux to the coral sites. In the southern Sea of Okhotsk one gorgonian habitat at 1,500 m depth is located in a modified lower Okhotsk Sea Intermediate Water, which may derive from mixing of Dense Shelf Water and Pacific Intermediate Water (Keigwin 1998; Wong et al. 1998). The deeper site at 3,000 m depth occurs in poorly oxygenated Pacific Deep Water (Yamamoto-Kawai et al. 2004).

Materials

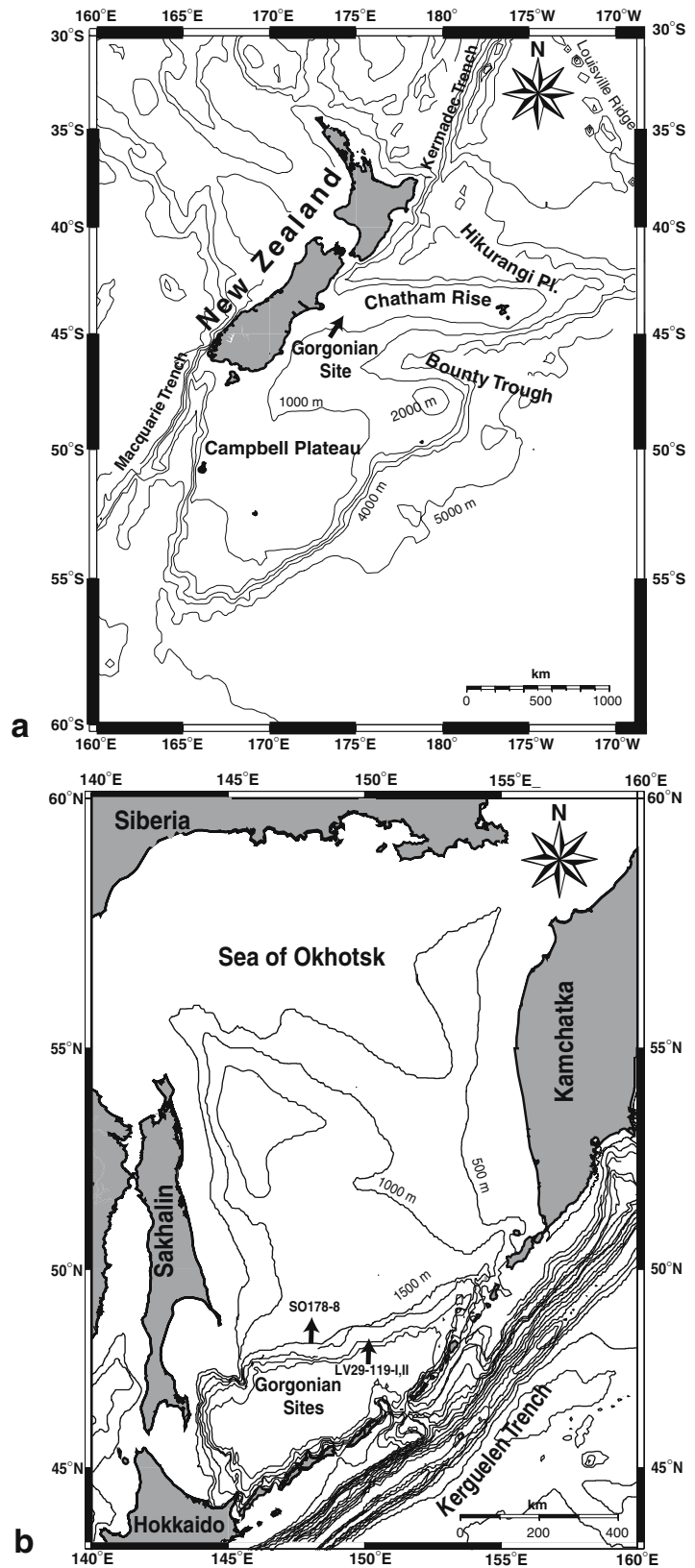
Fragments of isidid gorgonians were recovered by dredging. One dredge haul upslope of the volcanic Urry Knoll on southwestern slope of Chatham Rise (44°45′,90″S–44°46′,24″S; 174°23′,907″E–174°23′,902″E; 770–594 m depth) recovered a unique fossil skeleton (Fig. 2a) and a fragmented living isidid colony of the genus *Keratoisis* Wright (Fig. 3a). Hence, this site may represent a long-lived gorgonian habitat. In the Sea of Okhotsk two subrecent isidid specimens were collected at the deeper site (47°00′,656″N–46°59′,368″N; 150°14′,310″E–150°12′,348″E; 3,147–2,274 m depth), while a dredge haul at the shallower site (48°24′,63″N–48°24′,34″N; 147°58′,11″E–147°58′,12″E; 1,500–1,278 m depth) provided fragments of living colonies. The fossil skeleton from Chatham Rise with a maximum diameter of 60×25 cm showed a heavily bioeroded surface with a dense colonisation of hydroids and other cnidarians (Fig. 2a). The branched trunk was attached to the volcanic surface by a basal disk. Cross-cut slabs reveal a conspicuous horizontal growth banding (Fig. 2b–d) which is identical with the basic internal structure of the modern skeletal fragments.

Fragments of living gorgonian colonies recovered on Chatham Rise and on the shallow Okhotsk Sea site exhibited a reddish organic coenenchyme with polyps and numerous calcitic spicules around a skeletal axis (Fig. 3a). Though the coenenchyme was partly torn up by the dredging procedure, intact areas prove that the living coral colonies entirely cover their skeletal axes. Highly viscous slimes formed a matrix between this endoskeleton and the coenenchyme (Fig. 3a). The skeleton shows an alternation of calcitic internodes and organic nodes with a concentric horizontal banding in both stages (Fig. 3b–d). The well-preserved surface of the internodes is characterised by a growth lineation with a groove pattern running obliquely to their longitudinal axes. This striation is attributed to water channels of the coenenchyme (Langer 1989). Root-like calcareous processes form a holdfast anchoring the skeleton in a sandy

Fig. 1 Sampling areas.

a Topographic map of the microcontinent Zealandia. Occurrence of isidid gorgonians recovered at SO168-104 is indicated by *arrow*.

b Topographic map of the Sea of Okhotsk showing recovery sites of a live-collected specimen (SO178-8) and subrecent skeletons (LV29-119-I,II)

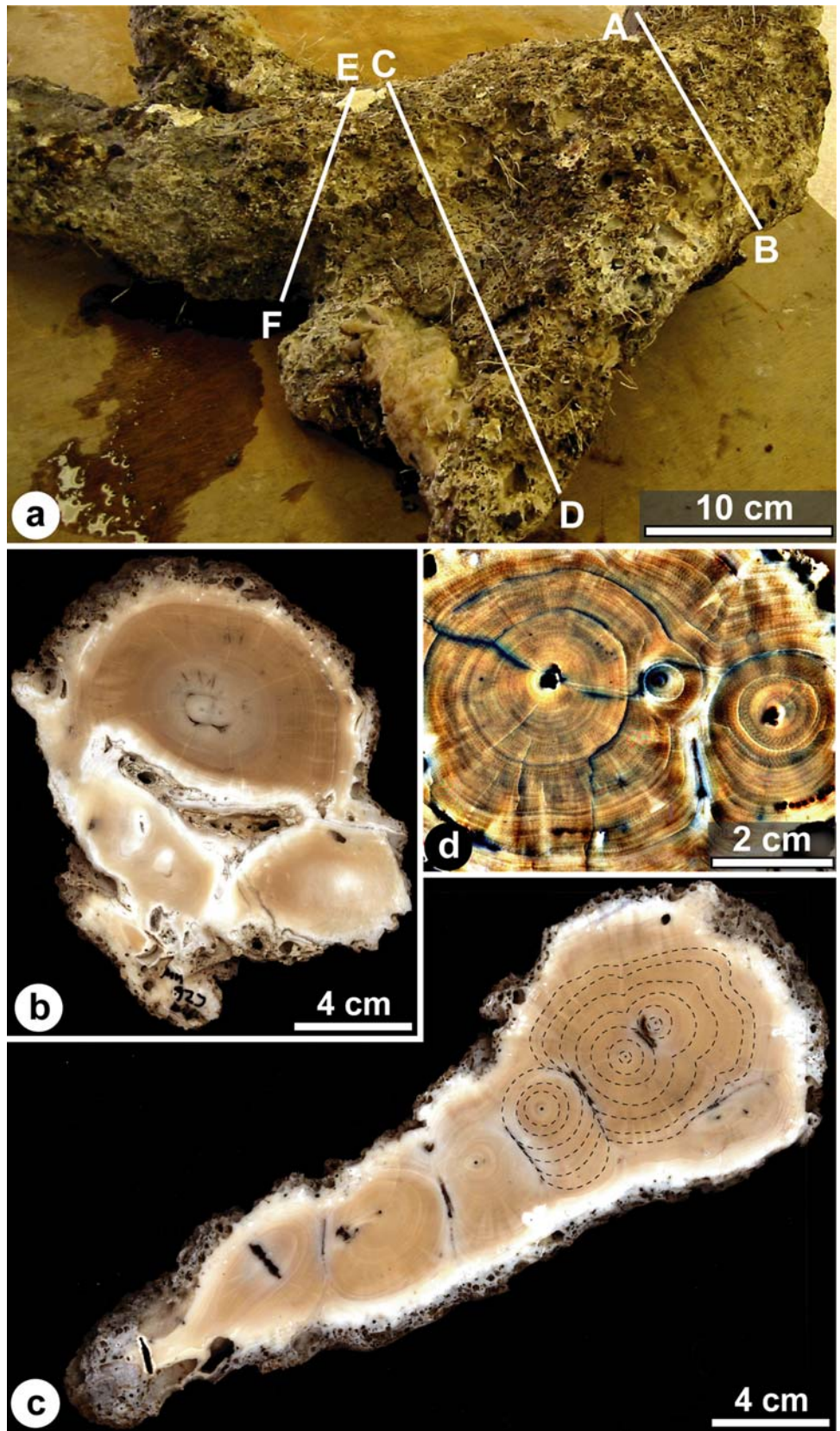


soft-bottom substratum. A fragmented live-collected colony in the Sea of Okhotsk resembles the modern Chatham Rise specimen. The subrecent Okhotsk skele-

tons are characterised by an identical growth structure, showing a somewhat greater thickness due to accretion of a larger number of growth rings (Fig. 3e).

Fig. 2 Fossil isidid gorgonian skeleton of Chatham Rise.

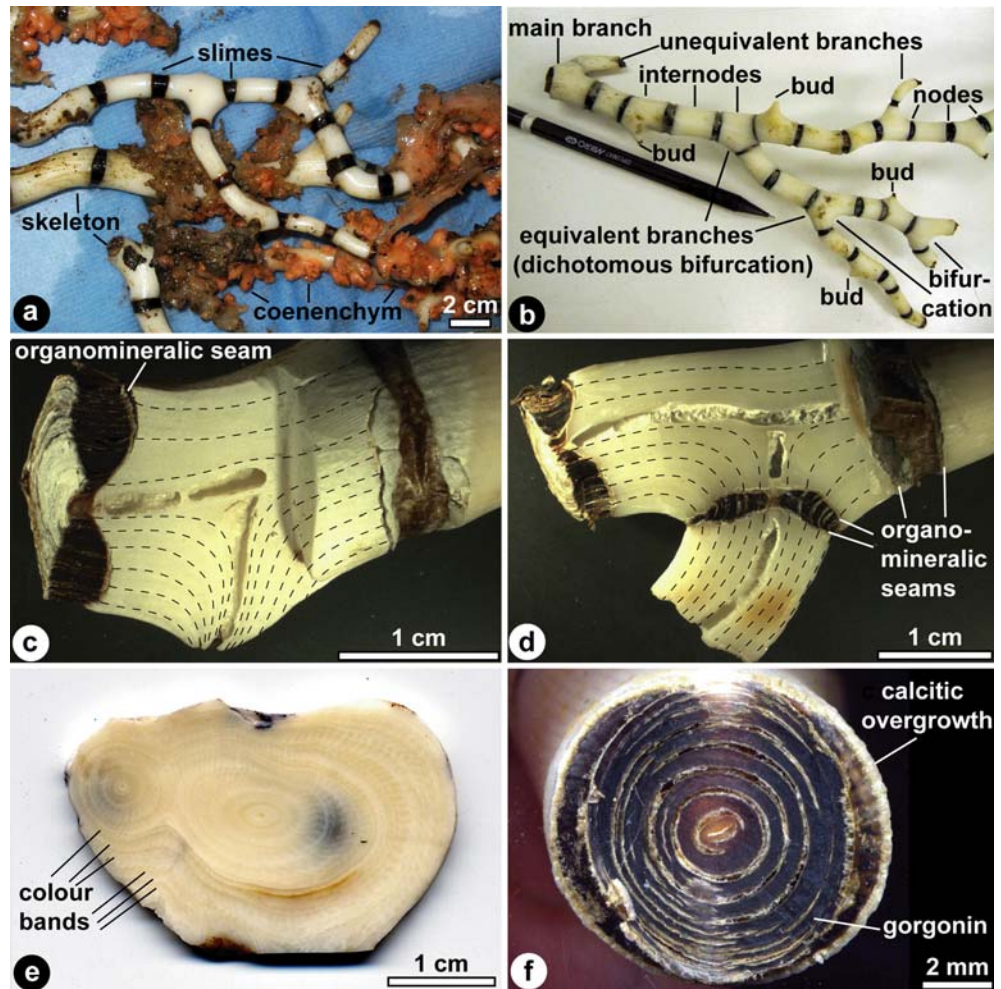
a Skeleton after dredge recovery, colonised by hydroids and heavily bored by sponges and bivalves. *Lines* indicate described cross sections. A–B: near base of skeleton; C–D: maximum lateral diameter and highest number of branches; E–F: beginning of dichotomous branching. **b** Slab of cross section A–B showing the trunk with two parallel central axes, surrounded by abundant growth rings. Note three branches in lower part of photograph oriented parallel to the trunk. White margins of the branches and thin bright lines penetrating vertically into the skeleton indicate diagenetically altered zones. **c** Cross section C–D with eight parallel branches. *Dotted lines* elucidate growth rings of the main stem and the adjacent younger branch. Note asymmetric unilateral growth of four branches towards lower part of image and strong condensation towards the opposite side. **d** Central part of cross section E–F with two branches showing slight to moderate asymmetry of growth rings. Note outer increments surrounding the two branches. Slab image modified by contrast increase



The modern and subrecent skeletal fragments reveal three branching types (Fig. 3b): (1) dichotomous bifurcation of two equivalent branches out of a main branch

at about a 60° angle, (2) unequivalent branching of a thin twig out of a thicker branch, and (3) budding on variously thick branches representing an aborted branch

Fig. 3 Live-collected isidid colony and fragments of modern skeletons of Chatham Rise. **a** Part of living gorgonian colony after dredge recovery. Note reddish coenenchyme being largely torn up by the dredging procedure. **b** Skeletal fragment of the colony after removal of organic tissue exhibiting three branching types. **c** Longitudinal section of a skeletal fragment showing growth increments (dotted lines) along a bud. **d** Dichotomous bifurcation of two equivalent branches illustrated in a longitudinal section. **e** Cross section cutting two unequal branches. Note obliquely cut node underneath the section surface (dark spot near the centre) and fibrous microfabric of growth bands. **f** Node in cross section with discontinuous desiccation cracks (bright rings). Note marginal calcitic overgrowth



growth without nodial development. Based on the characteristic branching of the colonies from the internodes and the arrangement of branches in two preferred planes (Grant 1976), the modern, subrecent and fossil specimens recovered from both hemispheres of the western Pacific are identified as *Keratoisis* Wright of the family Isididae (suborder Holaxonia in the order Gorgonacea of the subclass Octocorallia).

Methods

The samples were described and photographed on board immediately after their recovery. Later they were cut into 4–8 mm thick slabs, polished and photographed. In order to identify any specific skeletal elements and variability in the skeleton causing a banding pattern comparable to that of zooxanthellate scleractinian corals, the slices were analysed by X-ray images. The radiographies of 5 mm thick slabs were processed using a voltage of 50 kV and an X-raying time of 13–15 min. Sub-samples of 4.5×2.5 cm were taken from the slabs for preparation of 20 highly polished petrographic thin sections (25 μm

thickness) and two ultra-thin sections (9 μm thickness) applying normal and polarised transmitted light, reflected light and fluorescence (FITL excitation producing green fluorescence colours). The ultra-thin sections allowed for observation of the primary interference colours of calcite. For studying the skeletal ultrastructures under SEM using a CAMSCAN-Serie 2-CS 44 scanning electron microscope at the Institute of Geosciences, CAU Kiel, the reverse slab of thin section preparation was divided into several sub-samples of approximately 5×5 mm which were polished with a 2,000 grid, etched with diluted hydrochloric acid solution (8%), mounted on SEM stubs, and coated with gold–palladium.

Conventional ages of the New Zealand skeletons were determined by radiocarbon (^{14}C) in the Leibniz Laboratory for Age Determination and Isotope Research at Kiel. Carbonate mineralogy was determined using a Philips PW 1710 diffractometer with a cobalt $K\alpha$ tube. The quantitative proportion of high Mg-calcite was calculated from peak-area ratios, which were measured using the computer-based integration program MacDiff (Petschick 2000).

Results

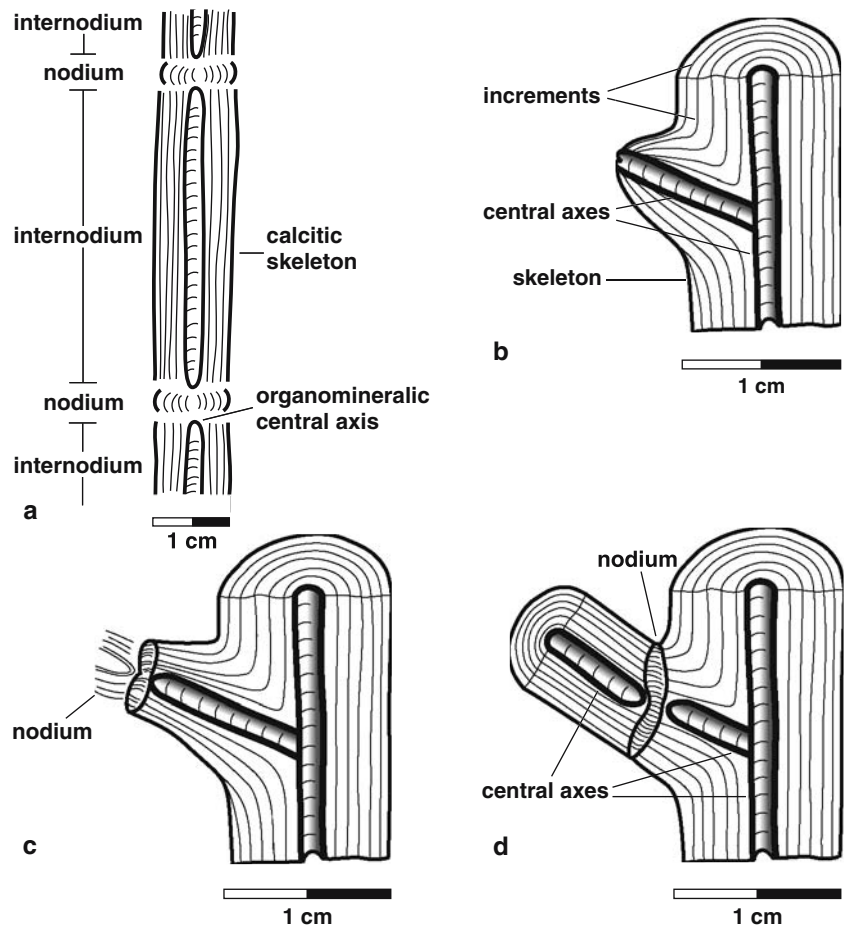
Macrostructure of isidid skeletons

Longitudinal growth of the isidid gorgonian endoskeleton is characterised by alternating nodes consisting of scleroprotein (gorgonin) fibres and calcareous internodes composed of Mg-calcitic crystals (Figs. 3b, 4a). While gorgonin is responsible for flexibility of the skeletal axis, calcite provides stability, allowing for coral growth in high-energy regimes. Lateral growth is characterised by accretion of numerous concentric growth rings around a hollow organo-mineralic central axis (Figs. 2, 3). While the increments of the nodes consist of microscopic laminae, polished slabs of cross-cut internodes exhibit thin bands of brighter and darker colours which are visible with the naked eye (Figs. 2d, 3e). Longitudinal sections through ramification sites of the modern skeletons show that concentric growth rings are symmetrically developed along dichotomously bifurcating, equivalent branches with similar thickness, running parallel to the central axes (Figs. 3d, 4d). Unequivalent, thinner branches (Fig. 4c) and small buds (Figs. 3c, 4b), on the other hand, exhibit continuous inner (older) bands paralleling the skeletal axis and condensed outer

(younger) rings pinching out laterally. The central tube of the skeleton lacks an open pathway at the branching sites and through the nodes (Fig. 3b–d), indicating a multi-step evolution.

Incremental growth mode and branching of the fossil isidid skeleton is basically the same as in modern *Keratoisis*. Major part of the skeleton shows an unequivalent branching pattern with twigs running \pm parallel to the main stem (Fig. 2b–d), whereas equivalent, dichotomous-like ramifications at about 60° angles are restricted to the younger skeleton (Fig. 2a, upper left). In contrast to the modern and subrecent specimens, adjacent branches of the fossil skeleton are laterally coalesced. This results in incremental unconformities along the margins of these branches, where numerous growth bands wedge out, while the outer increments which formed after amalgamation of the branches continuously surround the entire skeleton (Fig. 2c). Furthermore the fossil skeleton reveals a highly asymmetric growth towards one side and condensed sections on the opposite side (Fig. 2c). This provides evidence that the unidirectional trend of incremental growth may be influenced by the bottom current direction, possibly through nutrient flux. These structures contrast the highly concentric growth rings in the modern and subrecent skeletons. In further difference to the modern and subrecent *Keratoisis*

Fig. 4 Sketches elucidating branching modes and incremental patterns of isidid skeletons. **a** Longitudinal section illustrating the alternation of nodes and internodes and their growth increments. **b** Budding. Open tip of central tube indicates a non-terminated growth. **c** Unequivalent branching showing a node at the tip of the thinner branch. **d** Bifurcation of equivalent branches. Central axis of the internodes is interrupted by a node



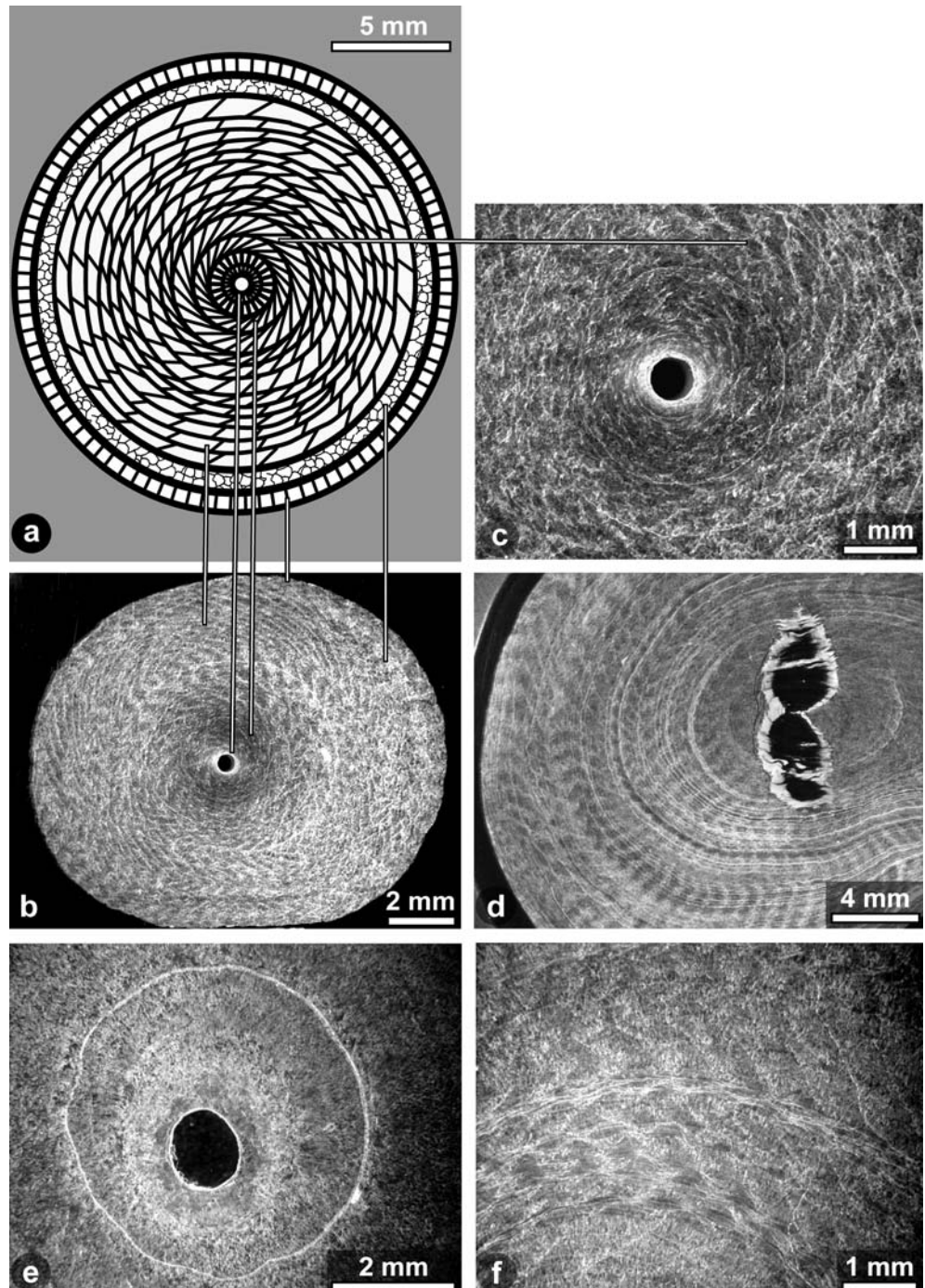
specimens, the fossil skeleton exhibits three major growth interruptions marked by conspicuous organic seams which are observed in all branches. The first prominent interruption of lateral accretion occurs between the juvenile and adult stage (Fig. 5e). The second interruption observed in the early adult stage marks the cessation of organic node formation. As a result, calcitic increments precipitated around the entire skeleton to form “carbonate crusts” (Grasshoff and Zibrowius 1983; Langer 1989) which envelope the nodes (Fig. 2c). A third growth interruption occurring in the late adult

stage characterises a change from tangential to radial arrangement of calcite crystals.

Lateral growth pattern and colour banding

Thin sections of skeletal cross sections photographed under reflected light provide a higher resolution of the growth bands compared to the polished slabs. A sketch (Fig. 5a) illustrates the lateral banding pattern of the modern skeletons: incremental growth starts on the

Fig. 5 Patterns of lateral growth banding in cross sections (sketch and thin sections, reflected light). **a, b** Microstructure of modern *Keratoisis* skeleton. Note predominantly tangential arrangement of crystal units and slight unconformities of growth rings. Sample 178-8 (Okhotsk Sea). **c** Close-up of image (b) showing the dark organic-rich juvenile stage and part of the brighter adult stage. Sample 178-8 (Okhotsk Sea). **d** Subrecent skeleton with a cross-cut node surrounded by numerous calcitic growth bands. Note fascicles of the adult part exhibiting two major orientations of longitudinal crystal axes, causing a conspicuous bright-dark alternation. Sample 119-II (Okhotsk Sea). **e** Fossil skeleton in a slightly oblique section. *Bright line* marking a growth interruption between juvenile and adult stages. Note blurred boundaries of organic-rich fibre crystals in the juvenile stage. Sample C9d-I (Chatham Rise). **f** Part of adult fossil skeleton showing variously oriented fascicle bundles and growth bands. Sample C9d-I (Chatham Rise)



25 μm thick organo-mineralic central axis, generating numerous concentric bands by continuous secretion of elongated organic-rich fibrous crystals upon each other. The juvenile stage surrounding the central axis consists of a few generations of radially oriented crystal units with a low length/width ratio (Fig. 5c) and enrichment of organic matter (Fig. 5b, c). The adult stage forming major part of the skeleton is characterised by a lesser amount of organic matter and tangentially arranged fibrous crystal bundles with increasing length/width ratios in course of incremental growth. In the outer adult stage one or two bright bands of granular crystals poor in organic matter are intercalated in the fibrous framework. The final growth stage shows a radial arrangement of crystal units. According to the prevailing tangential fabric in the skeleton, the modern Chatham Rise specimen corresponds to the species *Keratoisis tangensis* Grant. Subrecent skeletons of Okhotsk Sea (Fig. 5d) and the fossil skeleton of Chatham Rise (Fig. 5e, f) basically exhibit the same lateral alternation; they differ from the modern ones by their internal fabric of the organic-rich juvenile stage showing a cloudy appearance and a higher abundance of granular bands which is probably due to the longer-term growth of the individual branches.

The conspicuous colour banding of isidid skeletons is predominantly controlled by the orientation of the fibrous crystal bundles towards the image plane: in darker rings the longitudinal axes of the organic-rich fibrous crystals and crystal bundles are arranged parallel to the section plane, while in lighter bands the longitudinal crystal axes have an oblique to vertical orientation towards the image plane. The same effect is created within some growth layers, where a lateral pattern of darker and brighter crystal bundles is caused by an alternating parallel and oblique to vertical orientation (Fig. 5b, d, f). In addition, the bright organic-poor granular growth rings contribute to the colour banding, especially in the fossil Chatham Rise skeleton. The individual colour bands of 150–700 μm thickness show no resolution in X-radiographs which confirms that they are not comparable to the density banding of zooxanthellate scleractinians resulting from changes in the packing of crystals within the skeleton or from variation in size and spacing of the skeletal elements (Buddemeier 1974; Barnes and Lough 1993; Helmle et al. 2000).

Micro- and ultrastructure of collected isidid skeletons

Internodes

General features Basic constituents of the calcitic internodes and holdfast of isidid gorgonians are euhedral divergent-radial fibrous crystals which slightly enlarge towards the top and show blunt or skalenohedral ends (Figs. 6a–c, h, 8d). The longitudinal axis of these fibre crystals measures 2–4 μm . Individual fibres are surrounded by thin organic seams which are responsible for

the cream-coloured shade of the skeleton and a cloudy appearance in thin sections (Fig. 7a–f). Additionally, fibre crystals of the juvenile stage show solid inclusions responsible for its darker colour. Several generations of equally oriented crystal blades are arranged into bundles (Figs. 6c, d, h, 8a, c) or strongly divergent fans to hemispheroids (Figs. 6b, 8b) with an average length of 45 μm . Bundles and diverging fans (“fascicles”: Cohen and McConnaughey 2003) meet at angular boundaries, interfingering in a three-dimensional manner (Fig. 8c, d) and producing wavy boundaries between the individual generations (Figs. 5b, f, 6c, 8b). Individual crystal generations form growth lines within a fibre bundle which may be traced through several adjacent fascicles (Fig. 8a, b). In addition, some bright bands consisting of anhedral granular crystals which are characterised by poverty of organic matter, non-uniform interference colours and a somewhat undulous extinction (Figs. 6e–g, 8g, h), conformably alternate with the fibre bundle generations at irregular intervals. In spite of the somewhat blurred boundaries between both fabric types (Figs. 6e, f, 8g), the granular crystal growth stages are restricted to well-defined growth bands and hence represent primary structures. This skeletal microstructure of isidid gorgonians strikingly differs from that of scleractinian corals by the lack of density bands and of calcification centres, the latter representing fundamental skeletal elements of the scleractinian skeleton (Johnston 1980; Constantz 1986; Dullo 1986; Cuif and Dauphin 1998; Rollion-Bard et al. 2003; Cohen and McConnaughey 2003).

Mineralogy In difference to the aragonitic mineralogy of the scleractinian skeletons, the fibre and granular crystals of the isidid internodes are of a high-Mg-calcitic mineralogy with 7–10 mol% MgCO_3 . This XRD data corresponds with that of Bayer and Macintyre (2001).

Organic seams Thin organic seams lining the individual fibre crystals and the tips of the fascicles may represent matrix-derived glycoprotein compounds, i.e. remains of the biomineralisation process of the coral. On the other hand, thick deeply incised organic sheets running continuously along a growth ring of the fossil skeleton (Figs. 7e, 8e) document major interruptions of lateral growth at certain time intervals, when the coenenchyme suffered from partial necrosis or when the entire living coral colony died; hence foreign particles were adsorbed on the exposed skeleton. After a short time span, the skeleton was recolonised by isidid colonies of the same biologic species (J. Pätzold, personal communication). The different composition of both organic matter types is proved in thin sections under fluorescing light: while the thin linings of former glucidic-proteinaceous matrices deriving from the organism itself are non- or dull-fluorescing (Fig. 7g, upper left), foreign particulate organic matter rich in chlorophyll derivatives which may accumulate on the fossil skeleton during growth interruptions exhibits a pronounced bright fluorescence triggered by

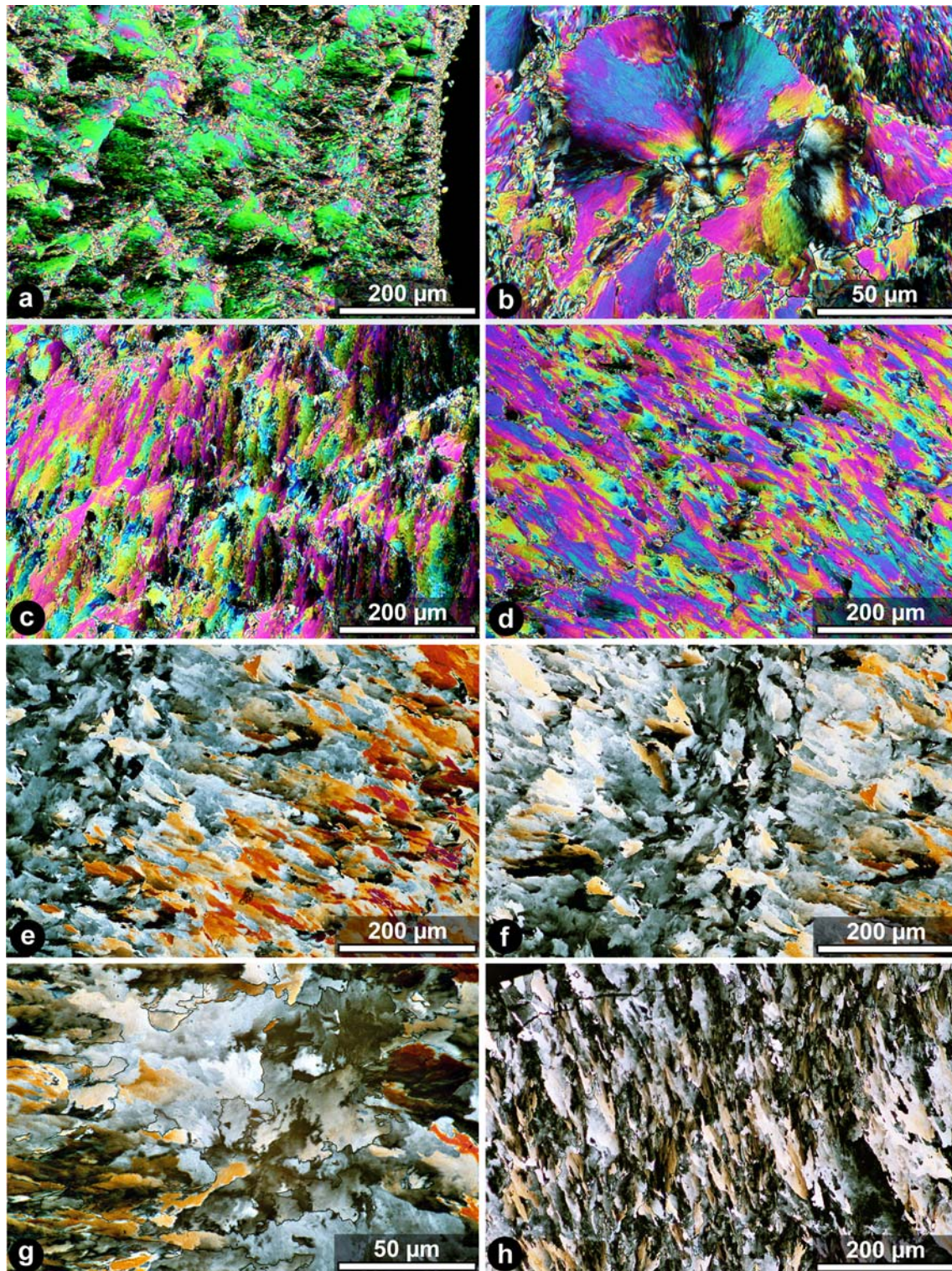


Fig. 6 Microstructure of internodes of modern *Keratoisis*, Chatham Rise, sample B1 (cross section; ultra-thin section in transmitted cross-polarised light). **a** Organo-mineralic central axis (on the right) and juvenile growth stage. Note radial growth of fibrous crystals arranged in bundles with a low length/width ratio. **b** Close-up of juvenile stage showing primary interference colours of Mg-calcite at an angle of 90° towards the position of image **a**. Crystallographic c-axes of fibre crystals composing the fan in centre are in parallel orientation towards the image plane, contrasting the

obliquely cut fibre crystals to the left. **c** Early adult stage, and **d** central part of adult stage showing increasing length/width ratios of fibre bundles. **e, f** Band of granular crystals (greyish interference colours) intercalated between fibre bundle generations (reddish colours) in the outer part of skeletal cross section; note somewhat blurred boundaries. **g** Close-up of granular crystals. Note highly anhedral granular crystals with non-uniform interference colours and a slightly undulous extinction. **h** Final growth stage with radial arrangement of fibre bundles

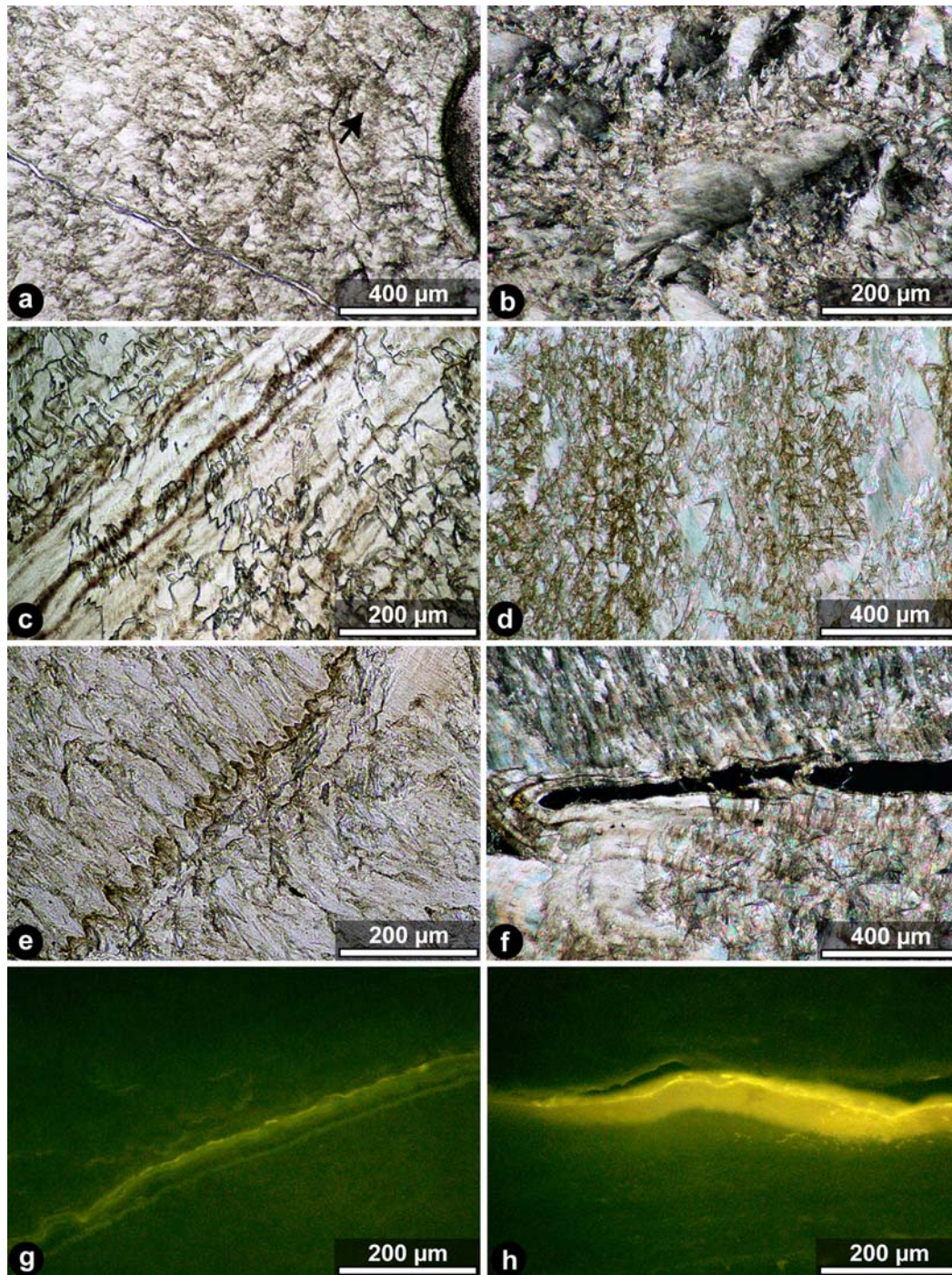


Fig. 7 Microstructure of internodes of isidid skeletons (cross sections; petrographic thin sections in transmitted and fluorescing light). **a** Organo-mineralic central axis with microgranular texture and surrounding skeleton at the base of fossil skeleton. Note angular unconformity between the radially and tangentially arranged fibre bundles at the boundary between juvenile and adult growth stages (*arrow*). Plane-polarised light. Sample C2b-II (Chatham Rise). **b** Diagenetic alteration at the margin of the skeleton. Note accretive crystallisation of fibre crystals to large anhedral crystal aggregates. Cross-polarised light. Sample C9d-IV (Chatham Rise). **c** Dark Fe/Mn-rich colour stripes passing through granular growth band in a subrecent skeleton. Plane-polarised light. Sample 119-II (Sea of Okhotsk). **d** Longitudinal section of a modern Chatham Rise skeleton showing an alternation of organic-

rich and organic-poor growth bands with indistinct boundaries. Image plane cuts the tips of steeply inclined crystallographic c-axes of fibres. Cross-polarised light. Sample BIV (Chatham Rise). **e** Organic seam between juvenile and adult stages in fossil skeleton enveloping the crystal tips and filling the relief. Plane-polarised light. Sample C3a (Chatham Rise). **f** Boundary between two nearly-coalesced branches of fossil skeleton. Note Fe/Mn-stained colour bands in lower and upper branch. Cross-polarised light. Sample C3a (Chatham Rise). **g** Seam of particulate organic matter marking the growth interruption between juvenile and adult stage of fossil skeleton by bright fluorescence. Sample C9d (Chatham Rise). **h** Accumulation of particulate organic matter in a residual void between two adjacent branches, distinguished by yellow fluorescence. Sample C9d (Chatham Rise)

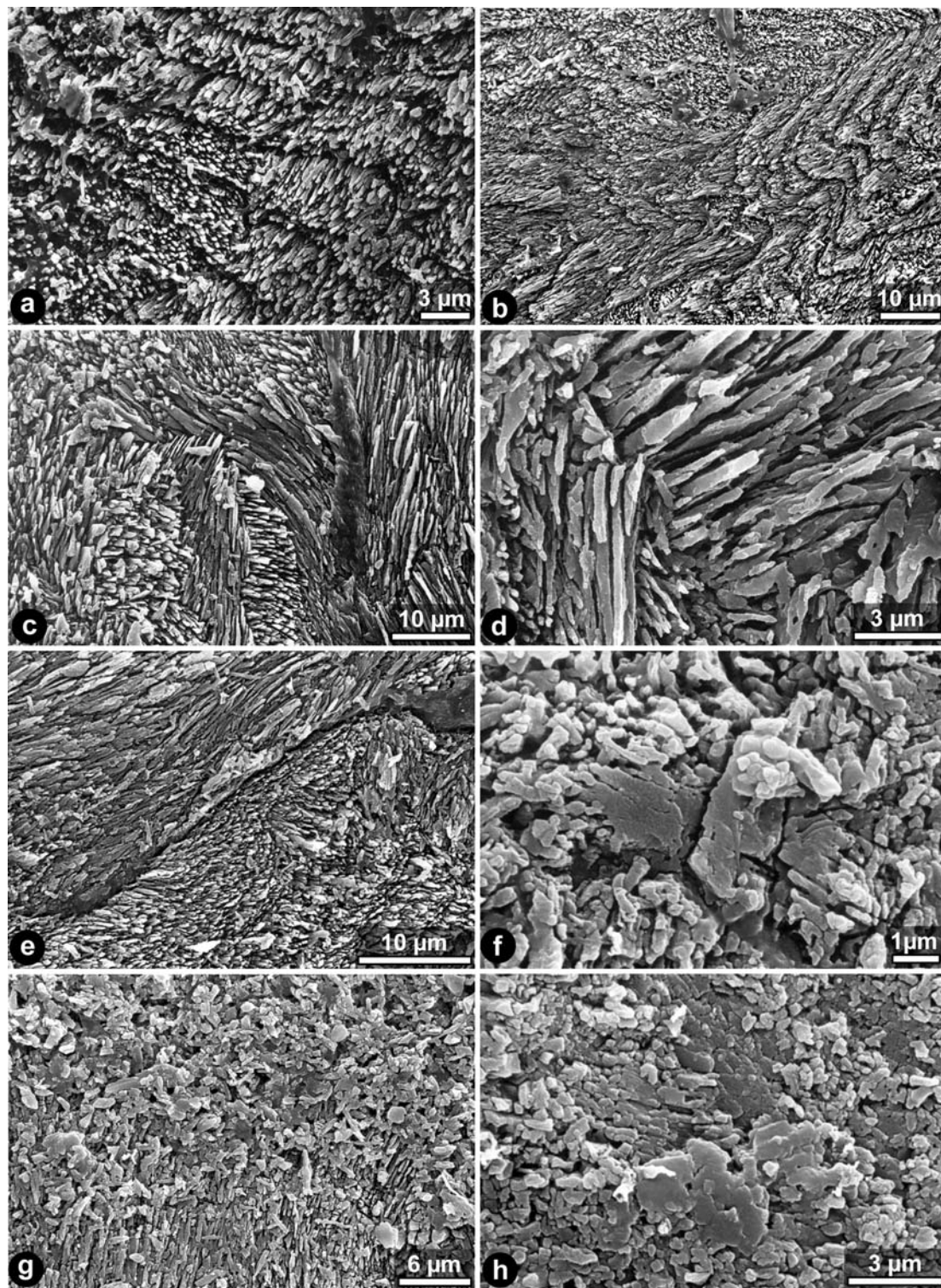


Fig. 8 Ultrastructure of internodes in cross sections of recent, subrecent and fossil isidid skeletons (SEM). **a** Crystal generations in a fibre bundle of the adult fossil skeleton. Sample C1b (Chatham Rise). **b** Same sample as in (a) showing a large fan composed of several crystal generations growing continuously upon each other. Note longitudinal crystal axes showing parallel orientation towards the image plane. **c** Typical three-dimensional interfingering of fascicles in the adult modern skeleton. Sample 178-8 (Okhotsk Sea). **d** Close-up of bladed fibre crystals with blunt to skalenohedral tips. Note arrangement in two diverging bundles meeting at an

angular boundary. Sample C2b-I, fossil skeleton (Chatham Rise). **e** Organic seam separating two unconformably abutting fascicles of varying orientation in the fossil skeleton. Sample C4 (Chatham Rise). **f** Accretive crystallisation of a few fibre crystals resulting in small crystal aggregates. Note subhedral crystal boundaries of the original fibre crystals (*centre*). Sample C4 (Chatham Rise). **g** Granular growth band (*top*) grading from fibre crystals (*base*) in the adult fossil skeleton. Sample C4 (Chatham Rise). **h** Close-up of granular crystals showing anhedral boundaries. Sample C4 (Chatham Rise)

the porphyrine rings of those compounds (Fig. 7g, centre). Foreign organic material may also be trapped in residual voids along the boundary of two nearly coalesced branches (Fig. 7h); here fibre bundles meet at angular unconformities (Fig. 7f).

Colour stripes In contrast to the organic seams occurring on the fascicle surfaces (Figs. 7e, 8e), dark colour stripes with blurred boundaries penetrate the crystal generations. They are most obvious in granular growth stages of the subrecent Okhotsk skeletons (Fig. 7c). In thin sections under reflected light, the stripes show a metallic lustre and hence may be caused by Fe/Mn ions incorporated in the calcite lattice.

Diagenesis The skeletons of all life-collected specimens were protected against bioerosion and other diagenetic alterations. The subrecent skeletons of Okhotsk Sea are also devoid of borings and show well-preserved microfabrics. The fossil skeleton of Chatham Rise, on the other hand, became heavily bioeroded by micro- and macroborers (sponges and bivalves) after death and decay of the coral colonies (Fig. 2a). The metabolic products of boring organisms such as organic acids induced carbonate dissolution and subsequent reprecipitation depending on the saturation degree with respect to CaCO_3 . Such diagenetically altered, somewhat bleached zones proceed radially from the outer margin of the skeleton and from the margins of individual, nearly coalesced branches towards the central axes, cutting through the primary growth bands (Fig. 2b–d).

Micro- and ultrastructure of diagenetically altered areas in the fossil skeleton reveal an accretive crystallisation of several fibre crystals. Accretive crystallisation starts with amalgamation of two blades along their longitudinal axes, linked with a one-step dissolution-reprecipitation process on microscale, whereas the individual crystals may preserve a subhedral fabric (Fig. 8f). Progressive accretion of fibres results in large anhedral crystal aggregates which commonly show a poikilotopic fabric of anhedral crystal hosts and enclosed euhedral to subhedral fibre crystal guests (Fig. 7b). These anhedral products of accretive crystallisation differ from the primary granular growth generations by large poikilotopic crystals, a commonly incomplete recrystallisation with preserved fibre bundle areas between the anhedral crystal aggregates, and a disconformable penetration from the margin towards the centre of the skeleton which irregularly intersects defined growth lines. On the other hand, they also formed during the major growth interruptions of the skeleton, being restricted to concentric growth bands.

Nodes

The nodes consist of small-scale concentric laminations around the central axis which are built by gorgonin fibres (Fig. 9a, d–f). Thin sections under cross-polarised

light exhibit transverse gorgonin fibres with a surface-normal or slightly oblique arrangement (Fig. 9d). The delicate laminae are prone to fungal borings. Irregular concentric fissures in the nodes with somewhat “hairy” boundaries (Figs. 3f, 9e) result from artificial desiccation after the coral recovery, linked with tearing up of gorgonin fibres.

The proteinaceous nodal laminae are anchored with the internodal calcite by organo-mineralic layers (Fig. 9b, c, g, h) which in thin sections exhibit a fibrous texture and an increasing organic content from the skeletal calcite to the gorgonin laminae (Fig. 9b). Thin organo-mineralic layers which regularly interfinger with individual fibre crystal generations of the skeleton elucidate the “anchoring” of the nodes with the internodes (Fig. 9c). The ultrastructure of these layers is characterised by a fibrillar meshwork of three-dimensionally interweaved filaments consisting of mixed organic matter (probably gorgonin) and a poorly crystalline mineral phase (probably a magnesium carbonate of similar composition as that of the internodes), providing rigidity and flexibility (Fig. 9g, h). Hence the organo-mineralic layers are the mediating link between the two-dimensionally arranged organic laminations of the nodes and the three-dimensionally interfingering calcitic fascicles of the internodes (Fig. 9g).

Under fluorescence light, the gorgonin laminae show no fluorescence in spite of brighter colours as compared with the calcitic skeleton. The connecting organo-mineralic layers appear almost as dark as the calcite and are non-fluorescing as well. This fluorescence behaviour of the nodes is caused by the mixed glucidic-proteinaceous macromolecular composition of the autochthonous, coral-specific organic framework (Cuif et al. 1999; Cuif and Dauphin 2005).

Age determination of Chatham Rise isidid skeletons

Fossil skeleton

Age determination with radiocarbon (^{14}C) was especially important in the fossil gorgonian skeleton which provided the key for reconstruction of the growth mode of isidid gorgonians due to its large diameter and complex branching. The conventional ^{14}C ages decrease in longitudinal section from the base of the main stem (lines A–B in Fig. 2a) to the younger branches (lines C–D and E–F in Fig. 2a) and in cross section from the central axis to the last diagenetically unaltered growth ring of a branch, indicating a simultaneous vertical and lateral growth. Since twigs branch out of the main stem at different times and further bifurcate at various growth intervals, ^{14}C ages implicate that branches of different age and varying numbers of growth rings occur at any cross section of the skeleton. The central axis at the base of the main stem provided a ^{14}C age of $3,985 \pm 30$ years BP (\pm range), while the youngest branch in section E–F gave an age of $3,680 \pm 30$ years BP at the central tube.

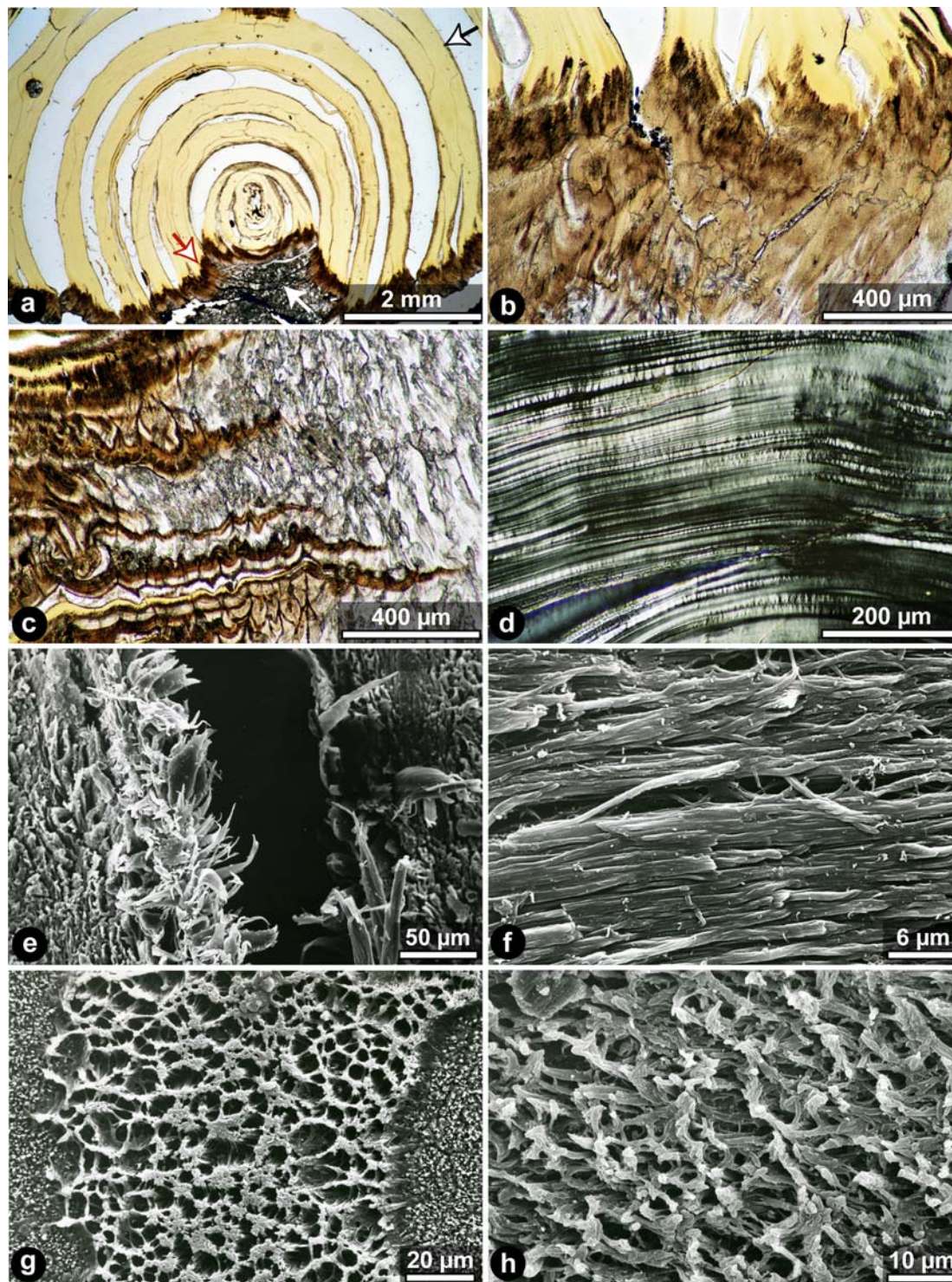


Fig. 9 Micro- and ultrastructure of nodes in the fossil isidid skeleton (cross sections; petrographic thin sections in transmitted light and SEM). **a** Node showing yellowish gorgonin rings (*arrow edged in black*), grey internodal calcite (*white arrow*), and connecting dark-brown organo-mineralic layers (*arrow edged in red*). Nodial “rings” derive from desiccation cracks. Plane-polarised light. Sample C10 (Chatham Rise). **b** Close-up of organo-mineralic layers. Note fibrous texture and irregular enrichment of dark-brown organic matter. Plane-polarised light. Sample C10 (Chatham Rise). **c** Organo-mineralic layers anchoring the gorgonin laminae with the skeleton. Note regular alternation of a gorgonin and an organo-mineralic layer with individual calcite

crystal generations (*lower part of image*). Plane-polarised light. Sample C2b (Chatham Rise). **d** Gorgonin laminae showing thin transverse elements in cross-polarised light. Sample C10 (Chatham Rise). **e** Burst gorgonin fibres along a desiccation crack showing a “hairy” appearance. Sample C2b-I (Chatham Rise). **f** Close-up of gorgonin fibres. Sample C2b-I (Chatham Rise). **g** Meshwork of organo-mineralic layers connecting the gorgonin with the underlying internodal calcite (*right and left margin*). Sample C6b (Chatham Rise). **h** Organo-mineralic meshwork illustrating the three-dimensionally interweaved fibrilles. Sample C6c (Chatham Rise)

Thus the fossil gorgonian skeleton provides a maximum record of 305 ± 30 years.

Linear lateral extension rates of the calcitic increments were calculated by means of ^{14}C data measured from centre to margin of several cross-cut branches. Assuming a constant growth rate and crystal size, calculated linear extension rates amount to $0.23\text{--}0.64 \text{ mm year}^{-1}$ (0.4 mm year^{-1} average). The growth periods of calcitic elements resulting from these rates are as follows: one fibre crystal generation of $3 \mu\text{m}$ length formed in 3 days, a fibre bundle or fascicle consisting of 3–4 crystal generations with $9\text{--}12 \mu\text{m}$ length in 8–11 days, a bundle of 3–5 fascicles with $36\text{--}60 \mu\text{m}$ length in 33–55 days (1–1.8 months), and a colour band consisting of 4–12 fascicle bundles with $150\text{--}724 \mu\text{m}$ length in 138–658 days (4.5–21 months). These data demonstrate that the macroscopic colour bands grow on annual, their microscopic sub-units on sub-annual time scales.

The linear extension rates of our fossil isidid skeleton are about one decimal power lower than the rates measured on azooxanthellate colonial scleractinian skeletons (e.g. 2.6 mm year^{-1} for *L. pertusa*: Mortensen and Rapp 1998). They roughly correspond, however, to the rates of some slower growing solitary scleractinians ($0.5\text{--}1 \text{ mm year}^{-1}$ for *D. cristagalli*: Risk et al. 2002; Adkins et al. 2004). Our values furthermore correspond well with those deduced from some primnoid gorgonians of the Gulf of Alaska ($0.36 \text{ mm year}^{-1}$ for *P. resedaeformis*: Andrews et al. 2002). On the other hand, they are clearly higher than those measured on *Keratoisis* from the Gulf of Alaska ($0.05\text{--}0.1 \text{ mm year}^{-1}$: Roark et al. 2005), but one order of magnitude lower than those of *Keratoisis* from the Davidson Seamount off California ($1.9\text{--}4.4 \text{ mm year}^{-1}$: Andrews et al. 2005). These data prove that accretion rates of the isidid genus *Keratoisis* may vary considerably, probably controlled by environmental parameters such as nutrients and currents or pH and alkalinity.

Live-collected skeleton

The live-collected isidid skeleton of Chatham Rise shows a bomb- ^{14}C signal (PMC values of > 90) in the outermost layers and a much lower (pre-bomb?) ^{14}C concentration at the central axis which gave a reservoir age of 735 or 650 ± 25 years BP (\pm range). The absolute age of the oldest portion of the live-collected skeleton may be calculated from the reservoir age of the DIC and from the excursion of ^{14}C increase in the intermediate water masses of the SW Pacific since 1950, when bomb- ^{14}C was introduced during atmospheric nuclear tests.

Growth mode

Results from skeletal morphology and absolute age determination allowed for reconstructing the growth mode of isidid gorgonians. Sketch of Fig. 10a illustrates

the incremental growth pattern of modern and fossil isidid skeletons in longitudinal sections: growth starts with secretion of an organo-mineralic axis followed by accretion of a lateral calcitic growth band (Stage I). During progressive vertical growth and bifurcation of equivalent (“A” in the sketch) and unequivalent (“B”) branches, lateral concentric growth rings are secreted simultaneously around the entire skeleton. As a result, the main stem accumulates most growth rings, while the tips of the youngest branches show just one growth band (Stage VI). In dichotomous branching type equivalent branches possess the same number of increments, whereas unequivalent twigs show a lesser number of increments than the branch they are splitting off.

Growth patterns in cross section are illustrated by growth rings (Fig. 10b). The sketch exhibits a scheme of lateral incremental accretion at selected time lines, illustrated in five growth stages. As soon as a new internode forms on top of the skeleton, the whole skeleton is enveloped by this internodal growth ring. Hence the trunk and main stem which the younger branches are splitting off have accreted more growth rings than the late-stage branches which bifurcate in the upper part of the skeleton. As a consequence, any cross section or time line of the skeleton cuts branches of different ages and varying numbers of growth rings in the individual branches.

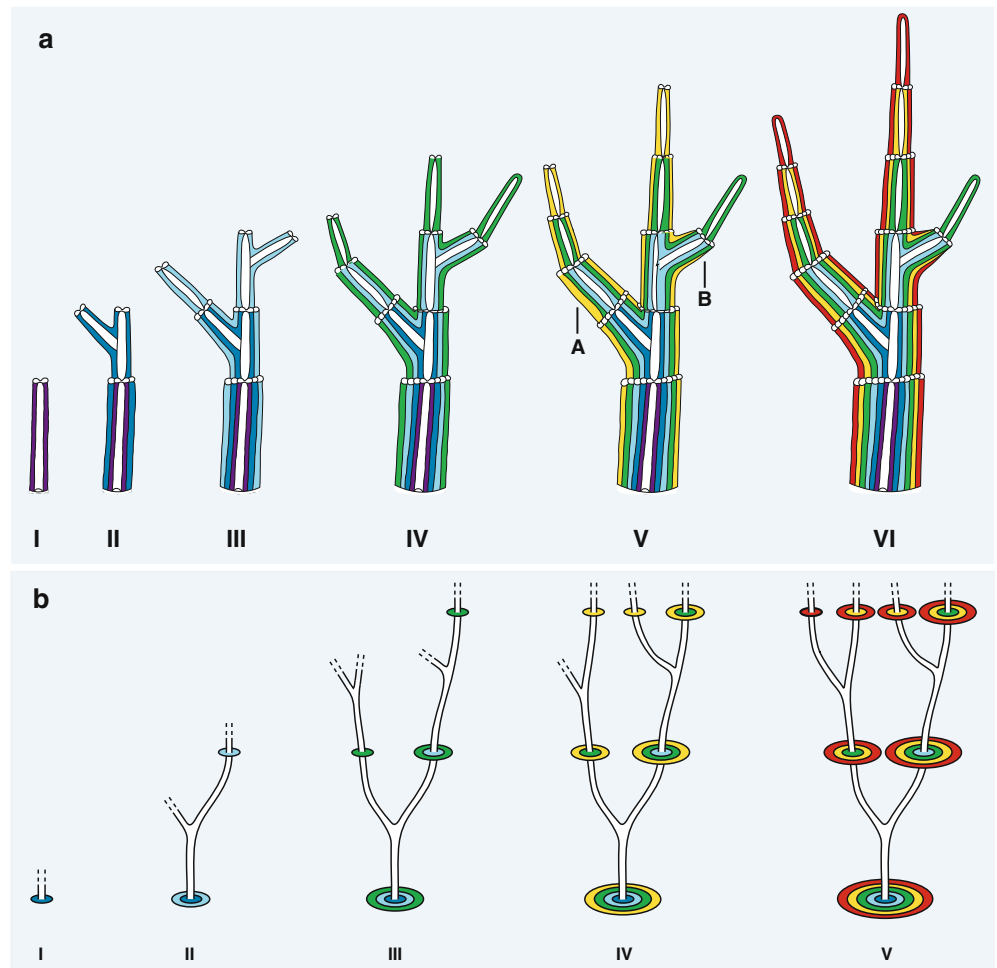
Discussion

Primary structures: fibre versus granular growth stages

The granular growth stages which are conformably intercalated in the fibre bundle framework of the isidid skeletons document a fundamental change of crystal fabric. In comparison with physico-chemical precipitation of fibrous and equant crystals which are characterised by high growth rates or slow crystal growth respectively (Tucker and Wright 1996), the granular crystal generations may form at lower growth rates than the fibre generations. In this case they might indicate a deterioration of environmental conditions, e.g. reduced nutrient supply.

In scleractinians, growth zonation within fibres may be due to a cyclic activity of the mineralising ectodermal cell layer leading to formation of organic-rich and organic-depleted micro-scaled growth layers (Cuif et al. 1999). Transferring this hypothesis to the isidid gorgonian skeletons, their irregular alternation of organic-rich fibre and organic-poor granular crystal growth stages may be controlled by changing activity of the calcite-precipitating endodermal cell layers. In addition, changing biochemical composition of the biomineralising matrices could be responsible for the alternation of crystal fabric styles in the isidid skeletons, thus reflecting a biochemical control. Further investigations are needed to unravel the origin and occurrence of granular growth stages in the fibrous isidid skeleton.

Fig. 10 Sketches of growth pattern of modern *Keratoisis*. **a** Longitudinal sections showing incremental growth in six stages. *A* equivalent branch; *B* unequivalent (*B*) branch. Growth of the unequivalent branch ceased during Stage IV in the sketch. **b** Growth pattern in cross section illustrated by growth rings. Lateral incremental accretion at selected time lines is illustrated in five growth stages



Early diagenetic features

In contrast to the fibre crystals in the fossil skeleton, the primary granular crystals did not suffer any accretive crystallisation. The uniform Mg-calcitic mineralogy of fibrous and granular growth rings with a restricted range of 7–10 mol% MgCO₃ obviously contrasts their micro- and ultrastructural heterogeneity, the latter being responsible for their differential susceptibility to diagenesis. A similar phenomenon is observed in scleractinians, where in spite of a uniform aragonitic mineralogy the centres of calcification are preferentially prone to diagenetic changes compared with the fibre crystals. It has to be checked if this variability which in scleractinians is related to the composition and spatial distribution of the organic matrices mediating crystal nucleation (Perrin 2003) also applies to bamboo corals.

Implications for a model of biomineralisation

Biomineralisation of corals has been intensively studied in zooxanthellate and non-zooxanthellate scleractinians over the past three decades (Sorauf 1972, 1980; Gladfelter 1982; Le Tissier 1991; Cuif et al. 1997; Cohen and

McConnaughey 2003; Allemand et al. 2004; Cuif and Dauphin 2005). Skeletal growth of scleractinians implies a matrix-mediated, extracellular secretion of calcareous biocrystals by the single-cell calcicoblastic ectodermal epithelium at the base of the polyps (Cohen and McConnaughey 2003; Perrin 2003). Repeatedly produced micron-thick growth layers lead to the formation of growth lines reflecting the successive positions of the secretory ectodermal layer (Cuif et al. 1999). Calcification of scleractinian skeletons proceeds via Ca²⁺-binding organic matrices which facilitate the nucleation and control the position of the initial crystallisation sites, the mineralogy and the orientation of the crystals (Cohen and McConnaughey 2003). The matrices are composed of an EDTA-insoluble framework and EDTA-soluble acidic macromolecules. The soluble compounds are organised in a monolayer (“β-sheet”) of negatively charged acidic macromolecules rich in aspartic/glutamic polypeptide chains (Mitterer 1978; Constantz and Weiner 1988; Gautret et al. 1997; Perrin 2003) and associated sulphated glucids (Dauphin 2001). These glycoproteins favour the interaction with metal ions (Ca²⁺), thus forming a nucleating surface. The EDTA-insoluble constructive matrix of neutral (uncharged) polymerised macromolecules serves as basement for the β-sheet to organize.

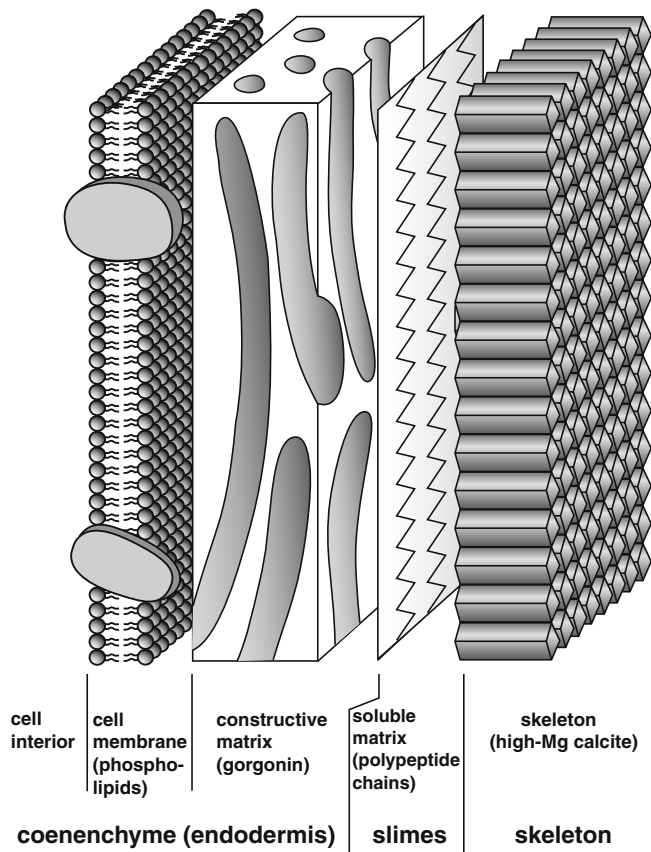


Fig. 11 Simplified biomineralisation model for *Keratoisis* sp. showing the major compounds of organic matrices

A common constituent of the constructive matrix is collagen, a scleroprotein consisting of about 1,000 amino acids arranged along a triple-helical polypeptide backbone (Mann 2001). Collagen fibres which may combine to concentric layers around the cells represent a major constituent of the extracellular polymeric matrices (EPS) in animal cells. Collagen was proved to form a major part of the insoluble matrix of the gorgonian taxa *Leptogorgia* and *C. rubrum* (Allemand et al. 1994).

Based on the similarity of the molecular structure of gorgonin and collagen, the following biomineralisation model is proposed for the isidid gorgonian endoskeleton (Fig. 11): gorgonin produced by cells of the endodermal epithelium acts as an insoluble structural framework in the mineralisation process, while the viscous slimes surrounding the skeleton represent the soluble polypeptide β -sheet. If this assumption proves to be correct, gorgonin does not only construct the nodes, but occurs throughout the calcitic internodes in form of organic seams surrounding the fibre crystals, which represent the remains of the insoluble matrices incorporated into the growing skeleton.

Acknowledgements We want to acknowledge the German Research Foundation (DFG) for substantial support through the Leibniz award (Du 129/33), the German Federal Ministry of Education and

Science (BMBF) for the SO168 and SO178 grants and the Ministry for Industry, Science and Technology of the Russian Federation for the LV29 grant. We are indebted to Prof. Dr. PM Grootes (Leibniz Labor for Age Determination and Isotope Research Kiel) for ^{14}C measurements, Dr. B. Bader and U. Schuldt (Department of Geosciences, CAU Kiel) for their support in the SEM lab, and D. Dettmar (Bochum) for thin section preparation. Two anonymous reviewers helped to improve the manuscript.

References

- Adkins JF, Cheng H, Boyle EA, Druffel ERM, Edwards RL (1998) Deep-sea coral evidence for rapid change in ventilation of the deep North Atlantic 15,400 years ago. *Science* 280:725–728
- Adkins JF, Henderson GM, Wang S-L, O'Shea S, Mokadem F (2004) Growth rates of the deep-sea scleractinia *Desmophyllum cristagalli* and *Enallopsammia rostrata*. *Earth Planet Sci Lett* 227:481–490
- Allemand D, Cuif J-P, Watabe N, Oishi M, Kawaguchi T (1994) The organic matrix of skeletal structures of the Mediterranean Red Coral, *Corallium rubrum*. In: Allemand D, Cuif J-P (eds) *Biomineralisation '93: 7th Int Symp Biomineralisation*. Bulletin de l'Institut océanographique, Monaco, Numéro spécial 14, 1:129–140
- Allemand D, Ferrier-Pagès C, Furla P, Houlbrèue F, Puverel S, Reynaud S, Tambuttè E, Tambuttè S, Zoccola D (2004) Biomineralisation in reef-building corals: from molecular mechanisms to environmental control. *C R Palevol* 3:453–467
- Andrews AH, Cordes EE, Mahoney MM, Munk K, Coale KH, Cailliet GM, Heifetz J (2002) Age, growth and radiometric age validation of a deep-sea, habitat-forming gorgonian (*Primnoa resedaeformis*) from the Gulf of Alaska. *Hydrobiologia* 471:101–110
- Andrews AH, Cailliet GM, Kerr LA, Coale KH, Lundstrom C, DeVogelaere AP (2005) Investigations of age and growth for three deep-sea corals from the Davidson Seamount off central California. In: Freiwald A, Roberts JM (eds) *Cold-water corals and ecosystems*. Springer, Berlin Heidelberg New York, pp 1021–1038
- Barnes DJ, Lough JM (1993) On the nature and causes of density banding in massive coral skeletons. *J Exp Mar Biol Ecol* 167:91–108
- Bayer FM, Macintyre IG (2001) The mineral content of the axis and holdfast of some gorgonian octocorals (Coelenterata: Anthozoa), with special reference to the family Gorgoniidae. *Proc Biol Soc Wash* 14:309–345
- Bernecker M, Weidlich O (2005) Azooxanthellate corals in the Late Maastrichtian—early Paleocene of the Danish basin: bryozoan, coral mounds in a boreal shelf setting. In: Freiwald A, Roberts JM (eds) *Cold-water corals and ecosystems*. Springer, Berlin Heidelberg New York, pp 3–25
- Bond ZA, Cohen AL, Smith SR, Jenkins WJ (2005) Growth and composition of high-Mg calcite in the skeleton of a Bermudian gorgonian (*Plexaurella dichotoma*): potential for paleothermometry. *Geochem Geophys Geosy* 6. DOI 10.1029/2005GC000911
- Buddemeier RW (1974) Environmental controls over annual and lunar monthly cycles in hermatypic coral calcification. *Proc 2nd Int Coral Reef Symp* 2:259–267
- Cohen AL, McConnaughey TA (2003) A geochemical perspective on coral mineralization. In: Dove M, Weiner S, de Yoreo J (eds) *Biomineralization*. *Rev Miner Geochem* 54:151–187
- Constantz BR (1986) Coral skeleton construction: a physico-chemically dominated process. *Palaios* 1:152–157
- Constantz B, Weiner S (1988) Acidic macromolecules associated with the mineral phase of scleractinian coral skeletons. *J Exp Zool* 248:253–258
- Cooke JP, Nelson CS, Crundwell MP, Spiegler D (2002) *Bolboforma* as monitors of Cenozoic paleoceanographic changes in the Southern Ocean. *Palaeogeogr Palaeoclimatol* 188:73–100

- Cuif J-P, Dauphin Y (1998) Microstructural and physico-chemical characterization of “centers of calcification” in septa of some Recent scleractinian corals. *Paläontologische Zeitschrift* 72:257–270
- Cuif J-P, Dauphin Y (2005) The Environment Recording Unit in coral skeletons—a synthesis of structural and chemical evidences for a biochemically driven, stepping-growth process in fibres. *Biogeosciences* 2:61–73
- Cuif J-P, Dauphin Y, Gautret P (1997) Biomineralization features in scleractinian coral skeletons: source of new taxonomic criteria. *Bol R Soc Esp Hist Nat (Sec Geol)* 92:129–141
- Cuif J-P, Dauphin Y, Gautret P (1999) Compositional diversity of soluble mineralizing matrices in some recent coral skeletons compared to fine-scale growth structures of fibres: discussion of consequences for biomineralisation and diagenesis. *Int J Earth Sci* 88:582–592
- Dauphin Y (2001) Comparative studies of skeletal soluble matrices from some Scleractinian corals and Molluscs. *Int J Biol Macromol* 28:293–304
- Dullo W-C (1986) Variation in diagenetic sequences: an example from Pleistocene coral reefs, Red Sea, Saudi Arabia. In: Purser BH, Schroeder JH (eds) Reef diagenesis. Springer, Berlin Heidelberg New York, pp 77–90
- Fenner J, Carter L, Stewart R (1992) Late Quaternary paleoclimatic and paleoceanographic change over northern Chatham Rise, New Zealand. *Mar Geol* 108:383–404
- Gautret P, Cuif J-P, Freiwald A (1997) Composition of soluble mineralizing matrices in zooxanthellate and non-zooxanthellate scleractinian corals: biochemical assessment of photosynthetic metabolism through the study of a skeletal feature. *Facies* 36:189–194
- Gladfelter EH (1982) Skeletal development in *Acropora cervicornis*: patterns of calcium carbonate accretion in the axial corallite. *Coral Reefs* 1:45–51
- Grant R (1976) The marine fauna of New Zealand: Isididae (Octocorallia: Gorgonacea) from New Zealand and the Antarctic. *New Zealand Oceanographic Institute Memoir* 66, Wellington
- Grasshoff M (1980) Isididae aus dem Pliozän und Pleistozän von Sizilien (Cnidaria: Octocorallia). *Senckenbergiana lethaea* 60:435–447
- Grasshoff M, Zibrowius H (1983) Kalkkrusten auf Achsen von Hornkorallen, rezent und fossil. *Senckenbergiana maritima* 15:111–145
- Grigg RW (1974) Growth rings: annual periodicity in two gorgonian corals. *Ecology* 55:876–881
- Grillo M-C, Goldberg WM, Allemand D (1993) Skeleton and sclerite formation in the precious red coral *Corallium rubrum*. *Mar Biol* 117:119–128
- Heikoop JM, Hickmott DD, Risk MJ, Shearer CK, Atudorei V (2002) Potential climate signals from the deep-sea gorgonian coral *Primnoa resedaeformis*. *Hydrobiologia* 471:117–124
- Helm C, Schülke I (2003) An almost complete specimen of the Late Cretaceous (Campanian) octocoral *Isis ramose* Voigt (Gorgonacea) from the Lower Saxony Basin, northwest Germany. *Cretaceous Res* 24:35–40
- Helmle KP, Dodge RE, Ketcham RA (2000) Skeletal architecture and density banding in *Diploria strigosa* by X-ray computed tomography. *Proc 9th Int Coral Reef Symp* 1:365–771
- Johnston IS (1980) The ultrastructure of skeletogenesis in hermatypic corals. *Int Rev Cytol* 67:171–214
- Keigwin LD (1998) Glacial-age hydrology of the far northwest Pacific. *Paleoceanography* 13:323–339
- Kocurko MJ (1989) Notes on the fossil octocorals and comparisons of some modern and ancient octocorals remains. *Tulane Stud Geol Paleontol* 21:105–115
- Langer M (1989) Haftorgan, Internodien und Sklerite von *Keratoisis melitensis* (GOLDFUSS, 1826) (Octocorallia) in the pliozänen Foraminiferenmergeln (“Trubi”) von Milazzo (Sizilien). *Paläontologische Zeitschrift* 63:15–24
- Le Tissier M (1991) The nature of the skeleton and skeletogenic tissues in the Cnidaria. *Hydrobiologia* 216/217:397–402
- Lewis JC, Barnowski TF, Telesnicki GJ (1992) Characteristics of carbonates of gorgonian axes (Coelenterata, Octocorallia). *Biol Bull* 183:278–296
- Lutringer A, Blamart D, Frank N, Labeyrie L (2005) Paleotemperatures from deep-sea corals: scale effects. In: Freiwald A, Roberts JM (eds) Cold-water corals and ecosystems. Springer, Berlin Heidelberg New York, pp 1081–1096
- Macintyre IG, Bayer FM, Logan MAV, Skinner HCW (2000) Possible vestige of early phosphatic biomineralization in gorgonian octocorals (Coelenterata). *Geology* 28:455–458
- Mann S (2001) Biomineralisation. Principles and concepts in inorganic materials chemistry. Oxford University Press
- Marschal C, Garrabou J, Harmelin JG, Pichon M (2004) A new method for measuring growth and age in the precious coral *Corallium rubrum* (L.). *Coral Reefs* 23:423–432
- Mitterer RM (1978) Aminoacid composition and metal binding capability of the skeletal protein of corals. *Bull Mar Sci* 28:173–180
- Mortensen PB, Rapp HT (1998) Oxygen and carbon isotope ratios related to growth line patterns in skeletons of *Lophelia pertusa* (Anthozoa, Scleractinia): implications for determination of linear extension rates. *Sarsia* 83:433–446
- Nelson CS, Cooke PJ, Hendy CH, Cuthbertson AM (1993) Oceanographic and climate changes over the past 160,000 years at Deep Sea Drilling Project Site 594 off southeastern New Zealand, southwest Pacific ocean. *Paleoceanography* 8:435–458
- Perrin C (2003) Compositional heterogeneity and microstructural diversity of coral skeletons: implications for taxonomy and control on early diagenesis. *Coral Reefs* 22:109–120
- Petschick R (2000) MacDiff 4.1.2 Powder Diffraction Software. Available from the author at: <http://www.servermac.geologie.uni-frankfurt.de/Staff/Homepages/Petschick/Geo4Mac/RainersSoftListE.html#Mineralogy>
- Risk MJ, Heikoop JM, Snow MG, Beukens R (2002) Lifespans and growth patterns of two deep-sea corals: *Primnoa resedaeformis* and *Desmophyllum cristagalli*. *Hydrobiologia* 471:125–131
- Risk MJ, Hall-Spencer J, Williams B (2005) Climate records from the Faroe-Shetland Channel using *Lophelia pertusa* (Linnaeus, 1758). In: Freiwald A, Roberts JM (eds) Cold-water corals and ecosystems. Springer, Berlin Heidelberg New York, pp 1097–1108
- Roark EB, Guilderson TP, Flood-Page S, Dunbar RB, Ingram BL, Fallon SJ, McCulloch M (2005) Radiocarbon-based ages and growth rates of bamboo corals from the Gulf of Alaska. *Geophys Res Lett* 32. DOI 10.1029/2004GL021919, 2005
- Rollion-Bard C, Blamart D, Cuif J-P, Juillet-Leclerc A (2003) Microanalysis of C and O isotopes of azooxanthellate and zooxanthellate corals by ion microprobe. *Coral Reefs* 22:405–415
- Sherwood OA, Heikoop JM, Sinclair DJ, Scott DB, Risk MJ, Shearer C, Azetsu-Sott K (2005) Skeletal Mg/Ca in *Primnoa resedaeformis*: relationship to temperature? In: Freiwald A, Roberts JM (eds) Cold-water corals and ecosystems. Springer, Berlin Heidelberg New York, pp 1061–1079
- Sinclair DJ, Sherwood OA, Risk MJ, Hillaire-Marcel C, Tubrett M, Sylvester P, McCulloch M, Kinsley L (2005) Testing the reproducibility of Mg/Ca profiles in the deep-water coral *Primnoa resedaeformis*: putting the proxy through its paces. In: Freiwald A, Roberts JM (eds) Cold-water corals and ecosystems. Springer, Berlin Heidelberg New York, pp 1039–1060
- Smith JE, Schwarcz HP, Risk MJ (2000) Paleotemperatures from deep-sea corals: overcoming “vital effects”. *Palaios* 15:25–32
- Sorauf JE (1972) Skeletal microstructure and microarchitecture in Scleractinia (Coelenterata). *Palaeontology* 15 (Part 1):88–107
- Sorauf JE (1980) Biomineralization, structure and diagenesis of the coelenterate skeleton. *Acta Palaeontol Pol* 25:327–343

- Thresher R, Rintoul SR, Koslow JA, Weidman C, Adkins J, Proctor C (2004) Oceanic evidence of climatic change in southern Australia over the last three centuries. *Geophys Res Lett* 31. DOI 10.1029/2003GL018869
- Tucker ME, Wright VP (1996) *Carbonate Sedimentology*. Blackwell
- Weinbauer MG, Brandstätter F, Velimirov B (2000) On the potential use of magnesium and strontium concentrations as ecological indicators in the calcite skeleton of the red coral (*Corallium rubrum*). *Mar Biol* 137:801–809
- Wong CS, Matear RJ, Freeland HJ, Whitney FA, Bychkov AS (1998) WOCE line P1W in the Okhotsk Sea 2. CFCs and the formation rate of intermediate water. *J Geophys Res* 103:15625–15642
- Yamamoto-Kawai M, Watanabe S, Tsunogai S, Wakatsuchi M (2004) Chlorofluorocarbons in the Sea of Okhotsk: ventilation of the intermediate water. *J Geophys Res* 109. DOI 10.1029/2003JC001919, 2004

**Variable Holocene Methane Emissions
from Cold Seeps on the Sakhalin Margin, Okhotsk
Sea Linked to Seismo-Tectonic Activity**

5 Lester Lembke-Jene^{1,2*}, Ralf Tiedemann³, Dirk Nuernberg¹,
Klaus Wallmann¹, Anatoly Obzhairov⁴, Wolf-Christian Dullo¹

10 ¹IFM-GEOMAR Leibniz-Institut fuer Meereswissenschaften,
Wischofstrasse 1-3, D-24148 Kiel, Germany

²Tethys Geoconsulting GmbH, Wischofstrasse 1-3, D24148
Kiel, Germany

³Alfred-Wegener-Institut fuer Polar- und Meeresforschung,
15 Am Alten Hafn 26, D-27568 Bremerhaven, Germany

⁴V.I. Il'ichev Pacific Oceanological Institute, 43
Baltiyskaya Street, Vladivostok 690041, Russia

* Corresponding Author: llemcke@ifm-geomar.de

Abstract

Planktic and benthic foraminifera from sediment cores recovered from a Giant Cold Seep Area (GCSA) at the NE Sakhalin margin, Okhotsk Sea, were studied with respect to
5 stable carbon isotopes for paleo-methane venting. Two representative cores show recurring intervals of depleted $\delta^{13}\text{C}$ during the past 3,500 and 7000 cal. yr BP, respectively. Minima values reach -32 ‰ in deep endobenthic species *N. labradorica*, and -4 ‰ to -6 ‰ in epibenthic
10 *Cibicides* spp. Parallel timeseries of the planktic *N. pachyderma* (sinistral) show according depletions, though with differing timing and intensity. The more depleted values are derived by secondary carbonate overgrowths that occurred synsedimentary with ongoing methane venting,
15 within the error uncertainties of the age models.

In constraining the lateral influence of the methane vents, two additional sediment cores several hundred kilometres to the south of the GCSA show distinct depletions in planktic foraminiferal $\delta^{13}\text{C}$. Thus, methane
20 anomalies within the water column were large enough to get transported over large distances to the downstream region of the GCSA, presumably in subsurface mixed layer, dichothermal water masses. Due to diagenetic overprinting of isotopic signals and unconstrained boundary conditions
25 we do not favor budget estimates for amounts of methane released to the atmosphere. Very likely, the influence from

submarine sources on the atmospheric methane concentrations as recorded in Greenland ice cores was rather small. Nonetheless, methane venting events may have caused short-term smaller fluctuations in the atmospheric CH₄ record.

5 The likely causes for variable methane venting on the Sakhalin margin are periods of increased seismo-tectonic activity along the Japan-Kuril-Kamchatka trench system and its connection to the tectonic settings in the Okhotsk Sea via the East Sakhalin and West Derugin Shear Zones.
10 Intervals of increased methane venting often coincide with times of increased tsunami frequency at the Hokkaido and Kamchatka coasts as well as with volcanic and emergence events on Kamchatka and Hokkaido. Specifically the most prominent time of active methane venting at the GCSA
15 between 1,200 and 1,800 cal. yr BP correlates with one of the most active periods of Shiveluch Volcano, Kamchatka, the widespread Jomon regression in Japan, and a three- to fourfold statistical increase in tsunami deposits at Kamchatka.

20 Though large uncertainties remain as consequence of potential dating errors in the marine records or reliability and significance of terrestrial references, these initial results suggest that a tectonic forcing of venting activity on the Sakhalin margin may have been
25 persistently operating during the last 7,000 yr. This may have consequences for assessing causes of venting

variability on active continental margins. In addition, submarine and onshore methane emissions did likely not stay constant through the Holocene, as is presently assumed in budget estimates for geological methane sources.

5

1. Introduction

Methane is a powerful greenhouse gas and its atmospheric concentration has varied naturally in the pre-industrial past (e.g. Blunier et al., 1995; Chappellaz et al., 1990; Petit et al., 1999). While the causes for this variability
10 are mainly attributed to source emissions by boreal and tropical wetlands (e.g. Blunier et al., 1995; Brook et al., 2000; Schaefer et al., 2006; Sowers, 2006), there remain smaller, but significant geological sources to the methane
15 budget such as submarine methane cold seeps, pockmark fields, or mud volcanoes (Etiope and Milkov, 2004; Judd et al., 2002; Milkov, 2000; Milkov, 2004). These are increasingly regarded as significant in volume and importance and knowledge about their significance and
20 variability is crucial for understanding both the global carbon cycle and the various components of the atmospheric methane budget (Judd, 2003; Kvenvolden, 2002; Kvenvolden and Rogers, 2005).

Contributions of marine seeps to the total atmospheric
25 methane budget are estimated to be around 20 to 30 Tg ± 5 (Etiope and Milkov, 2004; Judd, 2004; Judd et al., 2002),

but due to a lack of robust data, assessments change and large uncertainties exist (Hovland and Judd, 1992; Milkov and Etiope, 2005). The estimates remain largely unconstrained and, as a consequence are often assumed to stay constant over time (e.g. Ferretti et al., 2005). However, on geological timescales evidence exists for variable and sometimes abruptly increasing methane emissions that are widely ascribed to releases from submarine gas hydrate reservoirs (Dickens, 1999; Dickens, 2004; Kennett et al., 2000; Nisbet, 1992; Nisbet, 2002). Recently proposed dynamic interactions of gas hydrates and other source like hydrocarbon seeps with climate and oceanographic changes in the late Quaternary (Hill et al., 2006; Kennett et al., 2000; Nisbet, 2002) highlight the need for an improved understanding of submarine emissions, especially as their role and importance is currently discussed controversially (Brook et al., 2000; Cannariato and Stott, 2004; Dallenbach et al., 2000; Hill et al., 2004a; Kennett et al., 2000; Maslin et al., 2004; Nisbet, 2002) with regard to global change and its implications for future warming scenarios (Archer and Buffett, 2005; Buffett and Archer, 2004).

Inferred methane discharges from gas hydrates or gas seeps on continental margins take their main evidence from negative excursions in stable carbon isotopes of planktic and benthic foraminifera that are not easily explainable by

other sources alone (Hill et al., 2004b; Kennett et al., 2000; Millo et al., 2005a; Wefer et al., 1994). Most of these dissociation events are thought to result from episodes of rapid temperature rises in intermediate and deep waters, causing changes in the temperature-pressure stability field of gas hydrates (Buffett and Archer, 2004; Dickens and Quinbyhunt, 1994; Dickens and QuinbyHunt, 1997; Kennett et al., 2000). In addition, growing numbers of newly discovered extensive cold seep sites and revised estimates of vent activity led to a revision of the global contribution of methane from gas seeps and fluid vents (Judd, 2004). However, it is rather unclear if or how much these seeps vary in their activity and distribution on timescales longer than the last few years (Judd, 2003; Judd, 2004). Improved knowledge about long-term natural variability of geological methane sources is thus of major importance for our understanding of continental margins' seep characteristics, their contributions to the global carbon cycle, and natural greenhouse gas variability (Judd et al., 2002; Kvenvolden and Rogers, 2005).

In this paper, we present stable carbon isotope data from foraminifera that indicate widespread, highly variable methane venting activity during the last 7,000 cal. yr BP from a Giant Cold Seep Area (GCSA), located on the north-eastern Sakhalin continental margin in the Okhotsk Sea. We try to constrain the regional dispersal of these anomalies,

evaluate its significance for the Northern Hemispheric CH₄ budget, and hypothesize that increased paleoseismo-tectonic activity lead to Methane Venting Events (MVE) from natural cold seeps, thus invoking a tectonic feedback mechanism to the observed methane seepage variability in the Okhotsk Sea.

2. Study Area and Setting

The Okhotsk Sea, a marginal sea of the subarctic Northwest Pacific, hosts a large gas hydrate-bearing province on the continental margin off Sakhalin island (Fig. 2, Ginsburg et al., 1993; Ludmann and Wong, 2003; Matveeva et al., 2003). Today, this is a region where active methane venting occurs in considerable volumes and has been studied previously (Dafner et al., 1998; Obzhairov et al., 2000; Obzhairov et al., 2002; Yoshida et al., 2004). Gas hydrates have been successfully recovered in sediment cores (Fig. 2, core photo GE-99-24 Biebow et al., 2002; Ginsburg et al., 1993). Flux measurements and water column studies have shown that the region emits methane into the atmosphere from its submarine sources (Lammers et al., 1995). Even gas bubbles reaching the sea surface were reported from regions with water depths of more than 700m, indicating occasional rapid ascent of large gas bubbles through the water column (Biebow et al., 2002; Dullo et al., 2004). These regions in the Okhotsk Sea thus may have contributed to past

variations in the natural pre-industrial atmospheric methane budget by variations in methane venting or gas hydrate dissociations on geological timescales.

Previous studies have proven that submarine venting intensity in this region is linked to the regional tectonic setting with nearly all recorded seeps (currently more than 200) lined up along major tectonic fault zones, such as the INESSA shear zone and Lavrentiev fault and single seeps often occurring above individual smaller faults (Ludmann and Wong, 2003; Obzhairov et al., 2004; Shakirov et al., 2004).

The intensity of the discharge and the number and lateral expansion of active submarine gas seeps, and also of major Sakhalin mud volcanoes, varies on short timescales and correlates to seismo-tectonic activity as expressed by major earthquakes in the region (Obzhairov et al., 2004; Shakirov et al., 2004). In addition, studies of sediment cores from the Derugin Basin and seep areas also assume that long-term variability exists (Greinert et al., 2002).

Within the joint Russian-German joint projects KOMEX and KOMEX-SONNE, the Obzhairov Flare Giant Cold Seep Area (GCSA) has been studied for diverse questions, including constraining the gas-geochemistry of the water and the sediment column, the characterization of authigenic carbonate and barite formation, or the classification of the seep area and the origin of the seeping gas and fluids

(e.g. Greinert et al., 2002; Greinert and Derkachev, 2004; Ludmann and Wong, 2003; Matveeva et al., 2003; Obzhirov et al., 2004; Obzhirov et al., 2000; Obzhirov et al., 2002; Wallmann et al., 2006). In most sediment cores recovered
5 from this area, distinct layers of fossil venting activity were found, evidenced by the occurrence of chemoautotrophic mollusks, authigenic carbonate concretions, and textural and lithologic changes in the sediment column (Biebow et al., 2002; Greinert et al., 2002). A previous study
10 established a minimum age for the existence of the larger seep area of approximately 20,000 years (Greinert et al., 2002), based on radiocarbon dating of chemoautotrophic mollusks in deeper parts of sediment cores. While it is assumed that the observed patterns belong to past intervals
15 of variable vent activity and, more specifically, to events with largely increased methane seepage, no works have so far dealt with the temporal variability of palaeo-seep activity that is nonetheless assumed for the area. For simplicity, in the following we refer to shorter time
20 periods, which we connect with largely increased venting activity above the present level, as Methane Venting Events or MVE's.

3. Material and Methods

25 A number of shorter sediment cores were retrieved with different coring techniques from the GCSA during repeated

cruises with R/V Akademik Lavrentiev, R/V Marshal Gelovany, and R/V Sonne (in total more than 15 cores). However, due to technical constraints with rapidly expanding cores and textural disintegration by dissociating gas hydrates
5 directly after recovery, in almost all cases no permanent liners were used for coring, thus preventing post-cruise sampling for this study.

Gravity core GE99-24-2 (600m water depth) was recovered from the northern part of the „Obzhirov-Flare“ GCSA (Fig.
10 1b). On-board investigation immediately after recovery revealed the down-core occurrence of finely laminated gas hydrates starting at a core depth of about 320 cm below surface. We sampled this gravity core onboard with sufficient resolution in sample intervals ranging from 1 cm
15 to 5 cm.

We later also took samples from cores S0178-26 and S0178-42 during cruise R/V SONNE in 2004, though these cores could not be sampled continuously due to more abundant intersections with lamellae and pieces of gas hydrate and
20 because of parallel sampling for geochemical investigations of other groups. Accordingly, sampling was not continuous and had to be done in slabs of 2 to 4 cm thickness. Authigenic carbonate nodules were present in the cores at distinct intervals, together with remnants of vent fauna
25 (Calyptogena sp., Archarax sp.) like in most sediment cores we recovered previously. The S0178 cores serve as reference

that features reported here mainly from GE99-24 are no isolated pattern, but may be found on a local or even regional seep-wide scale.

All samples were freeze-dried, washed over a 63 μm screen, 5 dried, and separated in fractions (63-150, 150-250, 250-500, >500 μm). For stable isotope analysis, we picked a selection of the most abundant benthic species with different microhabitat patterns: (1) *Cibicidoides* spp. (representing *Cibicides mundulus* and *Lobatula lobatula*, 10 epibenthic), *Elphidium batialis* (epibenthic-shallow endobenthic, preferential detritus feeder), *Uvigerina peregrina* (shallow endobenthic), *Nonionellina labradorica* (intermediate endobenthic, well adapted to dysoxic conditions), and *Globobulimina auriculata* (deep 15 endobenthic, prefers low-oxygen settings). We mostly picked between three and five specimen per benthic sample, but during some anomalous intervals also analyzed single specimen with sufficient size and comparable preservation in order to study the intra-specific variability. In 20 addition, we routinely analyzed 15-20 specimen of planktic *Neogloboquadrina pachyderma* (s) from the 150-250 μm fraction for stable isotope analysis.

Samples were cracked open to remove dirt particles from the inside, if necessary cleaned ultrasonically in ethanol 25 p.a., roasted at 200 °C for 24h, and measured with a Finnigan MAT 252 with an online-coupled automated KIEL II

CARBO device and on a Thermo Finnigan Delta Advantage Plus coupled to a Thermo-Electron GasBench 2 preparation device at the ISOLAB-Stable Isotope Laboratory at IFM-GEOMAR, Kiel. Calibration is achieved via the international NBS19 5 and NBS 20 (National Bureau of Standards) as well as through an internal laboratory standard of Solnhofen limestone. Overall analytical reproducibility is ± 0.05 ‰ for $\delta^{13}\text{C}$ and ± 0.08 ‰ for $\delta^{18}\text{O}$. All values are reported as against the Vienna Pee Dee Belemnite Standard (‰ vs. V-PDB). All data reported in this study are stored 10 electronically at the WDC-MARE and made available through the PANGAEA database.

4. Age model and sediment characteristics

15 Age models for the two cores GE99-24 and SO178-26/42 from the vent locations are based on a total of seven AMS ^{14}C -dates of chemoautotrophic mollusk shell fragments (*Conchocele* and *Calyptogema* spp.) and, in one case, large fragments of an echinoid with excellent preservation. These 20 mollusks mark definite periods of methane venting activity at the core locations, they are useful independent indicators that methane venting actually did occur and that the observed $\delta^{13}\text{C}$ anomalies are no result of a temporally unrelated diagenetic process.

25 We used no planktic foraminifera for AMS ^{14}C -dating in the vent region, mostly because of a lack of sufficient numbers

of well-preserved tests in the obtained samples. Another concern is the possibility of introducing age offsets by methane-derived old radiocarbon in tests through diagenetic processes. While we routinely scan the tests for stable isotope analyses for preservation and diagenetic alterations, this is not feasible for the large amounts of specimen that are needed for AMS ^{14}C dates (1,000–3,000 specimen). Using shells of chemoautotrophic clams for dating instead helps to minimize these problems, as these taxa are easier to assess for alterations. This convenience comes at the price of increased age errors due to unconstrained knowledge about past variations in ventilation ages of bottom water masses. Dating benthic organisms introduces increased age uncertainty, because not only the local surface ocean reservoir effect ΔR may be insufficiently known; changes in the ventilation age of the intermediate water mass add more age offsets to the radiocarbon age. To a certain extent we tackled the problems by constraining the ventilation ages through $^{14}\text{C}_{\text{DIC}}$ dates of water samples and wood fragments in a core at the E' Sakhalin margin (Tiedemann, unpubl. data). After correction for a ventilation age offset of 800 yr and a ΔR of 500 yr, we calibrated all ^{14}C ages with the software Calib 5.01 using the MARINE04 calibrations dataset (Hughen et al., 2004). In the calibration process we assigned a ΔR uncertainty of ± 50 years to our data, based on recent

results for this region (Sarnthein et al., 2005, ^{14}C radiocarbon online database). We rejected two samples: KIA21961 in core 99-24 shows a clear age reversal. The derived younger age cannot be reconciled with lithostratigraphic and sedimentological data, or the other dates in the core and was thus discarded from the age model. We also tried to date a badly preserved mollusk fragment, in core S0178-42, which was altered by early diagenesis as later indicated by depleted $\delta^{13}\text{C}$ (ca. -30‰) values. Accordingly, the age determination showed an anomalous old age as compared to the other dates. We thus did not use this age in the preliminary, composite age model of the S0178 cores 26 and 42. We constructed a locally weighted Least Squared Error fit to the data points in both cores. The result a best-fit smooth curve through the 2σ error ranges of the respective age control points. The age model of core LV 28-4 is based on a total of 18 AMS ^{14}C radiocarbon dates on mixed samples of *N. pachyderma* (s) and *G. bulloides*, and benthic mollusks and gastropods in the older part of the core (AMS data available through PANGAEA). The age model for core LV29-78 is based on the correlation of a high-resolution (50 yr average sample spacing) chlorine record of that core to the chlorine record of nearby (less than 20 km) reference core LV29-79 (age model based on 13 AMS ^{14}C dates on mixed planktic foraminifera

and benthic mollusks) and to another reference core, LV28-4. Assumptions about ΔR are like above and a best fit was obtained by a fifth-order polynomial fit, matching all age control points within their 2σ error ranges. The age models of these cores are reported in detail elsewhere (Tiedemann et al., *subm.*). All original radiocarbon data are also stored at the WDC-MARE.

However, due to these different approaches and the use of benthic organisms, at present our age models are not more precise than ± 150 cal. years at best (with 2σ error range as derived from the calibration) and any conclusions relying on the timing of the records have to be viewed in the context of these uncertainties.

5. Results and Discussion

5.1. Characteristics of Methane Venting Events (MVE's) in the Obzhirov Flare Giant Cold Seep Area

For the characterization of the immediate seep area, we concentrate on core 99-24 as this is the most densely sampled core and it has also been the subject of previous studies (e.g. Matveeva et al., 2003). We think that the basic characteristics are valid for the interpretation of the other cores' features though they are less well studied due to technical constraints. We presume that methane

venting in the GCSA very likely has occurred during the entire time interval the cores cover, but generally no huge anomalies are found within the basal and uppermost sections of the cores from the area. This also holds for the sections where decomposing gas hydrates were found upon recovery of the core on deck (Fig. 2). This pattern is in accordance with studies we conducted on live benthic foraminifera at modern seep locations, where the CH_4 flux into the water column is often too weak at most locations to significantly alter the $\delta^{13}\text{C}$ composition of the DIC and most foraminiferal taxa.

Core 99-24 covers the Holocene interval between about 500 and 3,500 years, with the upper part missing due to sediment loss during core recovery. Deeper core penetration than the roughly 320 cm achieved here has generally not been possible with existing corers due to the abundance of gas hydrates in lenses and small blocks. Cores raised on subsequent cruises (LV29-50, S0178-26, S0178-42, S0178-36, etc.) are mostly much shorter, equally because of gas hydrate abundance in the cores (Biebow et al., 2002; Dullo et al., 2004).

The benthic foraminiferal $\delta^{13}\text{C}$ results differ significantly in timing and amplitude between different species. The core features obvious, repeated intervals during which anomalously negative $\delta^{13}\text{C}$ values occur around 3.2, 2.6, 2.4, 2.1, and 1.3 kyr BP (Fig. 3). These distinct, but smaller

and likely local, events frame a major event between 1,400-2,000 yr BP with very large anomalies. We principally attribute these negative $\delta^{13}\text{C}$ anomalies in core GE99-24 and other cores from the Obzhirov Flare GCSA, to largely increased methane venting activity during the reported time intervals. In the following, we refer to these Methane Venting Events as MVE, followed by a number (labelling as seen in Fig. 3 and Fig. 5). While the general timing of the $\delta^{13}\text{C}$ anomalies matches between different benthic species, interspecies offsets in amplitude are evident (Fig. 3). Specifically, we observe increasingly negative anomalous values with increasing microhabitat depth of the respective benthic species (Fig. 3). During the major anomaly, the epibenthic *Cibicidoides* spp. remain at values between -2 ‰ and -6 ‰, with few values below and with a large amplitude between the single datapoints, while the deeper infaunal taxa like *G. auriculata* or *N. labradorica* easily reach values around -10 ‰ to less than -20 ‰ in the same samples. A closer inspection also reveals large intra-specific variability within the same samples. Multiple single-specimen samples of *G. auriculata* within MVE 4 scatter between normal background values and minima of less than -10 ‰ (s. Table 2). Excellently preserved specimen of *G. auriculata* (i.e. transparent, glossy texture, unfilled, etc.) show $\delta^{13}\text{C}$ values of less than -10 ‰ and are bordered by normal background values of about -2 to -3‰ in

immediately adjacent or even the same samples (Fig. 3). Though *N. labradorica* is too small in most cases to be measured individually, we presume that this wide scatter of individual data persists in the other endobenthic species and some few measurements we were able to perform support this assumption. High $\delta^{13}\text{C}$ intra-specific variability matches the results of other studies on live faunae from vent locations (Hill et al., 2004b; Martin et al., 2004; Rathburn et al., 2003) as well as our own results from the same region (L. Lembke-Jene, subm. manuscript). We regard this pattern as additional indicator for highly variable CH_4 fluxes at the core location, perhaps on seasonal to inter-annual timescales, but surely on inter-decadal timescales according to an estimated average sample spacing of 10-50 years within the anomaly intervals. The values of planktic *N. pachyderma* (s) show the same general pattern with depleted $\delta^{13}\text{C}$ intervals (Fig. 3). However, distinct differences, compared to the benthic records, are an earlier onset of anomalously negative values and the recurrent minima within persistently depleted values between 2,900 and 1,300 yr BP. These differences between benthic and planktic $\delta^{13}\text{C}$ are too large to be explainable by sedimentological factors such as upward mixing of specimen by bioturbation or diagenesis, which should affect all specimens in the same samples at least qualitatively.

The early onset of $\delta^{13}\text{C}$ depletion of *N. pachyderma* (s) in core 99-24 at around 3,000 yr BP suggests that the area underwent a longer-term increase in methane-venting approximately between 2,900 and 1,300 yr BP, though our age control is not tight enough to constrain this assumption better. During this interval of generally increased venting activity at the GCSA, we assume that short-term periods with maximal seepage of CH_4 occurred right at the core location, leading to the short-term (probably less than 10 decades) extreme depletions of benthic values in specific intervals and pronounced minima in the *N. pachyderma* (s) record. These short events superimpose as a local effect on generally increased regional methane venting, leading to the species-specific temporal decoupling of $\delta^{13}\text{C}$ curves 15 between planktic and benthic foraminifera (Fig. 3)

5.2. Lateral Extent and Timing of Venting Events at the Sakhalin margin

Modern observations show that methane anomalies injected 20 into the water column at the GCSA get trapped within bottom and subsurface water masses and are then laterally transported with tidal currents and major current systems for large distances (Obzhirov et al., 2002; Yoshida et al., 2004), Cruise report). Today, large anomalies are mostly 25 found at 400 to 700 m water depth, where strong bottom currents transport CH_4 -enriched water masses down from the

continental shelf and southwards, as well as within the dichothermal temperature minimum layer around 50-200 m water depth (Biebow et al., 2002; Yoshida et al., 2004), which is the preferred habitat of sinistral *N. pachyderma* 5 (Bauch et al., 2002). Thus we presumed that large anomalies, induced into the water column at the GCSA, may be detectable in the downstream region southward along the eastern Sakhalin continental margin in the $\delta^{13}\text{C}$ records of *N. pachyderma* (s) of other cores, given sufficient temporal 10 resolution.

We compared the isotope records from the GCSA to two other high-resolution reference cores from the north-eastern and mid-eastern Sakhalin continental margin, LV29-78 and LV28-4, respectively. Both are located far outside venting areas 15 but downstream the Obzhirov Flare location, some hundred kilometres away from the original GCSA.

These cores show distinct, but considerably less pronounced anomalous negative $\delta^{13}\text{C}$ values in their planktic records during repeated intervals during the past 7000 yr BP 20 (Fig. 5). Restricted to those anomalies detectable in more than a single core and thus laterally widespread, we count thirteen MVE during the last 7,000 yr BP (marked and numbered in Fig. 5). Amplitudes of $\delta^{13}\text{C}$ and the detailed timings vary throughout the cores, however this should be 25 expected, given the relatively large error uncertainties in radiocarbon-based chronologies in the marine setting, the

independent chronologies of the respective cores and the abruptness and short duration of the original MVE events. In some cases, available sampling density is obviously insufficient to document particular MVE. Such is the case in LV29-78 at MVE 7 and 8 (Fig. 5), or in the *G. bulloides* record of LV28-4 between 4,000 and 1,800 yr BP (the species is absent during that time interval in most cores in the Okhotsk Sea, Fig. 5). We note, however, that in a few cases MVE 1, 3, and 9 (at about 200, 1,300, and 4,500 yr BP) were not clearly detectable in core LV29-78, though this core is located between the northerly GCSA and the more southerly located core LV28-4, which at least records MVE 1 and 3 in both species and MVE 2, though very moderately, in *N. pachyderma* (s). In core LV29-78, we do observe an increased variability in the recorded values around MVE 1 and 2, as well as a significant decrease in $\delta^{13}\text{C}$ values around 550 to 600 yr BP. As this core's chronology is attained via stacking and correlation of nutrient proxies to a nearby AMS ^{14}C -dated one (LV29-79), we speculate that our chronology is probably not good enough in this particular part of the record, as the reference core has a slightly disturbed uppermost section affecting the last ca. 500 yr BP. Future efforts with the help of additional AMS ^{14}C dates on two other parallel cores will help to resolve this issue.

In order to reduce the possibility of processes other than Methane venting to cause the observed anomalies in the cores LV28-4 and LV29-78 (like repeated diagenetic fronts), we scanned the respective benthic isotope records from both cores for according negative anomalies but could neither find a pattern as distinct nor as negative as in the planktic records. We also note that many of the more pronounced MVE are not made up of single values but show a trend in neighbouring values (Fig. 5) and have been, if possible, measured repeatedly to reassure us of the pattern.

To further constrain the region affected by the MVE, we checked other high-resolution records from the Kamchatka continental margin and the eastern Kuril Basin (i.e. the upstream region to the GCSA), but found no evidence for negative $\delta^{13}\text{C}$ anomalies in those records. This lets us conclude that the MVE are of a regional significance, but confined to the northeastern and northern margins near Sakhalin. They are mainly generated by increased abundance of methane seeps and more vigorous venting activity, likely with a distribution much like the current one (Obzhirov et al., 2004). In contrast we have no evidence for significant venting activity at other known locations of gas hydrate accumulation e.g. near the Kurile islands during the Holocene (Gaedicke et al., 1997).

Within the affected area, the $\delta^{13}\text{C}_{\text{DIC}}$ of the upper mixed layer at least is altered during the MVE as evident from negative amplitudes between -0.5 ‰ and -2 ‰, with an estimated average values of about -1 ‰. So far, under modern settings, we have encountered only very small $\delta^{13}\text{C}_{\text{DIC}}$ anomalies in near-bottom waters directly above gas seeps (see. $\delta^{13}\text{C}_{\text{DIC}}$ profile, Fig. 2) but not within the upper water column. Within the project's water chemistry studies, we searched for $\delta^{13}\text{C}_{\text{DIC}}$ anomalies in the upper mixed layer farther south of the venting areas but found none. However, based on only 15 water profiles analysed so far with 12 or 24 samples each, our lateral coverage may be still insufficient (Bauch et al., 2002, N. Andersen and H. Erlenkeuser, pers. comm.). Taken together, the paleo-MVE's must have had a larger and more powerful influence on the water column than the modern seeps (already more than 200 active flares today) with an estimated contribution to the atmospheric methane budget of about 0.13 Tg annually (Lammers et al., 1995).

20

5.3. Evaluation of postdepositional alterations of primary $\delta^{13}\text{C}$ signals

We note that the values reported here are more negative than most data from other sites (e.g. Hill et al., 2004a; Kennett et al., 2000; Maslin et al., 1998; Millo et al., 2005a; Ohkushi et al., 2005; Uchida et al., 2004), even if

25

in some of them diagenetic recrystallization of the foraminifera is admittedly involved (Millo et al., 2005a; Ohkushi et al., 2005; Uchida et al., 2004). Our extremely negative values exclude other causes than methane as the source for these depletions. Alternative causes have been discussed in other cases e.g. elevated fluxes of organic matter, changing pore-water O_2 conditions, and diagenesis (Stott et al., 2002; Torres et al., 2004). The first two processes would draw down the resulting $\delta^{13}\text{C}_{\text{DIC}}$ signal by no more than a few ‰, relative to ambient bottom water (Stott et al., 2002) and can thus not explain the minima in our records, no matter if caused by diagenesis or primary signals. Diagenesis, however, occurs in most vent settings and we assessed the possible influence and timing (L. Lembke-Jene, *subm. manuscript*).

15

As we pointed out, core GE99-24 is to date our best-sampled core, albeit not the only one. Though most other cores from the GCSA were originally sampled for pore water at large sample spaces and are thus not well suited for dating and isotope analyses, we analyzed other records, notably S0178-26 and LV29-50 nearby, though with larger error estimates and incomplete sampling due to abundant gas hydrates and carbonate concretions in the core (Fig. 5). Though both cores feature different sedimentation rates and characteristics, as well as different pore water chemistries and authigenic carbonate lithologies (Biebow et

20

25

al., 2002; Dullo et al., 2004; Matveeva et al., 2003), the anomaly events in the cores centre around the same temporal intervals, within the admittedly large sampling and age model errors. We infer that the regional vent system intensified during the major $\delta^{13}\text{C}$ anomaly events and that these MVE's are rather not the result of one isolated gas seep within the core location of GE99-24 at the Obzhirov Flare GCSA.

In settings where methane discharges from the sediment into the water column, large gradients in the pore-water carbonate chemistry occur, leading to the dissolution or recrystallization of carbonate sediment components as well as to precipitation of authigenic carbonate concretions of various mineralogies (Greinert et al., 2001; Greinert and Derkachev, 2004; Malone et al., 2002). These processes have been inferred as possible alternative causes for depleted $\delta^{13}\text{C}$ values in foraminifera (Cannariato and Stott, 2004; Torres et al., 2003), rather than the incorporation of CH_4 -derived and primarily methane-derived DIC into the pristine carbonate test of foraminifera. While it has been shown that foraminifera may yield depleted $\delta^{13}\text{C}$ values at cold seep sites (Hill et al., 2004b; Mackensen et al., 2006; Martin et al., 2004), questions remain about the connection to methane fluxes and the type of different seep settings (Cannariato and Stott, 2004; Torres et al., 2003). Thus in a palaeo-methane discharge setting one has to assess the

question of diagenetic alteration of foraminiferal test carbonate (Millo et al., 2005b; Ohkushi et al., 2005; Torres et al., 2003; Uchida et al., 2004).

In the cores from the Obzhirov Flare GCSA, we found distinct intervals with enhanced precipitation of authigenic carbonates in all sediment cores that we retrieved from the GCSA [Biebow, 2002 #348; Dullo, 2004 #365]. These intervals do sometimes, but not always, match with the $\delta^{13}\text{C}$ anomalies we observed in the foraminifera. However, one characteristic of these intervals is the co-occurrence of pristine and diagenetically altered foraminifera. Given the large negative $\delta^{13}\text{C}$ values we observe, especially in the endobenthic species *G. auriculata* and *N. labradorica*, we addressed contributions of secondary carbonate to the primary $\delta^{13}\text{C}$ signals, especially from authigenic carbonate precipitations and diagenetic recrystallisations. We are confident that secondary carbonate precipitation does have a small influence on our reported results, while recrystallisations play no significant role.

We only used specimens that were in pristine, very well-preserved conditions. Transparent or completely translucent test walls with glossy surfaces, no fillings of the chambers, no secondary carbonate overgrowths or recrystallised test parts, or any other alterations were the minimum requirement of our quality protocols using a

taphonomic preservation index before isotope measurements were performed. We extensively scanned our foraminiferal species assemblage with SEM (multiple scans of more than 200 specimen of all species) to detect relevant alterations in tests ultrastructures. We used semi-quantitative SEM-EDX - analyses of selected test walls, and a few additional analyses of Mg/Ca ratios at selected depth intervals to see whether secondary calcite precipitated on or in the tests. The SEM studies showed no changes in the ultrastructure of the tests, the tests are visually indistinguishable from specimens sampled alive from non-vent sites (under 2,000-20,000x magnifications) with no signs of recrystallisations. We know of no diagenetic process in foraminiferal carbonates that significantly alters the isotopic and chemical composition of the wall without affecting the microcrystalline ultrastructure. Mg/Ca analyses of foraminifera have been recommended as tool for quality control for samples from vent sites, because inorganically precipitated Mg-calcite yields Mg/calc ratios that are orders of magnitude higher than the ones commonly encountered in unaltered foraminifera (Torres et al., 2003). Preliminary Mg/Ca analyses on selected pooled samples of *U. peregrina* give no indication for significant diagenetic alteration (Table 1). While Mg/Ca values vary by about 1.5 mM M⁻¹, no obvious relation between higher Mg values and lower δ¹³C exists for *U. peregrina*, in fact the

lowest Mg/Ca value give a considerable depletion in δ¹³C of -4.61 ‰ (Table 1). However, we measured two additional samples of *G. auriculata*; one gave enriched values of 14.93 mM M⁻¹ together with minimal δ¹³C values of -15.55 ‰. The other one showed a normal value of 1.13 mM M⁻¹ with δ¹³C values between -1.56 ‰ and -4.13 ‰, the latter being significantly below average values from non-seep locations for the region. Accordingly, we presume that some of the very negative values (below about -10 ‰) in the two deep endobenthic species *N. labradorica* and *G. auriculata* may be due to additional secondary carbonate crystallisations. In a study of foraminiferal taphonomy at modern and fossil methane seeps we found different species-specific susceptibilities to taphonomic alterations that can lead to possible post-mortem authigenic carbonate components foraminifera of the species *N. labradorica* and *G. auriculata*. These two species seem to be more prone to precipitation of thin layers of high-Mg calcite inside their relatively thin test walls (*G. auriculata*) immediately after death. We thus do not exclude that some δ¹³C minima values in these two species may be derived from thin, secondary carbonate precipitations inside the tests. These post-mortem coatings in foraminiferal tests have been described as Fe-Mn-Mg carbonate phases or Kutnahorite in non-vent settings (Pena et al., 2005), and according to our results from modern seeps occur rapidly after the death of

the specimen on a synsedimentary timescale. Apart from the temporal factor, at least more than 50% of the original test would have to be recrystallized or the same amount would have to be added by authigenic carbonate growth inside the test to yield a $\delta^{13}\text{C}$ signal between -20 and -32 ‰, like observed during MVE'S (Fig. 3). According to our observations, this is not the case. The different shape of the isotopes curves, the Mg/Ca ratios of *U. peregrina*, and the coincident occurrence of isotope anomalies over large distances in two cores, plus the heavily depleted $\delta^{13}\text{C}$ values cannot be solely derived from diagenetic causes that are temporally unrelated the original MVE.

In summary, we conclude that an original methane-derived $\delta^{13}\text{C}$ signal exists in the foraminifera, an assumption which is also supported by the occurrence of negative anomalies in other cores at the same time rather than at comparable sediment depths or pore-water gradients, and in cores unaffected by methane venting. However, to follow a conservative approach, we do not use the observed absolute $\delta^{13}\text{C}$ values from Cores GE99-24 or S0178-26 within the GCSA for budget calculations or infer a direct relationship to the amount of discharged methane from them.

5.4. Constraints on budget calculations

Some estimate contributions to the atmospheric methane budget from submarine gas hydrate dissociation events (e.g.

de Garidel-Thoron et al., 2004; Kennett et al., 2000; Millo et al., 2005a). However, most of these calculations suffer from large uncertainties, caused by unconstrained assumptions about event duration, laterally affected areas, $\delta^{13}\text{C}$ endmembers of methane and DIC, diagenesis, etc. In most cases it was assumed from the analysis of a single site that the methane discharge affected a certain larger ocean area or a regional basin and a more or less uniformly methane-enriched water column (de Garidel-Thoron et al., 2004; Kennett et al., 2000; Millo et al., 2005a). In contrast, all studies on modern seeps and gas-hydrate provinces show that all these factors are highly variable on a spatially small scale, often within a few hundred meters within a seep area or directly above a vent site (Heeschen et al., 2005; Heeschen et al., 2003; Obzhirov et al., 2002; Sommer et al., 2006; Torres et al., 2002; Wallmann et al., 1997; Yoshida et al., 2004)

In consequence, we are hesitant to use $\delta^{13}\text{C}$ of foraminifera to calculate release budgets or to estimate the amount of methane released into the water column or even atmosphere during the MVE's. These uncertainties persist no matter if dissociations of gas hydrates or methane release by cold seeps are considered as the cause, with the latter being largely not discussed as a alternative cause for anomalies (Hill et al., 2004a; Kennett et al., 2000; Millo et al., 2005a; Smith et al., 2001; Uchida et al., 2004).

In our case we have some constraints on the lateral extent of the observed anomalies (NE and E Sakhalin continental margin). The average anomaly we observe in the mixed layer is around -1 ‰, affects a water depth of 0-250 m, as we found no anomalies in the bottom waters, and has an endmember $\delta^{13}\text{C}_{\text{CH}_4}$ value of around -45‰ (from measurements of $\delta^{13}\text{C}_{\text{CH}_4}$ and $\delta^{13}\text{C}$ of authigenic carbonates and $\delta^{13}\text{C}_{\text{CH}_4}$, K. Wallmann, pers. comm.). We set the background $\delta^{13}\text{C}_{\text{DIC}}$ value to 0 ‰, derived from modern water sample DIC measurements, assuming constant behaviour in a first-order approximation during the Holocene. The affected area is about 15,000 km², assuming a 50 km wide corridor between the core locations and about 300 km between the southernmost core LV28-4 and the Obzhirov Flare GCSA. We thus arrive at a volume of water affected by an average MVE of about 3000 km³. A simple mass-balance calculation (assuming DIC concentration of 2.3 $\mu\text{M kg}^{-1}$) then gives us an amount of about 1.5 Teragram (Tg) \pm 1 Tg of CH₄ that could dissociate to a certain extent into the atmosphere. This value is on the same order of magnitude of previous estimates (de Garidel-Thoron et al., 2004; Kennett et al., 2000). These studies took estimated event durations of one or more decades, in line with our chronologies. Depending on the duration and residence times in the water column, we theoretically reach annual flux values between 5 and 20 Tg CH₄. Given that the global annual flux from submarine methane seeps is

estimated to be 20 Tg yr⁻¹ (Judd, 2004; Judd et al., 2002) and the global flux from all geological sources about 45 Tg yr⁻¹ (Kvenvolden and Rogers, 2005), these calculated values are unrealistically high. Thus, we again stress that these estimates are rough guesses to give an idea about the theoretically possible magnitude of the events. In reality a couple of undetermined factors influence the true amount of CH₄ that is released into the water column and the atmosphere, such as: CH₄ residence time in water, oxidation of CH₄ to CO₂ during transit, lateral extent of venting area, ocean - atmosphere mixing processes influenced by sea-ice cover and wind speed, etc. We could easily increase our results by arbitrarily tuning these factors. However with our more conservative estimates we stay with or below previous assumptions by others (Kennett et al., 2000; Millo et al., 2005a) and nonetheless arrive at considerable volumes of theoretically released CH₄. Consensus exists that principle Holocene atmospheric CH₄ concentrations are caused by changes in Northern hemisphere boreal and tropical wetlands (Blunier et al., 1995; Chappellaz et al., 1997; Kennett et al., 2003). We are thus left with assessing if MVE's like the ones reported here do have a discernable influence on the global or hemispheric CH₄ budget. A quick comparison with the GRIP atmospheric CH₄ reconstruction (Blunier et al., 1995) shows no obvious correlation (which we did not expect anyway) to the MVE. We

thus subtracted the long-term development of CH₄ (derived as a 20-point running average) from the actual data to better assess short-term variability in the GRIP CH₄ record. Short-term fluctuations with an amplitude of ca. 20-40 ppbv exist in the GRIP CH₄ record (Fig. 5) though some are often near or below the reported error uncertainty and the temporal resolution is rather coarse (± 20 ppbv at 2?, Chappellaz et al., 1997).

At this point, we can only speculate that if methane dissociation from submarine geological sources is indeed a detectable source of CH₄ to the atmosphere, like others assumed (Hill et al., 2004a; Hill et al., 2006; Kennett et al., 2000; Kennett et al., 2003), then some of the short-term spikes in the GRIP CH₄ record may in fact be caused by geological CH₄ emissions such as our MVE at the Sakhalin margin. Notably, a number of GRIP CH₄ maxima match most of our MVE observations and the required magnitude of a CH₄ source (20-40 ppbv) is in accord with our crude estimate of possibly released CH₄ during periods of extended venting.

20

5.5. Causes for variable methane discharge

We discard the possibility of increased nutrient contents in the upper sediment column and subsequent in situ production of CH₄ as consequence of organic matter degradation as cause for the MVE's. Diverse nutrient proxies from a variety of cores show no correlating maxima

during or prior to the MVE's (Tiedemann et al., subm.). Two causes for temporally variable releases of methane from the Sakhalin margin remain: One is dissociation of gas hydrates within the sediment due to changes in the pressure-temperature stability field (Dickens and Quinbyhunt, 1994). However, during the Holocene no significant pressure field changes should occur in absence of large eustatic sea-level changes, so we are left with temperature as variable factor. Warming of bottom water masses is the only possible cause for such changes. However, gas hydrates are still abundant in all cores discussed here, and no sufficient temperature changes can be inferred from the $\delta^{18}\text{O}$ of the benthic foraminifera during the anomaly intervals (Fig. 4). In fact, the changes in $\delta^{18}\text{O}$ values are not systematic and would be smaller than 1-2 °C, insufficient to trigger larger melting of gas hydrates in our setting (P. Tishshenko, pers. comm.). In addition, pore-water geochemistry (e.g. measurements of chlorinity) in nearby cores from the same flare area indicate that dissociating gas hydrates are at present not the cause for ongoing methane releases, but rather the supply of deeper gas bubbles to the upper sediment column (Dullo et al., 2004; Matveeva et al., 2003). So the emitted methane primarily stems from free gas of rather uncertain depth origin, ascending with fluids and in bubbles through the sediment column along fracture zones and fault lines. This methane

20

25

is then released into the water column through a large number of discrete seeps within the region (Ginsburg et al., 1993; Obzhirov et al., 2004; Shakirov et al., 2004). Thus, the most plausible cause for increased methane concentrations in the water column is a temporal and lateral increase in seep activity and area during the MVE's.

We hypothesize that increases in seismo-tectonic activity affect the strength and distribution of the abundant gas seeps that are almost exclusively located along the East Sakhalin and West Derugin Shear Zones and the related fault systems on the Sakhalin continental margin (Fig. 1, Baranov et al., 2002; Shakirov et al., 2004). Seismo-tectonic activation of these fault systems leads to a joint increase in activity at submarine seeps and onshore mud volcanoes on Sakhalin as observed e.g. around the 1995 Neftegorsk City earthquake or the Sakhalin earthquake in summer 2001 (Obzhirov et al., 2004; Shakirov et al., 2004). The same processes have likely lead to large-scale increases in methane venting during the last 7,000 yr BP. times East Sakhalin Shear Zone during this period is responsible for enhanced methane discharge from the seep area.

Direct palaeo-seismological data to constrain this hypothesis are scarce in this region for the Holocene, pre-historical time period. We thus surveyed some datasets from rather heterogenous and more distant sources (e.g. volcanic

activity, palaeo-tsunamis, rapid local sea-level changes) that may be partly hampered by uncertain dating issues, regional ascription of individual events to large-scale seismo-tectonic patterns, local or regional significance, etc. (Bourgeois et al., 2006; Pinegina et al., 2003). We found no sufficient palaeo-data available about seismo-tectonic activity within the Okhotsk Sea or on Sakhalin.

In this light, probably the best sources are reconstructions of palaeo-tsunami activity at nearby coasts in Kamchatka and Japan (Bourgeois et al., 2006; Nanayama et al., 2003; Pinegina et al., 2003), which are thought to occur as result of large regional earthquakes along the Kuril-Kamchatka island arc. In addition, we use data about rapid uplifts in coastal regions of Hokkaido, Japan (e.g. Sawai and Nasu, 2005; Sawai et al., 2002) caused by tectonic movements and connected tectonically to Sakhalin along the West-Sakhalin Shear Zone and the Hokkaido-Sakhalin Shear Zone (Baranov et al., 2002; Shakirov et al., 2004). We also added a single record of large-scale debris avalanches triggered by volcanic activity at Shiveluch Volcano, Kamchatka to this compilation (Belousov et al., 1999; Ponomareva et al., 1998). Though connections to regional tectonic activity at the Sakhalin margin may be not directly proven, we assume that periods of large earthquakes may indicate a tectonically more active regime within the whole region. The lack of adequate proxy or

reference records for palaeo-seismo-tectonics made us include as diverse datasets as possible into our comparison but should be only regarded as a first order approximation as to whether fluid discharges on the Sakhalin margin do bear any correlation to the regional tectonic activity during the Holocene.

In fact, a striking temporal coincidence exists between the large MVE 3–5 we recorded directly at Obzhirov Flare and a three- to fourfold increase in the statistical abundance of large tsunami deposits at the Kamchatka Pacific coast between 1,000 and 2,000 yr BP (Fig. 6d, Pinegina et al., 2003) that indicate increased regional tectonic activity. A second maximum in tsunami deposits at NW-Pacific sites of (Pinegina et al., 2003) is between 3,000 and 4,000 yr BP, coincident with MVE 7 (and 8). However these tsunami frequencies are statistically averaged to 1,000 year-intervals, precluding a precise correlation. More specifically, significant increases in tsunami deposits occur at the Kamchatka margin in the Bering Sea in two key locations. At the time of MVE 4, the number of tsunami deposits per thousand years doubles between 1,000 and 1,500 yr BP at Cape Ozernol and and triples between 1,500 and 1,800 yr BP in the Soldatatskaya region (fig. 6c, Bourgeois et al., 2006). A second, smaller peak in the tsunami frequency at Soldatatskaya region likely matches the standardized record of (Pinegina et al., 2003) at 3,600 and

4,000 yr BP and is temporally coincident with MVE 7 and 8 (Fig. 6c).

In line with these observations, we note the most prominent occurrence of large debris avalanches at Shiveluch Volcano during the past 7,000 yr BP is between about 1,300 and 1,950 yr BP (events number VII to XI in: Belousov et al., 1999, report slightly different events, however; Ponomareva et al., 1998), at the same time of MVE 3, 4, and possibly 5 (fig.6). Over the entire range of our records, the Shiveluch volcano debris avalanche events VI to III exactly match our MVE 6 to 9 (Fig. 6e), and avalanche event I and II as well match MVE 13 at about 6,500 yr BP. MVE 1 is temporally not so well constrained, but is recorded in core SO26 and LV29–78 quite distinctly, and resembles Shiveluch avalanche XIII at 475–640 yr BP.

In the Hokkaido–N' Japan region, adjacent to the Okhotsk Sea, records of AMS ¹⁴C-dated, unusually large tsunami deposits (Nanayama et al., 2003), and emergence events on Hokkaido island (Sawai, 2001; Sawai and Nasu, 2005; Sawai et al., 2002) serve as second set of independent data for comparison. The former were caused by plate-boundary earthquakes at the Japan, Kuril, and Kamchatka trenches and likely ruptured multiple plate segments of 100–200 km length (Nanayama et al., 2003). The latter differ in some parts in timing to the tsunami records, but are based on other sedimentary settings and methods. Likewise, they are

thought to result from unusually large interplate earthquakes along the southwestern part of the Kuril subduction zone (Sawai and Nasu, 2005). Together these records match a surprisingly high number of MVE events at the Sakhalin margin (fig. 6 f and g), specifically MVE 1 to 4, 6 to 8, and 10 and 13. One has to consider that the ages in (Nanayama et al., 2003) are maximum ages of dated tsunami deposits and that the emergence records stretch only back to about 4,500 yr BP (Sawai and Nasu, 2005) so far. Thus precise information about the older part may be patchy and not well constrained as is also admittedly the case for the tsunami deposit records from Kamchatka (Bourgeois et al., 2006; Pinegina et al., 2003). However, as a reassurance (Nanayama et al., 2003) calculated an average recurrence interval of about 500 yr for large multisegment earthquakes, which is in agreement with average recurrence of MVE during the past 6,500 to 7,000 yr in the Okhotsk Sea.

Only three MVE, number 11, 12, and possibly 5, show no correlation to any major tectonic event from the records we compiled. These may have been more localized events in the Sakhalin region, for which we do not have any records available or less intense events in the Hokkaido-Kuril-Kamchatka region not discovered so far.

25

6. Conclusions

In sediment cores we retrieved from a Giant Cold Seep Area (GCSA) off NE Sakhalin island with prominent methane venting from more than 200 gas seeps, we observe largely original, negative $\delta^{13}\text{C}$ anomalies in multi-species benthic and planktic foraminifera time-series, unreported so far in this magnitude and detail from other locations. We ascribe these depletions in foraminiferal $\delta^{13}\text{C}$ to periods of enhanced methane venting during the last 7,000 yr BP, according to AMS ^{14}C -derived timescales for the cores. The depleted $\delta^{13}\text{C}$ signals are a mixture of primary $\delta^{13}\text{C}$ -depleted methane-derived carbon, incorporated into the test, and of thin secondary authigenic carbonate layers that crystallised mostly on the inside of tests. The magnitude of $\delta^{13}\text{C}$ depletions and the type of carbonate crystallisations makes it likely that the secondary calcite was precipitated synsedimentary with an incorporation of primary calcite, within the errors of the temporal resolution.

We find according negative $\delta^{13}\text{C}$ minima of about -0.5 ‰ to -1 ‰ in the planktic foraminiferal records of two other distant sediment cores located in the downstream region of the GCSA, outside methane seep areas. This indicates that the CH_4 venting events were large and massive enough to get transported further south with currents and get recorded on a regional scale in the mixed-layer (50-200 m water depth)

25

planktic *N. pachyderma (s)* and *G. bulloides*, in agreement with modern observations about lateral displacements of methane anomaly layers in the water column in the Okhotsk Sea. In total, we found evidence for thirteen Methane Venting Events (MVE) during the past 7,000 yr BP.

The most likely cause for these excursions are large temporal changes in the venting activity of the GCSA at the NE Sakahlin margin. Supported by recent observations (Obzhirov et al., 2004; Obzhirov et al., 2002; Shakirov et al., 2004) and with no other critical factors at hand that display relevant changes in the pressure-temperature stability field of gas hydrates, we assign the cause for these methane venting variations to large-scale changes in seismo-tectonic activity of the Japan-Kuril-Kamchatka trench system and its connected fault zones that extend into the Okhotsk Sea. The most prominent MVE 4 (or 3–5, sensu lato) correlate with increased tsunami activity at the Kamchatka coasts at about 1,200 and 1,800 yr BP. Most single MVE are correlated with distinct intervals of increased tectonic activity on Hokkaido island and Kamchatka as indicated by tsunami deposits, volcanic activity, and emergence events (Nanayama et al., 2003; Ponomareva et al., 1998; Sawai and Nasu, 2005). Notably, the mean recurrence interval for large tsunami events recorded in northern Japan is about 500 yr (Nanayama et al., 2003) and resembles the average recurrence interval of

the MVE's in the Okhotsk Sea. All records still suffer from chronological uncertainties and data gaps so far. However, the hypothesized coupling between a large-scale tectonic regime and variable methane emissions from natural sources on long time scales warrants further study, given the implications it may have on variable global gas fluxes on active continental margins and the according budget calculations used in determining causes for natural greenhouse gas variability.

10

Acknowledgements

We thank masters and crews of R/V Akademik Lavrentiev, R/V Marshal Gelovany, and R/V SONNE, as well as the respective shipboard scientific parties for their expertise and professional support during the cruises. We are indebted to S. Fessler, J. Heinze, and L. Haxhiaj for technical assistance, and we thank N. Stange for sample preparation and laboratory work. We acknowledge the funding of the projects KOMEX I and II, and KOMEX-SONNE178 by the German Federal Ministry for Education and Research (BMBF grants KOMEX II and SO178-KOMEX). LLJ and W-CD also acknowledge funding through DFG fund Du129/33 (Leibniz Award). We thank Tessa M. Hill and James P. Kennett for helpful comments on an earlier version of this work.

25

References

Archer, D. and Buffett, B., 2005. Time-dependent response of the global ocean clathrate reservoir to climatic and anthropogenic forcing. *Geochemistry Geophysics Geosystems*, 6.

Baranov, B.V. et al., 2002. Evidence for compressionally induced high subsidence rates in the Kurile Basin (Okhotsk Sea). *Tectonophysics*, 350: 63-97.

Bauch, D., Erlenkeuser, H., Winckler, G., Pavlova, G. and Thiede, J., 2002. Carbon isotopes and habitat of polar planktic foraminifera in the Okhotsk Sea: the 'carbonate ion effect' under natural conditions. *Marine Micropaleontology*, 871: 1-17.

Belousov, A., Belousova, M. and Voight, B., 1999. Multiple edifice failures, debris avalanches and associated eruptions in the Holocene history of Shiveluch volcano, Kamchatka, Russia. *Bulletin of Volcanology*, 61(5): 324-342.

Biebow, N., Kulinich, R. and Baranov, B. (Editors), 2002. Cruise Report R/V Akademik Lavrentiev Cruise LV29. GEOMAR Reports. GEOMAR Research Center for Marine Geosciences, Kiel, 190 pp.

Blunier, T., Chappellaz, J., Schwander, J., Stauffer, B. and Raynaud, D., 1995. Variations in Atmospheric Methane Concentration During the Holocene Epoch. *Nature*, 374(6517): 46-49.

Bourgeois, J., Pinegina, T.K., Ponomareva, V. and Zaretskaia, N., 2006. Holocene tsunamis in the southwestern Bering Sea, Russian Far East, and their tectonic implications. *Geological Society of America Bulletin*, 118(3-4): 449-463.

Brook, E.J., Harder, S., Severinghaus, J., Steig, E.J. and Sucher, C.M., 2000. On the origin and timing of rapid changes in atmospheric methane during the last glacial period. *Global Biogeochemical Cycles*, 14(2): 559-572.

Buffett, B. and Archer, D., 2004. Global inventory of methane clathrate: sensitivity to changes in the deep ocean. *Earth and Planetary Science Letters*, 227(3-4): 185-199.

Cannariato, K.G. and Stott, L.D., 2004. Evidence against clathrate-derived methane release to Santa Barbara Basin surface waters? *Geochemistry Geophysics Geosystems*, 5.

Chappellaz, J., Barnola, J.M., Raynaud, D., Korotkevich, Y.S. and Lorius, C., 1990. Ice-Core Record of Atmospheric Methane over the Past 160,000 Years. *Nature*, 345(6271): 127-131.

Chappellaz, J. et al., 1997. Changes in the atmospheric CH₄ gradient between Greenland and Antarctica during the Holocene. *Journal of Geophysical Research-Atmospheres*, 102(D13): 15987-15997.

Dafner, E., Obzhairov, A. and Vereshzhagina, O., 1998. Distribution of methane in waters of the Okhotsk and western Bering Seas, and the area of the Kuril Islands. *Hydrobiologia*, 362: 93-101.

5 Dallenbach, A. et al., 2000. Changes in the atmospheric CH₄ gradient between Greenland and Antarctica during the Last Glacial and the transition to the Holocene. *Geophysical Research Letters*, 27(7): 1005-1008.

de Garidel-Thoron, T., Beaufort, L., Bassinot, F. and
10 Henry, P., 2004. Evidence for large methane releases to the atmosphere from deep-sea gas-hydrate dissociation during the last glacial episode. *Proceedings of the National Academy of Sciences of the United States of America*, 101(25): 9187-9192.

15 Dickens, G.R., 1999. Carbon cycle - The blast in the past. *Nature*, 401(6755): 752-+.

Dickens, G.R., 2004. Global change - Hydrocarbon-driven warming. *Nature*, 429(6991): 513-515.

Dickens, G.R. and Quinbyhunt, M.S., 1994. Methane Hydrate
20 Stability in Seawater. *Geophysical Research Letters*, 21(19): 2115-2118.

Dickens, G.R. and QuinbyHunt, M.S., 1997. Methane hydrate stability in pore water: A simple theoretical approach for geophysical applications. *Journal of Geophysical
25 Research-Solid Earth*, 102(B1): 773-783.

Dullo, W.-C., Biebow, N. and Georgeleit, K. (Editors), 2004. SO178-KOMEX Cruise Report - Mass exchange processes and balances in the Okhotsk Sea. IFM-GEOMAR Reports. IFM-GEOMAR, Kiel, 125 pp.

5 Etiope, G. and Milkov, A.V., 2004. A new estimate of global methane flux from onshore and shallow submarine mud volcanoes to the atmosphere. *Environmental Geology*, 46(8): 997-1002.

Ferretti, D.F. et al., 2005. Unexpected changes to the
10 global methane budget over the past 2000 years. *Science*, 309(5741): 1714-1717.

Gaedicke, C. et al., 1997. Seismic stratigraphy, BSR distribution, and venting of methane-rich fluids west off Paramushir and Onkotan Islands, northern Kurils.
15 *Marine Geology*, 136(3-4): 259-276.

Ginsburg, G.D., Soloviev, V.A., Cranston, R.E., Lorenson, T.D. and Kvenvolden, K.A., 1993. Gas Hydrates from the Continental-Slope, Offshore Sakhalin Island, Okhotsk Sea. *Geo-Marine Letters*, 13(1): 41-48.

20 Greinert, J., Bohrmann, G. and Suess, E., 2001. Gas Hydrate-Associated Carbonates and Methane-Venting at Hydrate Ridge: Classification, Distribution and Origin of Authigenic Lithologies. In: C.K. Paull and W.P. Dillon (Editors), *Natural Gas Hydrates: Occurrences,
25 Distribution, and Detection*. *Geophysical Monograph*

Series. American Geophysical Union, Washington, DC, pp. 99-114.

Greinert, J., Bollwerk, S.M., Derkachev, A., Bohrmann, G. and Suess, E., 2002. Massive barite deposits and carbonate mineralization in the Derugin Basin, Sea of Okhotsk: precipitation processes at cold seep sites. *Earth and Planetary Science Letters*, 203(1): 165-180.

Greinert, J. and Derkachev, A., 2004. Glendonites and methane-derived Mg-calcites in the Sea of Okhotsk, Eastern Siberia: implications of a venting-related ikaite/glendonite formation. *Marine Geology*, 204(1-2): 129-144.

Heeschen, K.U. et al., 2005. Methane sources, distributions, and fluxes from cold vent sites at Hydrate Ridge, Cascadia Margin. *Global Biogeochemical Cycles*, 19(2).

Heeschen, K.U., Trehu, A.M., Collier, R.W., Suess, E. and Rehder, G., 2003. Distribution and height of methane bubble plumes on the Cascadia Margin characterized by acoustic imaging. *Geophysical Research Letters*, 30(12).

Hill, T.M., Kennett, J.P. and Spero, H.J., 2004a. High-resolution records of methane hydrate dissociation: ODP Site 893, Santa Barbara Basin. *Earth and Planetary Science Letters*, 223(1-2): 127-140.

Hill, T.M., Kennett, J.P. and Valentine, D.L., 2004b. Isotopic evidence for the incorporation of methane-derived carbon into foraminifera from modern methane seeps, Hydrate Ridge, Northeast Pacific. *Geochimica Et Cosmochimica Acta*, 68(22): 4619-4627.

Hill, T.M. et al., 2006. Climatically driven emissions of hydrocarbons from marine sediments during deglaciation. *Proceedings of the National Academy of Sciences of the United States of America*, 103(37): 13570-13574.

Hovland, M. and Judd, A.G., 1992. The Global Production of Methane from Shallow Submarine Sources. *Continental Shelf Research*, 12(10): 1231-1238.

Judd, A.G., 2003. The global importance and context of methane escape from the seabed. *Geo-Marine Letters*, 23(3-4): 147-154.

Judd, A.G., 2004. Natural seabed gas seeps as sources of atmospheric methane. *Environmental Geology*, 46(8): 988-996.

Judd, A.G., Hovland, M., Dimitrov, L.I., Gil, S.G. and Jukes, V., 2002. The geological methane budget at Continental Margins and its influence on climate change. *Geofluids*, 2(2): 109-126.

Kennett, J.P., Cannariato, K.G., Hendy, I.L. and Behl, R.J., 2000. Carbon isotopic evidence for methane

hydrate instability during quaternary interstadials.
Science, 288(5463): 128-133.

Kennett, J.P., Cannariato, K.G., Hendy, I.L. and Behl,
R.J., 2003. Methane Hydrates in Quaternary Climate
5 Change - The Clathrate Gun Hypothesis. American
Geophysical Union, Washington, DC, 216 pp.

Kvenvolden, K.A., 2002. Methane hydrate in the global
organic carbon cycle. Terra Nova, 14(5): 302-306.

Kvenvolden, K.A. and Rogers, B.W., 2005. Gaia's breath -
10 global methane exhalations. Marine and Petroleum
Geology, 22(4): 579-590.

Lammers, S., Suess, E., Mansurov, M.N. and Anikiev, V.V.,
1995. Variations of Atmospheric Methane Supply from
the Sea-of-Okhotsk Induced by the Seasonal Ice Cover.
15 Global Biogeochemical Cycles, 9(3): 351-358.

Ludmann, T. and Wong, H.K., 2003. Characteristics of gas
hydrate occurrences associated with mud diapirism and
gas escape structures in the northwestern Sea of
Okhotsk. Marine Geology, 201(4): 269-286.

20 Mackensen, A., Wollenburg, J. and Licari, L., 2006. Low
delta C-13 in tests of live epibenthic and endobenthic
foraminifera at a site of active methane seepage.
Paleoceanography, 21(2).

Malone, M.J., Claypool, G., Martin, J.B. and Dickens, G.R.,
25 2002. Variable methane fluxes in shallow marine
systems over geologic time - The composition and

origin of pore waters and authigenic carbonates on the
New Jersey shelf. Marine Geology, 189(3-4): 175-196.

Martin, J.B. et al., 2004. Relationships between the stable
isotopic signatures of living and fossil foraminifera
5 in Monterey Bay, California. Geochemistry Geophysics
Geosystems, 5.

Maslin, M., Mikkelsen, N., Vilela, C. and Haq, B., 1998.
Sea-level- and gas-hydrate-controlled catastrophic
sediment failures of the Amazon Fan. Geology, 26(12):
10 1107-1110.

Maslin, M., Owen, M., Day, S. and Long, D., 2004. Linking
continental-slope failures and climate change: Testing
the clathrate gun hypothesis. Geology, 32(1): 53-56.

Matveeva, T. et al., 2003. Geochemistry of gas hydrate
15 accumulation offshore NE Sakhalin Island (the Sea of
Okhotsk): results from the KOMEX-2002 cruise. Geo-
Marine Letters, 23(3-4): 278-288.

Milkov, A.V., 2000. Worldwide distribution of submarine mud
volcanoes and associated gas hydrates. Marine Geology,
20 167(1-2): 29-42.

Milkov, A.V., 2004. Global estimates of hydrate-bound gas
in marine sediments: how much is really out there?
Earth-Science Reviews, 66(3-4): 183-197.

Milkov, A.V. and Etiope, G., 2005. Global methane emission
25 through mud volcanoes and its past and present impact

on the Earth's climate—a comment. *International Journal of Earth Sciences*, 94(3): 490–492.

Millo, C., Sarnthein, M., Erlenkeuser, H. and Frederichs, T., 2005a. Methane-driven late Pleistocene delta C-13 minima and overflow reversals in the southwestern Greenland Sea. *Geology*, 33(11): 873–876.

Millo, C., Sarnthein, M., Erlenkeuser, H., Grootes, P.M. and Andersen, N., 2005b. Methane-induced early diagenesis of foraminiferal tests in the Southwestern Greenland Sea. *Marine Micropaleontology*, 58(1): 1–12.

Nanayama, F. et al., 2003. Unusually large earthquakes inferred from tsunami deposits along the Kuril trench. *Nature*, 424(6949): 660–663.

Nisbet, E.G., 1992. Sources of Atmospheric CH₄ in Early Postglacial Time. *Journal of Geophysical Research-Atmospheres*, 97(D12): 12859–12867.

Nisbet, E.G., 2002. Have sudden large releases of methane from geological reservoirs occurred since the Last Glacial Maximum, and could such releases occur again? *Philosophical Transactions of the Royal Society of London Series a-Mathematical Physical and Engineering Sciences*, 360(1793): 581–607.

Obzhairov, A. et al., 2004. Relations between methane venting, geological structure and seismo-tectonics in the Okhotsk Sea. *Geo-Marine Letters*, 24(3): 135–139.

Obzhairov, A.I., Astakhov, A.S. and Astakhova, N.V., 2000. Genesis and conditions of formation of authigenous carbonates in the quaternary sedimentary cover in the region of the Sakhalin-Deryugin gas anomaly (Sea of Okhotsk). *Oceanology*, 40(2): 258–266.

Obzhairov, A.I. et al., 2002. Methane monitoring in waters of the eastern shelf and slope of Sakhalin. *Geologiya I Geofizika*, 43(7): 605–612.

Ohkushi, K., Ahagon, N., Uchida, M. and Shibata, Y., 2005. Foraminiferal isotope anomalies from northwestern Pacific marginal sediments. *Geochemistry Geophysics Geosystems*, 6.

Pena, L.D., Calvo, E., Cacho, I., Eggins, S. and Pelejero, C., 2005. Identification and removal of Mn-Mg-rich contaminant phases on foraminiferal tests: Implications for Mg/Ca past temperature reconstructions. *Geochemistry Geophysics Geosystems*, 6.

Petit, J.R. et al., 1999. Climate and atmospheric history of the past 420,000 years from the Vostok ice core, Antarctica. *Nature*, 399(6735): 429–436.

Pinegina, T.K., Bourgeois, J., Bazanova, L.I., Melekestsev, I.V. and Braitseva, O.A., 2003. A millennial-scale record of holocene tsunamis on the Kronotskiy Bay coast, Kamchatka, Russia. *Quaternary Research*, 59(1): 36–47.

Ponomareva, V.V., Pevzner, M.M. and Melekestsev, I.V.,
1998. Large debris avalanches and associated eruptions
in the Holocene eruptive history of Shiveluch Volcano,
Kamchatka, Russia. *Bulletin of Volcanology*, 59(7):
5 490-505.

Rathburn, A.E. et al., 2003. Relationships between the
distribution and stable isotopic composition of living
benthic foraminifera and cold methane seep
biogeochemistry in Monterey Bay, California.
10 *Geochemistry Geophysics Geosystems*, 4.

Sawai, Y., 2001. Episodic emergence in the past 3000 years
at the Akkeshi estuary, Hokkaido, northern Japan.
Quaternary Research, 56(2): 231-241.

Sawai, Y. and Nasu, H., 2005. A 4500-year record of
15 emergence events at Onnetoh, Hokkaido, northern Japan,
reconstructed using plant macrofossils. *Marine
Geology*, 217(1-2): 49-65.

Sawai, Y., Nasu, H. and Yasuda, Y., 2002. Fluctuations in
relative sea-level during the past 3000 yr in the
20 Onnetoh estuary, Hokkaido, northern Japan. *Journal of
Quaternary Science*, 17(5-6): 607-622.

Schaefer, H. et al., 2006. Ice record of delta C-13 for
atmospheric CH₄ across the Younger Dryas-Preboreal
transition. *Science*, 313(5790): 1109-1112.

Shakirov, R., Obzhairov, A., Suess, E., Salyuk, A. and
Biebow, N., 2004. Mud volcanoes and gas vents in the
Okhotsk Sea area. *Geo-Marine Letters*, 24(3): 140-149.

Smith, L.M., Sachs, J.P., Jennings, A.E., Anderson, D.M.
5 and deVernal, A., 2001. Light delta C-13 events during
deglaciation of the East Greenland continental shelf
attributed to methane release from gas hydrates.
Geophysical Research Letters, 28(11): 2217-2220.

Sommer, S. et al., 2006. Efficiency of the benthic filter:
10 Biological control of the emission of dissolved
methane from sediments containing shallow gas hydrates
at Hydrate Ridge. *Global Biogeochemical Cycles*, 20(2).

Sowers, T., 2006. Late Quaternary Atmospheric CH₄ Isotope
Records Suggests Marine Clathrates Are Stable.
15 *Science*, 311: 838-840.

Stott, L.D. et al., 2002. Does the oxidation of methane
leave an isotopic fingerprint in the geologic record?
Geochemistry Geophysics Geosystems, 3.

Torres, M.E. et al., 2002. Fluid and Chemical fluxes in and
20 out of sediments hosting methane hydrate deposits on
Hydrate Ridge, OR, I: Hydrological provinces. *Earth
and Planetary Science Letters*, 201: 525-540.

Torres, M.E. et al., 2003. Is methane venting at the
seafloor recorded by delta C-13 of benthic
25 foraminifera shells? *Paleoceanography*, 18(3).

- Torres, M.E. et al., 2004. Gas hydrate growth, methane transport, and chloride enrichment at the southern summit of Hydrate Ridge, Cascadia margin off Oregon. *Earth and Planetary Science Letters*, 226(1-2): 225-241.
- Uchida, M., Shibata, Y., Ohkushi, K., Ahagon, N. and Hoshihara, M., 2004. Episodic methane release events from Last Glacial marginal sediments in the western North Pacific. *Geochemistry Geophysics Geosystems*, 5.
- Wallmann, K. et al., 2006. Kinetics of organic matter degradation, microbial methane generation, and gas hydrate formation in anoxic marine sediments. *Geochimica Et Cosmochimica Acta*, 70(15): 3905-3927.
- Wallmann, K. et al., 1997. Quantifying fluid flow, solute mixing, and biogeochemical turnover at cold vents of the eastern Aleutian subduction zone. *Geochimica Et Cosmochimica Acta*, 61(24): 5209-5219.
- Wefer, G., Heinze, P.M. and Berger, W.H., 1994. Clues to Ancient Methane Release. *Nature*, 369(6478): 282-282.
- Yoshida, O., Inoue, H.Y., Watanabe, S., Noriki, S. and Wakatsuchi, M., 2004. Methane in the western part of the Sea of Okhotsk in 1998-2000. *Journal of Geophysical Research-Oceans*, 109(C9): C09S12, doi:10.1029/2003JC001910.

25

Figure captions:

Figure 1: Study area, red lines are schematic sketches of shear zones and fault systems mentioned in the text [as in \Shakirov, 2004 #6; Baranov, 2002 #141; Baranov, 2002 #368], H-S: Hokkaido-Sakhalin Shear Zone (SZ), ES: East-Sakhalin SZ, WS: West-Sakhalin SZ, CS: Central-Sakhalin SZ, WD: West-Derugin SZ. black dots: downstream sediment core stations. insert: high-resolution backscatter image of GCSA, red dots: sediment core stations of KOMEX II and KOMEX S0178, in red letters: sediment core stations discussed in text, in orange: sediment cores with comparable isotopic and lithological features [Biebow, 2002 #348; Dullo, 2004 #365].

Figure 2: Modern seep characteristics at GCSA. Small upper insert left: Hydroacoustic image of rising gas and bubbles at Obzhirov Flare. Below, left: photo of lowermost core section in GE99-24, white patches are lenticular gas hydrate layers (photo: courtesy of J. Greinert). Middle panel: Methane concentrations in the water column for Obzhirov and Giselle Flare. Note large bottom water anomalies and an CH₄-enriched layer at Giselle Flare (Blue) around 200 m water depth. Right panel: $\delta^{13}\text{C}$ values show no discernable depletions in the bottom water at Giselle flare

(blue), but a depletion of about -0.5 ‰ at Obzhirov Flare (red) in the lowermost bottom water samples. Black line: $\delta^{13}\text{C}_{\text{DIC}}$ profile from non-vent station in Derugin Basin for comparison.

Figure 3: Stable carbon isotope profiles from Core GE99-24, Obzhirov Flare, GCSA. Gray background shading: intervals of $\delta^{13}\text{C}$ minima. Foraminiferal species are ordered according to their habitat: *N. pachyderma* (s)-planktic; followed by benthic species from top to bottom with increasing microhabitat depth in sediment and increasing tolerance to low-oxygen conditions.

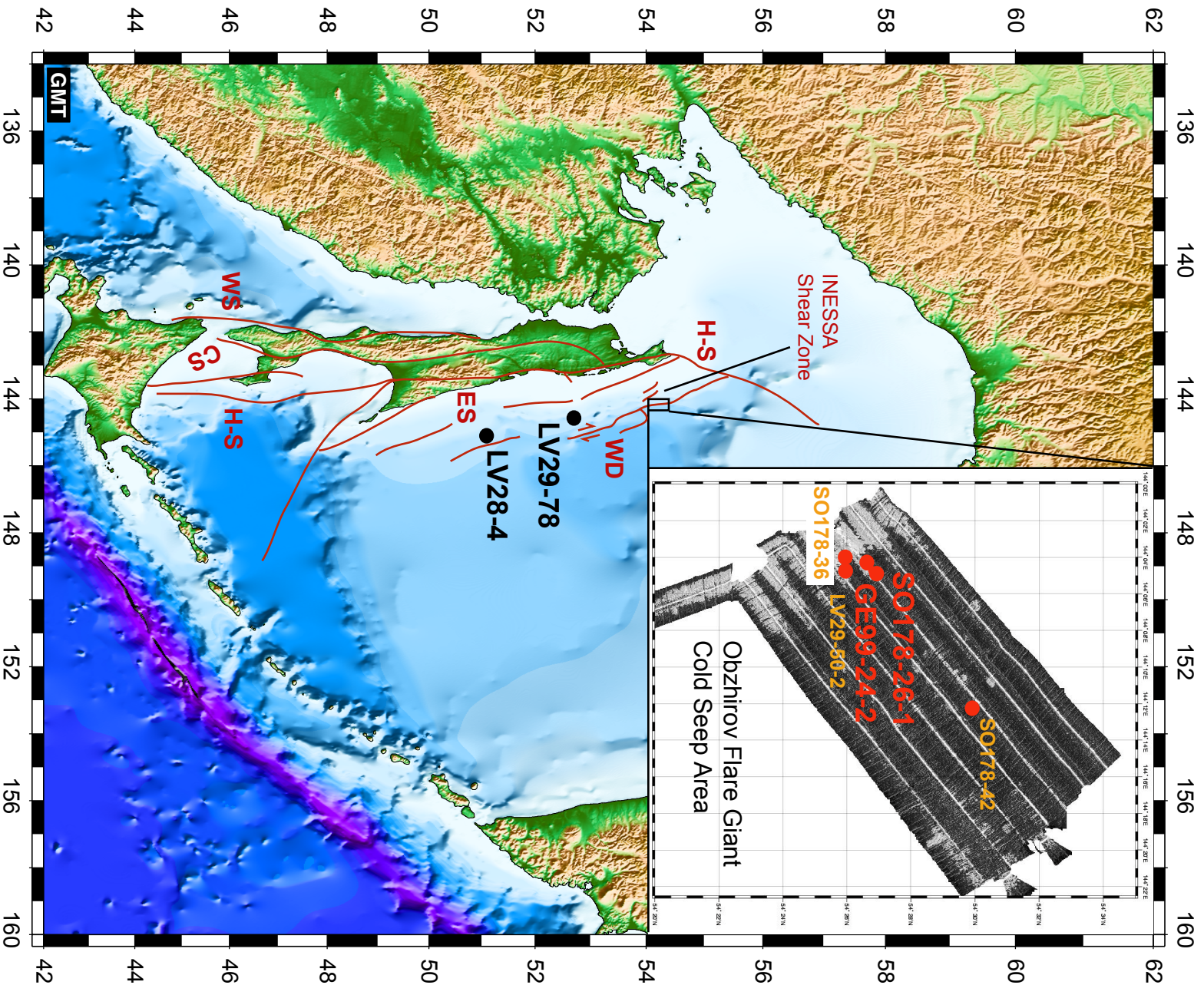
Figure 4: $\delta^{18}\text{O}$ profiles from core GE99-24. Order of species and time interval as in fig. 3. No direct connection between $\delta^{18}\text{O}$ and time intervals of increased CH₄ venting is evident that might indicate either temporally dislocated diagenesis or warming of bottom waters. However, note single specimen minima in $\delta^{18}\text{O}$ values, especially between 1.8 and 2.0 kyr BP and 3.0 and 3.2 kyr BP that might indicate a diagenetic component in the carbonate test.

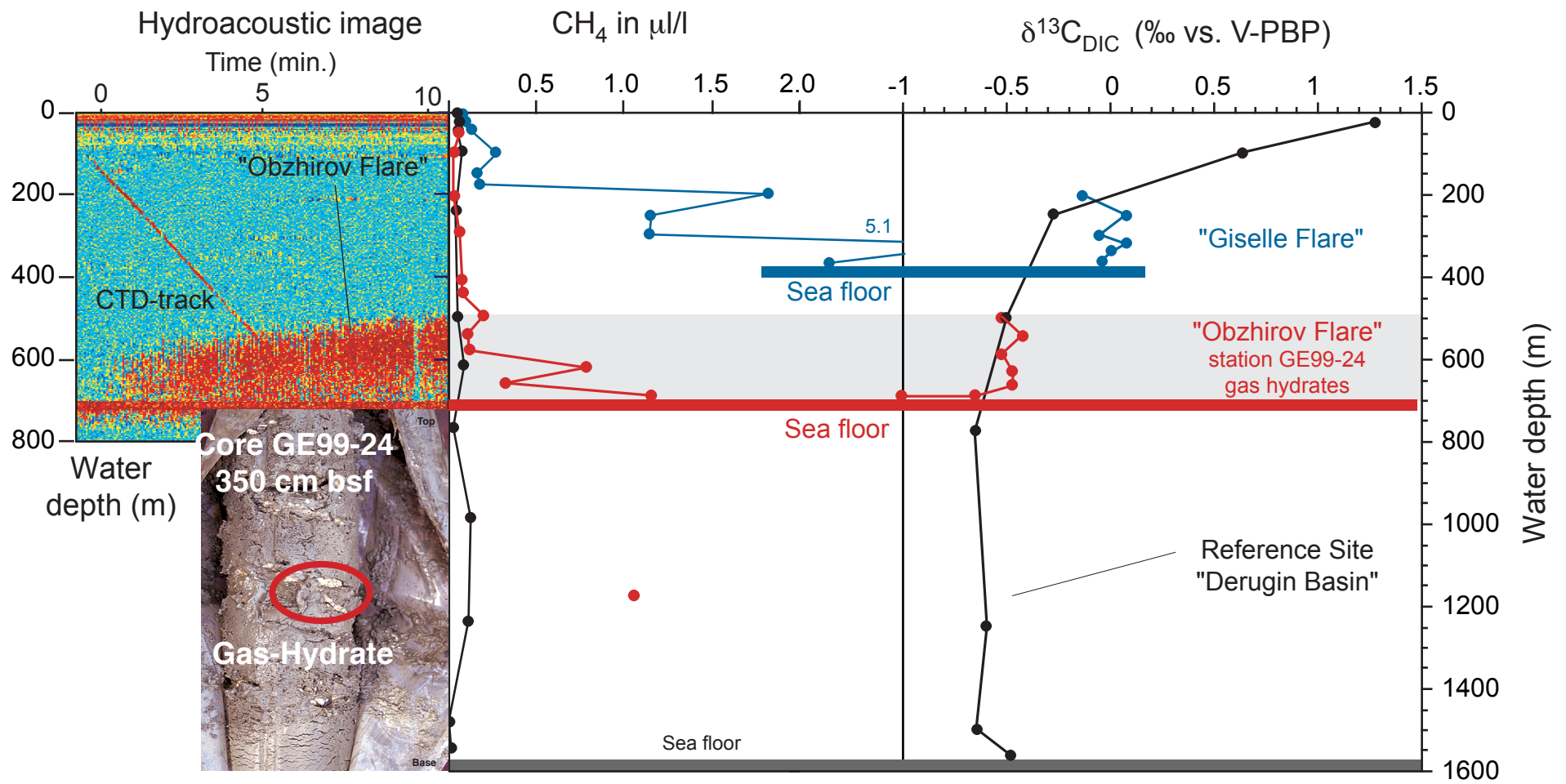
Figure 5: Compilation of regional $\delta^{13}\text{C}$ records from planktic foraminifera *N. pachyderma* (s), unless indicated otherwise. From top to bottom: Green - Core S0178-26, N' GCSA, sample intervals are larger and should be

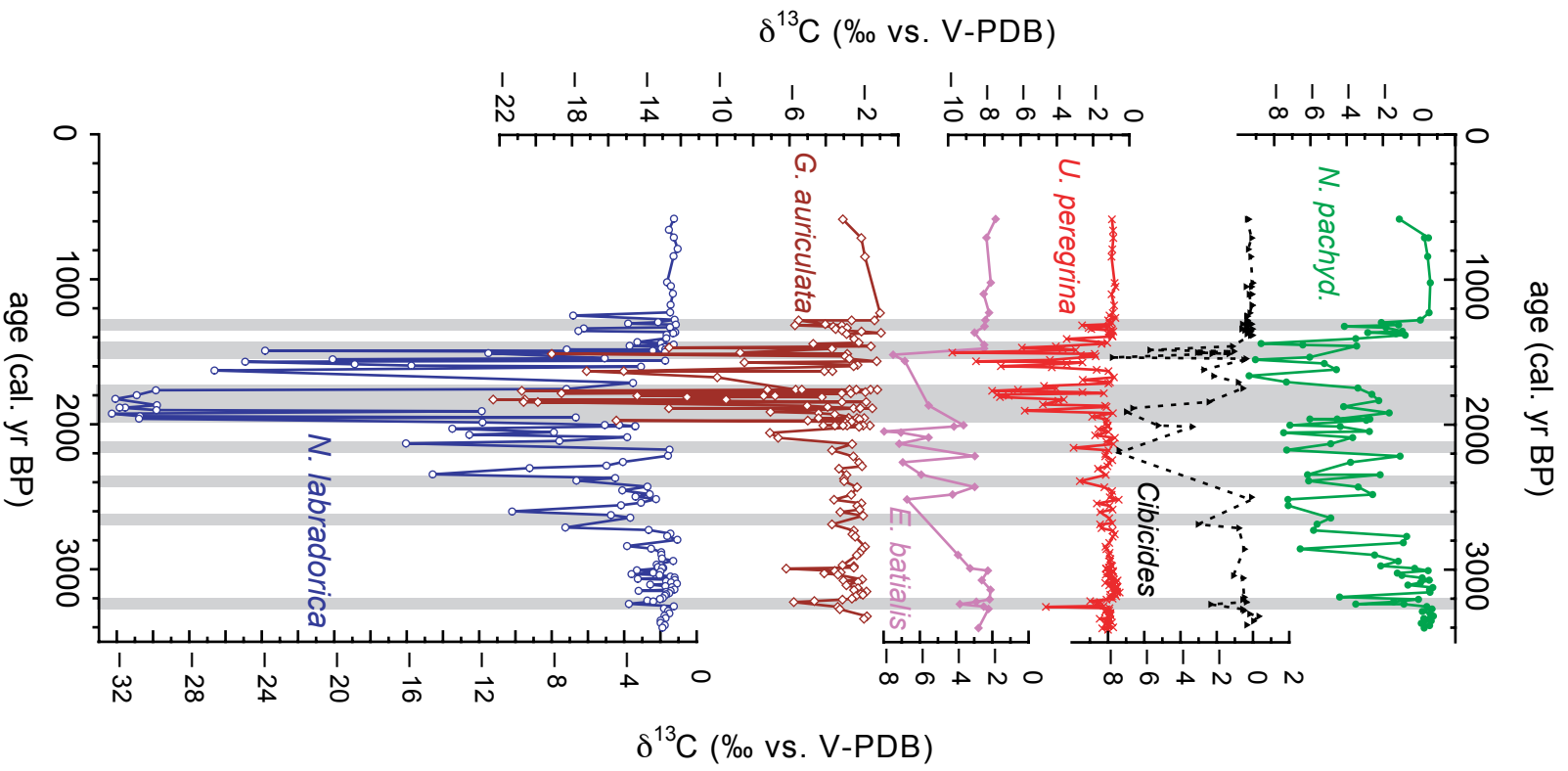
regarded as average values for the intervals. Red - Core GE99-24 E' Obzhirov Flare, 3-point smoothed record (fig. 3), light blue - Core LV29-78, NE' Sakhalin margin; purple - Core LV28-4, E' Sakhalin margin, upper pink curve is *G. bulloides* data which does not occur continuously during the Holocene in the Okhotsk Sea, thus the worse temporal resolution. *G. bulloides* has a slightly shallower habitat in the Okhotsk Sea and is presumed to calcify more during the earlier summer season, in contrast to *N. pachyderma* (autumn abundance maxima, Bauch et al. 2001, and own unpublished data). Dark blue - CH₄ concentrations of Greenland GRIP ice core (Blunier et al., 1995). We subtracted a 20-point running average from individual values to remove long-term trends, residuals are shown here. Black numbers the bottom are and gray bars indicate periods of inferred maxima in methane venting (i.e. $\delta^{13}\text{C}$ minima are detectable in more than an isolated record).

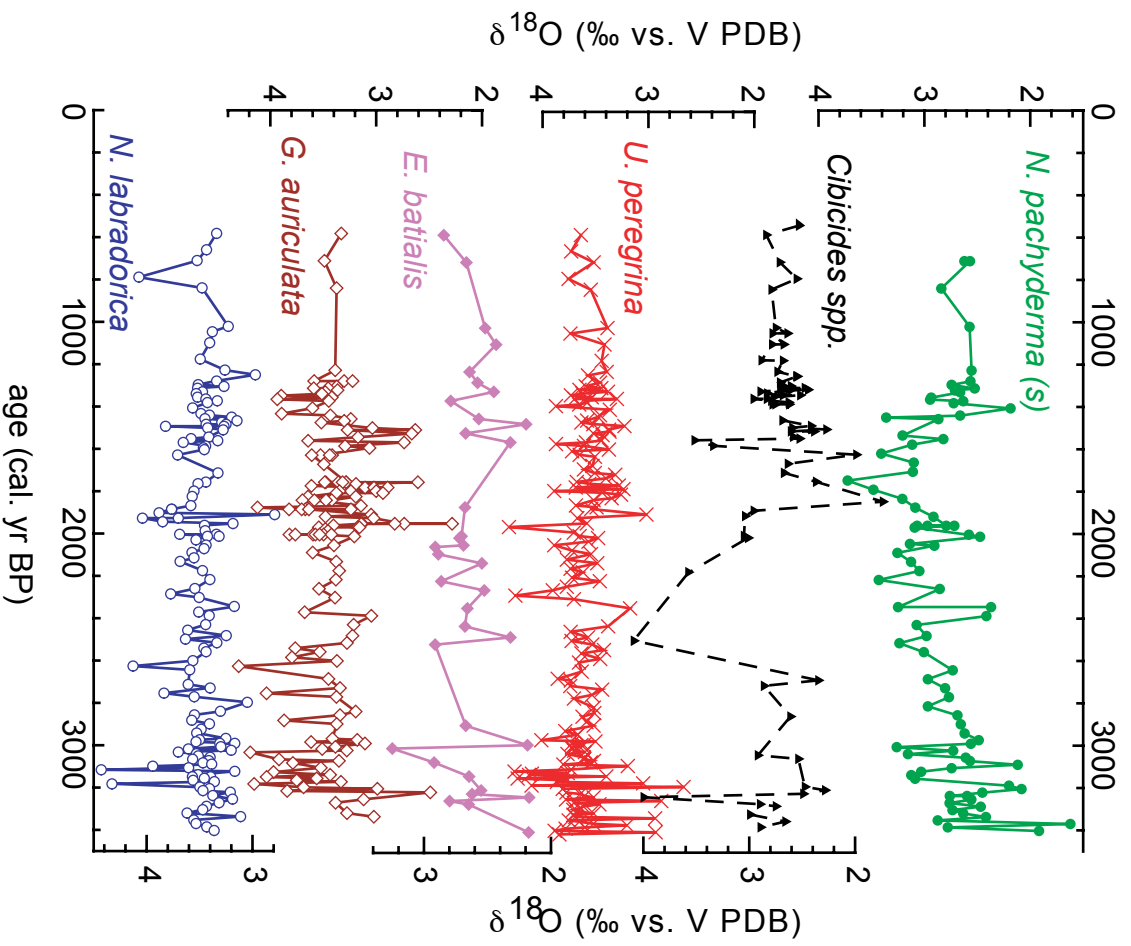
Figure 6: Compilation $\delta^{13}\text{C}$ data and different indicators for regional seismo-tectonic activity. a) Core GE99-24: *N. pachyderma* (s) 3-point smoothed $\delta^{13}\text{C}$ data as in fig. 5. b) Core GE99-24: *U. peregrina* 3-point smoothed $\delta^{13}\text{C}$ data. c) Calculated frequency of tsunami deposits at two locations at the Kamchatka coast in the Bering Sea, Red: Cape Ozernol, Blue: Soldatukaya

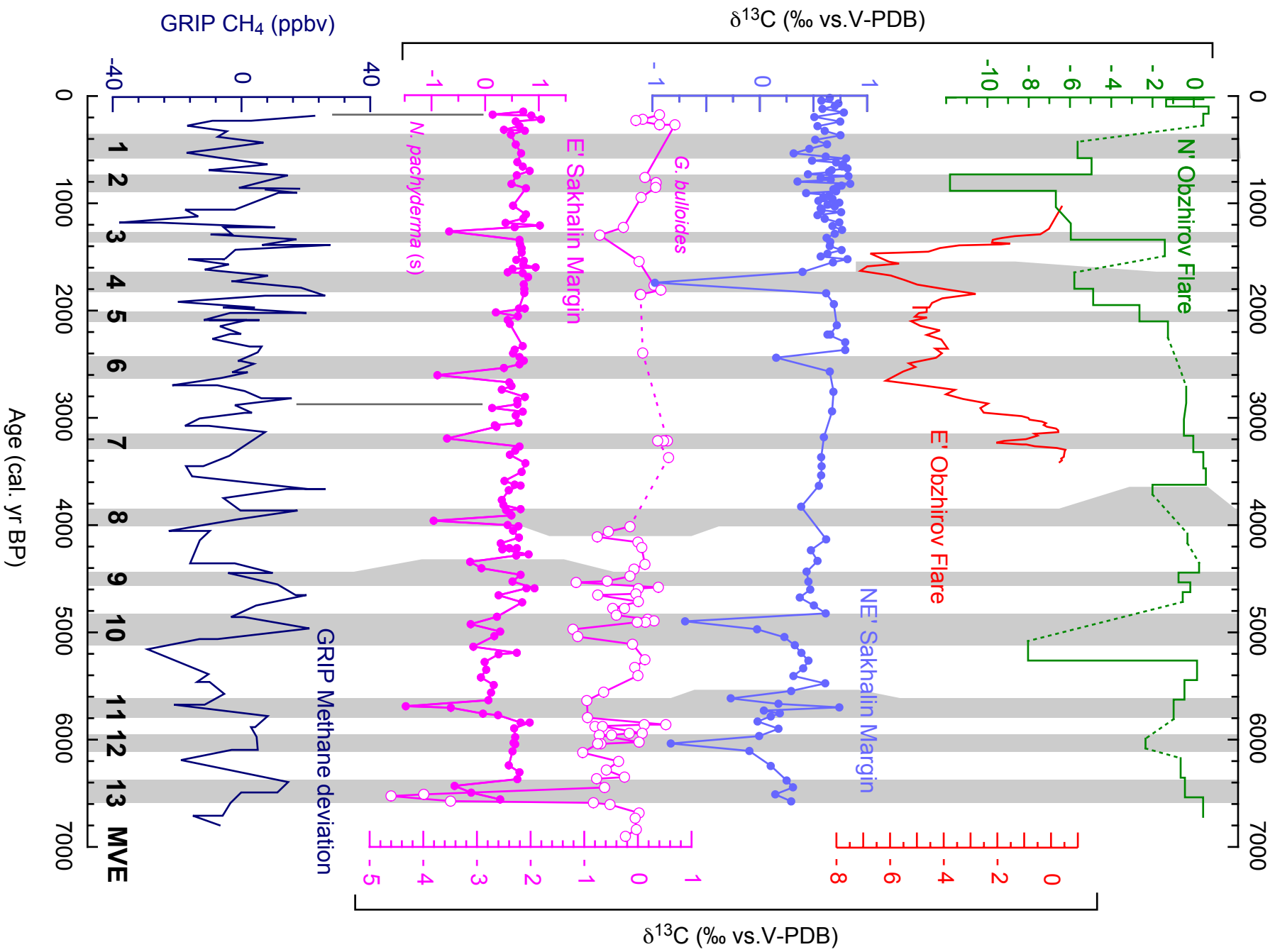
region. Frequency is given in number of tsunami deposits in 100 years for the last 4,000 years (data from: Bourgeois et al., 2006). d) Calculated frequency of tsunami deposits at the Pacific coast of Kamchatka, Frequency is given in number of events per standardized 1,000 year interval from the last 6,000 years. Data from Pinegina et al. (2003). The authors assumed that detection and sampling in the lower part of the record (i.e. older than about 5,000 yr BP) may be biased towards too low values. e) Red bars: Time intervals of radiocarbon-dated large debris avalanches at Shiveluch Volcano, Kamchatka (Ponomareva et al., 1998). Note the maximum of activity during prominent MVE 4. f) Inferred maximum ages (tephra chronology and AMS ^{14}C dating) for large tsunami deposits at northern Japan. These tsunamis are the results of large earthquakes and multisegment ruptures of plates at the Japan-Kuril trench system (Nanayama et al., 2003). g) Major emergence events at Onnetoh, E' Hokkaido, Japan (Sawai et al., 2002, 2005), caused by large interplate earthquakes. h) Planktic *N. pachyderma* (s) of core LV28-4 at E' Sakhalin margin. i) Planktic *N. pachyderma* (s) of core LV29-78 at NE' Sakhalin margin. Gray bars and MVE numbering as in fig. 5.

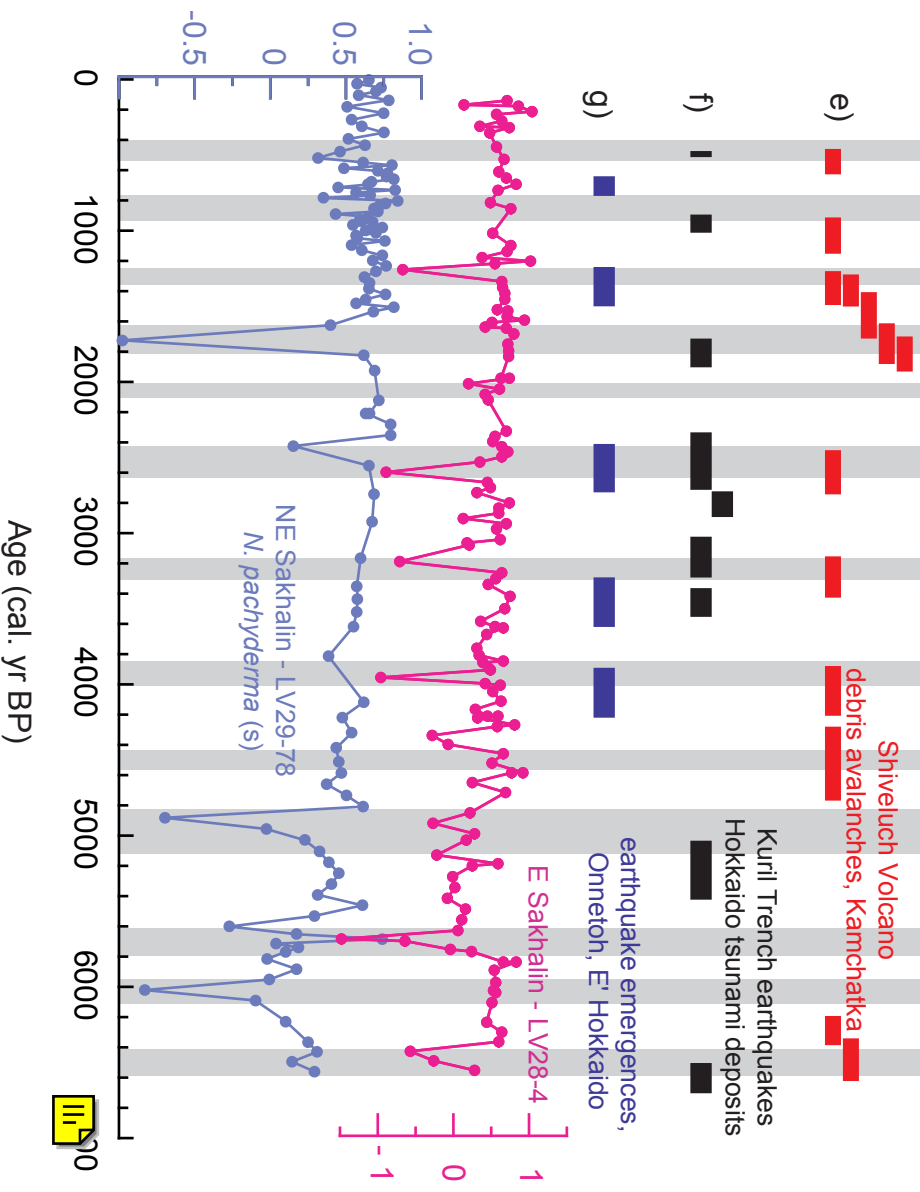
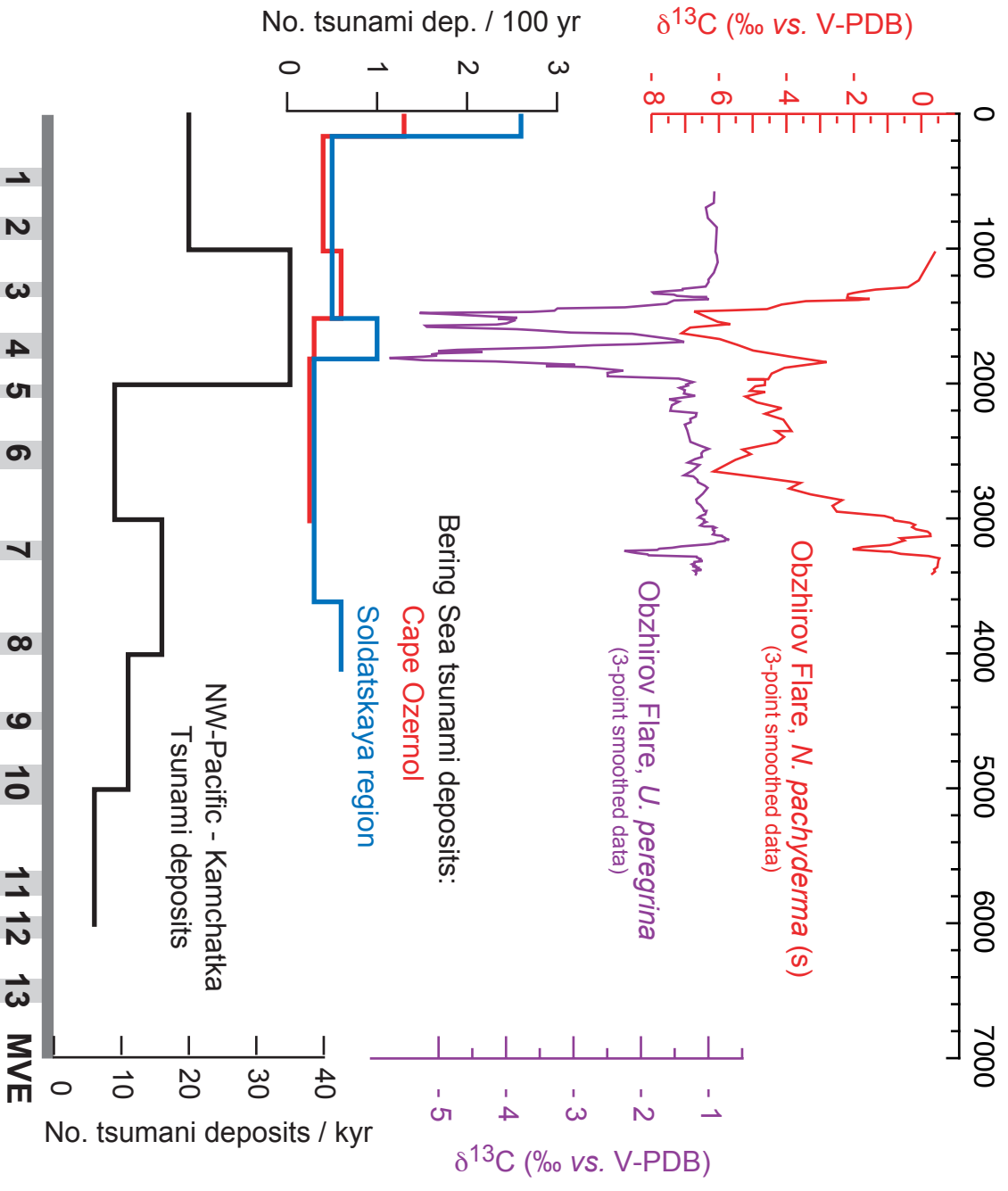












Age (cal. yr BP)



Table 1: Comparison Mg/Ca and $\delta^{13}\text{C}$ values for *U. peregrina*

depth (cm)	Age (cal. Yr BP)	MVE no.	core depth (cm)	n	$\delta^{13}\text{C}$ (‰ V-PDB)	$\delta^{18}\text{O}$ (‰ V-PDB)	Mg/Ca (mM/M)
12	820	--	10.5	3	-0.94 to -0.98	3.54 to 3.76	2.11
65	1540-1560	upper 4	64.5	3	-4.38 to -8.46	3.44 to 3.60	2.33
107	1900-1920	lower 4	105.5	2	-0.90 to -5.77	3.02 to 3.67	2.49
118	2000	--	117.5	1	-1.19	3.65	0.97
152	2300	(6)	152.5	1	-1.73	3.7	1.72
318	3250	7	317.5	1	-4.61	2.88	0.82

n: number of repeated isotope samples from sample aliquot

Table 2: Intrasample variability of *G. auriculata* during MVE 4 (sensu lato)

core depth (cm b. sf.)	Age (cal. yr BP)	n ¹⁾	Mean	Median	Min.	Max.	Std. Deviation	Mean Abs. Deviation
73.5	1630	4	-10.01	-9.61	-17.19	-3.63	7.16	6.16
88.5	1730	7	-3.70	-2.69	-7.22	-1.15	2.34	2.03
93.5+94.5	1800	5	-8.90	-7.43	-14.40	-4.21	4.07	3.30
98.5	1840	4	-11.35	-11.47	-20.68	-1.77	10.30	8.91
103.5	1880	5	-4.15	-2.13	-12.66	-1.43	4.77	3.40
111.5	1950	5	-2.81	-2.73	-4.40	-1.88	0.96	0.64
117.5	2000	7	-2.73	-2.82	-4.13	-1.56	0.92	0.74

1) n = Number of measured samples

A possible long-term CO₂ sink through submarine weathering of detrital silicates

Aloisi, G.^a, Wallmann, K.^b, Tishchenko, P.^c, Haeckel, M.^b, Pavlova, G.^c, Greinert, J.^d and Eisenhauer, A.^b

^aLaboratoire de Paléoenvironnements et Paléobiosphère, UMR CNRS 5125, Université Lyon 1, 2 rue Dubois, F-69622 Villeurbanne Cedex, France

^bLeibniz-Institut für Meereswissenschaften (IfM-GEOMAR), Wischhofstr. 1-3, D-24148 Kiel, Germany

^cPacific Oceanological Institute (POI), 43 Baltiyskaya St., Vladivostok 690041, Russia

^dInstitute of Geological and Nuclear Sciences, 30 Gracefield Road, PO Box 31 312, Lower Hutt New Zealand

The weathering of silicate minerals exposed on the continents is the largest sink of atmospheric CO₂ on time scales of millions of years. The rate of this process is positively correlated with global mean temperature and atmospheric CO₂ concentration, resulting in a negative feedback that stabilizes Earths' climate¹. Detrital silicates derived from the physical denudation of the continents are a major component of marine sediments². However, their geochemical behaviour is poorly understood and they are considered to be unimportant to the long-term carbon cycle. Here we show that in organic matter-rich sediments of the Sea of Okhotsk detrital silicates undergo intense weathering. This process is likely favoured by microbial activity, which lowers pore water pH and releases dissolved humic substances, and by the freshness of detrital silicates which originate from the cold, poorly weathered Amur River basin. Numerical simulations of early diagenesis show that submarine weathering rates in our study area are comparable to average continental weathering rates³. Furthermore, silicate weathering seems to be widespread in organic matter-rich sediments of continental margins, suggesting the existence of a significant CO₂ sink there. These findings imply a greater efficiency of the silicate weathering engine also at low surface temperatures, resulting in a weakening of the negative feedback between pCO₂, climate evolution and silicate weathering.

We studied the biogeochemical processes in sediments accumulated on the Sakhalin Slope, east of Sakhalin Island. Sakhalin Island is situated at the north-western boundary of the Sea of Okhotsk, a large marginal sea located in the north-western Pacific (Fig. 1a). Primary production in the Sea of Okhotsk is very intense during spring and autumn (120 – 160 g C m⁻² yr⁻¹), reaching a maximum of 250 g C m⁻² yr⁻¹ near the Amur river mouth during the warm season^{4,5}. Sedimentation on the Sakhalin Slope is dominated by biogenic opal and terrigenous inputs from the Amur river. Sediment transport is strongly affected by the east Sakhalin Current which flows southwards along the Sakhalin coast. The Holocene sedimentation rates are as high as 100 cm ky⁻¹ in the northern slope area and decrease towards the south by one order of magnitude⁶.

Consistent with the latitudinal gradient in sedimentation rate, the depth of sulfate penetration in Sakhalin Slope sediments decreases northwards, reflecting an increase in the rate of organic matter degradation (Fig. 1b). Due to the release of bicarbonate and sulfide ions, alkalinity builds up in the sulfate reduction zone. At the northernmost three sites, considerable amounts of alkalinity are produced also in the zone of methanogenesis (Fig. 1b). At other locations, this feature of alkalinity profiles is interpreted as due to alkalinity production via organic matter degradation^{7,8,9}. However, it is hard to reconcile this interpretation with the fact that methanogenesis produces only limited amounts of alkalinity¹⁰. Stimulated by these observations, we investigated the possibility that alkalinity production in the zone of methanogenesis is due to CO₂ conversion to HCO₃⁻ during submarine weathering of detrital silicates:

Detrital silicate + CO₂ + water => clay minerals + dissolved cations + dissolved silica + HCO₃⁻

We developed a numerical model based on the diagenetic theory of Berner¹¹ to investigate alkalinity production in Sakhalin Slope pore waters. The model is constrained by a large geochemical dataset collected at sites 29-2 and 13-6, where cores penetrated more than 20 m into the methanogenic zone recording the highest alkalinity values in the study area (up to 120 mEq./kg). A detailed description of the model and of the standard model runs for sites 29-2 and 13-6 is given in the Supplementary Information. The standard model runs, which do not consider silicate weathering processes, reproduce the alkalinity increase in the sulfate reduction zone (Fig. 2). In the methanogenic zone, however, the standard model runs strongly underestimate the measured alkalinity values (Fig. 2). Clearly, a source of alkalinity exists in the methanogenic zone which is not considered in the standard model runs.

A number of minor alkalinity sources can be excluded based on simple considerations. Exchange of H⁺ ions for metal cations on clay mineral surfaces produces alkalinity. This process, however, results in a maximum alkalinity production of about 6 mEq./kg in Sakhalin Slope sediments (see Supplementary Information for the calculation). Dissolution of biogenic barite (BaSO₄) in the zone of methanogenesis would trigger sulfate-based methane oxidation¹², producing alkalinity and dissolved barium. Dissolved barium concentrations, however, are in the micromolar range at the studied sites (data not shown), excluding this possibility. Some alkalinity could also be produced via methanogenesis using organic acid anions adsorbed to terrigenous clay particles but it is very unlikely that these acid anions are so abundant and labile that most of the alkalinity increase is caused by their degradation. Sakhalin Slope pore waters contain abundant humic and fulvic acids (up to 300 mg/l in core 13-6) which contain carboxylic acid groups and contribute to the measured alkalinity. Humic acids have a typical carboxylic content of 10 mEq. per g C and a C-content of about 50%¹³. Thus, humic acids may contribute only about 1.5 mEq./kg of alkalinity in Sakhalin Slope pore waters.

We found compelling geochemical evidence that detrital silicates are being weathered at sites 29-2 and 13-6, providing what we think is the best explanation for the production of alkalinity in the methanogenic zone. In the following, CaO* represents the carbonate-free calcium and approximates the calcium contained in silicates. The chemical index of alteration (CIA)¹⁴:

$$CIA = \frac{Al_2O_3}{Al_2O_3 + CaO^* + Na_2O + K_2O}$$

increases linearly downcore at both sites indicating an increase in the degree of weathering of the detrital material (unaltered sediments have CIA ≤ 50; completely altered sediments have CIA = 100) (Fig. 3a, Supplementary Figure 3a). This observation is confirmed by the downcore decrease in solid phase CaO*, MgO, Na₂O, K₂O and Sr relative to TiO₂ at site 29-2 (Fig. 3a) and of solid phase CaO*, MgO, Na₂O and Sr relative to TiO₂ at site 13-6 (Supplementary Figure 3a) (Ti is considered to be immobile during low temperature weathering processes¹⁵). These trends could reflect either a decrease through time in the degree of weathering of detrital silicates reaching the Sakhalin Slope, *in-situ* submarine weathering of detrital silicate, or both. However, the Ti-normalized cation trends are matched by the release of Mg, Na, K and Sr to pore fluids (Fig. 3b, Supplementary Figure 3b) suggesting that at least part of the downcore increase in sediment alteration is produced by an ongoing diagenetic process. Release of Ca to pore waters, which can be expected based on the CaO*/TiO₂ ratio in the solid phase, is evident only at the base on cores 29-2 and 13-6 (Supplementary Figures 1 and 2) because at shallower depths Ca is depleted due to carbonate precipitation.

Additional evidence is provided by Sr isotopes. Dissolved Sr at sites 29-2 and 13-6 is depleted in ⁸⁷Sr compared to modern sea water (Fig. 3b, Supplementary Figure 3b), implying the presence of a ⁸⁷Sr-poor strontium source in the sediments. Holocene biogenic carbonates can be excluded because their strontium isotope composition is equal to that of modern seawater (^{87/86}Sr = 0.7092; ref. 16). Detrital sediments deposited near our study area, instead, are more ⁸⁷Sr-depleted (0.707 < ^{87/86}Sr < 0.709; ref. 17) than Sakhalin Slope pore waters (Fig. 3b, Supplementary Figure 3b). The origin of these sediments is from the physical denudation of ⁸⁷Sr-poor igneous rocks outcropping in the Amur river basin^{18,19}. Weathering of detrital silicates from these sources explains

the ^{87}Sr depletion of Sakhalin Slope pore waters.

In further support of our submarine weathering hypothesis, conditions which favour silicate weathering on the continents are also met in Sakhalin Slope sediments. First, the detrital material deposited on the Sakhalin Slope has a low degree of chemical alteration ($\text{CIA} = 53 - 58$; Fig. 3a, Supplementary Figure 3a) and is therefore relatively fresh and reactive. This is due to the severe climatic conditions in the Amur river basin which preclude intense weathering on land³. Second, high organic productivity in the water column favours CO_2 production through methanogenesis and results in a low pore water pH, favouring the hydrolysis reactions involved in silicate dissolution²⁰. Modeled pH values in the methanogenic zone decrease with depth and are up to 1.8 pH units lower than seawater pH (~ 8.1) (Supplementary Figures 1 and 2). Third, the concentration of humic substances is extremely high (Fig. 3b; Supplementary Figure 3b). Downcore increasing trends in concentration suggest that humic substances are released to pore waters via organic matter degradation. In the subaerial weathering process, humic substances promote weathering reactions by forming complexes with metal cations on mineral surfaces, facilitating cation detachment and mineral dissolution²⁰. Their abundance in the methanogenic zone of the Sakhalin Slope argues in favour of their implication in silicate weathering reactions.

Accepting our silicate weathering hypothesis, the rate of silicate weathering at sites 29-2 and 13-6 can be estimated by considering this process in the diagenetic model and adjusting its rate such that the modeled alkalinity fits the measured values (Fig. 2). The best fit is obtained by imposing a silicate weathering rate equal to zero in the sulfate reduction zone and a linearly increasing weathering rate in the zone of methanogenesis. The maximum weathering rate ($10^{-5} \text{ mol CO}_2 \text{ consumed cm}^{-3} \text{ yr}^{-1}$) is about 10 times larger than the CO_2 consumption rate estimated for an open ocean site²¹ (see Supplementary Information for unit conversion), supporting our hypothesis that silicate dissolution is enhanced in organic matter-rich sediments. Furthermore, the depth-integrated weathering rates we constrained (70 and $100 \times 10^3 \text{ mol CO}_2 \text{ consumed km}^{-2} \text{ yr}^{-1}$ at sites 29-2 and 13-6, respectively) are comparable to the average silicate weathering rate in the 60 largest rivers basins of the world ($82 \times 10^3 \text{ mol CO}_2 \text{ consumed km}^{-2} \text{ yr}^{-1}$; average calculated from ref. 3).

An examination of the deep sea drilling geochemical database (http://www.iodp-usio.org/Data_Samples/default.html) shows that high amounts of alkalinity in the methanogenic zone are a common occurrence in organic-rich sediments (Table 1). For the reason detailed above, we think that the commonly proposed explanation, that of alkalinity production via organic matter degradation^{7,8,9}, is not plausible. Instead, it is likely that these are sites where submarine weathering of detrital silicates is taking place, implying the existence of a potentially relevant CO_2 sink in marine sediments.

The diagenetic degassing of marine sediments through mud volcanoes, cold seeps and benthic diffusive fluxes is a poorly constrained but potentially important source of CO_2 to the surficial system¹. Most of this CO_2 derives from the biological degradation of sedimentary organic matter. Submarine weathering of silicates has the potential to convert part of the organic matter-derived CO_2 to HCO_3^- , mitigating the sediment-ocean CO_2 flux.

Methods

Sampling

Cores were taken during expeditions with *RV Akademik M. A. Lavrentyev* in 1998 (cruise LV28) and *RV SONNE* in 2004 (cruise SO178) (Supplementary Table 6). Cores were cut into meter sections and moved into a cold room (4°C) where they were split longitudinally and immediately sub-sampled every meter. At each sub-sampling depth, 50 cm^3 of wet sediment were taken for pore water extraction via squeezing and 5 cm^3 for the determination porosity, POC and PON.

Pore water geochemistry

Pore waters were analysed on-board for dissolved ammonia, nitrate and sulfide using standard photometric procedures^{22,23}. Total alkalinity was determined by titration immediately after pore water separation²⁴. Dissolved calcium was determined immediately after pore water separation by complexometric titration. The remaining pore waters were later analyzed in the shore based

laboratory for dissolved sulfate and dissolved elements (Mg, Na, K, Sr, Ba) using ion-chromatography and ICP-AES, respectively. The stable isotope composition of dissolved strontium was measured un-spiked with a TRITON thermal ionization mass-spectrometer (TIMS) following standard procedures. The measured $^{87}\text{Sr}/^{86}\text{Sr}$ values were normalized to a $^{86}\text{Sr}/^{88}\text{Sr}$ ratio of 8.375209. Repeated measurements of the NBS951-standard throughout the course of this project gave a mean value of 0.710254 with a 2-sigma error of about 8 to 10 ppm. These values are in accord with the accepted value for NBS951 of 0.71025. The concentration of dissolved humic substances was determined by UV-adsorption spectroscopy at a wavelength of 254 nm using humic acid samples from Armur Bay, Vladivostok, as a standard solution. All analytical procedures applied on board research vessels and in our IFM-GEOMAR laboratories are documented in detail at http://www.geomar.de/zd/labs/labore_umwelt/Meth_englisch.html.

Sediment chemistry and physical properties

Total carbon, organic carbon and organic nitrogen were determined using a Carlo-Erba element analyzer (NA 1500). The carbonate content was determined from the difference between total carbon and organic carbon. The chemical composition of the sediment was determined with standard XRF methods. The concentration of Ca in minerals other than carbonates (CaO*) is calculated with the following formula:

$$\text{CaO}^* (\text{wt-}\%) = \text{CaO} (\text{wt-}\%) - \text{CaCO}_3 (\text{wt-}\%) \times \frac{56}{100}$$

The cation/Ti ratios are calculated using the weight-% concentration of the element oxides for the major elements and the ppm concentrations/1000 for Sr. The water content of wet sediments was determined by weight-loss upon freeze-drying. Porosity was calculated from the water content using a density of 1.025 g cm⁻³ for pore water and of 2.5 g cm⁻³ for dry sediments.

References

1. Berner, R.A. *The Phanerozoic Carbon Cycle: CO₂ and O₂*. Oxford University Press, New York (2004).
2. Li, Y.-H. and Schoonmaker, J.E. Chemical composition and Mineralogy of Marine Sediments in *Sediments, Diagenesis and Sedimentary Rocks* (ed Mackenzie, F.T.) Vol.7 *Treatise on Geochemistry* (eds. H.D. Holland and K.K. Turekian) 1-35 (Elsevier-Pergamon, Oxford, 2003).
3. Gaillardet, J., Dupré, B., Louvat, P. and Allègre, J.-C. Global silicate weathering and CO₂ consumption rates deduced from the chemistry of large rivers. *Chem. Geol.* **159**, 3-30 (1999).
4. Antoine, D., André, J.-M. and Morel, A. Oceanic primary production 2. Estimation of global scale from satellite (coastal zone color scanner) chlorophyll. *Glob. Biogeochem. Cycles* **10**(1), 57-69 (1996).
5. Broerse, A. T. C., Ziveri, P. and Honjo, S. Coccolithophore (-CaCO₃) flux in the Sea of Okhotsk: seasonality, settling and alteration processes. *Mar. Micropal.* **39**, 179-200 (2000).
6. Wong, H.K.T. *et al.* Bottom current-controlled sedimentation and mass wasting in the western Sea of Okhotsk. *Mar. Geol.* **201**, 287-305 (2003).
7. Pedersen, T.F. and Shimmielid, G.B. Interstitial water chemistry, Leg 117: contrasts with the Peru Margin; In: Prell, W.L., Niitsuma, N., *et al.*, *Proc. ODP, Sci. Res., 117*: College Station, TX (Ocean Drilling Program), 499-513 (1991).

8. Shipboard Scientific Party. Site 1084. In Wefer, G., Berger, W.H., and Richter, C., et al., *Proc. ODP, Init. Repts.*, 175: College Station, TX (Ocean Drilling Program), 339-384 (1998).
9. Shipboard Scientific Party. Site 1230. In D'Hondt, S.L., Jørgensen, B.B., Miller, D.J., et al., *Proc. ODP, Init. Repts.*, 201 (2003). Available from World Wide Web: http://www-odp.tamu.edu/publications/201_IR/chap_11/chap_11.htm.
10. Megonigal, J.P., Hines, M.E. and Visscher, P.T. Anaerobic Metabolism: Linkages to Trace Gases and Aerobic Processes in *Biogeochemistry* (ed W.H. Schlesinger) Vol. 8 *Treatise on Geochemistry* (eds. H.D. Holland and K.K. Turekian) 317-424 (Elsevier-Pergamon, Oxford, 2003).
11. Berner, R.A. *Early Diagenesis: A theoretical approach*, Princeton Series in Geochemistry, Princeton, N.J. (1980).
12. Boetius, A. et al. A marine microbial consortium apparently mediating anaerobic oxidation of methane. *Nature* **407**, 623-626 (2000).
13. Leenheer, J.A., Wershaw, R.L., Brown, G.K. and Reddy, M.M. Characterization and diagenesis of strong-acid carboxyl groups in humic substances. *Appl. Geochem.* **18**, 471-482 (2003).
14. Nesbitt, H.W. and Young, G.M. Early Proterozoic climates and plate motions inferred from major element chemistry of lutites, *Nature* **279**, 715-717 (1982).
15. Duzgoren-Aydin, N.S., Aydin, A. and Malpas, J. Re-assessment of chemical weathering indices: case study on pyroclastic rocks of Hong Kong. *Engineering Geology* **63**, 99-119 (2002).
16. Veizer, J. et al. $^{87}\text{Sr}/^{86}\text{Sr}$, $\delta^{13}\text{C}$ and $\delta^{18}\text{O}$ evolution of Phanerozoic seawater. *Chem. Geol.* **161**, 59-88 (1999).
17. Bollwerk, S. M. *Rezente submarine Barytbildung im Derugin Becken (Ochotskisches Meer)*. Ph.D. thesis. Christian Albrechts Universität, Kiel (2002).
18. Wu, F., Jahn, B., Wilde, S. and Sun, D. Phanerozoic crustal growth: U-Pb and Sr-Nd isotopic evidence from the granites in northeastern China. *Tectonophysics* **328**, 89-113 (2000).
19. Chen, J., Hsu, C. and Ho, K. Geochemistry of Cenozoic volcanic rocks and related ultramafic xenoliths from the Jilin and Helionjiang provinces, northeast China. *Journal of Asian Earth Sciences* **21**, 1069-1084 (2003).
20. Stumm, W. and Morgan, J. *Aquatic Chemistry, Chemical Equilibria and Rates in Natural Waters*, John Wiley and sons, 1022 pp (1996).
21. Maher, K., DePaolo, D.J. and Chiu-Fang Lin, J. Rates of silicate dissolution in deep-sea sediment: In situ measurement using $^{234}\text{U}/^{238}\text{U}$ of pore fluids, *Geochim. Cosmochim. Acta.* **68**(22), 4629-4648 (2004).
22. Grasshoff, K., Erhardt, M. and Kremling, K. *Methods of Seawater Analysis*, Verlag Chemie (1983).
23. Gieskes, J.M., Gamo, T. and Brumsack, H. *Chemical methods for interstitial water analysis aboard Joides Resolution*, Ocean Drilling Program, Texas A & M University (1991).

24. Ivanenkov, V. N. and Lyakhin, Y.I. Determination of total alkalinity in seawater. Methods of Hydrochemical Investigations in the Ocean. V. N. Ivanenkov. Moscow, Nauka Publ. House, 110-114 (in Russian) (1978).

Supplementary Information is linked to the online version of the paper available at www.nature.com/nature.

Acknowledgements This study was supported by the German Ministry of Education and Research (BMBF; Grant SO178-KOMEX).

Table 1 – Alkalinity production in methanogenic sediments

ODP Site	Location	Δ Alkalinity* (mEq./kg)
1252	Cascadia margin	50
1251	Cascadia margin	64
1250	Cascadia margin	30
1247	Cascadia margin	26
1246	Cascadia margin	57
1245	Cascadia margin	35
1244	Cascadia margin	30
1230	Peru Margin	105
1099	Antarctic peninsula	40
1084	Namibia margin	115
1082	Namibia margin	38
1078	Angola margin	39
997	Blake Ridge	109
995	Blake Ridge	94
994	Blake Ridge	88
789	Japan Sea	36
723	Oman margin	66
688	Peru margin	195
686	Peru margin	36
685	Peru margin	85
683	Peru margin	40

ODP – Ocean Drilling Program; *Difference between the highest alkalinity in the methanogenic zone and the alkalinity at the base of the sulfate-reduction zone. The data is available at: http://www.iodp-usio.org/Data_Samples/default.html

Figure legends

Figure 1

Early diagenesis on the Sakhalin Slope. a) Sampling locations on the Sakhalin Slope; b) Dissolved sulfate and alkalinity in Sakhalin Slope pore waters: filled circles, porewater sulfate concentrations (top axis); open circles, porewater alkalinity concentrations (bottom axis); light shaded area (zone of sulfate reduction); dark shaded area (zone of methanogenesis).

Figure 2

Dissolved alkalinity and silicate weathering rates at sites 29-2 and 13-6 on the Sakhalin Slope. Open circles, measured alkalinity concentrations (top axis); dashed line, model alkalinity concentration in the standard model runs where silicate weathering is not considered (top axis); line, model alkalinity concentration when silicate weathering is considered in the model (top axis); shaded area, rate of silicate weathering used in the modeling to obtain the best-fit between model alkalinity concentration and measured alkalinity concentration (bottom axis).

Figure 3

Chemical composition of sediments and pore waters of the Sakhalin Slope at site 29-2. a) chemical composition of the sediments; Ca* represents the carbonate-free calcium and approximates the calcium contained in silicate minerals; CIA = chemical index of alteration¹⁴. b) pore water dissolved cations, dissolved strontium isotope composition and concentration of dissolved humic substances; arrow, strontium isotope composition of modern seawater¹⁶; shaded area, strontium isotope composition of sediments near our study area¹⁷.

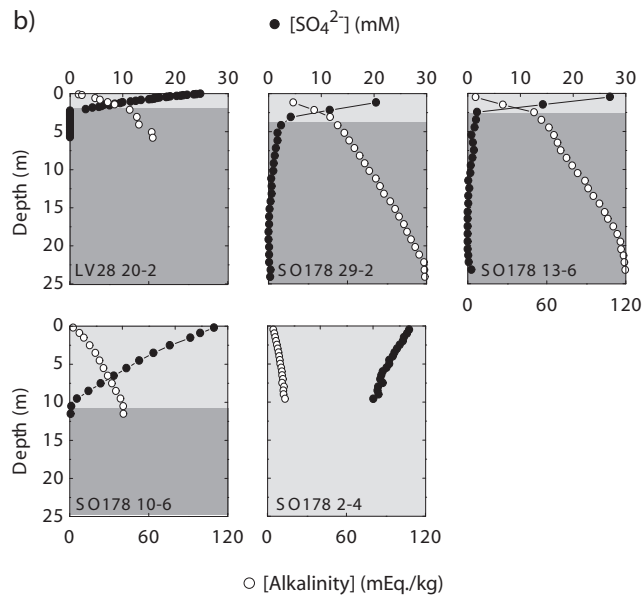
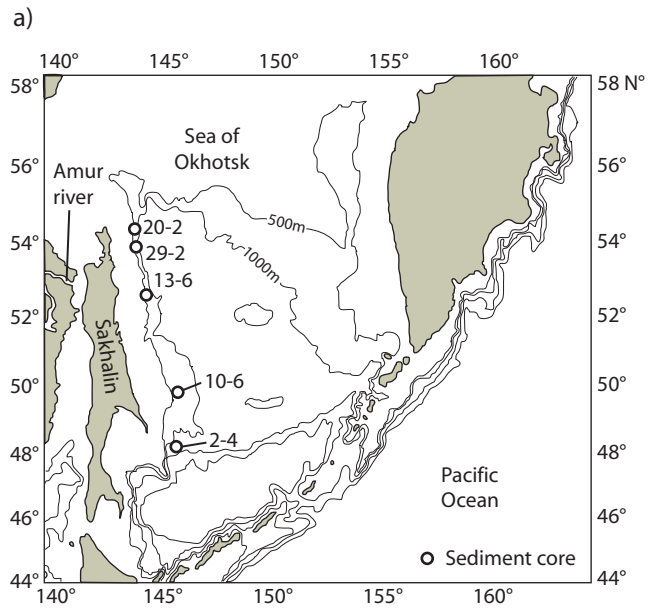


Figure 1

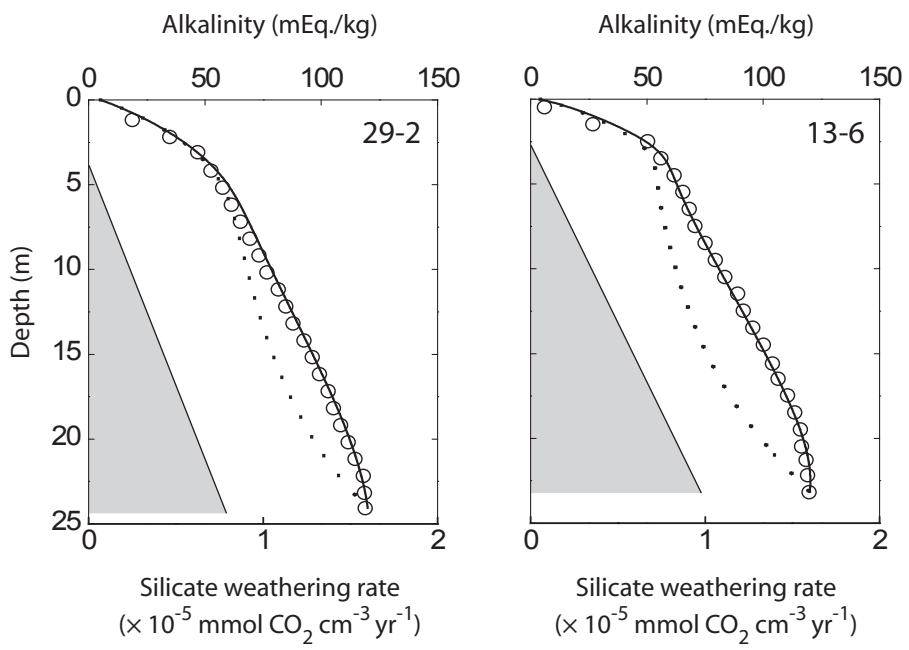


Figure 2

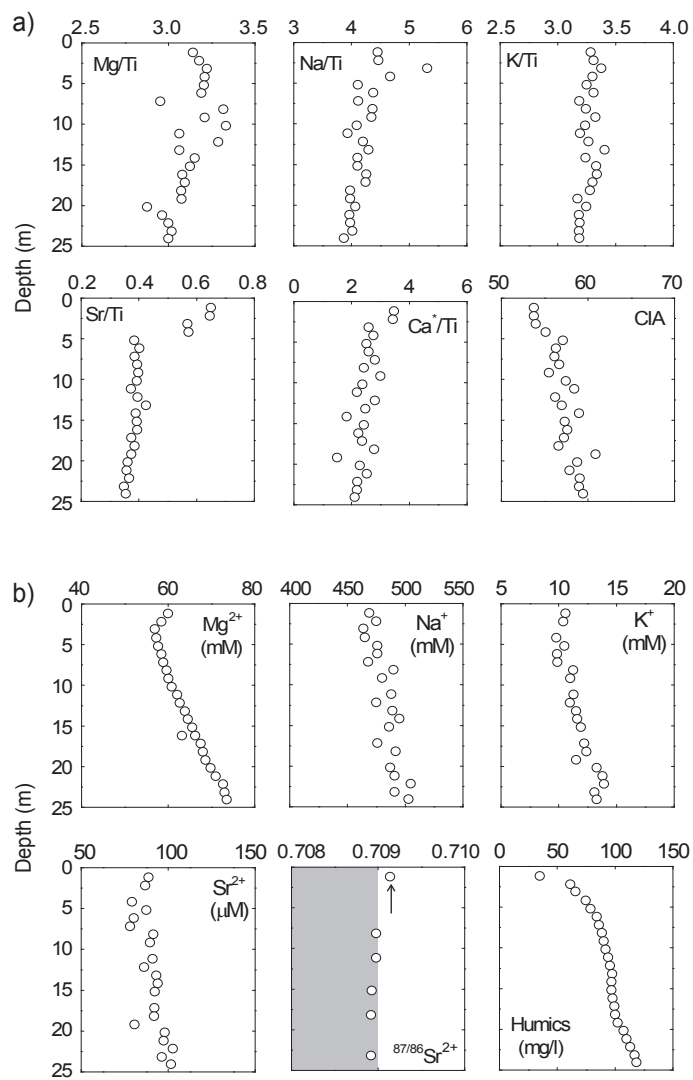


Figure 3

Supplementary information to accompany

A possible long-term CO₂ sink through submarine weathering of detrital silicates

by Aloisi et al.

Supplementary Methods describing the diagenetic model

Overview. The diagenetic model considers the degradation of organic matter (POM) via sulphate reduction and methanogenesis, the anaerobic oxidation of methane (AOM), carbonate precipitation, ammonia adsorption, sulphide removal via pyrite formation and silicate weathering (Supplementary Table 1). It considers the acid base equilibria involved in the dissociation of the weak acids H₂CO₃, H₂S and B(OH)₃ and calculates pH. It calculates the concentration-depth profiles of 3 solid species (particulate organic carbon, particulate nitrogen and adsorbed ammonia) and 10 dissolved species (SO₄²⁻, CH₄, NH₄⁺, Ca²⁺, H₂S, HS⁻, CO₂, HCO₃⁻, CO₃²⁻ and H⁺) forced by molecular diffusion, burial and the above microbial and chemical processes. Our pore water chemical data show no indication of bioturbation and bioirrigation. Thus, these processes are not considered in our model.

Supplementary Table 1. Biogeochemical processes considered in the diagenetic model

Process	Reaction
Sulfate reduction	$(\text{CH}_2\text{O})_{106}(\text{NH}_3)_{16} + 53\text{SO}_4^{2-} + 16\text{H}^+ \rightarrow 53\text{H}_2\text{S} + 16\text{NH}_4^+ + 106\text{HCO}_3^-$
Methanogenesis	$(\text{CH}_2\text{O})_{106}(\text{NH}_3)_{16} + 16\text{H}_2\text{O} \rightarrow 53\text{CH}_4 + 37\text{CO}_2 + 16\text{HCO}_3^- + 16\text{NH}_4^+$
AOM	$\text{CH}_4 + \text{SO}_4^{2-} \rightarrow \text{HCO}_3^- + \text{HS}^- + \text{H}_2\text{O}$
Ammonia adsorption	$\text{NH}_4^+ \Leftrightarrow \text{ADS}$
Carbonate precipitation	$\text{Ca}^{2+} + \text{CO}_3^{2-} \rightarrow \text{CaCO}_3$
Pyrite precipitation	$\text{FeOOH} + 1.5\text{H}_2\text{S} \rightarrow 0.5\text{FeS}_2 + 0.5\text{FeS} + 2\text{H}_2\text{O}$
Silicate weathering	$\text{CO}_2 \rightarrow \text{HCO}_3^-$

AOM, anaerobic oxidation of methane; ADS, adsorbed NH₄⁺.

Partial differential equations. Partial differential equations for solids and solutes were set-up following the classical approach used in early diagenesis modeling¹¹:

$$\text{Solute:} \quad \frac{\partial(\Phi \cdot C)}{\partial t} = \frac{\partial\left(\Phi \cdot D_s \cdot \frac{\partial C}{\partial x}\right)}{\partial x} - \frac{\partial(\Phi \cdot v \cdot C)}{\partial x} + \Phi \cdot R$$

$$\text{Solids:} \quad \frac{\partial((1-\Phi) \cdot G)}{\partial t} = -\frac{\partial((1-\Phi) \cdot w \cdot G)}{\partial x} + (1-\Phi) \cdot R$$

where x is depth, t is time, Φ is porosity, C is the concentration of dissolved species in mol per volume of pore water, v is the burial velocity of solutes, G is the concentration of solids in mass per mass of dry solids, w is the burial velocity of solids, and R defines the reactions occurring in the simulated sediment column.

To reduce the number of differential equations in our model we apply the approach of Van Cappellen and Wang²⁵ and consider the transport of the summed variables total alkalinity ($TA = 2 \times CO_3^{2-} + HCO_3^- + HS^- + B(OH)_4^- + OH^- - H^+$), dissolved inorganic carbon ($DIC = CO_2 + HCO_3^- + CO_3^{2-}$) and total dissolved sulphide ($TH_2S = H_2S + HS^-$). This results in three differential equations for the solid species (POC, PON and ADS) and seven differential equations for dissolved species (TA, DIC, TH_2S , SO_4^{2-} , CH_4 , NH_4^+ and Ca^{2+}). The dissolved boron species, $B(OH)_3$ and $B(OH)_4^-$, are not considered explicitly in the model but contribute in defining the acid-base equilibrium and pH (see next paragraph).

Acid-base equilibria. The concentration of the H_2S , HS^- , CO_2 , HCO_3^- , CO_3^{2-} species and pH are calculated based on the alkalinity conservation approach²⁶ for every sediment depth based on the salinity- and temperature-dependent stoichiometric equilibrium constants for the dissociation of the weak acids H_2CO_3 , H_2S and $B(OH)_3$ (ref. 27), the TA, DIC and TH_2S concentrations calculated by the model at every sediment depth and bottom water boron concentrations.

Depth-dependent variables. All depth-dependent variables are listed in Supplementary Table 2. Porosity is assumed to decay exponentially with depth due to steady-state compaction¹¹ where the initial porosity at zero depth (Φ_0), the porosity at infinite depth (Φ_f), and the attenuation coefficient (p) are derived from the data applying non-linear fitting techniques. Molecular diffusion coefficients (D_M) are calculated for the prevailing temperature (2°C) and salinity (35) using equations given by Boudreau²⁸. Transport of the DIC, TA and TH_2S species by molecular diffusion considers the individual concentration gradients of the various acid-base species (CO_2 , HCO_3^- , CO_3^{2-} , H_2S and HS^-) following the procedure of Van Cappellen and Wang²⁵. Archie's law is applied to consider the effects of tortuosity on diffusion coefficients and to calculate the coefficients for diffusion in sediments (D_S). The applied coefficient (Φ^2 corresponding to a $m = 3$ in Archie's law) is a good approximation for the fine-grained and water-rich sediments of the study area²⁹. Burial of solids and pore water is calculated considering steady state compaction¹¹. Sedimentation rates (w_f) are calculated using nitrogen mass balances as outlined in Wallmann et al.³⁰. The age-dependent kinetic constant for POC degradation is taken from Middelburg³¹ while the initial age (a_0) is determined by fitting the model to the POC data. Concentrations of dissolved species (C in mmol per cm^3 of pore water) are related to the corresponding concentrations of solid species (G given in wt-%) using conversion factors (r) which include the depth-dependent porosity, the average density of dry solids ($d_s = 2.5 \text{ g cm}^{-3}$) and the appropriate molecular weights (MW) of C, N and S. These factors are applied to calculate the release and consumption of solutes resulting from the turnover of solids (Supplementary Tables 3 and 4).

Supplementary Table 2. Depth-dependent constitutive equations used in the modeling.

Parameter	Constitutive equation
Porosity	$\Phi = \Phi_f + (\Phi_0 - \Phi_f) \cdot e^{-p \cdot x}$
Molecular diffusion in sediments	$D_s = \Phi^2 \cdot D_M$
Burial of solids	$w = \frac{w_f \cdot (1 - \Phi_f)}{1 - \Phi}$
Burial of pore water	$v = \frac{\Phi_f \cdot w_f}{\Phi}$
Age-dependent kinetic constant for POM degradation	$k_x = 0.16 \cdot \left(a_0 + \frac{x}{w} \right)^{-0.95}$
Factor converting G (wt-%) in C (mmol cm ⁻³)	$r = \frac{10 \cdot d_s \cdot (1 - \Phi)}{MW \cdot \Phi}$

Kinetic rate expressions. A novel rate law³⁰ was introduced to describe the effect of metabolite concentrations on the anaerobic degradation of particulate organic carbon (POC) in anoxic marine sediments:

$$R_{\text{POC}} = \frac{K_C}{C(\text{DIC}) + C(\text{CH}_4) + K_C} \cdot k_x \cdot \text{POC}$$

where R_{POC} is the POC degradation rate, $C(\text{DIC})$ is the concentration of dissolved inorganic carbon, $C(\text{CH}_4)$ is the ambient methane concentration in pore waters, k_x is an age-dependent kinetic constant, POC is the POC concentration and K_C is a Monod constant describing the inhibition of POC degradation by DIC and CH_4 . The age effects on POC degradation are considered using the approach introduced by Middelburg³¹. Ages were calculated from sediment depth and burial rate.

Other kinetic rate laws are defined in Supplementary Table 3. The rate of sulphate reduction is related to the POC degradation rate (R_{POC}) considering that reduction rates decrease at very low sulphate concentrations ($K_{\text{SO}_4} = 1 \text{ mM}$). Methane formation is inhibited in the presence of sulphate and is driven by POC degradation. The anaerobic degradation of methane is assumed to follow second order kinetics depending on both sulphate and methane concentrations³². The value of the kinetic constant (k_{AOM}) is defined by fitting the model to the sulphate data. Degradation of particulate organic nitrogen (PON) is linked to POC degradation considering Redfield stoichiometry and the N : C weight ratio (14/12).

Ammonia adsorption can be modeled as a linear equilibrium reaction where the depth-independent equilibrium constant K_{ADS} is defined as the ratio between adsorbed ammonia (ADS in mmol NH_4 (g dry solids)⁻¹) and dissolved ammonia ($C(\text{NH}_4)$ in mmol NH_4 (cm³ pore water)⁻¹) at equilibrium¹¹. In fine-grained marine sediments K_{ADS} attains a value of 1.7 cm³ g⁻¹ (ref. 33). We prefer to model ammonia adsorption using a kinetic approach because the equilibrium approach would demand the use of rather complicated differential-algebraic equations. However, the kinetic constant is set to a large value ($k_{\text{ADS}} = 1 \text{ mM yr}^{-1}$) so that equilibrium between dissolved and adsorbed ammonia is always maintained ($\text{ADS}/C(\text{NH}_4) = K_{\text{ADS}}$).

The rate of calcium carbonate precipitation and dissolution (in mmol Ca (cm³ pore water × yr)⁻¹) is considered to depend linearly on saturation state and to be proportional to a kinetic constant k_{CaCO_3} (in mmol Ca (cm³ pore water × yr)⁻¹) (Supplementary Table 3). The saturation state is calculated for every sediment depth considering the calcium and carbonate ion concentration and the solubility product (K_{SP}) of calcite²⁷. This approach has been applied successfully in previous studies of anoxic sediments^{32,34}.

Sulphide is removed from pore waters and transferred into the solid phase by the precipitation of pyrite, iron mono-sulphides, the formation of elemental sulphur and various organic sulphur compounds¹⁰. Pyrite is usually the main sulphur-bearing phase in anoxic marine sediments. Its formation rate is often limited by the availability of reactive ferric iron phases. The abundance and reactivity of these phases decreases with sediment depth³⁵. Hence, the rate of sulphide removal from pore waters is allowed to decrease exponentially with depth (Supplementary Table 3). The initial removal rate ($k_{\text{REM}}(0)$) and the corresponding attenuation coefficient (re) are determined by fitting the model to the dissolved H_2S data. A Monod term is added so that sulphide removal occurs only in the presence of dissolved sulphide ($K_{\text{REM}} = 0.1 \mu\text{M}$).

Silicate weathering transforms CO_2 into HCO_3^- . Because the factors affecting the rate of submarine silicate weathering are not known, the rate of this process is imposed. To compare silicate weathering rates calculated with our model with subaerial silicate weathering rates presented in Gaillardet et al.³, model rates (in mmol CO_2 consumed per cm^3 wet sediment per year) are integrated over the vertical distance of the core and converted in mol CO_2 consumed per km^2 seafloor per year.

Reaction rates are combined appropriately to define reaction terms which are applied in the differential equations for each solid and dissolved species (Supplementary Table 4). Conversion factors (r) are introduced to maintain the correct dimensions for solid and dissolved species concentrations. Stoichiometric coefficients are used to derive the release rates of metabolites from POC degradation rates.

Boundary values. Constant concentrations of dissolved species were prescribed at the upper and lower boundary of the model column (Dirichlet boundary conditions) while the vertical distribution of solids was simulated applying Dirichlet conditions at the upper boundary. The upper boundary of the model domain is situated not at the sediment/water interface but at the transition between oxic – suboxic surface layers affected by bioturbation and bioirrigation and the underlying anoxic sediment column. Undisturbed surface sediments were collected with a multi-corer at all investigated stations and pore water analysis revealed nitrate penetration depths of only 2 – 8 cm ³⁶. Hence, anoxic conditions prevailed already at shallow sediment depths. The coring devices used in this study to recover long sediment cores are not well-suited for the sampling of surface sediments. Therefore, the rapid degradation of POM via aerobic respiration, denitrification, Mn(IV)- and Fe(III)-reduction are not resolved in our data set and were thus not considered in the model. Concentrations of dissolved species used as boundary values were taken from our data set using samples taken at the upper most and deepest points of the studied sediment cores. DIC measurements are strongly affected by CO_2 degassing during core recovery and were not carried out on our samples. Therefore, DIC values at the upper and lower boundaries were chosen such that a realistic saturation state with respect to calcite resulted. The particulate organic carbon and total solid nitrogen data indicate that the organic matter content of sediments has changed through time. Thus, the POC concentration at the upper boundary was allowed to vary through time during the model runs. At site 29-2, the best fit of the POC and TN data was obtained with an upper boundary POC concentration of 2 wt-% during the deposition of sediments between 25 and 15 m depth and of 1.77 wt-% during the deposition of sediments between 15 and 0 m depth. At site 13-6, the upper boundary POC concentrations were 1.1 wt-% during the deposition of sediments between 23 and 20 m, 2.15 wt-% during the deposition of sediments between 20 and 11 m and 1.8 wt-% during the deposition of sediments between 11 and 0 m.

Numerical solution. Finite difference techniques (the method-of-lines code) are used to solve the model which have been successfully applied in previous models of early diagenesis^{32,34,37}. The set of 10 partial differential equations defining the model is converted into a large number of ordinary differential equations (ODE) by approximating the spatial derivatives with finite differences. A centred finite difference scheme is used for dissolved species while an upward scheme is applied for the transport of solids. The ODE system is set-up on an uneven grid with high resolution at the surface. It is solved and run into steady state using the NDSolve object of MATHEMATICA Version 5. The acid-base equilibria are solved separately, prior to model runs, for a wide range of

TA, DIC and TH2S. The Interpolation object of MATHEMATICA Version 5 is used to build a 3D interpolation function that the main transport-reaction model interrogates throughout the model runs to solve the acid-base equilibria at every sediment depth. A typical model run takes about one hour on a Pentium 4 PC.

Supplementary Table 3. Rates laws used in the modeling.

Rate	Kinetic Rate Law
Sulfate reduction	$R_{SR} = 0.5 \cdot \frac{C(\text{SO}_4)}{C(\text{SO}_4) + K_{\text{SO}_4}} \cdot r(\text{POC}) \cdot R_{\text{POC}}$
Methanogenesis	$R_{SR} = 0.5 \cdot \frac{K_{\text{SO}_4}}{C(\text{SO}_4) + K_{\text{SO}_4}} \cdot r(\text{POC}) \cdot R_{\text{POC}}$
Anaerobic oxidation of methane	$R_{\text{AOM}} = k_{\text{AOM}} \cdot C(\text{SO}_4) \cdot C(\text{CH}_4)$
PON degradation	$R_{\text{PON}} = \frac{14}{12} \cdot \frac{16}{106} \cdot R_{\text{POC}}$
Ammonia adsorption	$R_{\text{ADS}} = k_{\text{ADS}} \cdot \left(1 - \frac{\text{ADS}}{C(\text{NH}_4) \cdot K_{\text{ADS}}}\right)$
CaCO ₃ precipitation	$R_{\text{CaCO}_3} = k_{\text{CaCO}_3} \cdot \left(\frac{C(\text{Ca}) \cdot C(\text{CO}_3)}{K_{\text{SP}}} - 1\right)$
Sulphide removal	$R_{\text{REM}} = \frac{C(\text{H}_2\text{S})}{C(\text{H}_2\text{S}) + K_{\text{REM}}} \cdot k_{\text{REM}}(0) \cdot e^{-r \cdot x}$
Silicate weathering	$R_{\text{SIL}} = \text{imposed rate-depth profile}$

Supplementary Table 4. Rate expressions applied in the differential equations.

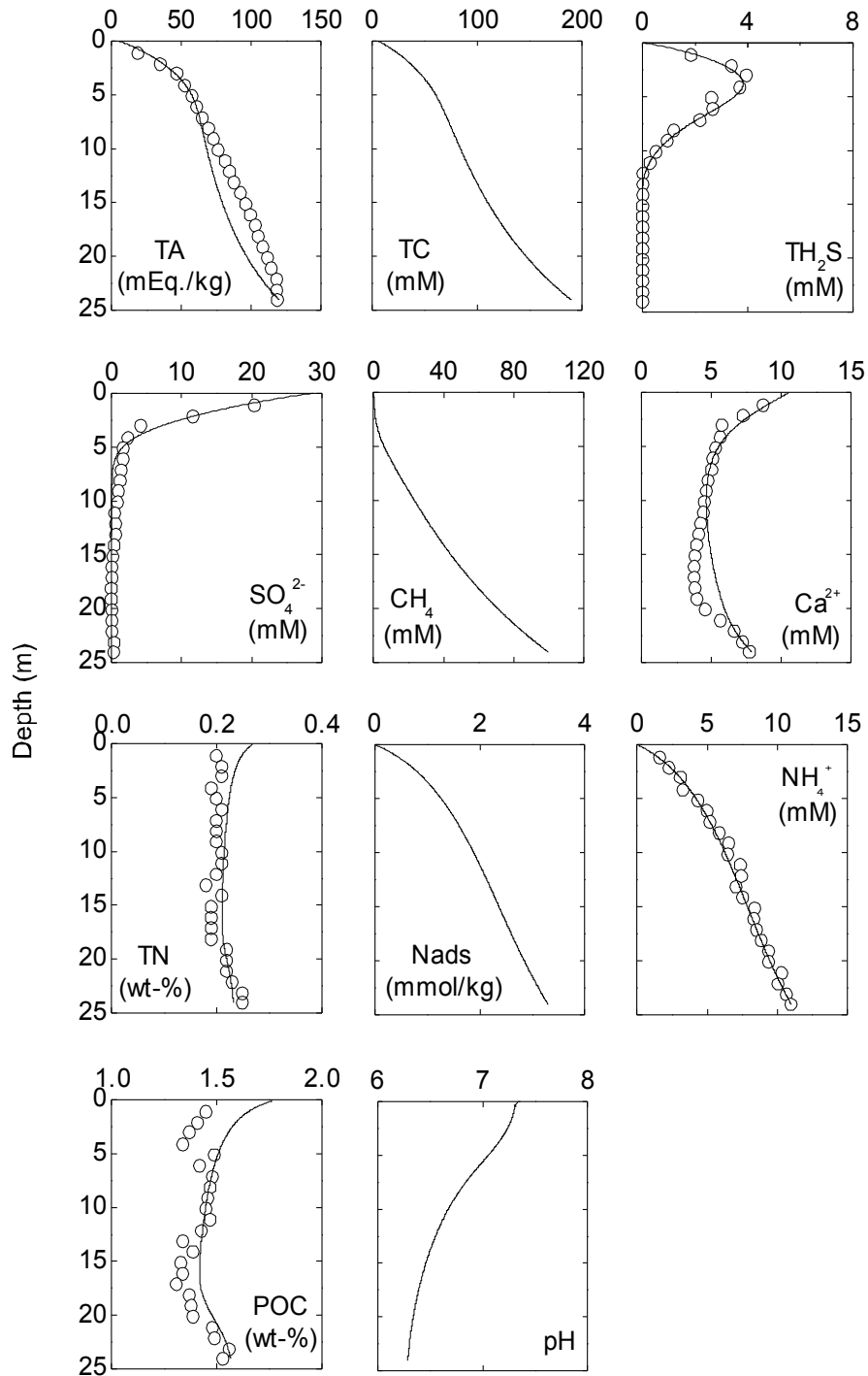
Species	Rates
Particulate organic carbon (POC)	$R(\text{POC}) = -R_{\text{POC}}$
Particulate organic nitrogen (PON)	$R(\text{PON}) = -R_{\text{PON}}$
Adsorbed ammonia (ADS)	$R(\text{ADS}) = +R_{\text{ADS}} \cdot \frac{d_s \cdot (1 - \Phi)}{\Phi}$
Sulphate (SO_4)	$R(\text{SO}_4) = -R_{\text{SR}} - R_{\text{AOM}}$
Methane (CH_4)	$R(\text{CH}_4) = +R_{\text{M}} - R_{\text{AOM}}$
Ammonia (NH_4)	$R(\text{NH}_4) = +r(\text{PON}) \cdot R_{\text{PON}} - R_{\text{ADS}}$
Calcium (Ca)	$R(\text{Ca}) = -R_{\text{CaCO}_3}$
Total alkalinity (TA)	$R(\text{TA}) = 2 \cdot R(\text{SO}_4) - 2 \cdot R_{\text{CaCO}_3} + 2 \cdot R_{\text{AOM}} + \frac{16}{106} \cdot r(\text{POC}) \cdot R_{\text{POC}} + R_{\text{SIL}}$
Dissolved inorganic carbon (DIC)	$R(\text{DIC}) = +r(\text{POC}) \cdot R_{\text{POC}} - R_{\text{M}} - R_{\text{CaCO}_3} + R_{\text{AOM}}$
Total dissolved sulphide (TH_2S)	$R(\text{H}_2\text{S}) = R_{\text{SR}} + R_{\text{AOM}} - r(\text{S}) \cdot R_{\text{REM}}$

Supplementary Discussion pertaining to the standard model runs for sites 29-2 and 13-6.

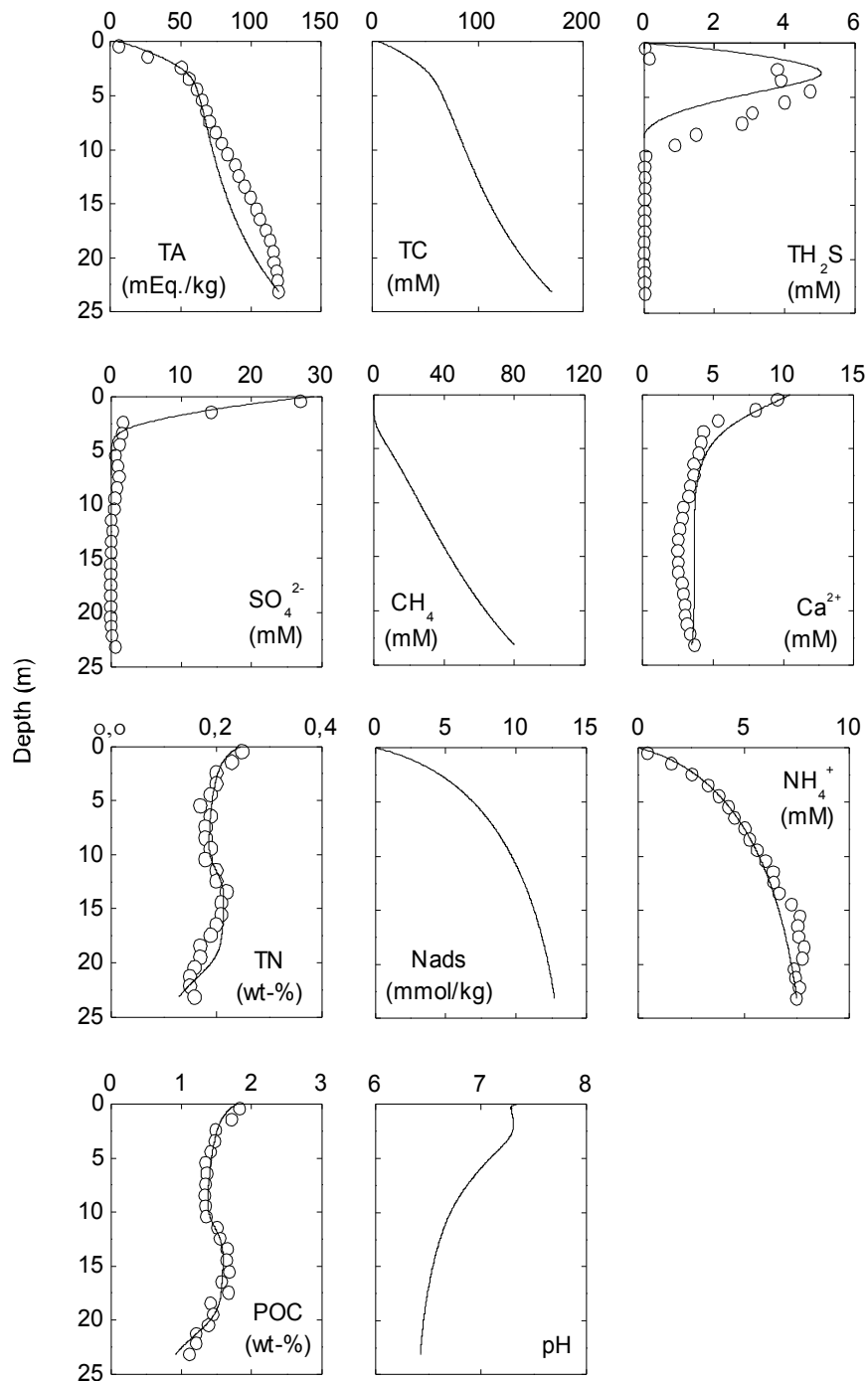
The standard model runs considers all biogeochemical process in Supplementary Table 1 except for silicate weathering. The scope of the standard model runs is twofold. First, they serve to constrain model parameters which describe the kinetics of diagenetic reactions (Supplementary Table 5). A good agreement between the data and the simulated profiles in the standard model runs (Supplementary Figures 1 and 2) demonstrates that the model can be used to simulate biogeochemical processes in Sakhalin Slope sediments. Second, the standard model runs are used to test if methanogenesis alone can explain the considerable amounts of alkalinity measured at sites 29-2 and 13-6.

Supplementary Table 5. Parameters derived in the standard model runs.

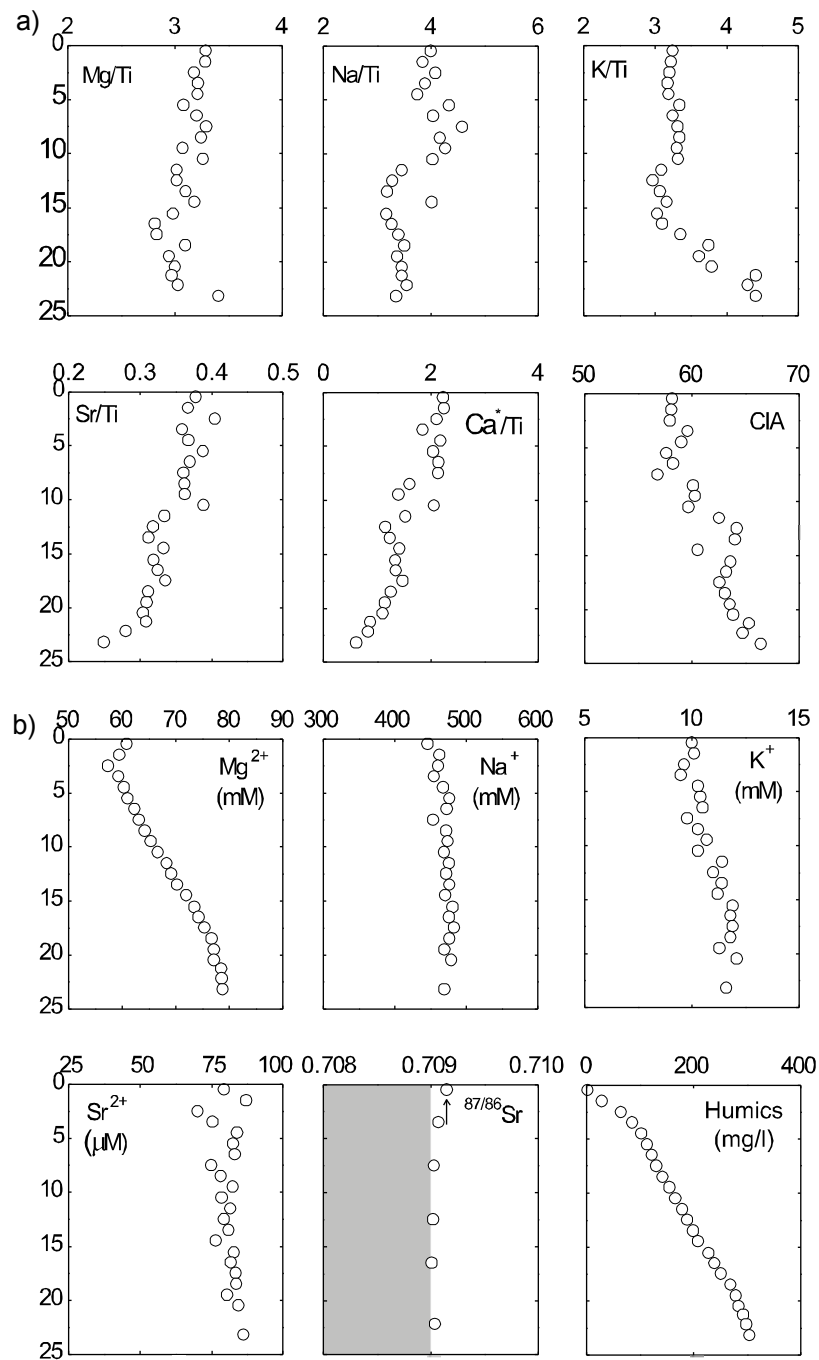
Parameter (Symbol and units)	Core 29-2	Core 13-6
Initial age of POM (a_0 in yr)	1000	300
Monod constant for inhibition of POM degradation by DIC and CH_4 (K_C in mM)	30	40
Monod constant for inhibition of CH_4 formation by SO_4 (K_{SO_4} in mM)	1.0	1.0
Kinetic constant for AOM (k_{AOM} in $\text{cm}^3 \text{ yr}^{-1} \text{ mmol}^{-1}$)	1.0	10
Constant for ammonia adsorption (k_{ADS} in $\text{cm}^3 \text{ g}^{-1}$)	0.3	1.7
Kinetic constant for sulfide removal (k_{REM} in $\text{wt}\% \text{ S yr}^{-1}$)	15×10^{-5}	30×10^{-5}
Attenuation constant for the exponential decrease in sulfide removal with depth (re in cm^{-1})	0.0023	0.00405



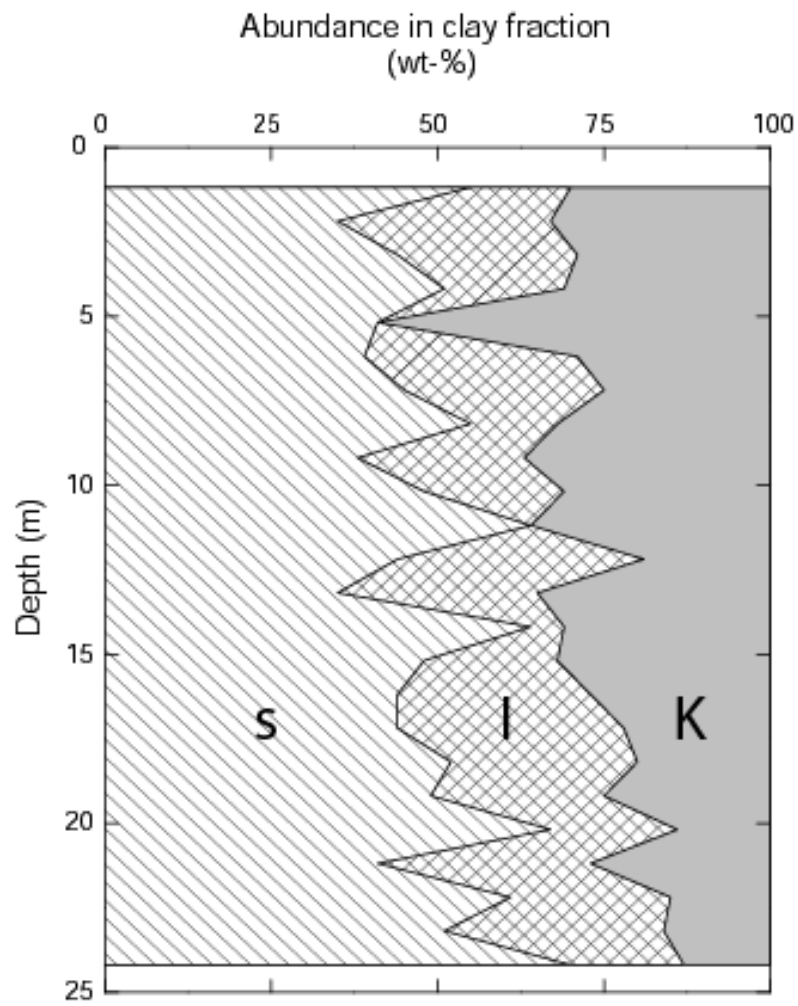
Supplementary Figure 1 – Results of the standard model run for site 29-2. Measured (open circles) and modeled (lines) concentration of total alkalinity (TA), total dissolved inorganic carbon (TC), total dissolved sulphide (TH₂S), dissolved sulphate (SO₄²⁻), dissolved methane (CH₄), dissolved calcium (Ca²⁺), total solid phase nitrogen (TN), adsorbed nitrogen (Nads), dissolved ammonia (NH₄⁺), particulate organic carbon (POC) and pH.



Supplementary Figure 2 – Results of the standard model run for site 13-6. Measured (open circles) and modeled (lines) concentration of total alkalinity (TA), total dissolved inorganic carbon (TC), total dissolved sulphide (TH₂S), dissolved sulphate (SO₄²⁻), dissolved methane (CH₄), dissolved calcium (Ca²⁺), total solid phase nitrogen (TN), adsorbed nitrogen (Nads), dissolved ammonia (NH₄⁺), particulate organic carbon (POC) and pH.



Supplementary Figure 3 - Chemical composition of sediments and pore waters of the Sakhalin Slope at site 13-6. a) chemical composition of the sediments; Ca* represents the carbonate-free calcium and approximates the calcium contained in silicate minerals; CIA = chemical index of alteration¹⁴. b) pore water dissolved cations, dissolved strontium isotope composition and concentration of dissolved humic substances; arrow, strontium isotope composition of modern seawater¹⁶; shaded area, strontium isotope composition of sediments near our study area¹⁷.



Supplementary Figure 4 – Mineralogical composition of the clay mineral fraction in Sakhalin Slope sediments at site 29-2. S – Smectite; I – Illite; K - Kaolinite

Supplementary Table 6. Location of sediment cores on the Sakhalin Slope

Station	Location		Water depth (m)	Recovery (m)
LV28 2-4	48°22.73'N	146°02.22'E	1265	6.0
SO178 10-6	49°44.88'N	146°00.48'E	613	11.5
SO178 13-6	52°43.88'N	144°42.65'E	713	23.7
SO178 29-2	53°50.00'N	144°14.23'E	771	24.3
LV28 20-2	54°26.52'N	144°04.09'E	685	5.0

Supplementary Discussion to estimate the maximum alkalinity theoretically produced by H⁺ exchange for cations on clay mineral surfaces in Sakhalin Slope sediments

The clay mineral fraction of Sakhalin slope sediments is composed of smectite (~ 50%) and a mixture of illite (~ 25%) and kaolinite (~25%) (Supplementary Figure 4). In cation exchange experiments with clays of similar composition, Motellier et al.³⁸ show that about 2 mEq/100g clay are exchanged when the pH is lowered from 7 to 6, which corresponds to the pH shift in methanogenic sediments at sites 29-2 and 13-6 (Supplementary Figures 1 and 2). Supposing that Sakhalin Slope sediments contain 50 % dry weigh of clays, with a density of dry solids equal to 2.5 g cm⁻³ and a porosity of 0.8, about 6 mEq of protons per litre of pore water are exchanged in Sakhalin slope sediments due to the shift in pH. Thus, cation exchange cannot explain the high amounts of alkalinity produced in the methanogenic zone of Sakhalin Slope sediments.

Supplementary discussion pertaining to the conversion of silicate dissolution rates estimated at ODP Site 984 in mol m⁻² s⁻¹ (ref. 21) into CO₂ consumption rates calculated by our diagenetic model (in mmol CO₂ cm⁻³ yr⁻¹; see figure 2)

The silicate dissolution rates reported in Maher et al.²¹ center around 10⁻¹⁷ mol m⁻² s⁻¹ (moles of silicate dissolving per m² of silicate grain surface per second; their figure 9b) which corresponds to 3.15 × 10⁻¹¹ mmol cm⁻² yr⁻¹ (millimoles of silicate dissolving per cm² of silicate grain surface per year). Multiplying this value by the Specific Surface Area (SSA) of silicate grains (in cm² of silicate grain surface per cm³ sediment) yields a silicate dissolution rate of 7.15 × 10⁻⁷ mmol cm⁻³ yr⁻¹ (millimoles of silicate dissolving per cm³ sediment per year). The SSA value used above (45360 cm²/cm³) is obtained from the SSA value reported in Maher et al.²¹ (~ 2.4 m² g⁻¹) considering a mineral density of 2.7 g cm⁻³, a porosity of 0.7 and a silicate content of 50% in the sediments²¹. Considering that the silicate dissolving is mostly plagioclase²¹ and that about 1.5 moles of CO₂ are consumed per mole of plagioclase dissolved, the silicate dissolution rate of Maher et al.²¹ corresponds, using the units of our diagenetic model, to about 1 × 10⁻⁶ mmol CO₂ cm⁻³ yr⁻¹.

Supplementary References

25. Van Cappellen, P. and Wang, Y. Cycling of iron and manganese in surface sediments: a general theory for the coupled transport and reaction of carbon, oxygen, nitrogen, sulfur, iron and manganese. *American Journal of Science* **296**, 197-243 (1996).
26. Luff, R., Haeckel, M and Wallmann, K., Robust and fast FORTRAN and MATLAB[®] libraries to calculate pH distributions in marine systems. *Computers and Geosciences* **27**, 157-169 (2001).
27. Millero, F.J. Thermodynamics of the carbon dioxide system in the oceans. *Geochim. et Cosmochim. Acta* **43**, 1651-1661 (1995).

28. Boudreau, B.P. *Diagenetic Models and their Implementation: Modeling Transport and Reaction in Aquatic Sediments*. Springer (1997).
29. Ullman, W.J. and Aller, R.C. Diffusion coefficients in nearshore marine sediments. *Limnol Oceanogr.* **27**, 552-556 (1982).
30. Wallmann, K., Aloisi, G., Haeckel, M., Obzhairov, A. and Tishchenko, P. Kinetics of organic matter degradation, microbial methane generation and gas hydrate formation in anoxic marine sediments. *submitted to Geochimica et Cosmochimica Acta*
31. Middelburg, J. J. A simple model for organic matter decomposition in marine sediments. *Geochim. Cosmochim. Acta* **53** 1577-1581 (1989).
32. Luff, R. and Wallmann, K. Fluid flow, methane fluxes, carbonate precipitation and biogeochemical turnover in gas hydrate-bearing sediments at Hydrate Ridge, Cascadia Margin: Numerical modeling and mass balances. *Geochim. Cosmochim. Acta* **67**(18), 3403-3421 (2003).
33. Mackin, J. E. and Aller, R.C. Ammonium adsorption in marine sediments. *Limnol. Oceanogr.* **29**(2), 250-257 (1984).
34. Luff, R., Wallmann, K., Grandel, S. and Schlüter, M. Numerical modelling of benthic processes in the deep Arabian Sea. *Deep-Sea Res. II* **47**(14), 3039-3072 (2000).
35. Raiswell, R. and Canfield, D.E. Sources of iron for pyrite formation in marine sediments. *Am. J. Science* **298**, 219-245 (1998).
36. Biebow, N. and Hütten, E. *KOMEX Cruise Reports*. Kiel, GEOMAR Research Center (2000).
37. Boudreau, B. P. A method-of-lines code for carbon and nutrient diagenesis in aquatic sediments. *Computers & Geosciences* **22**(5), 479-496 (1996).
38. Motellier, S. *et al.* Modelling of the ion-exchange properties and indirect determination of the interstitial water composition of an argillaceous rock. Application to the Callovo-Oxfordian low-water-content formation. *Appl. Geochem.* **18**, 1517-1530 (2003).

**Incorporation of methane-derived carbon in $\delta^{13}\text{C}$
of selected rose Bengal-stained benthic foraminifera
5 from cold seep sites in the Okhotsk Sea**

Lester Lembke-Jene^{1,2*}, Ralf Tiedemann³, Klaus Wallmann¹,
Wolf-Christian Dullo¹, Anatoly Obzhairov⁴,
10 Nils Andersen⁵, Dirk Nuernberg¹

15 ¹IFM-GEOMAR Leibniz-Institut fuer Meereswissenschaften,
Wisshofstrasse 1-3, D24148 Kiel, Germany.

²Tethys Geoconsulting GmbH, Wisshofstrasse 1-3, D-24148 Kiel,
Germany

20 ³Alfred-Wegener Institut fuer Polar- und Meeresforschung, Am
Alten Hafen 26, D-27568 Bremerhaven, Germany.

⁴V.I. Il'ichev Pacific Oceanological Institute, 43 Baltiyskaya
Street, Vladivostok 690041, Russia

⁵Leibniz-Institut fuer Altersbestimmung und Isotopenforschung,
25 Max-Eyth-Strasse 11-13, D-24118 Kiel, Germany

* Corresponding author: llemcke@ifm-geomar.de

Abstract

tba

1. Introduction

5 The world ocean's continental margins host vast deposits of
gas hydrates. These large reservoirs are susceptible to
changes in oceanographic and geological boundary conditions
and at present it is unknown if and to what extent
dissociations of these hydrates might trigger or amplify rapid
10 changes in the global climate system or create natural hazards
(Dickens, 2003; Dickens, 2004; Kvenvolden, 1999; Kvenvolden
and Rogers, 2005; Nisbet, 2002).

More recently, it was suggested that also rapid, millennial-
scale climatic variability in the more recent past, might have
15 been amplified or even triggered by hydrate dissociations,
ultimately leading to the „Clathrate-Gun Hypothesis“, with
highly responsive methane reservoirs on timescales as short as
decades (Hill et al., 2004a; Kennett et al., 2000; Kennett et
al., 2003).

20 However, especially the latter hypothesis is discussed
controversially (Blunier, 2000; Brook et al., 2000; Sowers,
2006). But even if methane dissociations may not be the cause
for millennial-scale rapid climate shifts, methane fluxes from
numerous cold seep sites, submarine mud volcanoes, and
25 hydrothermal vents likely exert a considerable influence on
the oceans' carbonate system and thus the global carbon cycle

(Dickens, 1999; Dickens, 2003; Etiope and Milkov, 2004; Judd,
2003; Milkov, 2004; Milkov and Etiope, 2005).

To date, the main proxy for tracking and identifying past
methane venting or dissociation events are stable carbon
isotopes preserved in the calcitic tests of foraminifera. This
5 rests on the assumption that foraminifera reliably record
distinctly negative excursions of $\delta^{13}\text{C}$ (Kennett et al., 2000;
Wefer et al., 1994), caused by isotopically depleted methane-
derived carbon (MDC). Recently, this approach was doubted,
10 questioning the reliability of foraminiferal $\delta^{13}\text{C}$ to record
times of methane discharge (Stott et al., 2002; Torres et al.,
2003) based on $\delta^{13}\text{C}$ data from live benthic foraminifera.

Instead, it was suggested that secondary, temporally
unspecified sedimentary diagenesis is a more likely cause for
15 $\delta^{13}\text{C}$ anomalies in foraminifera, induced by methane venting at
any time. Foraminifera in a cold-seep setting at Hydrate
Ridge, NE-Pacific do not incorporate MDC in equilibrium with
 $\delta^{13}\text{C}_{\text{DIC}}$ during venting events (Torres et al., 2003). However,
other studies using material from rather similar settings came
20 to conflicting conclusions, reporting that benthic
foraminifera do indeed record a MDC depleted $\delta^{13}\text{C}$ signal (Hill
et al., 2004b).

Given both the potentially large impact of the current gas-
hydrate reservoir on climate, slope stability, and the
25 carbonate system, both more proxies for methane venting in

earth's history as well as better understanding of proxies currently in use are needed.

Addressing the latter issue, we try to assess in which form methane-induced negative $\delta^{13}\text{C}$ signals are recorded in benthic foraminifera at different sites of active methane venting and with different fluxes of methane into the water column. The range of our sites comprises non-vent locations with a diffuse elevated methane background signal, clam fields and bacterial mats with differing concentrations of methane in the bottom water column. We contrast these results with sites with elevated but *ex situ*-generated higher methane concentrations in the bottom water and high organic matter deposition rates. We compare the intra- and interspecies-specific offsets in $\delta^{13}\text{C}$ at the different vent sites to the non-vent site settings, and discuss the implications for using benthic foraminiferal isotope studies as indicators for methane venting intensity, high OM flux, and the relevance of the results in comparison to previous studies from other settings.

2. Previous works

During the past few years, some studies have assessed the influence of methane venting on the isotopic composition of benthic foraminifera in cold seep areas (Hill et al., 2004b; Mau et al., 2006; Rathburn et al., 2000; Rathburn et al., 2003; Torres et al., 2003). Results are often contradictory and vary between locations or within the same region according

to different approaches (Hill et al., 2004b; Martin et al., 2004; Rathburn et al., 2003; Stott et al., 2002; Torres et al., 2003). As a side effect, due to technical and logistical limitations, some studies derive their material from a few sites in areas of established cold seep research (Hydrate Ridge, Monterey Bay) and samplings often yield low numbers of foraminifera that are suited for isotope analysis, thereby complicating e.g. statistical evaluation of the results.

In general, one group of studies suggest that live foraminifera do not record a significant depletion of their tests' $\delta^{13}\text{C}$ at methane seeps and do not faithfully record a $\delta^{13}\text{C}_{\Sigma\text{CO}_2}$ signal of the ambient bottom or pore water (Stott et al., 2002; Torres et al., 2003). In addition, significantly depleted $\delta^{13}\text{C}$ values in benthics, comparable to the ones from cold seep settings, can be obtained under dysoxic settings with steep porewater gradients without invoking dissociation of gas hydrates or methane venting (Stott et al., 2002).

In contrast, another group of studies maintains that absolute $\delta^{13}\text{C}$ values of benthics from methane seep areas are significantly depleted in their absolute values and can be differentiated from non-seep settings (Hill et al., 2004b; Mackensen et al., 2006). These negative anomalies in benthic foraminifers would in consequence allow the detection of paleo-methane discharge events in sediment sequences by anomalously low $\delta^{13}\text{C}$ values in foraminiferal carbonate. In support of these results, some concluded that under seep

5 settings, $\delta^{13}\text{C}$ of individual specimen show a higher variability (Martin et al., 2004; Rathburn et al., 2003), though the absolute values were not as severely depleted as in other studies (Hill et al., 2003; Hill et al., 2004b; Mackensen et al., 2006). We like to refer the reader to recent papers that give a good and concise overview about the problem in their introductions (Mackensen et al., 2006; Martin et al., 2004).

10 The current uncertainty of how methane fluxes from continental margins have varied in the geological past highlights the need for knowing whether stable carbon isotopes in carbonates faithfully record past and present methane discharges (Archer and Buffett, 2005; Dickens, 2003; Kennett et al., 2000; Kvenvolden and Rogers, 2005; Nisbet, 2002). Given the variety of foraminiferal taxa involved in previous studies and in paleoceanographic research, a better understanding of species-specific responses to high methane concentrations is an important factor. In essence, more studies from methane seep settings are needed to shed light on $\delta^{13}\text{C}$ patterns of benthic foraminifera that thrive at methane seeps or under high organic matter (OM) supply.

3. Study Area and Setting

25 The study area is located at the NE' continental margin of Sakhalin island, a region with more than 200 observed, often continuous, distinct gas flares that are mostly located in water depths between 300 m and 1000 m with (Ginsburg et al.,

1993; Obzhirov et al., 2002). The sites of individual seeps are located at large-scale tectonically active zones and often directly follow active individual faults (e.g. INESSA Shear Zone, Lavrentiev Fault (Ludmann and Wong, 2003; Wong et al., 2003)).

5 Today, the Okhotsk Sea emits methane into the water column and the atmosphere. Methane concentrations in the water column at the NE Sakhalin margin are high, maxima reach 488 to 981 nM kg^{-1} in near-bottom shelf waters (newly formed Dense Shelf Water, 200–300m) between 1998 and 2000 (Yoshida et al., 2004), 10 other studies find anomalies of similar magnitude near localized gas flares with maxima and within near-bottom tidal currents (Obzhirov et al., 2004; Obzhirov et al., 2002). Subsurface and surface concentrations vary widely, they range 15 between 3 (summer) and 385 nM kg^{-1} (before ice breakup), depending on the time of sampling (Lammers et al., 1995b; Yoshida et al., 2004). Emissions to the atmosphere are not well constrained, estimated annual rates are 0.13 Teragrams (Tg), all based on water column measurements and budget 20 calculations (Lammers et al., 1995b). However, other studies report lower concentrations and fluxes of only about 0.01 Tg (Yoshida et al., 2004). These differences of about one order of magnitude result from a number of factors: different 25 sampling years, differing assumptions about the affected areas, calculation factors such as wind speed, and varying methane concentrations at the NE Sakhalin margin on timescales

from hours (tidal currents) to seasons (stratification, ice cover breakup) and years. In any case, these methane fluxes constitute less than 1 % of the present atmospheric annual methane budget (Lammers et al., 1995a). This methane contribution to the northern hemisphere has likely varied and may have been much more prominent during episodes in the past (Obzhirov et al., 2004).

Our sites were chosen from a number of previously identified gas flare areas and have been studied intensively during the past years within the framework of the joint German-Russian Program KOMEX (Kurile-Okhotsk Sea Marine Experiment) e.g. (Lammers et al., 1995a; Matveeva et al., 2003; Obzhirov et al., 2000; Obzhirov et al., 2002; Shakirov et al., 2004; Wallmann et al., 2006). Specifically the Obzhirov Flare area has been monitored for a couple of years within this and other programs carried out by the Gas Geochemistry Group of the Pacific Oceanological Institute, Vladivostok (KOMEX - Methane Monitoring) (Obzhirov et al., 2000; Obzhirov et al., 2002). Methane concentrations in the water column near our Multicorer sites are significantly elevated and vary widely, from less than 8 to more than 860 nM kg⁻¹ in some of the deeper water samples. Sedimentary settings at the Multicorer stations varied from soft sediments with thick bacterial mats and large, rising gas bubbles to sites of authigenic carbonate concretions near the surface with a rich, chemo-autotrophic mollusk fauna.

4. Material and Methods

During Cruise S0178 "SONNE-KOMEX" of R/V SONNE we recovered a set of surface sediment profiles from various cold seep sites at the NE Sakhalin continental margin. From distinct venting areas we sampled two clam fields and one bacterial mat site at Obzhirov Flare. Additionally, we sampled two other bacterial mat sites at the more recently discovered Kitami and Chaos Flares, all with a TV-guided Multicorer System (for site coordinates, see table 1). This device allows the precise sampling of sediment surfaces with real-time video control and retrieves sufficient amounts of undisturbed, continuous sediment surface profiles together with the water-sediment interface and an amount of directly overlying bottom water. Sample recovery is usually eight parallel PVC tubes (9.5 cm diameter, 40 cm length). At all vent sites (bacterial mats and clam fields) methane was seeping into the water column as indicated by the video survey and subsequent methane measurements in the MUC-derived bottom waters (table 1). In some cases we observed distinct gas bubbles ascending from the sediment into the water column. In one case (S0178-46) the ascent of bubbles only ceased some time after the device retrieval at deck. Further details about the site locations and their characteristics are given in the map (Fig. 1) and Table 1. The deployments at each site were filmed and recorded on DVD's; movie sequences showing the actual bottom samplings

are stored at the WDC-MARE together with all other original data and are accessible through the PANGAEA database.

Since we wanted to compare the isotopic composition of benthic foraminifera at different types of methane-venting sites with typical continental margin sites that are rich in OM, we also sampled three margin sites (Fig. 1 and Table 1, Stations 14, 13, 29) outside distinct venting areas. We were sure that no gas seepage or venting processes were active at these non-vent sites due to the deployment of the TV-guided Multicorer. Thus, these „non-vent“ samples are also suited as a kind of sensitivity test of the foraminifera, which live under methane-enriched, but non-venting conditions.

In the following we use the shortened station numbers (e.g. „24“ instead of „S0178-24-1 TV-MUC“) and the abbreviations „BM“ for Bacterial Mat and „CF“ for Clam Field, the term „non-vent“ station refers to the stations outside gas flares (14, 13, 29) but with sometimes elevated CH₄ concentrations, while „background“ values are derived from areas within the Okhotsk Sea that are completely uninfluenced by methane seepage.

Pore and bottom water chemistry

Bottom water samples for isotope analysis and methane concentrations were taken from the lowermost water in the Multicorer tubes immediately after MUC recovery.

For stable isotope analyses of bottom water, we filled 100 ml of water into previously cleaned glass bottles, adding 0.2 ml

of saturated Hg Cl₂ solution to each sample to stop biological activity, and sealed the sample bottles with crimp caps and paraffin. All samples were stored under constant temperature (4 °C) during transport and shore-based storage until analyzed. For measuring the CH₄ content of bottom waters, 200ml were transferred into pre-cleaned, evacuated polypropylene bottles and measured directly onboard with a gaschromatograph according to methods outlined previously (Obzhirov, 1993; Obzhirov et al., 2004).

For pore-water chemical analyses, sediment was sliced into 1 cm-thick slabs in a 4 °C thermo-constant cold room shortly after retrieval, and squeezed with 2–4 bar using a polypropylene apparatus pressurized by argon and equipped with 0.45 µm cellulose acetate membrane filters to separate the pore water from the sediment matrix. Because pore water samples rapidly lose alkalinity during storage, we determined this parameter within some hours after sampling. The other ions proved to be more stable and were thus analyzed during the following days.

Samples for total alkalinity (TA) in pore water were analyzed within 2-3 hours after squeezing by direct titration in an open cell of 1 ml of pore water dispensed in 10 ml deionized water with 0.02 N HCl using the same procedure as with seawater titration (Bruevich's method). Bruevich's method is convenient to work with small sample volumes and avoids the errors caused by H₂S oxidation during titration. The

Brinkman/Dosimat 665 motor-driven piston burette reproducible to ± 0.001 ml in the delivered volume was applied for analysis. Replicate measurements (n=8) indicated stable values, analytical precision is ± 10 mM kg^{-1} for total alkalinity in pore water.

Sulfide samples were conserved with zinc acetate gelatine solution (23.8 mM in Zn acetate) adding 4 ml solution to 1 ml pore water. The Zn-bearing solution was added to fix sulfide as colloidal zinc sulfide whereas the gelatine was used to inhibit ZnS precipitation. The resulting ZnS colloidal solution was mixed with 40 ml phenylen-diamin and 40 ml $\text{FeCl}_3 \cdot 6\text{H}_2\text{O}$ and the absorbance was measured after 10 min to 1 hour at 670 nm using a Hitachi UV/VIS Spectrometer. A linear calibration curve was obtained in the concentration range of 0-57 μM SH_2S . The sulfide standard solution was titrated with sodium thiosulfate to determine the true concentration of the standard. Samples were diluted into the calibration range before reagent addition.

Dissolved phosphate was measured applying standard photometric procedures on a HitachiUV/VIS Spectrometer. Sulfide-bearing samples were acidified with HCl (20 μl conc. HCl per 3 ml sample) and bubbled with nitrogen gas prior to analysis. By this procedure, sulfide was converted into hydrogen sulfide and transferred into the atmosphere. For the analyses of phosphate, 2 ml of pore water sample or standard were diluted with 4 ml deionized Milli-Q water; subsequently 0.1 ml ascorbic acid and 0.1 ml heptamolybdate reagent were

added, and the absorbance was measured after 10 minutes at 880 nm.

Benthic Foraminifera Sampling

Live foraminiferal samples were collected from three parallel Multicorer tubes to provide a representative coverage of the sample area. We analyzed a subset of samples from these three parallel MUC tubes, the isotopic data yielded no significant difference. We are thus confident to report a locally representative dataset (i.e. within the chosen, individual seep structure). After bottom water sampling, the upper 10 cm of sediment were cut in 1 cm slices (if applicable, the upper 2 cm were cut in 0.5 cm slices), transferred to plastic bottles and poisoned with pure Ethanol (p.a.) spiked with rose Bengal. Rose Bengal remains the stain of choice for most micropaleontological studies and is well suited to compare this study's results with other's (Hill et al., 2004b; Mackensen et al., 2006; Martin et al., 2004; Rathburn et al., 2003). However, we are aware of the method's limitations as protoplasm may remain inside the specimen for several weeks after death and thus lead to an overestimation of the „live“ population (see also (Bernhard, 1988) for a comprehensive review of sampling techniques).

Samples were gently washed over a 63 μm sieve, dried and split in size fractions. For isotope analyses, we picked three to seven specimen each from the live and the dead fauna of the following species: *Cibicides* Group (i.e. *Cibicides mundulus*,

Lobatula lobatula), *Uvigerina akitaensis/peregrina*,
Globobulimina spp. (mostly *G. auriculata*), *Nonionellina*
labradorica, *Elphidium batialis*, and *Valvulineria sadonica*.
Due to the differing microhabitat and environmental
5 preferences, not all species were present over the entire
depth profile at each site. Due to the varying settings, at
some sites we did not find sufficient specimen for analysis,
e.g. species with smaller ecological adaptation capabilities
like *V. sadonica* were not present in bacterial mat (BM) sites.
10 We considered specimen as being recently alive if most or all
chambers were stained brightly red. The chosen species are the
most abundant larger species from the >250 μm fractions.
Previous studies pointed to the possible advantages of using
single foraminifera for detecting isotope anomalies in seep
15 settings, we thus measured all live specimen individually.

Before isotope measurements, all specimen were cleaned
manually, and roasted at 240°C for 24h to eliminate possible
contaminations from organic remains in the tests. All
foraminiferal samples were run in the IFM-GEOMAR Stable
20 Isotope Laboratory on a Thermo-Finnigan MAT 252 Isotope Ratio
mass Spectrometer coupled to an automated KIEL II carbonate
preparation device. Calibration is obtained via NBS 19 and 18
standards as well as an intercalibrated internal laboratory
standard of Solnhofen Limestone. External long-term precision
25 for $\delta^{13}\text{C}$ and $\delta^{18}\text{O}$ is $\pm 0.04\%$ and $\pm 0.06\%$, respectively; all

carbonate and water isotope values are reported here as
‰ vs. V-PDB.

5 5. Results

5.1. Site Characteristics and bottom-water chemistry

We grouped all eight sampled sites into three categories:
non-vent (NV), clam-field (CF), and bacterial mat (BM) sites,
10 according to their sedimentary settings as observed with
videocamera during search and sampling. All stations are
labelled with their shortened number, preceded by the group it
belongs to (e.g. S0178-22-1 TV-MUC from a clam field becomes
CF22). Accordingly, non-vent (NV) sites are NV14, NV13, and
15 NV29; clam field sites are CF22 and CF24, and sites with
bacterial mats are BM37, BM38, nad BM46.

At all three NV sites, thick deposits of fluffy phytodetritus
layers existed on top of the soupy sediment-water interfaces.
The thickness varied between 0.5 and 2 cm between the sites
20 (Table 1). Primary productivity and export production is
generally high in the Okhotsk Sea, as indicated by summer
chlorophyll a concentrations in surface water of about 3-5 mg
 cm^{-3} for the southern NV13 site and higher concentrations of 7-
12 mg cm^{-3} for the two northern locations (NASA, online SeaWiFS
25 dataset 1998). Sediments at all sites generally consisted of
clayey-silty diatom ooze with with radioalarians,

foraminifera, and rare lithogenic sand particles and nannoplankton. These sites showed no signs of direct methane discharge, but are partly under the influence of elevated methane concentrations in the bottom water. This flux could be generated *in situ* by AOM in the uppermost parts of the sediment with high supply of OM, however we found no additional evidence for this assumption in the multicorer pore-water profiles. More likely and in agreement with mapping of methane anomalies in the water column (A. Obzhirov, unpublished data), these elevated concentrations are caused by lateral transport of methane from flares to the non-vent locations with strong near-bottom tidal currents (Fukamachi et al., 2004; Obzhirov et al., 2002).

At CF sites, we sampled a wide size range of chemoautotrophic mollusks (some cm to less than a few mm) mainly of the genus *Thyasiridae*, with lower abundance of *Calyptogena* spp. (H. Sahling, pers. comm.). Carbonate concretions were abundant throughout the whole multicorer-profile at both CF sites, often building irregularly shaped, elongated clasts with wave-like surfaces and a light-medium gray color, ranging in size between less than one centimeter and large pavement-like structures that made sampling these chemoherm-clam fields difficult with the Multicorer, resulting in the recovery of only a few tubes at the CF sites. Lithologies and characteristics resemble carbonates previously described as cemented bioturbation casts in a semi-consolidated sediment

matrix (Greinert et al., 2001; Greinert and Derkachev, 2004). These are built synsedimentary with high contents of high-Mg calcite and aragonite. Stable isotope samples we measured from selected specimen clearly show the dominant influence of methane-derived carbon (MDC) with $\delta^{13}\text{C}$ values between -39 ‰ and -47 ‰. Due to the abundance of mollusks, carbonates, and other organisms, the structure of the CF sites is porous with uneven sediment surfaces and sometimes not clearly definable sediment-water interfaces.

The three sites covered with bacterial mats showed visible flux of gas bubbles during sampling at the seafloor and in some cases, the ascent of bubbles only ceased some time after retrieval of the cores at deck. Bacterial mats were evenly distributed at the sampling sites with diameters of more than a few meters. The thickness of the grey to white bacterial mats varied in thickness between a few millimeters and one centimeter, while completely covering all MUC-cores at the sediment-water interfaces.

The hydrography of the overlying bottom waters is rather uniform at all stations, independent of CH_4 influence by ascending fluids or bubbles (Table 2). Bottom water temperatures lie between 2.17 and 2.34 °C and salinities range between 34.05 and 34.10, indicating uniform hydrographic conditions, with the exception of NV14 where we measured a higher salinity of 34.41.

Methane concentrations vary largely between the different sites from near-background values at NV14 with 4.39 nM kg⁻¹ to highly elevated CH₄ concentrations of 1570.97 nM kg⁻¹ at BM37 (Table 2). The former is comparable to background values in the Okhotsk Sea that vary between ca. 0.5 and 0.9 nM kg⁻¹ for water masses deeper than approximately 1000 m. However, the CTD profile at the same station shows distinct methane anomalies of 8.70 to 46.66 nM kg⁻¹ in water depths between 150 and 800 m (A. Obzhirov, unpubl. data), confirming that methane-enriched intermediate water layers are advected from the shelf areas with abundant cold seeps comparable to the BM and CF sites we sampled for this study.

Both shallower NV sites have according CH₄ concentrations of 37.83 and 49.10 nM kg⁻¹, indicating that these sites are bathed in waters from actual vent sites, though no venting occurs at the actual locations. Clam field site CF22 yields a slightly higher CH₄ concentration of 64.58 nM kg⁻¹. The influence of methane flux from these locations may be thus not very large in comparison to sites with bubble ascent and bacterial mats. Indeed, at Hydrate Ridge flux studies show that clam fields emit three to fifteen times less methane than sites that are colonized by continuous bacterial mats (Sommer et al., 2006; Torres et al., 2002). These results are generally in correspondence with our two-, 15- and 24-fold increases in CH₄ concentrations between CF and BM sites.

At the bacterial mat (BM) stations of all three flares CH₄ concentrations within the bottom water layer were more

variable than at CF and NV sites. While CH₄ concentrations were only about twice as high at BM38 (Chaos Flare) than at CF22 or NV29, BM sites 46 (Obzhirov Flare) and 37 (Kitami Flare) yielded ten- to fifteen-fold concentration increases to values of 969.98 and 1570.97 nM kg⁻¹, respectively.

While these CH₄ concentrations are significant anomalies and reflect a highly supersaturated inventory in the water column in relation to the atmosphere, their influence on the carbonate chemistry is obviously too low by some orders of magnitude to affect δ¹³C_{DIC} of bottom waters and DIC concentrations significantly (CH₄ in nM kg⁻¹ vs. DIC in mM kg⁻¹). Only BM37, with the highest CH₄ flux, has a depleted δ¹³C_{DIC} signal of -0.92 ‰, compared to the other sites with uniform δ¹³C_{DIC} between -0.61 ‰ and -0.73 ‰ (within the error range), independent of the setting. To put the latter data in perspective, however, we note that these values are already lower than in previous studies that reported δ¹³C_{DIC} values ranging between -0.2 ‰ and -0.5 ‰ for the NE Sakhalin margin and the central Okhotsk Sea (Bauch et al., 2002; Itou et al., 2003). We therefore cannot rule out that all our δ¹³C_{DIC} values are depleted, possibly through the influence of methane-derived carbon (MDC) on the water column's DIC or by lacking intermediate water ventilation in the previous cold season.

Oxygen concentrations at two of the NV sites and the CF site are rather uniform; a slightly lower concentration of 54.7 μM at NV29 may be related to the maximum in phytodetritus deposition as well as the highest CH₄ concentration. Site NV14

has the lowest O₂ content of all sites as well as the lowest CH₄ levels, indistinguishable from background values. We ascribe this O₂-Minimum to a slightly deeper location of NV14 (more than 1100 m) directly at the Sakhalin margin, while the other sites are located less deep. In fact, hydrocast data from the same station 14 yielded rapidly decreasing values of 67.4 μM (699 m), 49.2 μM (798 m), and 33.2 μM (898 m) within that depth range. This supports the existence of a hydrographic boundary at the Sakhalin margin between water depths of 700 to 1000 m, with better ventilated and less saline, newly formed intermediate water masses above that depth.

At the CF sites, we only were able to determine O₂ concentrations at CF 22, as CF24 did not yield enough full and entirely closed MUC tubes upon recovery. Due to the similarity of the two sites we assume in the following the results for CF22 as being representative for CF24, too. Bottom waters above CF sites are relatively well oxygenated, comparable to NV sites. Two bacterial mat sites are slightly depleted in O₂, in accordance with stronger flux of gas into the water column and the occurrence of sulphate-reducing bacterial consortia. However, at site BM46 we observed higher O₂ concentrations than at all other sites as well as less negative δ¹³C_{DIC} values and the second highest CH₄ concentration, despite this site containing MUC tubes upon recovery still visibly bubbling from gas flux out of the sediment. In line with our observations,

we originally thought that BM46 would be the most O₂-depleted and CH₄-enriched site, contrary to the results. We tried to sample all bottom waters as closely to the sediment-water interface as possible, but we think that the abundant gas bubbles in this case may have lead to enhanced mixing with the rest of the bottom water column (ca 30 cm in the tubes) in the MUC tubes before sampling or with ambient water masses upon retrieval, thus leading to bottom water samples less depleted in O₂ and less enriched in CH₄. With regard to foraminiferal species adaptations, all sites would be classified as a suboxic habitat. The exception is anomalous site BM46 that would be classified as a low-oxygen setting, in clear contrast to all other bottom and pore water data from this location.

5.2. Pore-water profiles

The pore water data (Fig. 2) give evidence for rapid anaerobic methane oxidation (AOM) and complex mixing processes. Dissolved sulphate remained close to seawater values in the upper 5 cm and was rapidly consumed below that depth due to AOM. However, sulphate was not completely depleted and at one site sulphate concentrations increased again in the lower portion of the core. Total alkalinity and dissolved sulphide showed similar trends confirming that AOM was focused to a narrow sediment horizon at about 10-20 cm depth (Fig. 2). In the over- and underlying sediment horizons,

transport processes overprinted any sign of sulphate reduction, sulphide production and alkalinity generation. At station BM37, Ca and Mg concentrations measured indicated carbonate precipitation within the AOM zone (M. Haeckel, pers. comm.). Nutrient concentrations were generally low, confirming that sulphate was not reduced via degradation of particulate OM but rather by AOM. The high sulphate and sulphide concentrations at the base of the profiles show that methane is not delivered by rapidly ascending fluids because pore waters in the northern Sakhalin Slope area are essentially sulphate-free and sulphide-depleted at sediment depths of several meters (M. Haeckel, pers. comm.). Hence, methane is not supplied by deep fluids but rather by rising gas bubbles. The ascent of gas bubbles was directly observed at the seafloor during TV-MUC dives and is documented through numerous hydroacoustic measurements. Within the soft upper sediment layers, rising gas bubbles can induce eddy-diffusive mixing so that seawater is mixed into the surface sediment. Moreover, small-scale convection cells may be established by rising bubbles and by hydrate formation in underlying sediment layers adding further complexity to the transport processes prevailing in the studied surface sediments. It is thus likely that the increase in dissolved sulphate at the base of the multicorer sediments is caused by a hydrate-driven convection cell.

On the basis of these pore-water data and bottom water CH₄ concentrations, we assign to our stations an order of increasing methane derived carbon (MDC) influence: NV14, NV13, NV29; then followed by increasingly direct influence of

methane venting activity on the environment: CF22, CF24; BM38, BM46, BM37. The stations are shown in this order of increasing methane venting in figures 7 and 8 and in the tables 1–3.

5.3 Stable isotope data

5.3.1. Site-specific original $\delta^{13}\text{C}_{\text{FORAM}}$ data

We plotted the site-specific original $\delta^{13}\text{C}$ data of all species against depth, grouped into NV sites (Fig. 3), CF sites (Fig. 4), and BM sites (Fig. 5). We also compare the $\delta^{13}\text{C}$ characteristics of our sites to „background“ values without any methane influence for each species (Fig. 3–5). Commonly these background values are derived from established studies on benthic foraminifera (e.g. McCorkle et al., 1997; McCorkle et al., 1990; Rathburn et al., 2003). We prefer to use average values of datasets from the same region (Table 3). These are derived from depth profiles of rose Bengal-stained benthic foraminiferal assemblages from 20 sites located at the continental margins of the Okhotsk Sea; the complete species assemblage and isotope data are reported separately (Biebow et al., 2002, Bubenchshikowa et al., subm.).

Non-Vent Sites (stations NV14, NV13, and NV29)

Epibenthic *Cibicides* spp. are commonly expected to record the $\delta^{13}\text{C}_{\Sigma\text{CO}_2}$ of ambient bottom waters (Corliss et al., 2002;

Mackensen et al., 2000; McCorkle et al., 1997; McCorkle et al., 1990). At our NV sites, *Cibicides* spp. at all three locations are rather indistinguishable from each other and mainly range between -0.2 and -0.5 ‰, which is slightly above the $\delta^{13}\text{C}_{\text{DIC}}$ of bottom waters. In the case of these stations we decided to report some additional values of only weakly stained specimen from greater sediment depths that possibly were not alive at the time of sampling. However, despite this loosened quality criteria, no offset between the brightly stained specimen (within the upper 2 cm sediment) and deeper buried, weakly stained ones, is evident (Fig. 3). The widest scatter of $\delta^{13}\text{C}_{\text{Cib.}}$ occurs at station NV29, the most CH_4 -enriched location, independent of sediment depth. We did not correct for eventual species-specific offsets between *C. mundulus* and *L. lobatula*, as we have no sufficient regional data to specify a potential offset in detail. $\delta^{13}\text{C}$ of *U. peregrina* and *V. sadonica* cannot be distinguished from background values, they range between -0.9 ‰ to -1.4 ‰, and -0.8 ‰ to -1.2 ‰, respectively, both with a relatively narrow scatter of data. However, at station NV29, two *V. sadonica* show anomalously negative values of -1.6 ‰ and -2.4 ‰. Both species occur at nearly all samples throughout the complete sediment profile, but do not show depth-related trends in $\delta^{13}\text{C}$, in line with concepts for isotope incorporation at specific microhabitat depths, though migration of specimen happens throughout the inhabited upper sediment column; McCorkle, 1990 #296;

Mackensen, 2000 #214]. Scatter of single datapoints is wider than previously reported from pooled samples of other studies, (e.g. McCorkle et al., 1997, amongst a number of studies) but we ascribe most of this variability to the fact that single-specimen analyses show natural intra-sample deviations of 0.2 ‰ within a population. Together with the highly variable natural background settings in the Okhotsk Sea like seasonal sea ice cover, large inter-annual OM flux changes, these factors can account for larger intra-sample variability in all three species. The above-average scattered *Cibicides* spp. data in particular may be due to single-specimen measurements due to small masses of individual samples, so standard deviations within the this group are a bit larger due to technical limitations with smaller sample gas volumes on the IRMS.

In NV 14, we only found two specimens of *E. batialis*, both with $\delta^{13}\text{C}$ closely matching background values. At NV13 in contrast, *E. batialis* occurred down to a depth of 4.5 cm with a large scatter in $\delta^{13}\text{C}$, ranging from -1.53 ‰ to less than -2.60 ‰. At NV29, intra-specific variability was large as well (-1.57 ‰ to -2.68 ‰), however the species apparently did not reach the MLD within the upper 11 cm but occurred throughout the profile. *E. batialis* shows the most negative $\delta^{13}\text{C}$ under NV settings, in line with background averages (Table 3).

G. auricuata is abundant in all three NV stations, but occurs mostly deeper within (i.e. below ca. 5cm b.sf.) the sediment. At sites NV13 and NV14, $\delta^{13}\text{C}_{\text{Ga}}$ varied in a similar way between -

0.78 ‰ and -1.71 ‰, with NV13 having slightly lighter values (Fig. 3). In contrast to these two sites at NV29 specimen occurred also within the upper sediment column and had slightly lighter values between -1.20 and -2.56‰. As we found 5 *G. auriculata* specimen in the deepest samples at all sites, we assume that more specimen may live even deeper (>12 cm b.sf.) in the sediment.

We found *N. labradorica* in low abundances only at site NV13 and NV29, with $\delta^{13}\text{C}$ values mirroring background values at NV13, 10 and slightly depleted values of two specimens at NV29 (-1.86 ‰ and -1.75 ‰ vs. -1.2 ‰). In accordance with the isotope data, the MLD of *N. labradorica* seemed to vary considerably at both sites, as at NV13 we probably did not reach the MLD, while at NV29 *N. labradorica* occurred only in the upper 2 cm.

15 Taken together, distribution and isotope values suggest that site NV29 is set apart from the other two NV sites in that endobenthic species stay distinctly deeper in the sediment column than at other sites (Fig. 3). The larger number of isotopically lighter endobenthics buried deeper in the 20 sediment shows that deep endobenthics have ecological advantages in living (i.e. calcifying) at greater sediment depths at site NV29. However, the $\delta^{13}\text{C}$ results from the NV settings were not depleted enough to support factors other than high OM flux with associated O_2 pore-water gradients in 25 influencing $\delta^{13}\text{C}$ (McCorkle et al., 1997; Stott et al., 2002),

regardless of the elevated CH_4 concentrations we found in the bottom waters of NV13 and NV29 (Table 2).

Clam Field Sites CF22 and CF24

5 The two Clam Field Sites we sampled were both characterized by very uneven sediment surfaces, with numerous chemoautotrophic mollusks with sizes ranging between a few millimeters and several centimeters. Some stained specimen were found in the >1000 μm fractions of the foraminiferal 10 samples, indicating active methane seepage at the locations at the time of sampling.

15 Compared to NV settings, foraminiferal absolute $\delta^{13}\text{C}$ values are lower at the CF sites. At both sites we found rather abundant *C. mundulus* and also a few *L. lobatula*, with a MLD of about 4 to 5 cm b.sf. This distribution is likely due to the very porous and channel-like structure of the sediments formed by densely packed mollusk shells, thus creating internal sediment-water interfaces below the actual sediment surface where epibenthic species can thrive. $\delta^{13}\text{C}_{\text{CIB}}$ at CF22 range 20 between -0.07 and -2.28 ‰, with a mean of -1.10 ‰, slightly depleted against the $\delta^{13}\text{C}_{\text{DIC}}$ of -0.63 ‰. At CF24 no $\delta^{13}\text{C}_{\text{DIC}}$ information is available, but $\delta^{13}\text{C}_{\text{CIB}}$ is slightly higher than at CF22, with a range between -0.87 ‰ and 0.01 ‰ and a mean of - 0.54 ‰. While these changes are not large, compared to the 25 non-vent sites with similar CH_4 concentrations, $\delta^{13}\text{C}_{\text{CIB}}$ are lower at CF sites and more unevenly distributed.

$\delta^{13}\text{C}$ data of *U. peregrina* show a wide scatter at both sites without depth gradients. While in CF22 we observed a MLD of 6-7 cm b.sf., we found *U. peregrina* even in the deepest samples (11 cm b.sf.). Thus, we may have missed individuals living deeper buried in the sediment. Individual tests range from -2.15 ‰ to -0.93 ‰ at CF22 and from -2.16 ‰ to -1.11 ‰ at CF24 with averages of -2.12 ‰ and -1.57 ‰, respectively. In remarkable contrast to the NV sites, $\delta^{13}\text{C}$ values of *G. auriculata*, and *N. labradorica* are nearly similar to *U. peregrina* at both CF sites, implying that under CF vent conditions, these species calcify under rather similarly.

Bacterial Mat Sites BM 38, BM46, and BM37

As mirrored in the pore-water profiles, BM settings are unfavorable conditions for most foraminiferal species. While we do not report on species composition or abundance data, for clarity we note that in the three BM sites, abundances of all taxa are much lower than at all other sites. All species were at or near their MLD within the depth ranges of the three profiles. At all sites we found rare (between one and three) specimen of *C. mundulus*, which showed widely scattered $\delta^{13}\text{C}$.

At BM38, a single *C. mundulus* within the top layer had -0.89 ‰, while at BM46 two *L. lobatula* within the upper 2cm had values of -0.28 and -0.38 ‰. At BM37, with the highest CH_4 -flux, two specimens from the upper centimeter yielded $\delta^{13}\text{C}$ values of -0.79 ‰ and -1.88 ‰, respectively. In general, these

values correspond to the $\delta^{13}\text{C}_{\text{DIC}}$ of the sites, which is not extremely depleted.

Likewise, specimen of *V. sadonica* and *G. auriculata* are rare in all three sites. *V. sadonica* was absent in BM46 and *G. auriculata* in BM46. We cannot derive detailed information about MLD's from these few specimens, but all were found within the upper 3 to 4 cm of the sediment column. Results show that $\delta^{13}\text{C}$ mostly mirrors background values, which in connection with the low abundance, lets us suspect that these two species do not calcify under vent conditions at the BM sites. Likely, these specimens were either dead for some time or alternatively change into dormancy since the onset of intense methane venting.

U. peregrina is relatively abundant and was the only species that we found at all sites (not considering the sole *Cibicides* in BM38). The MLD of *U. peregrina* may be coupled to changes in alkalinity, phosphate, and sulphide within the pore-water, with steeper or shallower gradients being more important than absolute values. Decreasing MLD from 8 cm in BM38 to less than 3-5 cm in BM37 (Fig. 3) corresponds with roughly similarly increasing H_2S , PO_4 and alkalinity (Fig. 2). At all three sites, $\delta^{13}\text{C}_{\text{UP}}$ is less depleted than at the CF sites and more comparable to NV and even background values (Fig. 3). At BM37, $\delta^{13}\text{C}_{\text{UP}}$ seems to be more variable in the uppermost part of the sediment column, where $\delta^{13}\text{C}_{\text{UP}}$ varies between -0.10 ‰ and -1.59 ‰, whereas below 1.5 cm $\delta^{13}\text{C}$ ranges between -1.23 ‰ and -

1.43 ‰. A broad, singular $\delta^{13}\text{C}$ cluster between 2 and 3 cm b.s.f. reflects a local H_2S minimum in the pore-water profile (Fig. 2), however, given the few datapoints, these features may well occur by pure chance.

5 Interestingly, in the two BM sites with lower vent activity, only one species in addition to *U. peregrina* occupies the deeper sediment column habitat in relatively high abundances. At BM38, it is *E. batialis*, while at BM46 this is *N. labradorica*. In both cases, these species also display the
10 most negative $\delta^{13}\text{C}$ values reaching less than -3 ‰ in individual samples. In BM37, however, with the highest CH_4 flux, both species co-occur but are restricted to the uppermost sediment column and small numbers. This indicates that they near their limits for survival in that particularly active vent setting.

5.3.2. Normalized oxygen and carbon isotopes

15 In order to assess and compare foraminiferal $\delta^{18}\text{O}$ and $\delta^{13}\text{C}$ independent of the local hydrographic properties, in the following we refer to normalized $\delta^{18}\text{O}$ and $\delta^{13}\text{C}$ values. Normalized $\delta^{13}\text{C}$, which we refer to as $\Delta\delta^{13}\text{C}$, is the foraminiferal $\delta^{13}\text{C}_{\text{calcite}}$ from which we subtract the $\delta^{13}\text{C}_{\text{DIC}}$ of bottom water (Table 2). For normalized $\Delta\delta^{18}\text{O}$, we subtract from
20 the foraminiferal $\delta^{18}\text{O}_{\text{calcite}}$ the $\delta^{18}\text{O}_{\text{ec}}$ value for equilibrium calcite, calculated from the measured bottom water $\delta^{18}\text{O}_{\text{water(SHOW)}}$

and temperature. For this latter calculation we use the curve fit of (Shackleton, 1974) for the data of (O'Neil et al., 1969) and the conversion factor for V-SMOW to V-PDB of (Hut, 1987). The isotope data of all stations are shown as $\Delta\delta^{18}\text{O}-\Delta\delta^{13}\text{C}$
5 scatter plots, grouped into species (Fig. 6). Statistical patterns (median, quartiles, etc.) for each species and station are shown in box and whisker plots for $\Delta\delta^{13}\text{C}$ (Fig. 7 and 8) and are completely listed in table 4. As previous studies hypothesized that a larger scatter of individual
10 values may indicate methane vent settings, we also routinely show and discuss the standard deviations (s) and ranges (min. - max.) of values (Table 4 and Fig. 6-9).

Cibicides spp.

15 *Cibicides* spp. show relatively small variability at NV sites, there $\Delta\delta^{13}\text{C}_{\text{Cib}}$ means range between 0.20 ‰ and 0.31 ‰ with standard deviations σ between 0.18 and 0.23 (Table 4). Likewise, results for $\Delta\delta^{18}\text{O}_{\text{Cib}}$ show negative offsets to $\Delta\delta^{18}\text{O}_{\text{ec}}$ with means between -0.13 ‰ and -0.55 ‰, and with σ between
20 0.10 and 0.34. While both $\Delta\delta^{13}\text{C}_{\text{Cib}}$ and $\Delta\delta^{18}\text{O}_{\text{Cib}}$ show offsets, σ are within values comparable to previous studies (McCorkle et al., 1997; McCorkle et al., 1990). However, the data shows that *Cibicides* spp. at NV sites does not calcify in equilibrium with seawater $\delta^{18}\text{O}_{\text{ec}}$.

25 $\Delta\delta^{13}\text{C}_{\text{Cib}}$ for clam field sites CF22 and CF24 are depleted relative to NV sites with mean values of -0.47 ‰ and 0.09 ‰,

respectively, and significantly larger σ for CF22 (0.58) and only slightly larger σ for CF24 (0.24). Due to the few specimens, we summarized all values for bacterial mat sites under one designation (BM, Table 4, Fig. 7), though this influences statistical integrity. Individual $\Delta\delta^{13}\text{C}_{\text{cib}}$ at BM sites seem not much depleted relative to NV sites (Fig. 6), though mean values of -0.15‰ are a bit lower than those of NV sites and have a significantly higher σ of 0.52 (Table 4). As expected, $\Delta\delta^{18}\text{O}_{\text{cib}}$ show no significant change between non-vent and vent conditions, though the range of $\Delta\delta^{18}\text{O}_{\text{cib}}$ and σ is larger at BM sites (Table 4), but this may be an artefact of the low number of individuals, combined with the pooling of all three BM sites.

15 *V. sadonica*

This species is not well investigated so far, however it constantly occurs in many locations in the Okhotsk Sea (Bubenchshikova, pers. comm.) and as it can be often found in sediment core section where both *U. peregrina* and *Cibicides* spp. are absent, may justify further study to determine its suitability as isotope proxy. $\Delta\delta^{13}\text{C}_{\text{vs}}$ are depleted, NV results may indicate calcite precipitation rather close to bottom water $\delta^{13}\text{C}_{\Sigma\text{CO}_2}$ with mean values between -0.26 and -0.46‰ and small scatter ($\sigma=0.02-0.19$). This is a small negative offset compared to $\delta^{13}\text{C}_{\text{DIC}}$, whereas *Cibicides* spp. show a comparable positive offset. We tentatively assume that $\Delta\delta^{13}\text{C}_{\text{vs}}$ results may

be due to a phytodetritus-induced depletion in $\delta^{13}\text{C}_{\text{DIC}}$. Three specimen from CF22 are significantly depleted by -0.95‰ , indicating influence of MDC on the $\Delta\delta^{13}\text{C}_{\text{vs}}$, though the species apparently does not thrive under methane vent settings (low abundances in CF and BM sites). However, $\Delta\delta^{18}\text{O}_{\text{vs}}$ is nearly in equilibrium with $\delta^{18}\text{O}_{\text{ec}}$ at all sites with means between -0.28‰ and $+0.11\text{‰}$ and σ between 0.09 and 0.28, regardless of the settings. In fact, *V. sadonica* in this sample set is the species closest to $\delta^{18}\text{O}_{\text{ec}}$, while both *U. peregrina* and *Cibicides* spp. that are commonly used for paleoceanographic reconstructions, show small but distinct offsets (fig. 6, table 4).

U. peregrina

15 At NV sites, *U. peregrina* has a narrow range of slightly depleted $\Delta\delta^{13}\text{C}_{\text{up}}$ between -0.26‰ and -0.46‰ . We note that $\Delta\delta^{13}\text{C}_{\text{up}}$ values decrease and σ increases at NV29 with elevated CH_4 concentrations, independent of supposedly similar OM fluxes at sites NV14 and NV29. $\Delta\delta^{13}\text{C}_{\text{up}}$ show larger depletions at clam fields CF22 and 24 (-1.49‰ and -0.95‰ , respectively) than at all sites with bacterial mats (-0.38‰ to -0.77‰). Standard deviations are small and comparable at NV sites ($\sigma = 0.13-0.16$), and grow larger at sites of methane venting, independent of the type ($\sigma = 0.24-0.39$, Table 4). An exception is site BM37, with the maxima in CH_4 and pore-water H_2S

concentrations, where $\Delta\delta^{13}\text{C}_{\text{UP}}$ (-0.38 ‰) and σ (0.17) are statistically similar to NV sites.

Single $\Delta\delta^{18}\text{O}_{\text{UP}}$ are seemingly scattered more than 0.5 ‰ (Fig. 6), especially from NV14 and NV29. $\Delta\delta^{18}\text{O}_{\text{UP}}$ values are enriched by 0.24-0.39 ‰ (with NV13 as an exception), independent of the setting, and are thus not in equilibrium with water $\delta^{18}\text{O}_{\text{ec}}$. Due to the large number of specimen in this dataset, the sites form visibly distinct clusters (Fig. 6). Clam field sites CF22 and 24 show pronounced shifts towards depleted $\Delta\delta^{13}\text{C}_{\text{UP}}$ and narrower $\Delta\delta^{18}\text{O}_{\text{UP}}$ ranges, while the northern Non-Vent sites NV14 and NV29 indicate a broadened $\Delta\delta^{18}\text{O}_{\text{UP}}$, but smaller $\Delta\delta^{13}\text{C}_{\text{UP}}$ range. Data from individual BM sites overlap with other sites and intermingle with the other two settings (Fig. 6).

E. batialis

This species represents a special case in its isotopic characteristics. Large $\Delta\delta^{13}\text{C}_{\text{EB}}$ offsets are apparent for all sites, including non-vent conditions and range between -1.28 ‰ and -1.86 ‰ (Table 4). Standard deviations are high for all sites (0.27-0.54), with a slight increase towards BM sites. Minimum $\Delta\delta^{13}\text{C}_{\text{EB}}$ values are near -2 ‰ at all sites, indicating strong secondary (microhabitat or "vital") effects on $\delta^{13}\text{C}_{\text{EB}}$ composition.

Following the $\Delta\delta^{13}\text{C}_{\text{EB}}$ results, $\Delta\delta^{18}\text{O}_{\text{EB}}$ mean values are more depleted than in the other species, with values between -0.44 ‰ and -0.71 ‰, and become more depleted with increasing

vent activity (Table 4). However, standard deviations remain within accepted ranges for all sites (0.10-25) with the exception of BM38 with $\sigma = 0.42$. From the individual data (Fig. 6), we checked if *E. batialis*' $\Delta\delta^{18}\text{O}$ and $\Delta\delta^{13}\text{C}$ values are positively correlated, regardless of individual sites. A linear regression through all data gives:

$$f(x)_{\text{all}} = -0.4484 + 1.7508 x \quad r = 0.72 \quad (1)$$

Restricting the regression to the site (BM38) with most pronounced covariance gives:

$$f(x)_{\text{BM38}} = -0.9112 + 1.3321 x \quad r = 0.87 \quad (2)$$

We checked all datasets for similar correlations, but found no species that displayed sufficiently high correlation coefficients. In some instances, though, single sites indicated positively correlated $\Delta\delta^{18}\text{O} - \Delta\delta^{13}\text{C}$ relationships. However, we assume that "vital" effects hold for all specimens of a given species, regardless of the setting. Except for *E. batialis* this was not the case.

G. auriculata

G. auriculata shows decreasing $\Delta\delta^{13}\text{C}_{\text{GA}}$ mean values with increasing vent activity, from -0.47 ‰ at Site NV14 to -1.73 ‰ at the combined BM46 and BM37 sites. Standard deviations match

this behavior, with steadily increasing σ from 0.27 to 0.39 at NV sites, to 0.44 and 0.48 at CF sites, up to 0.96 at the combined BM sites (Table 4). While individual $\Delta\delta^{13}\text{C}_{\text{GA}}$ from different settings overlap in their $\Delta\delta$ O-C characteristics (Fig. 6), trends to more negative disequilibria $\Delta\delta^{13}\text{C}_{\text{GA}}$ are visible. While individual values may suggest O-C covariance as observed in *E. batialis*, regressions remain rather insignificant ($r_{\text{max}}=0.32$ for all sites) and are not shown here. Accordingly, $\Delta\delta^{18}\text{O}_{\text{GA}}$ mainly varies on a small scale between 0.40 ‰ and 0.43 ‰, with of NV13 (0.63) and BM37+46 (0.28) as the minimum and maximum means. Related σ vary between 0.09 and 0.41, without correspondence to different settings.

Thus, *G. auriculata* shows a systematically decreasing $\Delta\delta^{13}\text{C}_{\text{GA}}$ mean values with increasing vent activity with relatively small intra-sample variability.

N. labradorica

This species does not occur at all stations in abundance, accordingly we had to group it into one CF setting (with CF22 and 24) and a NV setting (combined NV13 and 29).

$\Delta\delta^{13}\text{C}_{\text{NL}}$ is depleted by an average of -0.83 ‰ in NV settings, with a range (-1.15 ‰ to -0.44 ‰) comparable to other endobenthic species. At clam fields, $\Delta\delta^{13}\text{C}_{\text{NL}}$ are further depleted by about -0.5 ‰ to -1.28 ‰ (mean). *N. labradorica* shows two different patterns at the BM sites. At BM46, where the species apparently thrives, it incorporates very negative

$\delta^{13}\text{C}$, leading to mean $\Delta\delta^{13}\text{C}_{\text{NL}}$ of -2.01 ‰, the most negative average $\Delta\delta^{13}\text{C}$ we encountered in this study, together with a rather large σ of 0.77. At BM37 however, $\Delta\delta^{13}\text{C}_{\text{NL}}$ is on average less depleted than at all other vent locations. Mean $\Delta\delta^{13}\text{C}_{\text{NL}}$ values and σ match the ones of NV sites with -0.83 ‰ and 0.40, respectively.

Notably, we observe systematically decreasing $\Delta\delta^{18}\text{O}_{\text{NL}}$ averages and standard deviations from -0.83, $\sigma = 0.24$ (NV13+29) to -0.72 ‰, $\sigma = 0.90$ (BM37) with increasing vent activity (Table 4).

6. Discussion

6.1. Gas venting at the N' Sakhalin Slope and its influence on $\delta^{13}\text{C}_{\text{foram}}$

At the vent sites, pore-water geochemistry and CH_4 concentrations suggest conditions comparable to those at other typical vent locations that have previously been the topic of benthic foraminiferal $\delta^{13}\text{C}$ studies (Hill et al., 2004b; Mackensen et al., 2006; Rathburn et al., 2003; Torres et al., 2003). In the Okhotsk Sea, methane concentrations in the order of 1,000 nM kg^{-1} have often been reported in the water column within flare zones and near actual methane seepage from the sea floor (e.g.: Biebow et al., 2002; Obzhirov, 1993; Obzhirov

et al., 2004). Together, these facts show that we sampled representative locations for each (NV, CF, BM) of the characteristic settings of methane seepage (Torres et al., 2002).

5 However, at most vent locations, CH₄ flow rates vary on timescales between hours and years (Obzhurov et al., 2004; Sommer et al., 2006; Torres et al., 2002; Yoshida et al., 2004) and large differences exist in flux estimates e.g. (Luff and Wallmann, 2003; Torres et al., 2002), with short-term
10 changes between dormant and high seep activity ascribed to tidal dynamics, alternating bubble dynamics, current conditions and stratification patterns (Heeschen et al., 2005; Torres et al., 2002). As we took only a “snapshot” with our MUC-sampling, direct comparisons of fluxes are precluded and
15 we thus cannot reliably assess, during which exact periods of seep activity foraminifera secret their tests (Torres et al., 2003).

Our normalized $\Delta\delta^{13}\text{C}$ data show that in environments with no methane venting but elevated CH₄ concentrations in bottom
20 waters (NV settings), all species show offsets that are in accordance with their inferred microhabitats and calcification depths preferences (Fig. 7). We observed no differences between background values and absolute $\Delta\delta^{13}\text{C}_{\text{foram}}$ at NV sites (Fig. 3). Absolute and normalized values mean values from NV
25 sites are in agreement with the data others have reported from Pacific locations at continental margins. While not all

species we studied have been dealt with before (McCorkle et al., 1997; McCorkle et al., 1990; Rathburn et al., 1996), closely related species exhibit very similar values. *Cibicides* spp. are e.g. close to or slightly above equilibrium in
5 ($\Delta\delta^{13}\text{C}_{\text{Cib}}$ at NV sites. The same similarities are apparent for *U. peregrina*, while *G. aff. pacifica* and *E. excavatum* show larger depletions in (McCorkle et al., 1997) relative to the species we studied (*G. auriculata* and
10 *E. batialis*, respectively). These differences may be due either to species-specific offsets or to the extremely high OM supply and thick phytodetritus deposits we encountered at the NV sites.

At the clam fields (CF) all species show a distinct depletion
15 in $\Delta\delta^{13}\text{C}$ and a wider range (σ) within the data. The isotopic composition within the species assemblage experiences a negative shift of about -0.2 ‰ to -1 ‰ (Fig. 7), relative to NV conditions. Interestingly, this negative anomaly in all taxa shifts the epibenthic *Cibicides* spp. into the domain of
20 the shallow endobenthic *U. peregrina* in NV settings, while the latter now ranges within the values for deep endobenthics under NV settings (Fig. 7).

These results from CF sites support that, in general, benthic foraminifera record elevated methane concentrations through
25 depleted absolute and normalized values (Hill et al., 2004b; Mackensen et al., 2006), as well as through higher scatter of

individual $\delta^{13}\text{C}$ values (Rathburn et al., 2003). However, the methane concentrations at CF sites with depleted $\Delta\delta^{13}\text{C}$ values is rather small and in magnitude more comparable to our NV sites rather than to more significant methane emissions from the BM sites. Clam fields at cold seeps are not necessarily strong emitters of methane into the water column. In fact, recent studies have shown that the benthic fauna acts as highly efficient filter, consuming the majority of methane released by upward fluid flow (e.g. Sommer et al., 2006; Torres et al., 2002). In addition, empirical and modelling data e.g. from other locations (e.g. Hydrate Ridge) imply that at least temporally downward fluxes of seawater into the sediment column occur especially at clam fields, thereby creating small convection cells within a seep area or fostering lateral fluxes within the sediment column (Linke et al., 2005; Torres et al., 2002; Tryon et al., 1999). In line with these more sophisticated studies, our pore water profiles and CH_4 concentrations suggest at least about an order of magnitude stronger methane fluxes from BM than from CF (or NV) sites, corroborated by independent modelling and empirical studies [K. Wallmann, unpublished data; Biebow, 2002 #348].

Yet, the two species most widely applied in paleoceanography, *U. peregrina* and *Cibicides* spp., would not necessarily indicate CH_4 venting in their $\Delta\delta^{13}\text{C}$ signatures and in their absolute mean values at these sites (Fig. 7). Significant depletions in $\delta^{13}\text{C}$ are restricted to deeper endobenthic species

in the BM sites. Even then site BM37, which we assume as the highest CH_4 flux site, shows the limitations of benthic foraminifera to record CH_4 venting directly when bacterial mats, high CH_4 concentrations, and strongly poisonous conditions (high H_2S concentrations) prevail (Fig. 5 and 7). All species seem to get close to their respective limits of survival. Species either are absent from the live community or seem to migrate in smaller numbers towards the uppermost part of the sediment, reducing their MLD's (Fig. 5). The results are average $\delta^{13}\text{C}$ and $\Delta\delta^{13}\text{C}$ values that are virtually indistinguishable from the reference data at NV settings (Fig 7). Thus, the strongest CH_4 -emitting environment is not recorded in most species isotopic records. We acknowledge, though, that *G. auriculata* is an exception to this pattern with average values that remain around the negative offsets recorded for CF sites. But these *Dd13C* offsets in *G. auriculata* are well in the range of -2 ‰ to -3 ‰ and are based on only a few specimens. Isolated in a record, they may be hardly discernable from values that are depleted by low oxygen conditions, as $\delta^{13}\text{C}$ differences between *Cibicides* sp. and Globobuliminids have been proposed to record changes in bottom water oxygenation (McCorkle et al., 1997).

To determine why foraminifera respond so differently to increasing vent conditions and changes in environmental conditions (CF vs. BM), we discuss more closely possible incorporation patterns of MDC into the tests.

6.2. Species-specific $\delta^{13}\text{C}$ and $\delta^{18}\text{O}$ signatures at non-vent and CH_4 -influenced cold vent locations

5

Basically, two mechanisms have been proposed for the incorporation of MDC into foraminiferal tests at vent settings. The first is based on geochemical gradients, i.e. the rather direct uptake of isotopically lighter DIC that is partly modified by MDC that was previously oxidized in the water column. An alternative mechanism to deplete tests' $\delta^{13}\text{C}$ may be to influence the internal carbon pool for calcification by altering the food source $\delta^{13}\text{C}$ signature. Abundant, isotopically depleted, food at methane seeps like bacterial consortia may be an ecological advantage for foraminifera, perhaps with the help of symbiotic processes (Hill et al., 2003; Hill et al., 2004b; Mackensen et al., 2006; Rathburn et al., 2000; Torres et al., 2003). However, while food $\delta^{13}\text{C}$ is known to influence the $\delta^{13}\text{C}$ signal in planktic foraminifers by up to about 10 ‰, this mechanism to date remains unproven for benthic foraminifera (Mackensen et al., 2006). In addition, other unknown, so-called species-specific "vital" effects, based on microhabitat or dietary preferences, may alter the isotopic composition of benthic foraminifera (McCorkle et al., 1997; McCorkle et al., 1990; Rathburn et al., 1996). On the basis of their extensive datasets, (Rathburn et al., 2003)

reviewed possible causes for $\delta^{13}\text{C}_{\text{foram}}$ depletions and concluded that most likely $\delta^{13}\text{C}_{\text{foram}}$ values reflect the pore-water geochemistry, with possible influences of organic aggregates and bacteria that determine microhabitat patterns and match species' preferences. The relative importance, however, of biological, ecological, and physical factors remains unclear, in line with later studies (Hill et al., 2003; Mackensen et al., 2006; Torres et al., 2003).

5

Our data suggests that species' $\delta^{13}\text{C}$ change differently in response to different vent locations, pore-water chemistry, and CH_4 concentrations. Accordingly, we think that a species-specific, but variable combination of the factors outlined before, best matches the isotope results we got from our sites. In the following, we discuss possible influences on the $\delta^{13}\text{C}$ for each species separately. Further, we divide the species into two different groups.

10

15

One group, *Cibicides* spp., *U. peregrina*, *V. sadonica*, and *G. auriculata*, incorporates MDC in their tests and shows slight depletions in $\Delta\delta^{13}\text{C}$, but only until they near their limits for survival in BM sites. There, their $\Delta\delta^{13}\text{C}$ are less negative or not significantly depleted, though CH_4 influence is more intense. These species may have no advantage in living under more intense methane-venting BM conditions with more sulfidic and thus more demanding habitats. Accordingly, they retain their relative species-specific differences in $\Delta\delta^{13}\text{C}$ towards each other, confirming previous observations from

20

25

other seep sites (Rathburn et al., 2000; Rathburn et al., 2003). For ease of use, though simplified, we call this group "CH₄-conservative" taxa.

The other group comprises *E. batialis* and *N. labradorica*.

5 These two species differ from the other in that they have more depleted δ¹³C signatures in specific BM sites than in CF settings. In addition, each of the two species dominates the fauna at one BM site (Fig. 5); they occur throughout the respective sediment column and have more depleted values than
10 the co-occurring *U. peregrina*. This leads us to conclude that these two species have additional ecological capabilities, allowing them to better adapt to the sulfidic conditions at these BM sites. More depleted Δδ¹³C relative to other taxa under BM settings (Fig. 7) let us conclude that factors in
15 addition to the ones relevant in the first group are responsible for incorporation of MDC into the tests, possibly related to symbiosis or dietary preferences. Accordingly, we term them "CH₄-adapted" taxa.

20 **6.2.1. Cibicides spp.**

This group consists of two epifaunal species: *L. lobatula* and *C. mundulus*, which in our case show no discernable isotopic offsets between each other. We also briefly include *V. sadonica* as it shares many features but is not abundant
25 enough for a detailed statistical analysis. Under NV settings the *Cibicides* spp. group is positively offset to ambient δ¹³C_{DIC}

by about +0.4 ‰. We attribute this offset mainly to the temporal variability of the δ¹³C_{DIC} bottom water signal. Previous surveys in the Okhotsk Sea indicate that typical values for δ¹³C_{DIC} at the NE Sakhalin margin are around -0.3‰ at 600 m water
5 depth (H. Erlenkeuser, unpublished data), thus slightly higher than measured here and more in line with the δ¹³C derived from *C. mundulus* and *L. lobatula*. While a phytodetritus (or „Mackensen“-) effect (Mackensen et al., 1993) may develop in specimen of *Planulina wuellerstorfi*, it is not described for
10 these two species and previous studies of *C. mundulus* in the Okhotsk Sea show that the test should accurately reflect δ¹³C_{ΣCO₂} of the ambient bottom water, though phytodetritus deposits were present upon some sample recoveries (Bubenchshikova et al., subm. manuscript).

15 We note that comparable offsets of about +0.4‰ relative to δ¹³C_{DIC} have been described in *L. lobatula* from samples off NE-Greenland and Antarctic continental margins (Mackensen and Bickert, 1999; Mackensen et al., 2000). These positive deviations were ascribed to seasonal preferences in
20 calcification patterns during times with seasonal sea ice cover, when the δ¹³C_{DIC} is supposed to be higher by better ventilated intermediate waters formed through brine rejection in polynias (Mackensen and Bickert, 1999; Mackensen et al., 2000). A similar mechanism is likely responsible in the
25 Okhotsk Sea, where renewed ventilation of bottom waters mostly

takes place during late autumn to early spring (e.g. Shcherbina et al., 2003; Shcherbina et al., 2004).

However, the striking similarity of *Cibicides*-specific $\delta^{13}\text{C}$ offsets to $\delta^{13}\text{C}_{\text{DIC}}$ between two distant regions demands further studies to clarify whether not unspecified „vital“ effects rather than seasonal effects may bias the $\delta^{13}\text{C}$ signal of some species within this widely used group.

Cibicides spp. apparently responds to moderately elevated CH_4 concentrations at CF22 with depleted absolute $\delta^{13}\text{C}$ and $\Delta\delta^{13}\text{C}$ values and significantly lowered average $\delta^{13}\text{C}$ values at CF sites (Fig. 3 and 6). Median and mean $\Delta\delta^{13}\text{C}$ decrease more than 0.4 to 0.6 ‰, relative to NV conditions (Table 4, Fig. 7).

However, at CF24 and the BM sites, contrary to expectations, $\Delta\delta^{13}\text{C}$ mean and median values of both species are not depleted further, but remain close to $\delta^{13}\text{C}_{\text{DIC}}$ and CF settings. *Cibicides* spp. show larger standard deviations for BM settings, which indicate a more heterogeneous DIC environment for calcification or increased influence of other effects such as food supply with MDC. *Cibicides* spp. is an epibenthic suspension feeder. The deeper occurrence in the CF sites is likely due to the more porous nature of the microenvironment with numerous small-scale channels, colonizing tubeworms, mollusks, etc. These create small-scale pseudo-sediment surfaces deeper within the sediment, where *Cibicides* spp. finds hospitable living conditions. In addition, these CF sites are characterized by temporarily variable gas and fluid

flows and flow reversals of bottom water into the sediment, thus serving the species that has a low tolerance against low-oxygen conditions. In contrast, at BM sites *Cibicides* spp. apparently survive, but do not thrive under these unfavorable settings with stronger fluxes of CH_4 and higher sulphide gradients (Fig. 3) in the sediment column, though food sources (*Beggiatoa* mats) are abundant. Strong gradients in H_2S , reducing conditions, and high CH_4 are the more dominant factors that limit the ability of *Cibicides* spp. (and *V. sadonica*) to incorporate more negative MDC.

6.2.2 *U. peregrina*

U. peregrina is better adapted to lower oxygen and perhaps more sulfidic conditions than *Cibicides* spp. and *V. sadonica*. The species apparently occurs in all settings studied here. But the isotope results for *U. peregrina* show a pattern comparable to the one of *Cibicides* spp. (Fig 7). Relatively constant $\Delta\delta^{13}\text{C}$ depletions at NV sites, which are likely caused by microhabitat preferences and according pore-water $\delta^{13}\text{C}_{\text{DIC}}$ (McCorkle et al., 1997; Rathburn et al., 1996), changes into depleted $\Delta\delta^{13}\text{C}$ values at CF sites. Depletions are larger than in *Cibicides* spp. and indicate the incorporation of MDC. In contrast, at BM sites, $\Delta\delta^{13}\text{C}$ mean and median values are nearly indistinguishable from NV settings, though the species is abundant in nearly all BM.

This indicates that *U. peregrina* can survive and possibly even calcify under stronger anoxic or sulfidic conditions, in accordance with previous observations (Hill et al., 2004b; Rathburn et al., 2000; Rathburn et al., 2003; Torres et al., 2003). However, isotopes data from BM imply that the species does not calcify deeply in the sediment column. So while living conditions in greater depths may be favorable to a certain extent, e.g. to avoid predatory pressure, calcification in these depths is either not an advantage or the $\delta^{13}\text{C}$ is not influenced by MDC anymore. The latter seems unlikely, given the depletions observed at CF sites. An alternative possibility may be that *U. peregrina*, like *P. wuellerstorfi* (Mackensen et al., 2006), uses micro-environments that resemble near-surface conditions in greater sediment depth, such as burrows or channels from macrofauna, thereby ameliorating the otherwise too hostile surroundings. (Schmiedl et al., 2004) e.g. observed in non-seep sites a deep infaunal occurrence of the otherwise shallow endobenthic cogeneric *U. mediterranea* and suggested an association with macrofaunal burrows which in turn make available a microhabitat with geochemical characteristics similar to the topmost sediment column.

In essence, *U. peregrina* resembles a low-tolerance species in the BM settings, though it is able to survive under certainly already toxic conditions. Ecological thresholds seem to be reached at H_2S concentrations between 1,000 and 2,000 μM if one

accepts the MLD at BM46 and BM37, (Fig. 2 and 5). Another limiting, but yet unproven factor may be that too high alkalinity concentrations (more than about 8-10 mEq kg^{-1}) may hinder the species' calcification mechanism at this depth (Fig. 2).

6.2.3. *G. auriculata*

G. auriculata, is a species that is rather well adapted to low-oxygen conditions, in many cases presumed to live near the oxic-anoxic boundary under non-vent conditions if we consider other closely related Globobuliminids as indicative of ecological and microhabitat preferences (McCorkle et al., 1997; McCorkle et al., 1990; Rathburn et al., 1996; Schmiedl et al., 2004). It has been inferred that $\delta^{13}\text{C}$ differences between *Globobuliminida* spp. and epibenthic *Cibicides* spp. can be used to derive information about bottom water oxygen contents (e.g. Rathburn et al., 1996). While this interpretation is not straightforward for our NV sites (NV14 with highest $\delta^{13}\text{C}_{\text{GA}}$ has lowest O_2 content), the species seems to indicate increasingly dysoxic-anoxic conditions within the sediments by decreasing Dd^{13}C values over the entire range of our sites (fig. 7). $\Delta\delta^{13}\text{C}$ averages are well within the range of results from other sites (table 5 Hill et al., 2004b; Rathburn et al., 2003). Like in the other species, while negative $\Delta\delta^{13}\text{C}$ offsets may be not below values reported from other regions (Mackensen and Bickert, 1999; McCorkle et al., 1997; McCorkle

et al., 1990; Rathburn et al., 1996; Torres et al., 2003), they are significantly depleted compared to corresponding data from the same region (Table 3) and as such can be used as an indicator for seep activity. However, though the species may thrive under low-oxygen settings, under conditions of stronger CH_4 flux (BM sites) and accordingly more sulfidic environments only very few specimen of *G. auriculata* occur in two BM samples and it is absent from one site altogether (Fig. 5, BM38). This is in striking contrast to the endobenthic *N. labradorica* from the second group, which thrives in at least one site and occurs in another one much more abundantly. From the $\Delta\delta^{13}\text{C}$ data and the lower abundance it appears to us that *G. auriculata* does not change its preferred microhabitat near an anoxic-oxic pore-water boundary in methane-vent settings or its survival strategy. However, while at CF sites this oxic-anoxic boundary may be well developed, under BM settings these pore-water interfaces get fewer and are possibly more restricted, e.g. to small pockets along fluid-flow channels or locally O_2 -producing bacterial consortia.

In contrast to specimens from the second group, *G. auriculata* retains inter-species $\Delta\delta^{13}\text{C}$ differences irrelevant of the setting (Fig. 3-5, 7), thus indicating that the principle modes of isotope incorporation and calcification do not shift between non-vent and vent settings and represents the microhabitat, geochemical, and dietary preferences assumed for this species (Goldstein and Corliss, 1994; Rathburn et al.,

1996; Schmiendl et al., 2004), even under vent settings (Rathburn et al., 2003). As in the case of *U. peregrina*, we think that $\Delta\delta^{13}\text{C}_{\text{GA}}$ can be mainly explained by microhabitat preferences. However, at present we do not know what exactly causes the composition of the tests' $\delta^{13}\text{C}$ in these species, even under non-vent conditions. The more depleted $\Delta\delta^{13}\text{C}_{\text{GA}}$ values at BM sites may in part be caused or at least additionally depleted by an isotopically more negative food sources like methanotrophic bacterial consortia. The cogenetic *G. pacifica*, like *U. peregrina*, is a deposit feeder that ingests large amounts of sediment together with bacterial cells (Goldstein and Corliss, 1994). If dietary preferences of benthic foraminifera have a discernable influence on the tests' $\delta^{13}\text{C}$ (which still remains unproven), isotopically more depleted methanotrophic bacteria may have lowered *G. auriculata*'s $\delta^{13}\text{C}$. However, while small differences between ingested particles were observed by (Goldstein and Corliss, 1994) between *U. peregrina* and *G. pacifica*, to us it remains unconvincing that a similarly depleted $\delta^{13}\text{C}$ signal does not appear in *U. peregrina* at the same sites if food plays a prominent role in determining $\delta^{13}\text{C}$.

6.2.4. Incorporation patterns of MDC in "CH₄-conservative" species

Our results for this group suggest that these species are restricted in their ability to record $\delta^{13}\text{C}$ anomalies at methane

seeps to settings which are still comparably well ventilated or at least retain minimum amounts of oxygen for survival. Foraminifera stay alive under the more hostile BM settings with high H₂S gradients under cm-thick mats of bacteria.

5 However, absolute $\delta^{13}\text{C}$ and normalized $\Delta\delta^{13}\text{C}$ indicate that either tests were built during less intense venting intervals at the sediment surface or species' reproduction and calcification is restricted to short intervals or small areas with more favorable living conditions (e.g. small sub-mm pockets with remnants of bottom water within the upper sediment). Neither species seemed to take a clear advantage of the more abundant and isotopically extremely depleted bacterial food source at the BM sites (Fig. 5 and 7). To us, this makes unlikely the assumption that any of the species incorporated discernable negative $\delta^{13}\text{C}$ via metabolic CO₂ derived from MDC-depleted food sources as suggested (Bernhard et al., 2001; Hill et al., 2004b; Mackensen et al., 2006). More likely, *Cibicides* spp. and *U. peregrina* incorporate $\delta^{13}\text{C}_{\text{DIC}}$ analog to NV settings, for *Cibicides* spp. linearly related to $\delta^{13}\text{C}_{\text{DIC}}$ and in the case of *U. peregrina* and *G. auriculata* additionally mediated by microhabitat preferences. The used DIC is depleted by MDC on a small sub-sample scale in microhabitats that are sufficiently supplied with O₂, e.g. by alternating fluid flow directions at CF sites (Torres et al., 2002; Tryon et al., 1999). These sites may be highly heterogeneous in their geochemistry on a small scale that is not resolved by current sampling

techniques. Microhabitat heterogeneity has been inferred previously to explain smaller intra-sample $\delta^{13}\text{C}$ differences in non-vent settings (Loubere et al., 1995; Rathburn et al., 1996). Current pore-water and faunal sampling may simply not resolve the microhabitats on a "foraminiferal" (i.e. μm -mm) lateral and vertical scale. Given the steeper gradients in $\delta^{13}\text{C}_{\text{DIC}}$ pore-water profiles at seep than at non-seep locations (Rathburn et al., 2003; Torres et al., 2003), we would expect $\delta^{13}\text{C}_{\text{DIC}}$ under these conditions to vary vertically and horizontally by several per mille, even within less than a centimeter, enough to yield $\delta^{13}\text{C}_{\text{DIC}}$ comparable to our $\delta^{13}\text{C}_{\text{foram}}$ values. This larger microhabitat heterogeneity in pore-water characteristics under vent settings may also explain to a certain extent larger standard deviations in $\Delta\delta^{13}\text{C}$ under increased venting intensity (Fig. 8) and the larger $\Delta\delta^{13}\text{C}$ differences we encountered.

In addition, foraminifera with low tolerance towards calcification under low-oxygen or sulfidic habitats perhaps migrate to less hostile refuges e.g. near sub-centimeter fluid flow channels, tube worms, etc. that are abundant at vent settings, depending on the temporally varying intensity of methane and sulfide fluxes. However, (Rathburn et al., 2003, Rathburn, 1996 #357) assumed unlikely that foraminifera migrate several centimeters in depth for near-surface calcification and deeper food consumption, because of the considerable energy necessary for burrowing movements. In vent

settings, we think that these distances may be rather small (i.e. sub-cm) and perhaps the only chance for these taxa to survive. Other more species-specific strategies may come into play, too. It was observed e.g. that *P. wuellerstorfi* are mostly attached to pogonophoran tube worms at Håkon Mosby Mud Volcano (Mackensen et al., 2006). As one possible explanation, the isotopically depleted metabolic CO₂ derived from these organisms may be dissociated through the organic walls and then be used together with ambient DIC for calcification.

Though unproven, we assume less likely the alternative hypothesis that epibenthic suspension feeders calcifying close to $\delta^{13}\text{C}_{\text{DIC}}$ under NV conditions regardless of their food, change to a calcification mode under vent settings, where food-derived MDC is incorporated into the test. Basically, the same assumption should hold true for the shallow endobenthic deposit feeder *U. peregrina* that ingests bacteria with sediment particles at locations with no seepage. While the same feeding mechanism may be used in vent settings, apparently such a bacterial diet should influence the tests' $\delta^{13}\text{C}$, regardless of a CF or a BM setting. As this is not the case (Fig. 7), we assume that for *U. peregrina* other factors than food preferences account for the incorporation of MDC in the $\delta^{13}\text{C}$. These remain to be determined, but are likely a combination of microhabitat preferences and movements forced by toxic environments as well as geochemical gradients (Rathburn et al., 2003).

We regard *Cibicides* spp, *U. peregrina*, *G. auriculata*, and perhaps *V. sadonica* as a rather homogenous group of conservative "lower-tolerance" species with regard to methane venting environments, which do record MDC in their tests, but only as long as they are able to thrive. CF settings provide these conditions, but some BM sites with more prominent seepage do not. Due to their lower tolerance towards more sulfidic and dysoxic environments, these species may have threshold minimum $\delta^{13}\text{C}$ values below which they do not survive and thus would not record more prominent venting directly (Torres et al., 2003). This stands in contrast to the two other species, *N. labradorica* and *E. batialis* that seem to adopt species-specific strategies to cope with strongly reducing, CH₄-rich environments. However, the "CH₄-conservative" species may, too, exhibit much more negative absolute values than we encountered in other vent settings, caused by small-scale variability of preformed $\delta^{13}\text{C}_{\text{DIC}}$ of bottom and pore-waters (Hill et al., 2004b) or adaptation to micro-scale settings with supply of MDC (Mackensen et al., 2006).

6.2.5. *N. labradorica*

N. labradorica represents a special case with regard to its $\Delta\delta^{13}\text{C}$ characteristics because it shows continuously decreasing values from NV to CF and to BM sites (Fig. 3-5). It also shows the overall $\Delta\delta^{13}\text{C}$ minimum we encountered in this study (at site BM46). There, the species also occurs in abundance despite an

H₂S-rich, toxic environment. *N. labradorica* thus seems better adapted to dysoxic and specifically to toxic environments than the CH₄-conservative species.

One major ecological difference to the other species in this study is that *N. labradorica* sequesters chloroplasts, i.e. it retains the photosynthetic organelles of its prey while discarding the rest (Bernhard and Bowser, 1999). The specific advantage that this chloroplast retention may provide has been rather unclear, but is observed as well in other species that are well adapted to dysoxic to anoxic settings such as *Nonellina stella*, *Stainforthia fusiformis*, or *Virgulinema fragilis* (Bernhard, 2003; Bernhard and Alve, 1996; Bernhard and Bowser, 1999; Grzymski et al., 2002). It was assumed that these organelles provide metabolic products or ease nitrogen limitations and let these species survive in sulfidic settings (e.g. Bernhard et al., 2001; Grzymski et al., 2002). In one of these species, *V. fragilis*, a second bacterial endobiont was observed recently in addition to the harbored chloroplasts, indicating a multiple symbiosis in a sulfur-rich, dysoxic setting (Bernhard, 2003). It was suggested that these bacteria consume the respiratory-inhibitant H₂S, while leaving some oxygen available for foraminiferal mitochondria to keep phosphorylation going on, probably supported by the occurrence of the sulfide-oxidising *Beggiatoa* in the vicinity of the foraminifer, keeping the sulfide content of pore-waters tolerable (Bernhard, 2003). Notably, stable isotope analyses

showed strongly depleted δ¹³C values in these specimens. While we did not study the same species, we hypothesize that *N. labradorica* may follow a similar survival strategy in the H₂S-rich sediments we encountered at the BM sites. In this case, the depleted Δδ¹³C values of *N. labradorica* would be caused by isotopically depleted bicarbonate that is produced by the sulfate reduction as proposed by (Bernhard, 2003), and not by direct oxidation of methane. In consequence, negative δ¹³C values in *N. labradorica* would not be a primary indicator of intense methane venting, but of the intensity of sulfate reduction within the microhabitat of the species. Of course, both processes co-occur at cold seeps and cannot be disentangled from a foraminiferal δ¹³C value alone.

6.2.6. *E. batialis*

E. batialis is next to *N. labradorica* the only species that seemingly thrives in methane-enriched BM settings (Fig. 5 - BM38). At that site, *E. batialis* displays Δδ¹³C values similar to *N. labradorica* at site BM46, thus suggesting either a common incorporation mechanism or comparable survival strategy in H₂S-enriched, methane-vent settings. A number of species closely related to *E. batialis* have been reported to show ultrastructural evidence for chloroplast sequestration and occur in variable dysoxic or anoxic settings with functionally intact chloroplasts inside (for a review, see: Bernhard and Bowser, 1999, and references therein). However, in addition

E. batialis shows a pronounced covariation of $\Delta\delta^{18}\text{O}$ and $\Delta\delta^{13}\text{C}$ (Fig. 6). Such a positive correlation is rather atypical for benthic foraminifera. Most deep-sea benthic foraminifera build their tests near isotopic equilibrium with surrounding $\delta^{13}\text{C}_{\Sigma\text{CO}_2}$ of bottom or pore waters (Mackensen and Bickert, 1999; McCorkle et al., 1997; McCorkle et al., 1990; Rathburn et al., 1996). In case of isotopic disequilibria reported so far, $\delta^{13}\text{C}$ is solely affected while $\delta^{18}\text{O}$ remains either in equilibrium or offset constantly, suggesting metabolic influences on the internal foraminiferal DIC pool, or microhabitat or seasonal preferences not resolved by the studies (e.g. Corliss et al., 2002; Rathburn et al., 1996; Rathburn et al., 2000). Here, *E. batialis* values indicate a kinetic isotope fractionation in this species (McConnaughey, 1989a; McConnaughey, 1989b), characteristic for rapidly growing and calcifying organisms (McConnaughey, 1989a, and references therein). Indeed *Elphidium* spp. is a genus that has a highly opportunistic behavior. It reacts to changing environmental conditions with switching microhabitats, e.g. attaching to polychaete worm tubes in H_2S -rich settings. It responds fast to non-continuous food supply, and endures starvation periods with dormancy or agglutinated encystment (Linke and Lutze, 1993). *E. batialis* may be also capable of shifting its nutritional strategy according to environmental conditions (Linke and Lutze, 1993), a factor which would make a food-derived depleted $\delta^{13}\text{C}$ signal in this species more likely than the other we studied.

However, we do not observe higher $\Delta\delta^{13}\text{C}$ depletions compared to *N. labradorica* at BM settings, with abundant bacteria as additional food source. A pronounced dynamic adaptation of *E. batialis* to hostile living conditions is thus likely responsible for the prolonged survival at some BM sites and the incorporation of depleted MDC into the tests. In line with the observed $\Delta\delta^{18}\text{O} - \Delta\delta^{13}\text{C}$ covariance, we assume that *E. batialis* grows extremely rapidly in the Okhotsk Sea, even more so under BM settings, as the correlation coefficient for the linear regression (Fig. 5) is significantly higher for the BM38 site than for the others.

6.3. Implications for studies of palaeo-methane vents.

The fact that foraminiferal $\Delta\delta^{13}\text{C}$ values in the open and better mixed clam field settings are lower than in the more significantly emitting BM settings means that foraminiferal $\delta^{13}\text{C}$ is no well-suited proxy for the rate or magnitude of a given methane discharge event in the past, though one can infer from a wider scatter of data and depleted $\delta^{13}\text{C}$ values that a seep at a given point of time was active. A detailed approach with numerous single specimen analyses and statistic evaluation against nearby background sites would reveal sites of past gas discharge in sediment records (Hill et al., 2004a; Hill et al., 2004b; Kennett et al., 2000). In this regard we agree with others (Hill et al., 2006; Mackensen et al., 2006;

Rathburn et al., 2000; Rathburn et al., 2003). However, even then it cannot be automatically deduced that a large catastrophic release of gas hydrate has occurred (de Garidel-Thoron et al., 2004; Hill et al., 2004a; Kennett et al., 2000), as more localized cold seep venting could well produce a similar isotopic signature in the benthic foraminiferal fauna. We thus recommend to use additional indications of past seep/dissociation that might occur in the sediment column such as biomarkers indicating methanotrophy and their stable isotopes, but also significant occurrences of chemoautotrophic macrofauna fossils (vesicomyid clams, gastropods, fossilized tube worms, authigenic carbonate concretions' chemistry, etc.) may help identify fossil seep sites and distinguish them from gas hydrate dissociation events.

Apart from the apparent question, namely whether one can deduce past episodes of methane venting from $\delta^{13}\text{C}_{\text{foram}}$, another challenge remains to be tackled, namely to mechanistically understand how different benthic foraminiferal taxa incorporate isotopes under environmental conditions that near their ecological survival limits. As we apparently approached the survival limits for all species in site BM37 with a fauna at the edge of surrender to a hostile, sulfide-rich environment, it may be questionable that foraminifera are able to record prolonged, strong methane releases from cold seeps. In consequence, cold seeps may be not a suited analog for understanding the mechanisms of large-scale gas hydrate

releases. Sites of highest seepage are likely not inhabited (Mackensen et al., 2006) and might go unnoticed in the geological record. Furthermore, single sediment records do not necessarily witness large-scale events, they may record highly localized venting with limited impact on a regional or global scale. Thus, laterally widespread records would be needed to assess the history of submarine methane seepage at continental margins. In this regard, distal records that indicate depletions in $\delta^{13}\text{C}$ may be more helpful as they witness regional or basin-wide depletion of $\delta^{13}\text{C}_{\text{DIC}}$ in the water column (Martin et al., 2004; Torres et al., 2003).

Taken at face value, our data suggests that $\delta^{13}\text{C}$ of pristine foraminifera alone is no sufficient proxy for indicating discharge of large amounts of methane in the geological past. On the contrary, if values reported from fossil records really stem from pristine tests as suggested (de Garidel-Thoron et al., 2004; Hill et al., 2003; Hill et al., 2004a), the study of modern seep settings may well be inadequate in drawing conclusions about mechanisms operating on regionally larger scales and affecting the water column DIC chemistry in a larger way (Kennett et al., 2003). However, to date a main shortcoming of theories about paleo-methane dissociation events to be conclusive is a lack of records both in the temporal and spatial domain that with additional proxies give unambiguous evidence of methane release (Hill et al., 2006). Budget and model studies mostly rule out the dominant forcing

of Greenhouse gas concentrations by submarine methane releases in comparison to wetlands (Brook et al., 2000; Buffett and Archer, 2004; Dallenbach et al., 2000) and show that only a fraction of the total atmospheric methane variations may be due to geological sources (Maslin et al., 2004; Maslin and Thomas, 2003). As these amounts are still by no means small, but mostly remain unconsidered in today's budget calculations (Etiope and Milkov, 2004; Judd, 2003; Judd, 2004; Milkov, 2004; Milkov and Etiope, 2005), a better understanding of the dynamics in submarine geological methane emissions seems mandatory.

7. Conclusions

We reported stable isotope patterns from six selected live (rose Bengal-stained) benthic foraminiferal species derived from a wide range of non-seep and cold seep settings at the continental margin off northeast Sakhalin in the Okhotsk Sea. To our knowledge, these are the first reported isotope datasets of live foraminifera from this region. Absolute and normalized $\delta^{13}\text{C}$ values of all species record isotopically depleted methane-derived carbon in their test to variable extents. The degree of depletion is generally small but distinct, depending on the species and is accompanied by an increase in intraspecific $\Delta\delta^{13}\text{C}$ variability, as expressed in larger standard deviations.

BM sites yield stronger pore-water geochemical gradients and higher concentrations of toxic H_2S and methane in the sediment column. In contrast, the strongest $\delta^{13}\text{C}$ depletions occurred at CF sites for most taxa. At BM sites, $\delta^{13}\text{C}$ depletions were minor, but differed according to the species' individual ecological limits in a sulfidic, methane-enriched setting. Most species do not take advantage of more abundant bacterial food sources at BM sites, and show less depleted $\delta^{13}\text{C}$ in these settings. We conclude that traditional mechanisms (microhabitats, pore-water gradients, etc.) can explain $\delta^{13}\text{C}$ depletions if one takes into account that pore-water $\delta^{13}\text{C}_{\text{DIC}}$ may change below sampling resolution and that foraminifera dynamically change their life positions and strategies within the pore space. *N. labradorica* and *E. batialis* differ from the other species in that they thrive in BM sites and incorporate more negative $\delta^{13}\text{C}$ values. Both species likely retain chloroplasts in their tests for yet unknown endobiontically mediated metabolic processes that may enhance survival capacities under sulfidic and anoxic conditions. One such process may be a multiple symbiosis with sulfide-oxidising bacteria from bacterial mats that facilitate foraminiferal survival and provide isotopically depleted bicarbonate ions that are used for test construction, thus leading to more depleted $\delta^{13}\text{C}$ in these taxa.

Acknowledgements

We thank captain and crew of R/V SONNE as well as the shipboard scientific party for professional and friendly support during SO178. We are grateful for technical support by Anke Bleyer, Bettina Domeyer, and Lulzim Haxhiaj. We gratefully thank Nicole Stange for help in sample preparation. This study was funded by the German Ministry for Education and Research Grant "SONNE178-KOMEX". LLJ and WCD acknowledge support by DFG grant Du129/33 (Leibniz-Prize to WCD). We thank Tessa Hill, Jim Kennett, and Tony Rathburn for helpful comments on an earlier version of the manuscript and {insert reviewers} for critical comments that improved the manuscript.

References

- 15 Archer, D. and Buffett, B., 2005. Time-dependent response of the global ocean clathrate reservoir to climatic and anthropogenic forcing. *Geochemistry Geophysics Geosystems*, 6.
- 20 Bauch, D., Erlenkeuser, H., Winckler, G., Pavlova, G. and Thiede, J., 2002. Carbon isotopes and habitat of polar planktic foraminifera in the Okhotsk Sea: the 'carbonate ion effect' under natural conditions. *Marine Micropaleontology*, 871: 1-17.
- 25 Bernhard, J.M., 1988. Postmortem Vital Staining in Benthic Foraminifera - Duration and Importance in Population and

Distributional Studies. *Journal of Foraminiferal Research*, 18(2): 143-146.

- Bernhard, J.M., 2003. Potential symbionts in bathyal foraminifera. *Science*, 299(5608): 861-861.
- 5 Bernhard, J.M. and Alve, E., 1996. Survival, ATP pool, and ultrastructural characterization of benthic foraminifera from Drammensfjord (Norway): response to anoxia. *Marine Micropaleontology*, 28: 5-17.
- 10 Bernhard, J.M. and Bowser, S.S., 1999. Benthic foraminifera of dysoxic sediments: chloroplast sequestration and functional morphology. *Earth Science Reviews*, 46: 149-165.
- Bernhard, J.M., Buck, K.R. and Barry, J.P., 2001. Monterey Bay cold-seep biota: Assemblages, abundance, and ultrastructure of living foraminifera. *Deep-Sea Research Part I-Oceanographic Research Papers*, 48(10): 2233-2249.
- 15 Biebow, N., Kulinich, R. and Baranov, B. (Editors), 2002. Cruise Report R/V Akademik Lavrentiev Cruise LV29. GEOMAR Reports. GEOMAR Research Center for Marine Geosciences, Kiel, 190 pp.
- 20 Blunier, T., 2000. Paleoclimate - "Frozen" methane escapes from the sea floor. *Science*, 288(5463): 68-69.
- 25 Brook, E.J., Harder, S., Severinghaus, J., Steig, E.J. and Sucher, C.M., 2000. On the origin and timing of rapid changes in atmospheric methane during the last glacial period. *Global Biogeochemical Cycles*, 14(2): 559-572.

- Buffett, B. and Archer, D., 2004. Global inventory of methane clathrate: sensitivity to changes in the deep ocean. *Earth and Planetary Science Letters*, 227(3-4): 185-199.
- Corliss, B.H., McCorkle, D.C. and Higdon, D.M., 2002. A time series study of the carbon isotopic composition of deep-sea benthic foraminifera. *Paleoceanography*, 17(3).
- Dallenbach, A. et al., 2000. Changes in the atmospheric CH₄ gradient between Greenland and Antarctica during the Last Glacial and the transition to the Holocene. *Geophysical Research Letters*, 27(7): 1005-1008.
- de Garidel-Thoron, T., Beaufort, L., Bassinot, F. and Henry, P., 2004. Evidence for large methane releases to the atmosphere from deep-sea gas-hydrate dissociation during the last glacial episode. *Proceedings of the National Academy of Sciences of the United States of America*, 101(25): 9187-9192.
- Dickens, G.R., 1999. Carbon cycle - The blast in the past. *Nature*, 401(6755): 752-+.
- Dickens, G.R., 2003. Rethinking the global carbon cycle with a large, dynamic and microbially mediated gas hydrate capacitor. *Earth and Planetary Science Letters*, 213(3-4): 169-183.
- Dickens, G.R., 2004. Global change - Hydrocarbon-driven warming. *Nature*, 429(6991): 513-515.
- Etiopo, G. and Milkov, A.V., 2004. A new estimate of global methane flux from onshore and shallow submarine mud volcanoes to the atmosphere. *Environmental Geology*, 46(8): 997-1002.
- Fukamachi, Y. et al., 2004. Transport and modification processes of dense shelf water revealed by long-term moorings off Sakhalin in the Sea of Okhotsk. *Journal of Geophysical Research-Oceans*, 109(C9): C09S10, doi:10.1029/2003JC001906.
- Ginsburg, G.D., Soloviev, V.A., Cranston, R.E., Lorenson, T.D. and Kvenvolden, K.A., 1993. Gas Hydrates from the Continental-Slope, Offshore Sakhalin Island, Okhotsk Sea. *Geo-Marine Letters*, 13(1): 41-48.
- Goldstein, S.T. and Corliss, B.H., 1994. Deposit feeding in selected deep-sea and shallow-water benthic foraminifera. *Deep-Sea Research I*, 41(2): 229-241.
- Greinert, J., Bohrmann, G. and Suess, E., 2001. Gas Hydrate-Associated Carbonates and Methane-Venting at Hydrate Ridge: Classification, Distribution and Origin of Authigenic Lithologies. In: C.K. Paull and W.P. Dillon (Editors), *Natural Gas Hydrates: Occurrences, Distribution, and Detection*. Geophysical Monograph Series. American Geophysical Union, Washington, DC, pp. 99-114.
- Greinert, J. and Derkachev, A., 2004. Glendonites and methane-derived Mg-calcites in the Sea of Okhotsk, Eastern Siberia: implications of a venting-related

ikaite/glendonite formation. *Marine Geology*, 204(1-2): 129-144.

Grzyski, J., Schofield, O.M., Falkowski, P.G. and Bernhard, J.M., 2002. The function of plastids in the deep-sea benthic foraminifer, *Nonionella stella*. *Limnology and Oceanography*, 47(6): 1569-1580.

Heeschen, K.U. et al., 2005. Methane sources, distributions, and fluxes from cold vent sites at Hydrate Ridge, Cascadia Margin. *Global Biogeochemical Cycles*, 19(2).

10 Hill, T.M., Kennett, J.P. and Spero, H.J., 2003. Foraminifera as indicators of methane-rich environments: A study of modern methane seeps in Santa Barbara Channel, California. *Marine Micropaleontology*, 49(1-2): 123-138.

Hill, T.M., Kennett, J.P. and Spero, H.J., 2004a. High-
15 resolution records of methane hydrate dissociation: ODP Site 893, Santa Barbara Basin. *Earth and Planetary Science Letters*, 223(1-2): 127-140.

Hill, T.M., Kennett, J.P. and Valentine, D.L., 2004b. Isotopic evidence for the incorporation of methane-derived carbon
20 into foraminifera from modern methane seeps, Hydrate Ridge, Northeast Pacific. *Geochimica Et Cosmochimica Acta*, 68(22): 4619-4627.

Hill, T.M. et al., 2006. Climatically driven emissions of hydrocarbons from marine sediments during deglaciation.
25 *Proceedings of the National Academy of Sciences of the United States of America*, 103(37): 13570-13574.

Hut, G., 1987. Consultants group meeting on stable isotope reference samples for geochemical and hydrological investigations, International Atomic Energy Agency, Vienna.

5 Itou, M., Ono, T. and Noriki, S., 2003. Provenance of intermediate waters in the western North Pacific deduced from thermodynamic imprint on delta C-13 of DIC. *Journal of Geophysical Research-Oceans*, 108(C11).

Judd, A.G., 2003. The global importance and context of methane escape from the seabed. *Geo-Marine Letters*, 23(3-4): 147-154.

Judd, A.G., 2004. Natural seabed gas seeps as sources of atmospheric methane. *Environmental Geology*, 46(8): 988-996.

15 Kennett, J.P., Cannariato, K.G., Hendy, I.L. and Behl, R.J., 2000. Carbon isotopic evidence for methane hydrate instability during quaternary interstadials. *Science*, 288(5463): 128-133.

Kennett, J.P., Cannariato, K.G., Hendy, I.L. and Behl, R.J.,
20 2003. *Methane Hydrates in Quaternary Climate Change - The Chlathrate Gun Hypothesis*. American Geophysical Union, Washington, DC, 216 pp.

Kvenvolden, K.A., 1999. Potential effects of gas hydrate on human welfare. *Proceedings of the National Academy of
25 Sciences of the United States of America*, 96(7): 3420-3426.

- Kvenvolden, K.A. and Rogers, B.W., 2005. Gaia's breath - global methane exhalations. *Marine and Petroleum Geology*, 22(4): 579-590.
- Lammers, S., Suess, E. and Hovland, M., 1995a. A Large Methane Plume East of Bear Island (Barents Sea) - Implications for the Marine Methane Cycle. *Geologische Rundschau*, 84(1): 59-66.
- Lammers, S., Suess, E., Mansurov, M.N. and Anikiev, V.V., 1995b. Variations of Atmospheric Methane Supply from the Sea-of-Okhotsk Induced by the Seasonal Ice Cover. *Global Biogeochemical Cycles*, 9(3): 351-358.
- Linke, P. and Lutze, G.F., 1993. Microhabitat preferences of benthic foraminifera—a static concept or a dynamic adaptation to optimize food acquisition. *Marine Micropaleontology*, 20: 215-234.
- Linke, P., Wallmann, K., Suess, E., Hensen, C. and Rehder, G., 2005. In situ benthic fluxes from an intermittently active mud volcano at the Costa Rica convergent margin. *Earth and Planetary Science Letters*, 235(1-2): 79-95.
- Loubere, P., Meyers, P. and Gary, A., 1995. Benthic foraminiferal microhabitat selection, carbon isotope values, and association with larger animals: A test with *Uvigerina peregrina*. *Journal of Foraminiferal Research*, 25: 83-95.
- Ludmann, T. and Wong, H.K., 2003. Characteristics of gas hydrate occurrences associated with mud diapirism and gas escape structures in the northwestern Sea of Okhotsk. *Marine Geology*, 201(4): 269-286.
- Luff, R. and Wallmann, K., 2003. Fluid flow, methane fluxes, carbonate precipitation, and biogeochemical turnover in gas hydrate-bearing sediments at Hydrate Ridge, Cascadia margin: Numerical modelling and mass balances. *Geochimica Et Cosmochimica Acta*, 67: 3403-3421.
- Mackensen, A. and Bickert, T., 1999. Stable Carbon Isotopes in Benthic Foraminifera: Proxies for Deep and Bottom Water Circulation and New production. In: G. Fischer and G. Wefer (Editors), *Use of Proxies in Paleoceanography: Examples from the South Atlantic*. Springer-Verlag, Berlin Heidelberg, pp. 229-254.
- Mackensen, A., Hubberten, H.-W., Bickert, T., Fischer, G. and Fuetterer, D.K., 1993. The $\delta^{13}\text{C}$ in benthic foraminiferal tests of *Fontbotia wuellerstorfi* (Schwager) relative to the $\delta^{13}\text{C}$ of dissolved inorganic carbon in southern ocean deep water: Implications for glacial ocean circulation models. *Paleoceanography*, 8(5): 587-610.
- Mackensen, A., Schumacher, S., Radke, J. and Schmidt, D.N., 2000. Microhabitat preferences and stable carbon isotopes of endobenthic foraminifera: clue to quantitative reconstruction of oceanic new production? *Marine Micropaleontology*, 40(3): 233-258.
- Mackensen, A., Wollenburg, J. and Licari, L., 2006. Low delta C-13 in tests of live epibenthic and endobenthic

- foraminifera at a site of active methane seepage. *Paleoceanography*, 21(2).
- Martin, J.B. et al., 2004. Relationships between the stable isotopic signatures of living and fossil foraminifera in Monterey Bay, California. *Geochemistry Geophysics Geosystems*, 5.
- Maslin, M., Owen, M., Day, S. and Long, D., 2004. Linking continental-slope failures and climate change: Testing the clathrate gun hypothesis. *Geology*, 32(1): 53-56.
- 10 Maslin, M.A. and Thomas, E., 2003. Balancing the deglacial global carbon budget: the hydrate factor. *Quaternary Science Reviews*, 22(15-17): 1729-1736.
- Matveeva, T. et al., 2003. Geochemistry of gas hydrate accumulation offshore NE Sakhalin Island (the Sea of Okhotsk): results from the KOMEX-2002 cruise. *Geo-Marine Letters*, 23(3-4): 278-288.
- 15 Mau, S. et al., 2006. Estimates of methane output from mud extrusions at the erosive convergent margin off Costa Rica. *Marine Geology*, 225(1-4): 129-144.
- 20 McConnaughey, T., 1989a. ^{13}C and ^{18}O isotopic disequilibrium in biological carbonates: I. Patterns. *Geochimica Et Cosmochimica Acta*, 53: 151-162.
- McConnaughey, T., 1989b. ^{13}C and ^{18}O isotopic disequilibrium in biological carbonates: II. in vitro simulation of kinetic isotope effects. *Geochimica Et Cosmochimica Acta*, 25 53: 163-171.
- McCorkle, D.C., Corliss, B.H. and Farnham, C.A., 1997. Vertical distributions and stable isotopic compositions of live (stained) benthic foraminifera from the North Carolina and California continental margins. *Deep-Sea Research Part I-Oceanographic Research Papers*, 44(6): 5 983-1024.
- McCorkle, D.C., Keigwin, L.D., Corliss, B.H. and Emerson, S.R., 1990. The Influence of Microhabitats on the Carbon Isotopic Composition of Deep-Sea Benthic Foraminifera. *Paleoceanography*, 5(2): 161-185.
- 10 Milkov, A.V., 2004. Global estimates of hydrate-bound gas in marine sediments: how much is really out there? *Earth-Science Reviews*, 66(3-4): 183-197.
- Milkov, A.V. and Etiope, G., 2005. Global methane emission through mud volcanoes and its past and present impact on the Earth's climate-a comment. *International Journal of Earth Sciences*, 94(3): 490-492.
- 15 Nisbet, E.G., 2002. Have sudden large releases of methane from geological reservoirs occurred since the Last Glacial Maximum, and could such releases occur again? *Philosophical Transactions of the Royal Society of London Series a-Mathematical Physical and Engineering Sciences*, 20 360(1793): 581-607.
- O'Neil, J.R., Clayton, R.N. and Mayeda, T.K., 1969. Oxygen isotope fractionation in divalent metal carbonates. *J. Chem. Phys.*, 51: 5547-5558.

- Obzhairov, A., 1993. Gas Geochemical Fields of near-Bottom Water Layer of the Seas and Oceans (in Russian). NAUKA, Moscow.
- Obzhairov, A. et al., 2004. Relations between methane venting, geological structure and seismo-tectonics in the Okhotsk Sea. *Geo-Marine Letters*, 24(3): 135-139.
- Obzhairov, A.I., Astakhov, A.S. and Astakhova, N.V., 2000. Genesis and conditions of formation of authigenous carbonates in the quarternary sedimentary cover in the region of the Sakhalin-Deryugin gas anomaly (Sea of Okhotsk). *Oceanology*, 40(2): 258-266.
- Obzhairov, A.I. et al., 2002. Methane monitoring in waters of the eastern shelf and slope of Sakhalin. *Geologiya i Geofizika*, 43(7): 605-612.
- Rathburn, A.E., Corliss, B.H., Tappa, K.D. and Lohmann, K.C., 1996. Comparisons of the ecology and stable isotopic composition of living (stained) benthic foraminifera from the Sulu and South China Seas. *Deep-Sea Research I*, 43(10): 1617-1646.
- Rathburn, A.E., Levin, L.A., Held, Z. and Lohmann, K.C., 2000. Benthic foraminifera associated with cold methane seeps on the northern California margin: Ecology and stable isotopic composition. *Marine Micropaleontology*, 38(3-4): 247-266.
- Rathburn, A.E. et al., 2003. Relationships between the distribution and stable isotopic composition of living benthic foraminifera and cold methane seep biogeochemistry in Monterey Bay, California. *Geochemistry Geophysics Geosystems*, 4.
- Schmiedl, G., Pfeilsticker, M., Hemleben, C. and Mackensen, A., 2004. Environmental and biological effects on the stable isotope composition of recent deep-sea benthic foraminifera, from the western Mediterranean Sea. *Marine Micropaleontology*, 51(1-2): 129-152.
- Shackleton, N.J., 1974. Attainment of isotopic equilibrium between ocean water and the benthonic foraminifera genus *Uvigerina*: Isotopic changes in the ocean during the last glacial. *Cent. Nat. Sci. Colloq. Int.*, 219: 203-209.
- Shakirov, R., Obzhairov, A., Suess, E., Salyuk, A. and Biebow, N., 2004. Mud volcanoes and gas vents in the Okhotsk Sea area. *Geo-Marine Letters*, 24(3): 140-149.
- Shcherbina, A.Y., Talley, L.D. and Rudnick, D.L., 2003. Direct observations of North Pacific ventilation: Brine rejection in the Okhotsk Sea. *Science*, 302(5652): 1952-1955.
- Shcherbina, A.Y., Talley, L.D. and Rudnick, D.L., 2004. Dense water formation on the northwestern shelf of the Okhotsk Sea: 1. Direct observations of brine rejection. *Journal of Geophysical Research-Oceans*, 109(C9): C09S08, doi:10.1029/2003JC002196.
- Sommer, S. et al., 2006. Efficiency of the benthic filter: Biological control of the emission of dissolved methane

from sediments containing shallow gas hydrates at Hydrate Ridge. *Global Biogeochemical Cycles*, 20(2).

Sowers, T., 2006. Late Quaternary Atmospheric CH₄ Isotope Records Suggests Marine Chlathrates Are Stable. *Science*, 311: 838-840.

5 Stott, L.D. et al., 2002. Does the oxidation of methane leave an isotopic fingerprint in the geologic record? *Geochemistry Geophysics Geosystems*, 3.

Torres, M.E. et al., 2002. Fluid and Chemical fluxes in and out of sediments hosting methane hydrate deposits on Hydrate Ridge, OR, I: Hydrological provinces. *Earth and Planetary Science Letters*, 201: 525-540.

10 Torres, M.E. et al., 2003. Is methane venting at the seafloor recorded by delta C-13 of benthic foraminifera shells? *Paleoceanography*, 18(3).

15 Tryon, M.D. et al., 1999. Measurements of transience and flow cycling near episodic methane gas vents, Hydrate Ridge, Cascadia. *Geology*, 27: 1075-1078.

Wallmann, K. et al., 2006. Kinetics of organic matter degradation, microbial methane generation, and gas hydrate formation in anoxic marine sediments. *Geochimica Et Cosmochimica Acta*, 70(15): 3905-3927.

20 Wefer, G., Heinze, P.M. and Berger, W.H., 1994. Clues to Ancient Methane Release. *Nature*, 369(6478): 282-282.

Wong, H.K. et al., 2003. Bottom current-controlled sedimentation and mass wasting in the northwestern Sea of Okhotsk. *Marine Geology*, 201(4): 287-305.

Yoshida, O., Inoue, H.Y., Watanabe, S., Noriki, S. and 5 Wakatsuchi, M., 2004. Methane in the western part of the Sea of Okhotsk in 1998-2000. *Journal of Geophysical Research-Oceans*, 109(C9): C09S12, doi:10.1029/2003JC001910.

Figure Captions

Figure 1: Map of northeastern continental margin off Sakhalin, with locations of non-vent Multicorer sites. Blue box show the locations of vent sites within the flare area on a backscatter image derived from a profile shot during SO178. Excerpt pictures are from locations of nearby individual gas flares as an example for gas seepage in the area.

Figure 2: Porewater profiles for vent sites against sediment profile depths (in cm below surface). From top left to bottom right: sulphide (H_2S) (in μM). Sulphate (in mM), alkalinity (in mEq kg^{-1}). Phosphate (in μM). Note that H_2S is plotted on a logarithmic scale. Site legends all as in the SO_4 plot.

Figure 3: Non-vent (NV) sites. Sites are ordered with increasing methane concentrations in bottom water, from top to bottom: NV14, NV13, and NV29. Absolute d^{13}C values of benthic species against depth (cm below surface). Values from intervals are set at 0.5 cm intervals (e.g. 1-2 cm slab at 1.5 cm). Values at 0 cm are from a separately sampled phytodetritus ("fluff") layer. Black filled circles: *Cibicides mundulus* and *Lobatula lobatula*, red diagonal crosses: *Uvigerina peregrina*, empty violet rhomb: *Elphidium batialis*, brown asterisks: *Valvulineria sadonica*, green open circles: *Nonionellina labradorica*, upright blue crosses: *Globobulima auriculata*.

Figure 4: Clam field vent (CF) sites. Sites are NV22 (top) and NV24 (bottom) in no order as there are no methane concentrations for NV24. d^{13}C values of benthic species against depth (cm below surface). Other legends are as in fig. 3. Only live *Cibicidoides* spp.

are shown, but deeper specimens are likely due to very uneven and rough sediment surfaces in clam field settings.

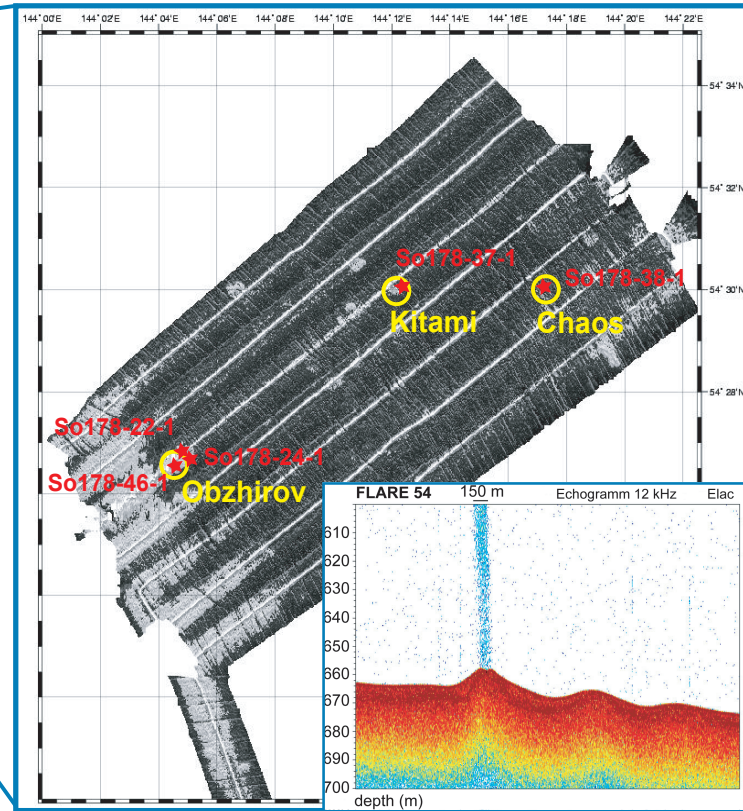
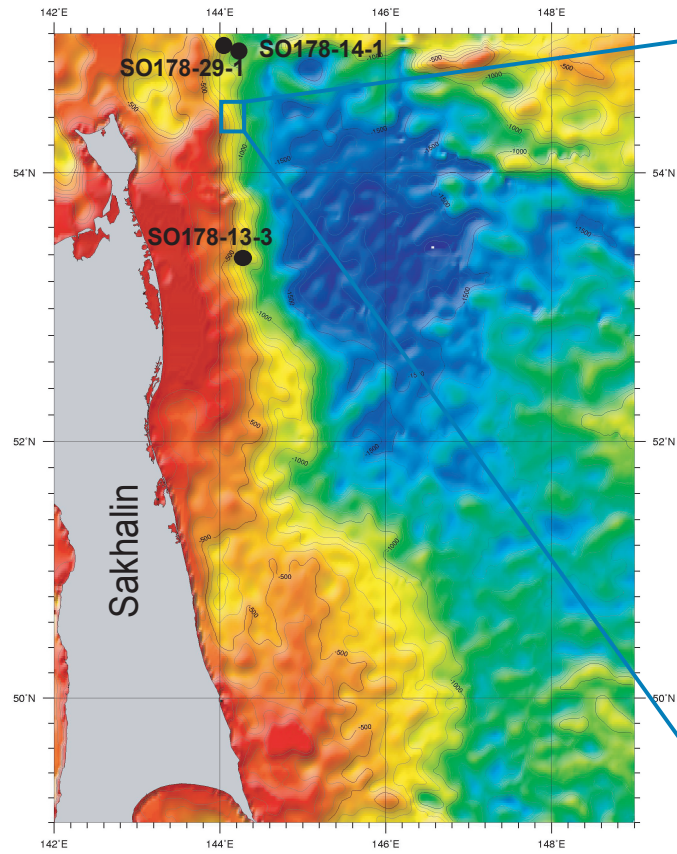
Figure 5: Bacterial mat vent (BM) sites. Sites are ordered with increasing methane concentrations in bottom water, from top to bottom: BM38, BM46, and BM37. Absolute d^{13}C values of benthic species against depth (cm below surface) Data legends as in fig. 3.

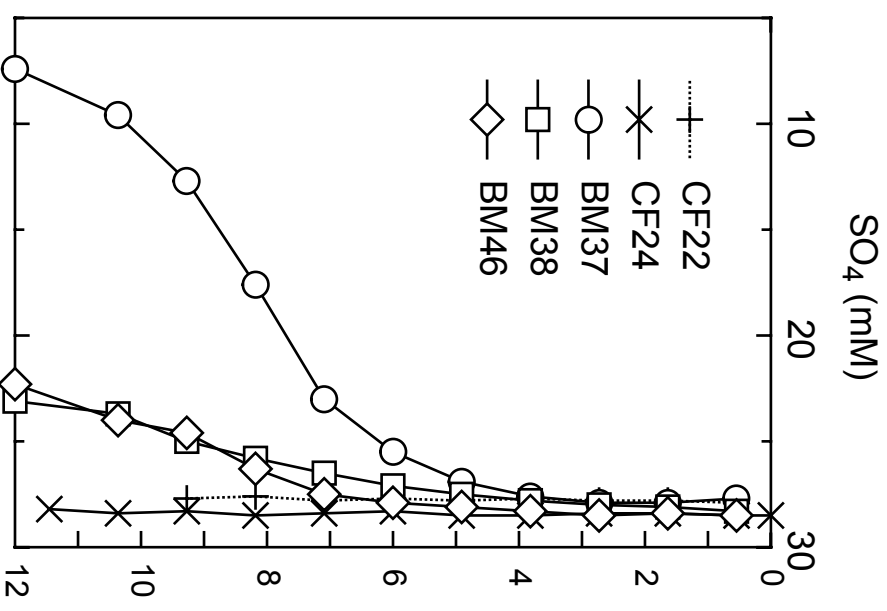
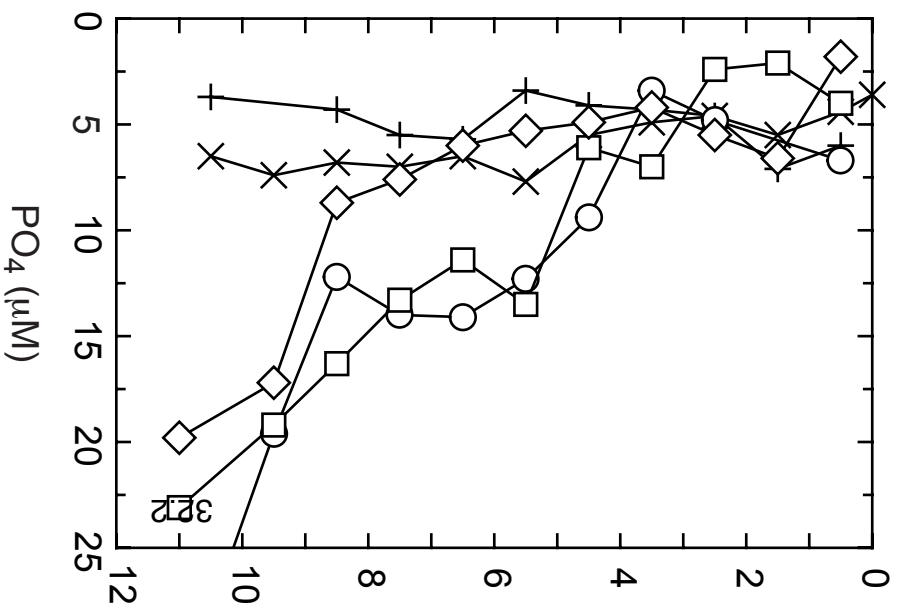
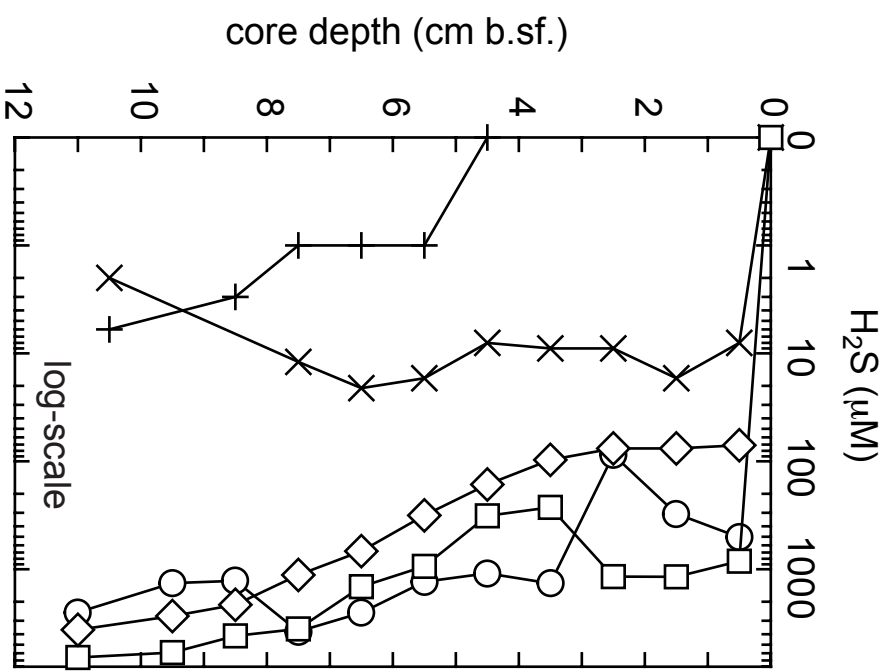
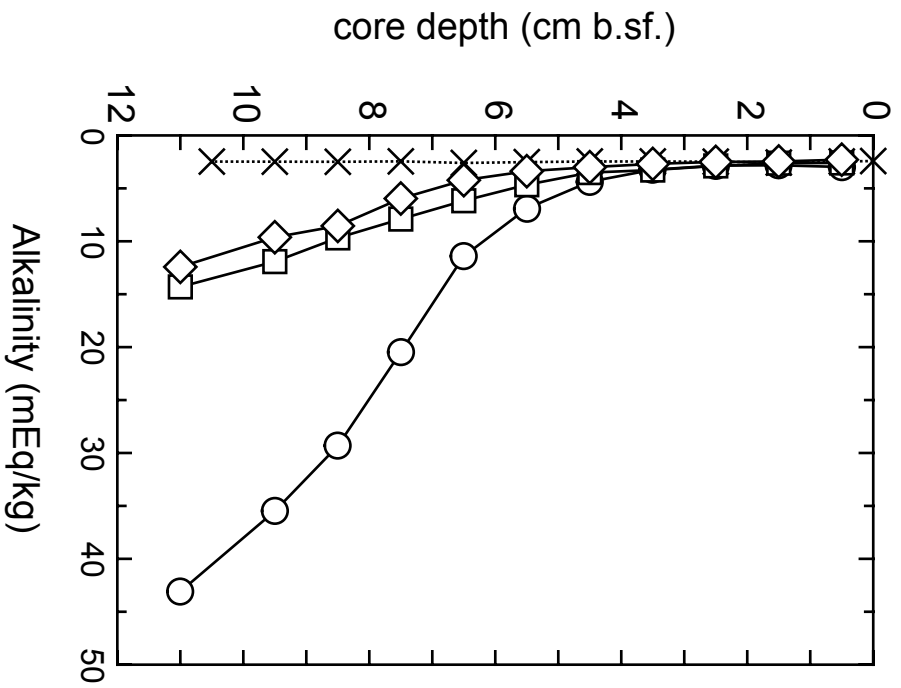
Figure 6: Dd^{18}O (i.e. $\text{d}^{18}\text{O}_{\text{foram}} - \text{d}^{18}\text{O}_{\text{ec-water}}$) vs. Dd^{13}C (i.e. $\text{d}^{13}\text{C}_{\text{foram}} - \text{d}^{13}\text{C}_{\text{DIC}}$) scatter plots. All isotope values are in ‰ vs. V-PDB. Plots are species-specific for (from top left to bottom right): *Cibicides* spp., *V. sadonica*, *U. peregrina*, *E. batialis*, *G. auriculata*, *N. labradorica*. Please note scale changes on both axes between different species. Stations are grouped as follows: NV sites = filled colored symbols, CF sites crosses, BM sites = open black symbols. Stations are: blue rectangles = NV14, black filled circle = NV13, green diamonds = NV29. Black upright crosses = CF22, red diagonal crosses = CF24. Open black rectangle = BM38, open black diamond = BM46, open black circle = BM37. Some single did not fit the scales, missing data are marked by symbol to the left of graph and is listed in dataset.

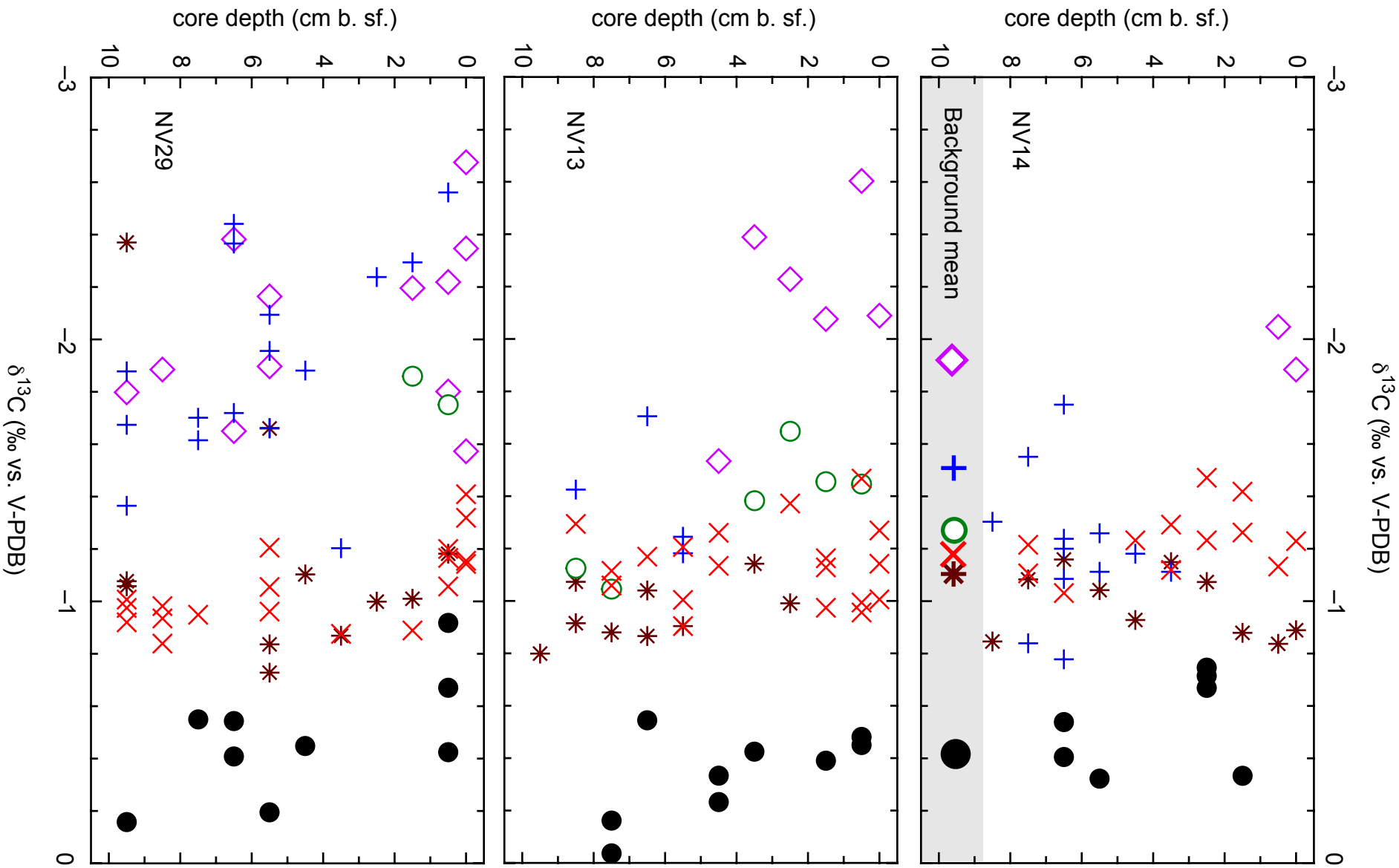
Figure 7: Species-specific box-and-whisker plots for Dd^{13}C . Station numbers on the y-axes. The vertical line in the box is the median value, the upper and lower ends of the boxes mark the upper quartile (median value of the upper half of the data points) and the lower quartile (median value of the lower half of the data points). Extending lines indicate the minimum and maximum values, while small and large dots represent close or far outliers, respectively. Light blue

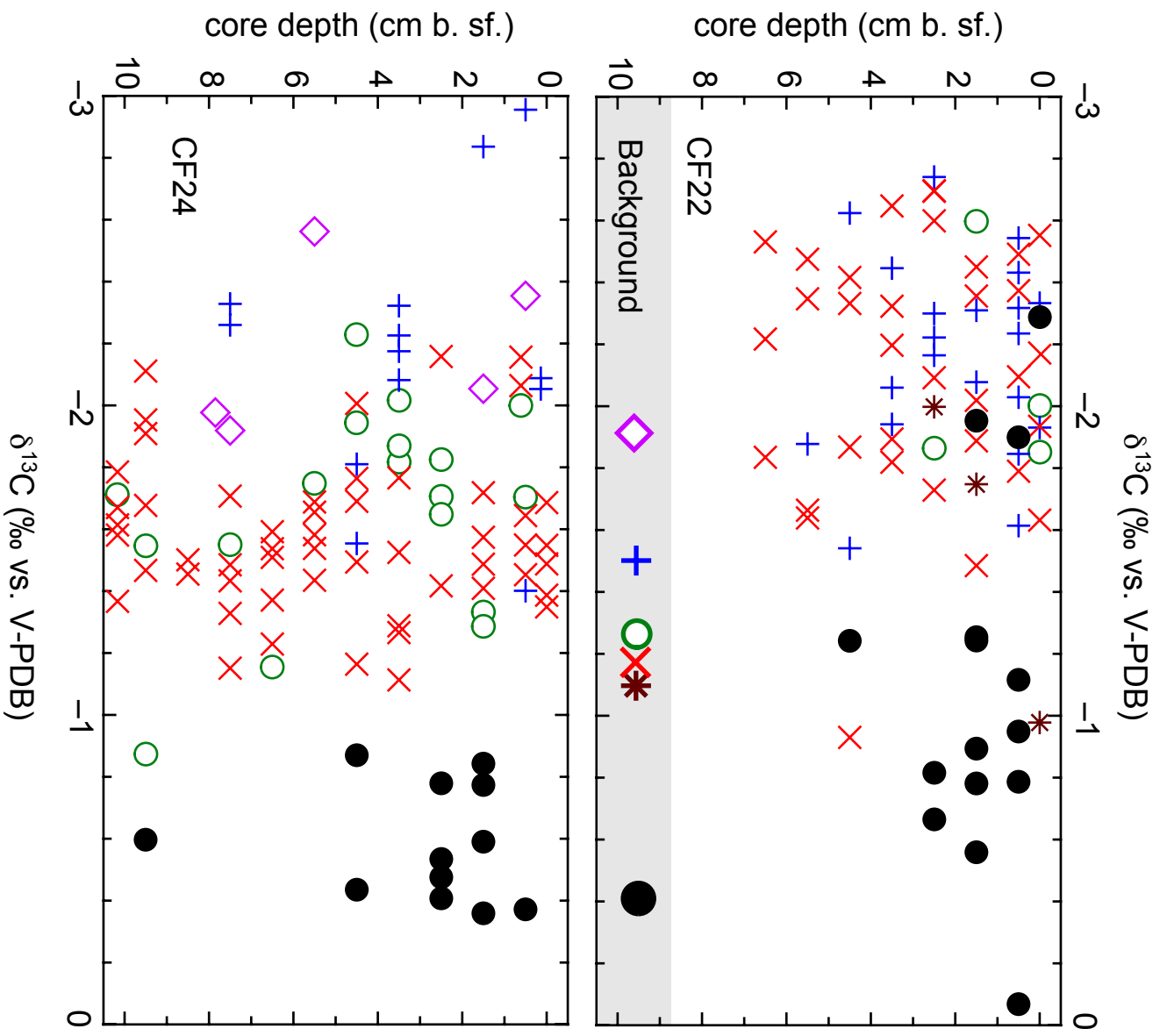
shading highlights the CF sites, darker blue shading the BM sites.

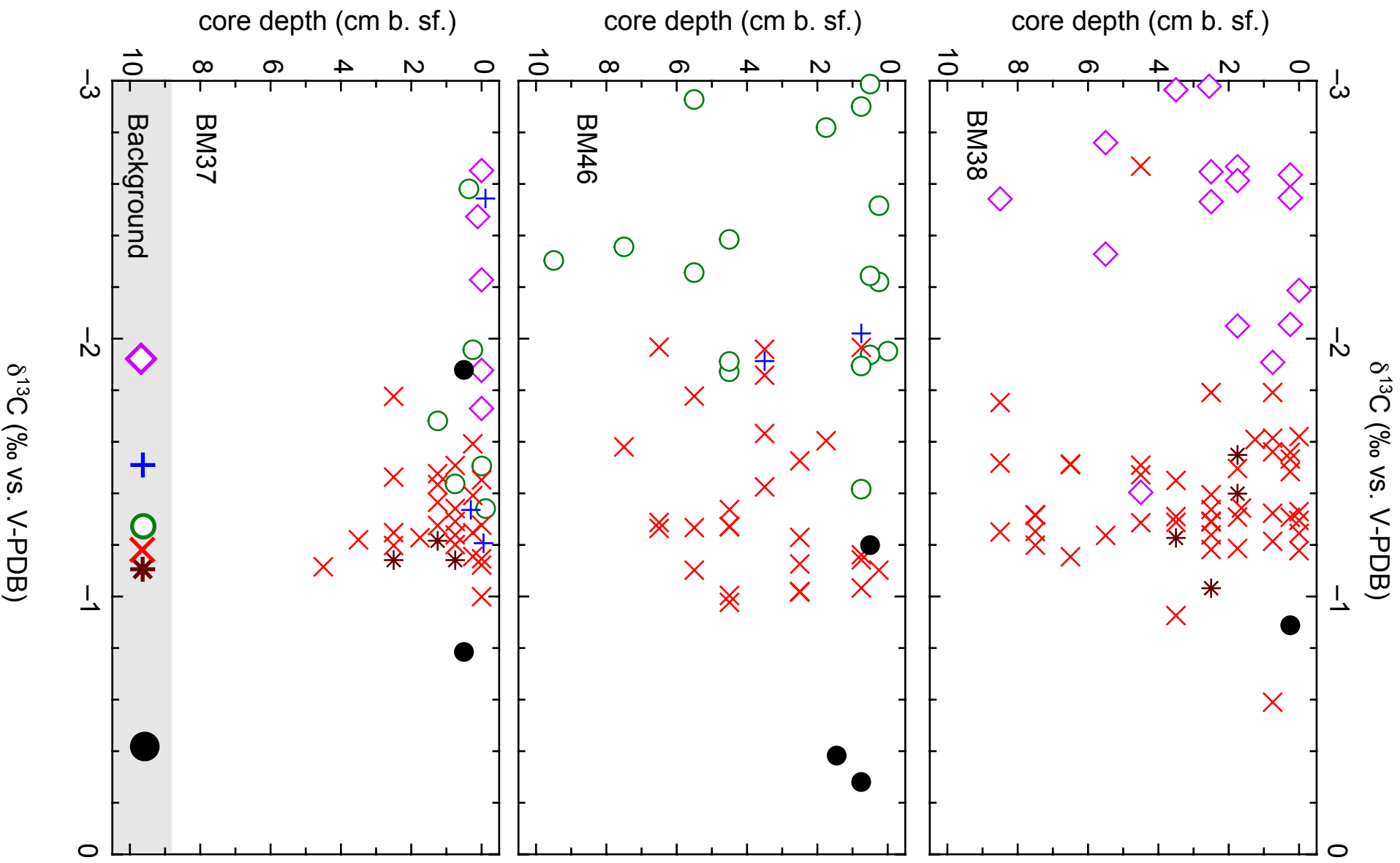
Figure 8: Comparison of species-specific standard deviations (s) of $\delta^{13}C$ (left y-axis) with methane concentrations (right y-axis) for every site. Please note that CH_4 concentrations (thick gray line) are on a logarithmic scale, while s (colored thin lines) are on a linear scale. MUC station numbers (x-axis) in order of increasing CH_4 concentrations. s are: *Cibicides* spp. = Black filled circles, *U. peregrina* = red crosses, *V. sadonica* = brown asterisks, *E. batialis* = violet open diamonds, *G. auriculata* = blue upright crosses, *N. labradorica* = green open circles. All connecting lines for s values are dotted, full lines between stations indicate that these sites were pooled for statistical analysis (see table 4).

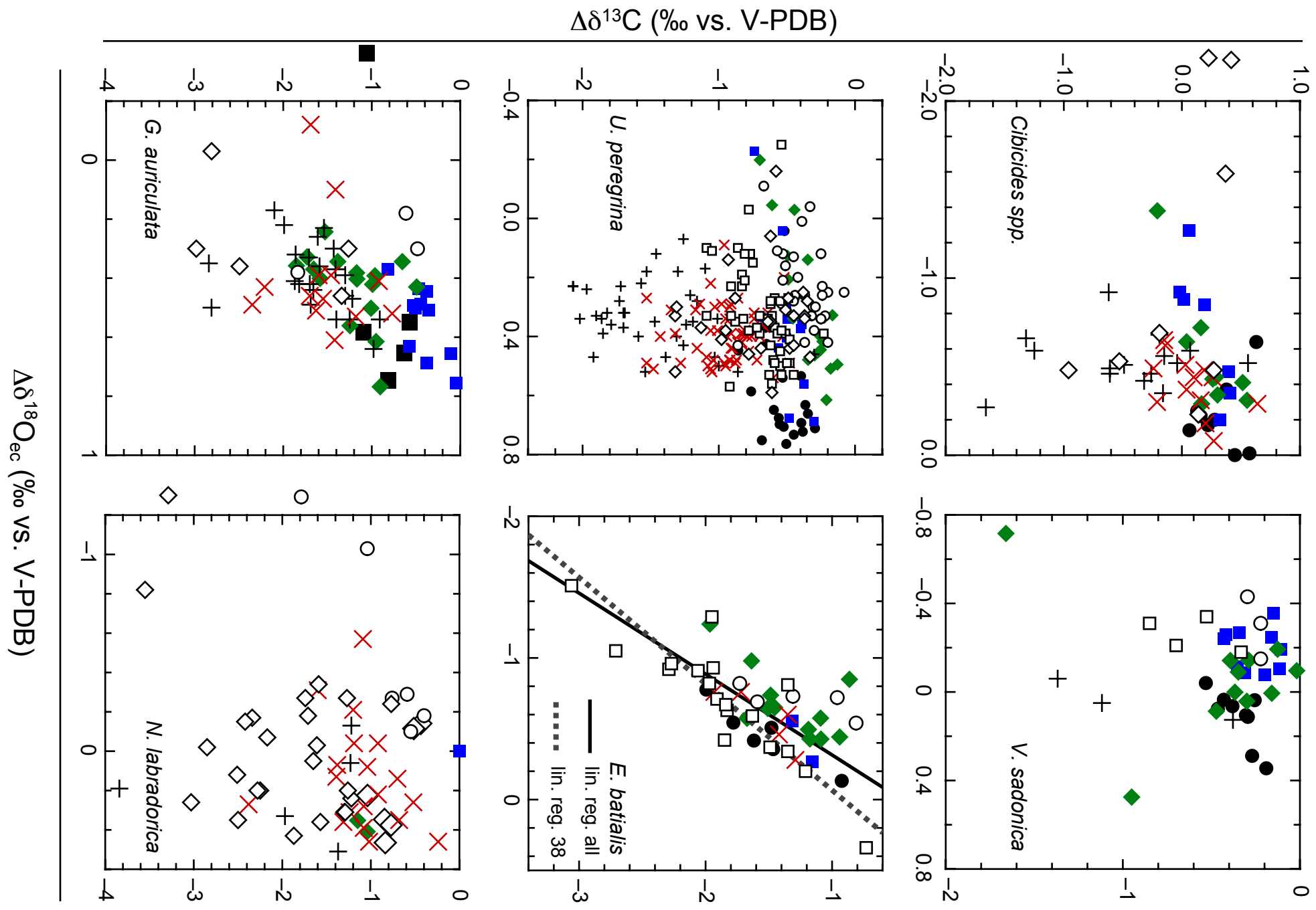


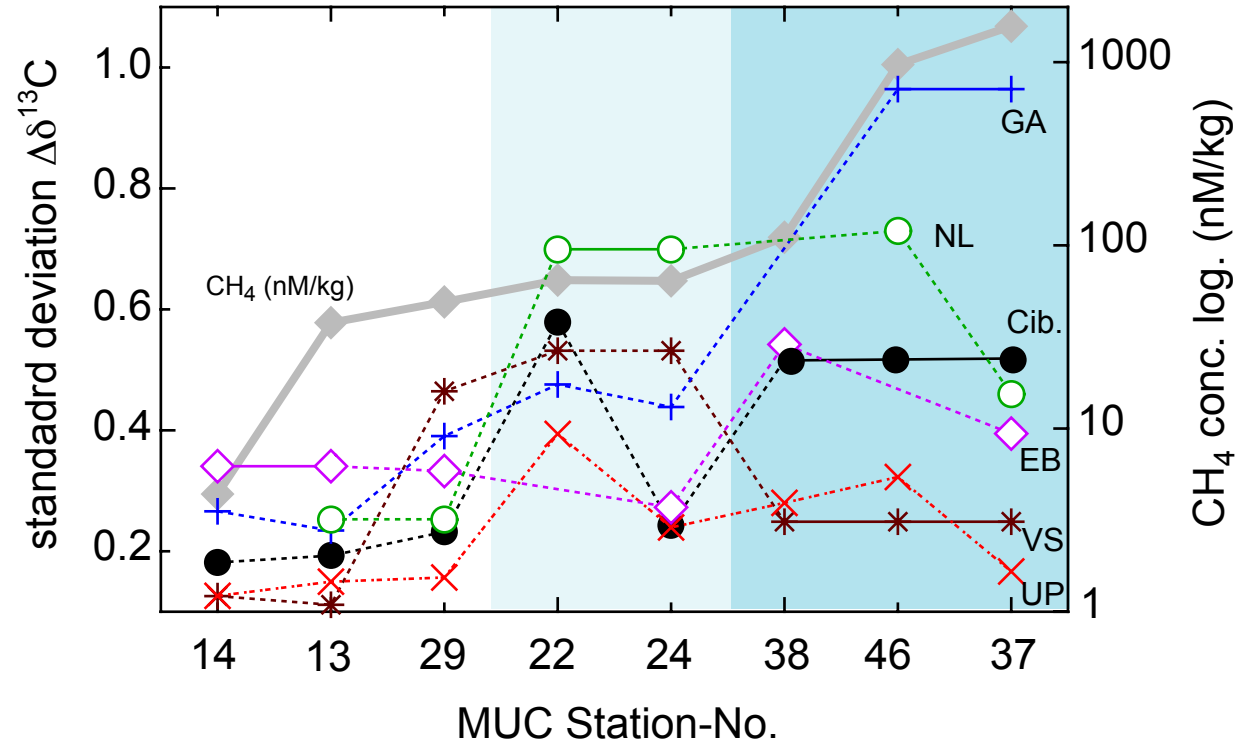












Stat. Nr.	Latitude N	Longitude E	water depth (m)	Recovery	Location	Remarks
SO178-13-3	52°43.880	144°42.648	702	7 liners	NE Sakhalin margin	App. 2 cm thick phytodetritus ("fluff") layer on top of sediment surface. Very soft-fluid upper 2 cm sediment.
SO178-14-4	53°24.094	144°39.977	1104	7 liners	NE Sakhalin margin	App. 1-2 cm thick phytodetritus ("fluff") layer on top of sediment surface. Very soft-fluid upper 2 cm sediment.
SO178-29-1	53°50.009	144°14.244	770	8 liners	NE Sakhalin margin	App. 1-2 cm thick phytodetritus ("fluff") layer on top of sediment surface. Very soft-fluid upper 2 cm sediment.
SO178-22-1	54°26.778	144°04.847	688	7 liners	Obzhirov Flare	Many clams recovered. Uneven surface due to clams.
SO178-24-1	54°26.785	144°04.902	689	3 liners	Obzhirov Flare	Many clams recovered, uneven surface with small caverns and holes down to 6 cm sediment depth.
SO178-37-1	54°30.071	144°12.337	871	7 liners	Kitami Flare	App. 5mm-thick Beggiatoa bacterial mat on top of sediment surface. Sediment strongly degassing.
SO178-38-1	54°30.076	144°17.261	962	7 liners	Chaos Flare	App. 5mm-thick Beggiatoa bacterial mat on top of sediment surface. Sediment strongly degassing.
SO178-46-1	54°26.660	144°04.812	689	7 liners	Obzhirov Flare	App. 5mm-thick Beggiatoa bacterial mat on top of sediment surface. Sediment strongly degassing. Gas bubbles rising in two tubes while on deck.

Table 2: Bottom water hydrography and geochemistry

Stat. Nr.	T (°C)	S	O ₂ (μM/kg)	CH ₄ (nM/kg)	DIC (mM/kg)	δ ¹³ C (‰ vs. V-PBD)	δ ¹⁸ O (‰ vs. V-SMOW)	δ ¹⁸ O _{ec} (‰ vs. V-
SO178-13-3	2.22	34.06	62.4	37.83	2.356	-0.61	-0.57	2.82
SO178-14-4	2.27	34.41	29.9	4.39	2.397	-0.73	-0.36	3.01
SO178-29-1	2.24	34.05	54.7	49.10	2.360	-0.71	-0.34	3.04
SO178-22-1	2.2 *	34.1*	61.5*	64.58	2.366*	-0.63	-0.45	2.94
SO178-24-1	2.2 *	34.1*	61.5*	-- π	2.366*	-- π	-0.50	2.89
SO178-37-1	2.27	34.05	48.1	1570.97	2.363	-0.92	-0.35	3.02
SO178-38-1	2.34	34.05	40.1	110.72	2.380	-0.7	-0.34	3.01
SO178-46-1	2.17	34.05	72.5	969.98	2.353	-0.65	-0.43	2.97

* Values are a mean of 8 nearby (<1 km) CTD stations at the near-bottom water depth

π MUC water samples did not reflect the ambient hydrochemistry and were discarded. We suspect contamination with upper water masses upon retrieval.

† Values for δ¹⁸O equilibrium calcite were calculated after Shackleton (1974) using the data of XXXX and a conversion factor of Hut

Table 5: Pore-water geochemistry data

Station	core depth (cm b.sf.)	H ₂ S (μ M)	PO ₄ (μ M)	Alkalinity (mEq/kg)
22	0.5	0	6.0	x
22	1.5	0	7.1	x
22	2.5	0	4.6	x
22	3.5	0	4.3	x
22	4.5	0	4.1	x
22	5.5	1	3.4	x
22	6.5	1	5.7	x
22	7.5	1	5.5	x
22	8.5	3	4.3	x
22	9.5	x	x	x
22	10.5	6	3.7	x
<hr/>				
24	0.0	0	3.6	2.42
24	0.5	8	4.4	2.46
24	1.5	17	5.5	2.56
24	2.5	9	4.6	2.48
24	3.5	9	4.9	2.46
24	4.5	8	5.5	2.46
24	5.5	17	7.7	2.52
24	6.5	21	6.5	2.60
24	7.5	12	7.0	2.45
24	8.5	0	6.8	2.49
24	9.5	0	7.4	2.48
24	10.5	2	6.5	2.47
<hr/>				
37	0.5	506	6.7	2.98
37	1.5	306	x	2.82
37	2.5	87	4.8	2.85
37	3.5	1353	3.4	3.24
37	4.5	1091	9.4	4.37
37	5.5	1306	12.3	6.90
37	6.5	2531	14.1	11.41
37	7.5	3773	14.0	20.47
37	8.5	1280	12.2	29.33
37	9.5	1345	19.6	35.49
37	11.0	2509	32.2	43.09
<hr/>				
38	0.0	x	x	x
38	0.5	842	4.0	2.60
38	1.5	1175	2.1	2.62
38	2.5	1170	2.4	2.88
38	3.5	267	7.0	3.27
38	4.5	320	6.1	3.51
38	5.5	940	13.5	4.66
38	6.5	1450	11.4	6.17
38	7.5	3572	13.3	7.90
38	8.5	4143	16.3	9.68
38	9.5	5913	19.2	11.92
38	11.0	6569	23.1	14.31
<hr/>				
46	0.5	71	1.8	2.29
46	1.5	76	6.6	2.46
46	2.5	76	5.5	2.50
46	3.5	97	4.2	2.69
46	4.5	164	4.9	3.00
46	5.5	317	5.3	3.38
46	6.5	680	6.0	4.23
46	7.5	1130	7.6	5.96
46	8.5	2134	8.7	8.55
46	9.5	2715	17.2	9.62
46	11.0	3639	19.8	12.42

Table 6: Compilation of previously published mean, minima, maxima from other vent locations for *Cibicides* spp. , *U. peregrina* , *Gobobulimina* spp.

Location	type	core-no.	$\delta^{13}\text{C}$ <i>Cibicides</i> spp.				$\delta^{13}\text{C}$ <i>U. peregrina</i>				$\delta^{13}\text{C}$ <i>Gobobulimina</i> spp.				Study
			Min.	Max.	mean	n	Min.	Max.	mean	n	Min.	Max.	mean	n	
Hydrate Ridge	non-vent	22MC	--	--	--	--	--	--	-0.83	?	--	--	--	--	Torres et al. (2003)
	non-vent	13MC	--	--	--	--	-0.62	-0.59	--	?	--	--	--	--	
Hydrate Ridge South	BM	37AD	--	--	--	--	-2.77	-1.77	--	?	--	--	--	--	
	BM	37AD	--	--	--	--	-2.03	-0.79	--	?	--	--	--	--	
Hydrate Ridge South	BM	3812/3813	-5.94	0.18	-3.01	8	-5.10	-0.41	-2.59	29	-3.63	-2.29	-2.84	3	Hill et al. (2004)
	CF	--	--	--	--	0	-2.29	-0.46	-1.28	13	--	--	--	--	Hill et al. (2004)
Haakon Mosby MV	unspec. MV	Atl18	--	--	-1.27	2	--	--	--	--	--	--	--	--	Mackensen et al. (2006)
	unspec. MV	Atl22	--	--	-1.07	3	--	--	--	--	--	--	--	--	
	unspec. MV	Atl25d	--	--	-3.29	2	--	--	--	--	--	--	--	--	
	background	Atl28	--	--	-0.03	2	--	--	--	--	--	--	--	--	
	unspec. MV	PS660002-3	--	--	-2.17	3	--	--	--	--	--	--	--	--	
	unspec. MV	PS660015-2	--	--	-0.77	5	--	--	--	--	--	--	--	--	
Eel River	CF	2	--	--	--	--	--	--	-0.96	1	--	--	-2.53	1	Rathburn et al. (2000) (pooled samples)
	CF	4	--	--	--	--	-1.51	-0.88	-1.13	7	--	--	--	--	
	CF	5	--	--	--	--	-1.53	-0.51	-1.19	7	--	--	-2.84	1	
Monterey Bay	CF	1780/TC30	--	--	--	--	-0.85	-0.04	-0.50	27	-2.23	-0.41	-1.28	26	Rathburn et al. (2003)
	BM	1780/TC67	--	--	--	--	-1.04	-0.61	-0.82	3	-1.50	-1.12	-1.28	3	
	CF	1781/31	--	--	--	--	-2.05	-0.21	-0.91	37	-5.36	-2.77	-4.01	5	
Sakhalin Margin	NV	14, 13, 29	-0.92	0.02	-0.43	26	-1.47	-0.84	-1.13	50	-2.56	-0.78	-1.58	32	This study
	CF	22, 24	-2.29	0.09	-0.84	28	-2.70	-0.93	-1.79	92	-3.47	-1.40	-2.34	36	
	BM	38, 37, 46	-1.88	-0.28	-0.90	6	-2.67	-0.59	-1.36	104	-3.63	-1.18	-2.40	8	

CF: Clam Field; BM: Bacterial Mat; MV: Mud Volcano
n: number of samples